Genetically Encoded Red and Far-red Fluorescent Indicators for Redox Signaling

Yu Pang

MS, Pharmaceutical Sciences, Temple University, 2016

A Dissertation presented to the Graduate Faculty

of the University of Virginia in Candidacy for the Degree of

Doctor of Philosophy

Department of Chemistry

University of Virginia

May 2023

May 2023

ABSTRACT

Reactive oxygen species (ROS) are typical examples of “the dose makes the poison”. When they are generated under physiological concentrations, they play critical roles in various biological functions, such as cell differentiation, tissue regeneration and inflammation response. On the other hand, when ROS were overproduced, they can cause damage to biomolecules, including DNA, protein and lipids and lead to many diseases’ initiation and progression. Therefore, monitoring the ROS signaling in biological system are essential for studying redox biology to further tackle the mechanism of different diseases.

Genetically encoded redox indicators (GERIs) are emerging as powerful tools for redox signaling detection in living systems. GERIs can measure real-time signals in the natural cellular context with minimal toxicity. Besides, by attaching specific localization sequences to the N- or C-terminus, GERIs can be readily localized to different subcellular compartments with super spatial and temporal resolution. In addition, GERIs present as plasmids or viral vectors, which can be easily adapted to various biological study systems and shared across different labs.

Red and far-red fluorescent proteins (FPs) have several advantages. First, compared to shorter wavelength emitters (blue FP/green FP), they are less cytotoxicity to the cells. Second, the red and far-red spectrums are within the “optical window” for maximal cell and tissue penetration, leading to reduced sample scattering and autofluorescence. Third, they provide additional channels in combination with blue/green FP for multicolor and multiparameter imaging.

In this thesis, I focus on developing red and far-red GERIs for the detection of different redox molecules. Based on our previous work—TrxRFP1, I performed directed evolution and enzymatic screening to develop a second-generation thioredoxin biosensor, TrxRFP2. I also used a similar strategy to fuse Trx2 enzyme with rxRFP1.1 to build a biosensor, MtrxRFP2, for detecting thioredoxin signaling in the mitochondria compartment. I tested both TrxRFP2 and MtrxRFP2 in vitro and different subcellular domains of cultured mammalian cells. This work expanded the collection of GERIs for thioredoxin signaling detection.

Another strategy was employed to develop a red GERI for peroxynitrite (ONOO-). Using a genetic code expansion technology, *p*-boronophenylalanine (*p*BoF) was introduced to a site close to the chromophore of a circularly permuted red FP scaffold (cpRFP). I performed thorough in vitro characterizations of this indicator. I also assessed its performance in mammalian cells in response to chemically and physiologically-related stimulations. X-ray crystallography and NMR methods were applied to investigate the response mechanism of this indicator.

Hydrogen peroxide (H_2O_2) play critical roles in many cellular processes and imaging the H_2O_2 signaling is always important for understanding the redox metabolism in biological system. I created a red GERI for H_2O_2 detection based on the brightest RFP mScarlet-I. I first generated a circularly permutated FP—cpmScarlet. Next, I fused two H_2O_2 sensory domains OxyR at the N- and C- terminus of cpmScarlet to build up the H_2O_2 indicator. I utilized protein engineering and directed evolution to improve the indicator brightness and responsiveness. I finally identified a candidate showing a good response to H_2O_2 with minimal photoactivation. This candidate was termed SHRIMP (a circularly

permutated mScarlet-based genetically encoded hydrogen peroxide red fluorescent indicator with high brightness and minimal photoactivation). I tested SHRIMP performance in HEK 293T cells and macrophages in response to chemically and physiologically-related stimulation. SHRIMP was also applied to isolated mouse islets to detect H_2O_2 generation with chemical stimulation. Last, SHRIMP was combined with a green calcium indicator for multiparameter imaging in mammalian cells.

I also further expanded the GERIs spectrum to the far-red region by creating a redox-active far-red fluorescent protein -- rxcpmMaroon1. I first fused the zinc hook domain which contains active cysteines with a circularly permutated far-red fluorescent protein (cpmMaroon185). Next, I performed further site-specific and random mutagenesis to improve the protein expression and redox responsiveness of the variant. Last, I characterized rxcpmMaroon1 in vitro as well as in cultured mammalian cells to test its performance in response to redox stimulation.

ACKNOWLEDGEMENTS

To begin, I want to express my sincere gratitude to my Ph.D. advisor, Hui-wang Ai, for his extensive support and enlightening guidance throughout my Ph.D. training. His mentorship provided me with the opportunity to step into the field of chemical biology and acquire diverse techniques. Additionally, I would like to thank my dissertation committee members, David Cafiso, Andreas Gahlmann, Cliff Stains, and Lian-wang Guo, for their valuable input and feedback on my research.

I am grateful to my colleagues, without whom I would not have been able to complete my Ph.D. degree. In particular, I want to thank Hao Zhang, Jing Zhang, and Yiyu Zhang for their coordination and hard work on our collaborations. I cherish the time we spent discussing life and science and wish everyone the best in their future endeavors.

I extend my heartfelt appreciation to my parents for their unconditional support, understanding and love throughout the years. Their hard work and efforts made it possible for me to explore my passion.

I want to express my sincere gratitude to the friends I made in Charlottesville. Our five years together were full of many firsts – first time camping, first 10-mile hiking, first Zumba/body pump classes, first time fishing/golfing. It wouldn't have been possible for me to live such a wonderful life without their companionship and love. I also want to thank my long-distance friends, both in the US and globally, for taking the time to share both the happy and sad moments with me. I believe the distance only strengthened our friendship.

Lastly, I want to dedicate my gratitude and love to my husband, Pengbo Guo. Thank you for driving long distances to visit me and thank for the many miles our 2014 Hybrid

Camry spent with us. We have shared 13 years of laughter and tears, and I eagerly look forward to our future journey together.

TABLE OF CONTENTS

LIST OF FIGURES

LIST OF TABLES

Chapter 1 Genetically Encoded Fluorescent Redox Indicators for Unveiling Redox Signaling and Oxidative Toxicity

This chapter is converted from a published paper: Pang, Yu, Hao Zhang, and Hui-wang Ai. "Genetically encoded fluorescent redox indicators for unveiling redox signaling and oxidative toxicity." *Chemical Research in Toxicology* 34, no. 8 (2021): 1826-1845. Pang, Yu and Hao Zhang contributed equally to this work.

1.1 Abstract

Redox-active molecules play essential roles in cell homeostasis, signaling, and other biological processes. Dysregulation of redox signaling can lead to toxic effects and subsequently cause diseases. Therefore, real-time tracking of specific redox-signaling molecules in live cells would be critical for deciphering their functional roles in pathophysiology. Fluorescent protein (FP)-based genetically encoded redox indicators (GERIs) have emerged as valuable tools for monitoring the redox states of various redox-active molecules from subcellular compartments to live organisms. In the first section of this review, we overview the background, focusing on the sensing mechanisms of various GERIs. Next, we review a list of selected GERIs according to their analytical targets and discuss their key biophysical and biochemical properties. In the third section, we provide several examples, which applied GERIs to understanding redox signaling and oxidative toxicology in pathophysiological processes. Lastly, a summary and outlook section are included.

1.2 Introduction of GERIs

Redox-active proteins (e.g., thioredoxin (Trx) and glutaredoxin (Grx)) and small molecules (e.g., various reactive oxygen species (ROS) and reactive nitrogen species (RNS)) are essential for maintaining cellular and physiological homeostasis.[1-5] They are involved in cell signaling and numerous physiological processes, such as cell cycle and differentiation, embryogenesis, inflammation, and tissue regeneration.[1-5] For example, cell growth factors, such as epidermal growth factor (EGF) and platelet-derived growth factor (PDGF), can increase the production of hydrogen peroxide (H_2O_2), a type of ROS, to promote signal transduction of the receptor tyrosine kinases (RTKs).[6] Another well-known example is that phagocytes can generate ROS/RNS bursts to clear pathogens.[7, 8] Redox-active molecules are also crucial for many pathological processes. Dysregulation of the cellular redox states can lead to oxidative stress, which is considered a central mechanism of toxicity in various tissues and organs.[9] Oxidative stress can cause damage to different biomolecules such as DNA, proteins, and lipids, leading to the initiation and progression of diverse diseases, including cancer, neurodegeneration, respiratory stress, and kidney disorders.[10-17] There is significantly increasing interest and demand in detecting and monitoring redox-active molecules in live cells and organisms.

An extensive array of methods and assays have been developed to detect redox-active molecules and processes. These methods include electron paramagnetic resonance (EPR) spectroscopy,[18] chemiluminescence assays,[19] and fluorescence assays based on either small molecule-based synthetic dyes[20-24] or genetically encoded redox indicators(GERIs).[25-29] GERI-based fluorescence methods have gradually gained popularity for several reasons: First, these indicators can be expressed by cell machinery, providing chances to measure redox signals in the natural cellular contexts while introducing minimal toxicity. Second, using tissue-specific

promoters or subcellular localization sequences, GERIs can be readily localized to specific tissues and subcellular compartments, giving superior spatial and temporal resolution over small molecule synthetic dyes. Also, GERIs can be disseminated as plasmids or viral vectors, enabling convenient and broad adaptation by other interested researchers. Moreover, GERIs with compatible colors for different redox parameters have enabled the simultaneous monitoring of multiple redox signals to unveil the interplays between several redox-active molecules or processes.

A classical fluorescent protein (FP) consists of an endogenous chromophore surrounded by a stable 11-stranded β-barrel structure, which shields the chromophore from the external environment.[30] The earliest strategy to make GERIs was introducing cysteine pairs into the scaffolds of single FPs (**Figure 1.1A**). The introduced cysteine residues at appropriate locations can reversibly form intramolecular disulfide bonds upon sensing a change in the redox environment.[31, 32] The formation of the disulfide bonds leads to a conformational change in the scaffolds of FPs, which consequently modulates the chromophore's photophysical properties. Researchers can thus record these changes by examining fluorescence excitation or emission (i.e., intensity, peak shape or wavelength, or lifetime). To date, a color palette of GERIs has been developed by using this strategy.[31-34] However, these indicators often have limited specificity and respond to the general redox environment changes. To overcome this limitation, alternative GERIs have been created by fusing a redox-sensitive FP with a selected redox-active enzyme (e.g., Grx, Trx, and oxidant receptor 1 (Orp1)) to form a redox relay (**Figure 1.1B**).[35-37] The rationale behind this is that the fused enzyme can improve sensor specificity by reacting with specific redox-active molecules because the redox status of the enzyme is kinetically coupled with the redox status of the nearby, redox-sensitive FP in the same fusion construct.

In addition to the GERIs mentioned above, other GERIs were developed using a different approach, which fuses redox sensory domains with circularly permutated FPs (cpFPs).[38] cpFPs are engineered FP variants with a different topology from the wide-type FPs.[38] To create a cpFP, the original N- and C- termini of a wild-type FP are connected using a flexible linker, while the new N- and C- termini are created near the chromophore.[38] The sensory domains are fused to the cpFP via these new termini, so the spectral properties are more readily modulated by structural rearrangements originated from the interaction or reaction of the redox sensory domains with analytes (**Figure 1.1C**). For example, a family of GERIs for sensing H_2O_2, namely HyPers,[39-43] was developed by fusing OxyR, an H_2O_2-activated transcription factor, to circularly permuted yellow FP (cpYFP) or red FP (cpRFP). Oxidation of these OxyR-based GERIs increases their fluorescence.

In some other examples, the sensory domains do not react with redox molecules but rather bind analytes (**Figure 1.1D**). Moreover, the sensory domain may bind multiple analytes with distinct affinities. With this unique feature, researchers can apply this type of GERIs to measuring the ratio of analytes rather than the absolute concentration changes of a specific analyte. A classic GERI of this type is SoNar for monitoring the nicotinamide adenine dinucleotide (NAD^+/NADH) redox couple.[44]

Alternatively, GERIs have been developed by incorporating noncanonical amino acids (ncAAs) into FPs using an expanded genetic code (**Figure 1.1E**). Using molecular biology, researchers can integrate codons for ncAAs into the DNA-coding sequence of an FP.[45] Co-expression of the modified FP gene with an engineered tRNA/synthetase pair in live cells, cultured in the presence of the corresponding ncAA, enables the site-specific incorporation of the ncAA

into the FP.[45] By selecting suitable ncAAs with unique functional groups, the ncAAs may bind to or react with analytes of interest, further modulating the fluorescence of FPs.[45-48]

In addition to those above single FP-based GERIs, GERIs involving multiple FPs and often based on Förster resonance energy transfer (FRET) have also been developed. FRET describes an energy transfer process from a donor chromophore to an acceptor chromophore with suitable distance, spectral overlap, and dipole coupling.[49, 50] When FRET occurs, the donor's fluorescence emission decreases, whereas the emission from the acceptor increases. The acceptor-to-donor emission ratio changes based on FRET efficiency, which is sensitive to the distance and relative dipole orientation of the donor and acceptor chromophores.[49] In FRET-based GERIs, a redox sensory element is often sandwiched between a donor FP and an acceptor FP. In response to an analyte, the sensory element undergoes a conformational change. Consequently, the distance and geometry between the donor and the acceptor are altered, and the FRET efficiency between the two FPs changes.[51] (**Figure 1.1F**). One commonly used sensory element is an artificial redox linker (RL) containing adjacent or dispersed cysteine residues between an FP-based FRET pair. The redox of the cysteine pair can alter the distance between FPs and change the FRET efficiencies between them.[52] In another example, two repeats of the C-terminal cysteine-rich domain of yeast Yap1 transcriptional factor[53] were sandwiched between a cyan FPs (CFPs), Cerulean,[54] and a YFP, Citrine,[55] resulting in a Redoxfluor indicator.[56] Oxidation of the cysteine-rich domain decreases the FRET efficiency from Cerulean to Citrine, giving a redox-dependent emission-ratiometric readout. FRET-based GERIs provide ratiometric readouts, which are advantageous because such readouts are less likely affected by variations such as instrumental setups and sensor expression levels. However, FRET-based GERIs usually have larger molecular weights and lower dynamic range (a.k.a. the fold of signal change) than single FP-based indicators. Additionally, the FPs in

the same FRET indicator may possess different pH sensitivity, brightness, photostability, and maturation rate, thereby affecting responses and complicating result interpretation.

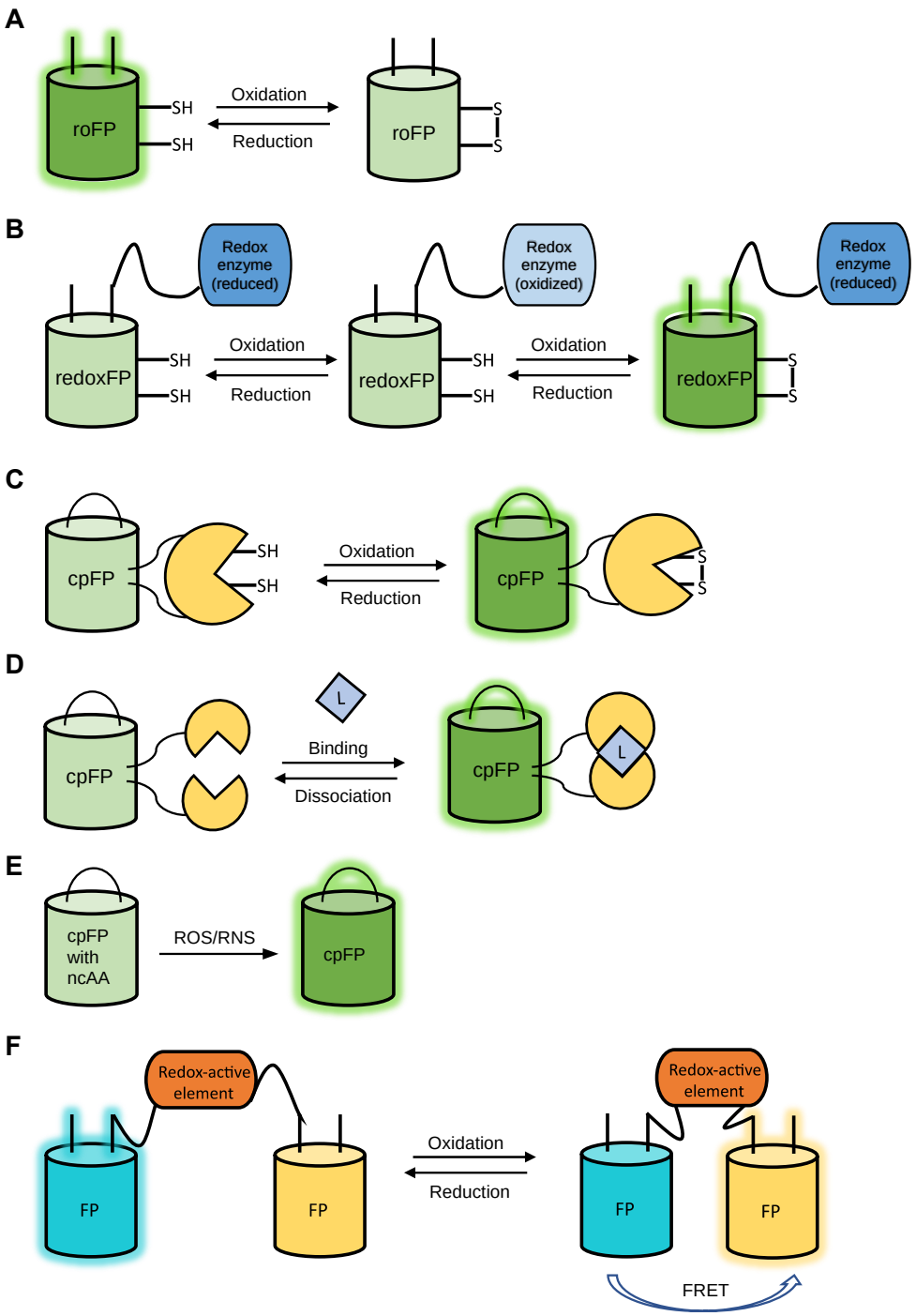

Figure 1.1 Illustration of the sensing mechanisms of common GERIs.

(**A**) A cysteine pair is introduced into FP and the reversible disulfide bond modulates the FP fluorescence. (**B**) A redox-active enzyme is genetically fused to a redox-active FP and the redox status of the enzyme is kinetically coupled with the redox of the redox-active FP. (**C**) A cpFP is fused with a redox sensory domain in an optimized configuration with which the redox reaction in the sensory domain is capable of modulating the fluorescence of cpFP. (**D**) A cpFP is fused with

sensory elements capable of ligand binding. (**E**) GERIs containing special noncanonical amino acids (ncAAs) react with specific ROS or RNS, causing FP fluorescence changes. (**F**) A redox-sensory element is sandwiched between a FP-based FRET pair and the redox status of the sensory element modulates FRET efficiency.

1.3 GERIs by Analyte Types

In this section, we discuss a list of selected GERIs according to analytical targets. The discussions focus on their key biophysical and biochemical properties. All of these GERIs have been applied to live-cell imaging, and some have been used in multicellular organisms and animals. Examples of these applications are further discussed in the next section, "Selected applications of GERIs".

1.3.1 GERIs for General Thiol Redox

GERIs in this category were generated by directly introducing cysteine residues into FP scaffolds (**Table 1.1**). These cysteines can form disulfide bonds upon oxidation, while the oxidized disulfide bonds can be reversibly reduced (**Figure 1.1A**). Moreover, the selected residue positions are typically close to the chromophore, so the redox reaction alters the fluorescence of FPs. In principle, the introduced cysteines in redox-sensitive FPs can equilibrate with an extensive array of intracellular thiols and disulfides. Because the reduced (GSH) and oxidized (GSSG) glutathione are highly abundant in most live cells and organisms, these redox-sensitive FPs are often considered indicators for the redox of GSH/GSSG. Furthermore, Grx in live cells may catalyze the redox equilibration between redox-sensitive FPs and the glutathione pool.

Table 1.1 Representative redox-sensitive FPs.

GERIs	Disulfide Bond	λ_{ex}, (nm)	λ_{em}, (nm)	Midpoint potential $E^{o'}$ (mV)	Recommended pH control
rxYFP[57]	C149-C202	512	523	−261	YFP
roGFPs[31]	C147-C204 or/and C149-C202	400/475 or 400/490	510	−272~-299	pH resistant in the excitation-ratiometric mode
roGFP1-iX[58], ERroGFP-S4[59]	C147-C204	395 and 465	505	−229~-246	pH resistant in the excitation-ratiometric mode
rxRFPs[33, 34]	N- and C-terminal cysteines	576	600	−244~-324	pHRFP
rxmRuby2[60]	C148-C200	560	600	−265	mRuby2
Oba-Q series[61]	C147-C204	370/380/430	425/440/480	−232~-249	pH resistant at physiological pH
Re-Q series[62]	C147-C204	430/515	480/525	−251~-286	pH resistant at physiological pH
roUnaG[63]	C56-C64	498	527	−275	pH resistant
FROG/B[64]	C149-C202	400(Abs)	460/510	-293	NA

1.3.1.1 rxYFP

The first developed single FP-based GERI is redox-sensitive yellow FP (rxYFP).[57] Two cysteine mutations (N149C and S202C) were introduced into YFP. In response to oxidation, the formation of an intramolecular disulfide bond between the two surface residues on the adjacent β-strands of the FP leads to a 2.2-fold fluorescence decrease with peak emission at 523 nm. The redox midpoint potential of rxYFP is −261mV, implying its broad suitability for use in common intracellular compartments.[57] Because rxYFP is sensitive to pH changes and chloride ions,[65, 66] extra caution is required when using this indicator.

1.3.1.2 roGFPs

To generate an intrinsically ratiometric redox-sensitive FP that is insensitive to chloride, researchers developed a series of redox-sensitive green FPs (roGFPs) by introducing two cysteine residues into residues on neighboring β-strands of enhanced green FP (EGFP).[31] Both roGFP1 and roGFP2 have two excitation peaks. The peak at ~ 400 nm corresponds to the chromophore's protonated form, while the peak at ~ 480 nm represents the chromophore's anionic form. The oxidation of roGFP1 or roGFP2 favors the protonated neutral chromophore, leading to increased fluorescence excitation at ~ 400 nm (F_{400}) and a concomitantly decreased fluorescence excitation at ~ 480 nm (F_{480}).[31] Thus, roGFP1 and roGFP2 can provide an excitation-ratiometric readout (F_{400}/F_{480}). In addition, the fluorescence intensity of roGFP1 or roGFP2, when excited at wavelengths close to either of the two peaks, is pH-sensitive, but the ratiometric readout (F_{400}/F_{480}) is less sensitive to pH changes, resulting in a unique advantage of roGFPs over rxYFP.[31] When using roGFP1 and roGFP2 in actual studies, we must consider several differences between them. First, the primary excitation peak of roGFP1 is at ~ 400 nm, while the predominant excitation peak

of roGFP2 is at ~ 490 nm. Moreover, the midpoint redox potential of roGFP1 is −291 mV, different from roGFP2 (−272 mV). Both roGFP1 and roGFP2 are more reducing and show more significant fluorescence changes (*a.k.a.* larger dynamic range) than rxYFP.[31, 67]

Using a similar strategy, researchers introduced cysteine pairs to alternative residue sites in EGFP to derive roGFP3 and roGFP4. Meanwhile, a total of four cysteine residues (two pairs) were introduced into EGFP to create roGFP5 and roGFP6.[31] Among these roGFPs, roGFP3 has the most negative midpoint redox potential (−299 mV), making it suitable for use in highly reducing subcellular compartments such as the cell nucleus and mitochondria;[31] roGFP2 has the least negative midpoint redox potential (-272 mV), but it is still not adequate for use in oxidizing subcellular compartments such as the endoplasmic reticulum (ER).[31] Thus, in a subsequent study, single amino acids were inserted into the main chain of roGFP1 at a location adjacent to the active cysteine 147 to lower the thermodynamic stability of the disulfide bond, resulting in a new family of roGFP1-derived GERIs (roGFP1-iX) with midpoint potentials of −229 to −246 mV.[58] A particular mutant, roGFP1-iL, with a midpoint redox potential of −229mV, is best suited for imaging redox dynamics in ER.[58] A similar effort was devoted to modifying roGFP2, but the resultant roGFP2-iL mutant has a much-reduced dynamic range.[68] Furthermore, because of the low fluorescence of ER-targeted roGFP-iL resulting from inefficient folding, mutations from superfolder GFP (sfGFP)[69] were introduced into roGFP-iL to derive ER-targeted roGFP-S4 (ERroGFP-S4), which has much-improved brightness and dynamic range for reliable monitoring of redox change in the ER.[59]

Recently, Nocross et al. fused roGFPs with RFPs to create sensors with partial red fluorescence.[70] In this case, sensitized red emission was generated via FRET from roGFPs to RFPs

while the redox properties of roGFPs were retained.[70] These new indicators were used along with roGFPs to monitor redox dynamics in multiple cellular compartments simultaneously.

1.3.1.3 rxRFPs

Red-shifted GERIs can enhance tissue penetration and provide new capabilities for multiparameter imaging along with GFP-based indicators. Our research group developed the first redox-sensitive RFP (rxRFP) from a circularly permutated RFP, mApple[71] (cpmApple).[33] The cpmApple fragment, sufficient for autocatalytic chromophore formation, was derived from R-GECO1, a red fluorescence Ca^{2+} indicator.[72] Unlike rxYFP and roGFPs, in which cysteine pairs were inserted to residues at the surface of the FP β-barrel, rxRFP was developed by adding cysteine residues to the N- and C- termini of cpmApple, followed by subsequent optimization of other residues adjacent to the cysteine residues.[33] The resultant rxRFP has a single excitation peak at 576 nm, a single emission peak at 600 nm, and a 4-fold fluorescence increase upon oxidation from the fully reduced state. In the same study, pHRFP, a red fluorescent pH indicator with a similar pKa to rxRFP, was developed and used as a pH control in live-cell imaging experiments.[33] To further match rxRFP with different midpoint redox potentials of various subcellular compartments, our group developed several rxRFP variants (rxRFP1.X) by mutating the amino acids in proximity to the inserted cysteines residues. rxRFP1.1.-1.4 have midpoint redox potentials ranging from −324 to −244 mV and respond to redox perturbations when localized to suitable subcellular compartments such as the cell nucleus, mitochondria, and ER in mammalian cells.[33, 34]

1.3.1.4 rxmRuby2

Another reported redox-sensitive RFP, rxmRuby2,[60] was generated by introducing surface-exposed cysteine residues into the β-barrel of mRuby2,[73] an RFP in the wild-type topology. rxmRuby2 showed fluorescence decrease upon oxidation and fluorescence increase upon reduction and responded to various oxidants and reductants. For example, both GSSG and diamide can oxidize rxmRuby2 *in vitro* to a higher degree than H_2O_2. On the other hand, only a strong reductant, dithiothreitol (DTT), but not bacterial Trx or nicotinamide adenine dinucleotide phosphate (NADPH), can directly reduce rxmRuby2. It is worth noting that the fluorescence of rxmRuby2 is still sensitive to pH changes, and researchers should include proper controls in their experiments of interest.[60] rxmRuby2 has been fused with mClover,[73] a GFP variant. The fusion construct can give out a ratiometric readout and has shown reversible responses to redox changes in live cells.[60]

1.3.1.5 Oba-Q and Re-Q series

Oxidation balance sensed quenching proteins (Oba-Q)[61] are GERIs with fluorescence significantly quenched upon oxidation. Cysteine residues were first introduced into residues 147 and 204 of several CFPs and a blue FP (BFP).[61] An extra amino acid was then inserted after Cys147，followed by additional mutations around Cys147 for better quantum yield and dynamic range.[61] In particular, Oba-Qs was derived by introducing three mutations (I146N/S147CD/Q204C) into a CFP named Sirius,[74] while Oba-Qc was generated by introducing three mutations (I146G/S147CE/Q204C) into a mutated CFP (CFP').[61] The maximal fluorescence intensity change of Oba-Qs is 6.3-fold, while that of Oba-Qc is only 2.3-fold. The midpoint redox potential values of Oba-Qs and Oba-Qc are −232 mV and −249 mV, respectively, making them suitable for use in

the ER, a relatively oxidizing subcellular compartment.[61] Similarly, introducing mutations (I146G/S147CE/Q204C) into an enhanced BFP, EBFP2,[75] derived Oba-Qb, an indicator better suited for reducing subcellular compartments due to its more negative redox potential (−263 mV).[61] The same engineering strategy has been applied to additional CFPs and YFPs, such as mTurquise[76] and Venus.[77] Some of these proteins show fluorescence decrease upon reduction. Such response is opposite to that of Oba-Q, and this new group of proteins was thus named reduction-sensed quenching proteins (Re-Q).[62] The midpoint redox potentials of this new series of proteins span a broad range from −251 to −286 mV.

1.3.1.6 roUnaG

The above-mentioned redox-sensitive FPs were all derived from *Aequorea victoria* GFP (avGFP) or avGFP-like proteins, and the formation of their chromophores requires molecular oxygen (O_2). Consequently, these GERIs are not well compatible with hypoxic or anoxic conditions. An oxygen-independent GFP, UnaG, was developed in 2013.[78] The binding of the protein to a cofactor, bilirubin (BR), a catabolic product of heme metabolism, triggers the fluorescence of UnaG.[79] By introducing a cysteine pair (E56C/D64C) to consecutive β-strands of UnaG, roUnaG is the first oxygen-independent GERI.[63] The mutant with the double mutations (E56C/D64C) shows slow oxidation kinetics due to backbone constraint, and the introduction of an additional K54T substitution reduced the size of a sidechain close to Cys56 and improved the oxidation kinetics.[63] roUnaG (UnaG-E56C/D64C/K54T) works well under hypoxia and anoxic conditions and shows an 8-fold fluorescence increase upon oxidation. In addition, the fluorescence of roUnaG is resistant to pH changes, overcoming a significant limitation of GERIs derived from avGFP-like proteins.[63] With a single excitation and a single emission peak, roUnaG only provides

intensiometric readouts, but it has been fused with an RFP, mCherry,[80] for ratiometric readouts.[63, 79]

1.3.1.7 FROG/B

The wild-type avGFP[81] has two major absorption peaks at ~ 400 and 480 nm, corresponding to its chromophore's neutral and anionic forms, respectively. The engineering of avGFP has resulted in variants with only one absorption peak. One such widely known example is EGFP,[82] with a single absorption peak at ~ 480 nm, while other FP variants such as Sapphire[83] and mKalama[75] have a single absorption peak at ~ 400 nm at neutral pH. After absorbing ~ 400 nm light, mKalama emits blue light at ~ 460 nm, while Sapphire emits green light at ~ 510nm via a process known as excitation state proton transfer (ESPT). Using a cysteine pair to modulate the efficiency of ESPT, a single-FP-based GERI called FROG/B has recently been developed with dual emission at ~ 460 and 510 nm upon excitation at ~ 400 nm.[64] The oxidation of FROG/B enhances ESPT, resulting in a shift of its emission from blue to green. The overall response at pH 7 is ~ 5-fold in terms of the green-to-blue emission ratio, and the response is fully reversible.[64] FROG/B has a midpoint redox potential of −293 mV at pH 7.0, lower than rxYFP and roGFP. Thus, FROG/B is well suited for monitoring weak oxidative stress.[64] FROG/B is unique due to its emission ratiometric response. It is of note that the green-to-blue emission ratio of FROG/B in the oxidized state is still quite sensitive to pH changes.[64]

1.3.2 GERIs for GSH/GSSG

Although redox-sensitive FPs in the above category are often considered to sense the redox of GSH/GSSH in live cells, their direct equilibration with glutathione is slow in the absence of

Grx. Therefore, these redox-sensitive FPs have been fused with Grx to derive a new family of GERIs. Placing a redox-sensitive FP close to Grx generates a redox relay that kinetically couples the redox of the redox-sensitive FP with the redox of the glutathione pool (**Figure 1.1B**). The relay between Grx and redox-sensitive FPs increases response kinetics and specificity but does not change their midpoint redox potentials. This fusion strategy is highly generalizable, and in theory, can be applied to any redox-sensitive FP. Below we discuss several selected examples.

1.3.2.1 rxYFP-Grx1p

The first redox-relay fusion probe, rxYFP-Grx1p, was developed by the Winther lab.[84] The coupling of yeast Grx1p with rxYFP significantly increased the oxidation kinetics of rxYFP by GSSG. Since the redox reaction of rxYFP-Grx1p is independent of endogenous Grx, redox measurements can be performed in diverse subcellular compartments and organisms. In addition to faster kinetics, rxYFP-Grx1p provides nearly absolute glutathione specificity due to its low reactivity to other oxidants.[84] The crystal structure of the fusion protein indicated that the Grx1p and rxYFP do not have specific contact.[85] Thus, it is speculated that the enhanced thiol-disulfide exchange efficiency between Grx1p and rxYFP might result from a spatial constraint.[85] The linker limits the diffusion that drives Grx1p and rxYFP apart and enhances their collision in solution, thereby favoring the thiol-disulfide exchange between them.[85]

1.3.2.2 Grx1-roGFP2

Grx-roGFP2 is probably the most well-characterized indicator for real-time monitoring of the glutathione redox status.[35] The thiol-disulfide exchange between Grx and roGFP2 is achieved through a symmetrical ping-pong process which transfers the disulfide bonds via a monothiol

mechanism.[86] The exchange between glutathione and the indicator happens through three consecutive steps, which are fully reversible. In the first step, the nucleophilic cysteine of Grx1 specifically reacts with GSSG to form a mixed Grx1-glutathione disulfide intermediate. The intermediate subsequently reacts with one of the two thiols on roGFP2, generating S-glutathionylated roGFP2. Last, glutathionylated roGFP2 forms an intramolecular disulfide bond through rearrangement.[27] There are two reasons why Grx1-roGFP2 has very high specificity for GSH/GSSG redox pair. First, Grx can specifically respond to glutathione redox, and its specificity is maintained in the fusion probe. Second, Grx1-roGFP2 is not capable of interacting with the Trx system because of the steric constraints.[27] The kinetics of electron flux from the reduced probe to GSSG is enhanced at least 100,000 times compared to roGFP2. With its improved dynamic equilibration with GSH/GSSG, Grx-roGFP2 is an excellent tool for studying short-lived and weak oxidative events invisible to non-fused roGFP2.[35]

1.3.2.3 Grx1-roCherry

To create a red GERI for glutathione redox, Shokhina et al. developed roCherry, a redox-sensitive RFP.[87] Two cysteine residues were inserted at residues 150 and 203 of mCherry[80] to create the prototypic roCherry. A threonine insertion after Cys150 and an additional point mutation (S151E) were then introduced to increase structural mobility and dynamic range.[87] Grx1 was then fused to the N-terminus of roCherry via a floppy linker from the Peredox indicator.[88] The resultant Grx1-roCherry provides intensiometric readouts with a single excitation peak at ~589 nm and a single emission peak at ~610 nm. The probe does not directly respond to H_2O_2 *in vitro* but shows a detectable response to H_2O_2 in live cells. It was speculated that H_2O_2 could shift the GSH/GSSG ratio in live cells. Grx1-roCherry loses its activity after incubation with 2-acetylamino-3-[4-(2-

acetylamino-2-carboxy-ethylsulfanylthiocarbonylamino)phenylthiocarbamoylsulfanyl]propionic acid (2-AAPA), a glutathione reductase (GR) inhibitor.[87, 89] Compared to Grx1-roGFP2, Grx1-roCherry is less specific and displays a response to a high concentration of nitric oxide.[87]

1.3.3 GERIs for the redox of Trx

Trx is a class of small, 12-kDa antioxidant proteins broadly found in all three domains of life.[90] Trx facilitates the reduction of its interacting proteins via cysteine thiol-disulfide exchange.[91] There is continuous interest in developing GERIs to monitor the redox status of live-cell Trx.

1.3.3.1 TrxRFP

Early attempts to develop GERIs for the redox of Trx by fusing Trx with roGFPs were unsuccessful. The most feasible explanation is that Trx, unlike Grx, cannot form redox relays with roGFPs due to geometric constraints.[27] Our research group developed TrxRFP, the first GERI for sensing Trx redox.[36] TrxRFP was engineered by directly fusing human Trx1 (hTrx1) with rxRFP through a Gly-Ser-rich linker to create a redox relay, which couples the active cysteines of hTrx1 (C32 and C35) to the active cysteine pair in rxRFP (**Figure 1.1B**). Other non-essential Cys residues in hTrx1 were mutated to Ser to avoid crosstalk with the glutathione system.[92] rxRFP is in a circularly permuted topology with cysteine residues located at the C- and N-termini of the cpFP, possibly allowing an efficient disulfide exchange with hTrx1. TrxRFP can be reduced explicitly by Trx reductase (TrxR) in the presence of NADPH, while rxRFP alone shows no response to TrxR and NADPH. Therefore, it is proposed that the TrxR enzyme system reduces the disulfide in hTrx1, and the thiols are subsequently transferred to rxRFP1 through the redox relay.[36] The process is reversible, and the reduced TrxRFP can be oxidized by thioredoxin peroxidase (TPx) in the

presence of H_2O_2. TrxRFP does not present a significant response to H_2O_2, GSSG, Grx1, or Trx-related proteins (TRPs), confirming its specificity for Trx redox. TrxRFP1 has been combined with Grx1-roGFP2 to monitor Trx and glutathione redox parallelly. The redox of glutathione and Trx1 can each be disturbed individually without affecting the other in mammalian cells.[36] Auranofin, a TrxR reductase inhibitor,[93] at low levels in mammalian cells shifts TrxRFP1, but not Grx1-roGFP2, to a more oxidized state.[36]

1.3.3.2 CROST

Change in the redox state of Trx (CROST) is a group of FRET-based GERIs for Trx in photosynthetic bacteria. CROST1 and CROST2 were made by sandwiching fragments derived from Trx-targeted proteins (CP12-2 or CP12) conserved among photosynthetic organisms, between a CFP (mTurquoise Δ11) and a cpYFP (cpVenus).[76, 77, 94] Elevated Trx oxidation promotes the disulfide bond formation in CP12-2 or CP12, decreasing the FRET donor and acceptor's distance and enhancing FRET efficiency (**Figure 1.1F**).[94] While CROST1 has a midpoint redox potential of −266 mV at pH 7.5, CROST2 has a more negative midpoint redox potential (−296 mV).[94] CROST1 and CROST2 display differential responses to different Trx isoforms from plants or cyanobacteria, potentially due to the difference in the midpoint redox potentials. Both indicators have been used for monitoring the redox change of Trx in chloroplasts.[94]

1.3.4 GERIs for H_2O_2

H_2O_2 is an important reactive oxygen species and an essential signaling molecule.[95] Several GERIs for H_2O_2 are now available. Below we discuss a few selected examples (**Table 1.2**).

Table 1.2 **Representative GERIs for H_2O_2.**

GERIs	Sensory Domain	Signal	λ_{ex}, (nm)	λ_{em}, (nm)
roGFP2-Orp1[37]	Orp1	GFP	390/480	510-530
roGFP2-Tsa2ΔC_R[96]	Tsa2	GFP	405/488	510
roGFP2-Tpx1.C169S[97]	Tpx1.C169S	GFP	405/488	510
HyPer[39]	OxyR (*E. coli*)	cpYFP	420/500	516
HyPer2[40]	OxyR (*E. coli*)	cpYFP	420/500	516
HyPer3[41]	OxyR (*E. coli*)	cpYFP	420/500	516
HyPerRed[42]	OxyR (*E. coli*)	cpmApple	575	605
HyPer7[43]	OxyR (*N. meningitidis*)	cpYFP	400/500	520
NeonOxIrr[98]	OxyR (*E. coli*)	cpmNeon Green	508	520
TriPer[99]	OxyR (*E. coli*)	cpYFP	405/488	~ 516
OxyFRET[100]	Yap1	FRET	435	535/480
PerFRET[100]	Yap1 and Orp1	FRET	435	535/480
Prx2-based FRET[101]	Prx2	FRET	488	525/625

1.3.4.1 roGFP2-Orp1

A redox relay was created (**Figure 1.1B**) by fusing roGFP2 to Orp1, a yeast peroxidase,[102] resulting in roGFP2-Orp1 that can sense H_2O_2.[37] The proximity between roGFP2 and Orp1 converts physiological H_2O_2 signals into measurable fluorescent signals. Oxidation of Orp1 by H_2O_2 first generates an intramolecular disulfide bond between C36 and C82 in Orp1, and the disulfide bridge is subsequently transferred to roGFP2 through a thiol-disulfide exchange. Orp1 can generate a disulfide bridge in roGFP2 using H_2O_2 in a near-stoichiometric way.[37] Oxidized roGFP2-Orp1 is reduced by the Trx and Grx/glutathione systems. Thus, the readout of roGFP2-Orp1 is affected by both H_2O_2-induced oxidation and Trx/Grx/glutathione-induced reduction.[37] Using a similar strategy, roGFP2 has recently been linked to peroxiredoxins (Prxs) lacking resolving Cys, leading to roGFP2-Tsa2ΔC_R[96] (2-Cys Prx from *S. cerevisiae*) and roGFP2-Tpx1.C169S.[97] These two Prx-based GERIs are sensitive to very low concentrations of H_2O_2 (their limits of detection were estimated to be a few nanomolar). To date, the applications of roGFP2-Tsa2ΔC_R and roGFP2-Tpx1.C169S are mostly limited to yeast.

1.3.4.2 HyPers

HyPers are a family of H_2O_2 indicators made by inserting a cpFP into a H_2O_2 sensory domain derived from bacterial transcriptional factor OxyR (**Figure 1.1C**).[39-43] Upon oxidation, the active Cys199 of OxyR is repelled by the hydrophobic pocket and forced into proximity with Cys208 to form an intramolecular disulfide bond.[103] Disulfide bridge formation results in conformational changes of OxyR, which can modulate the fluorescent signal of the inserted cpFP. The oxidation of HyPers can be reversed by cellular enzymes engaged in the thiol-disulfide exchange.[39-43]

The first indicator of this family, HyPer, was created by integrating a cpYFP between 205 and 206 sites of *Escherichia coli* (*E. coli*) OxyR regulatory domain (Oxy-RD).[39] HyPer is an excitation-ratiometric indicator with two excitation peaks at ~420 and ~500 nm and a single emission peak at ~516 nm. Upon oxidation, the fluorescence excited at 420 nm (F_{420}) decreases, while the fluorescence excited at 500 nm increases (F_{500}). The maximal ratiometric excitation change (F_{500}/F_{420}) can be up to ~ 3-fold.[39] In 2011, an advanced version of HyPer named HyPer2 was developed by introducing a single point mutation A406V to the sensory domain OxyR-RD. HyPer2 displays an improved dynamic range, which is twice of that of HyPer.[40] Later on, HyPer3 was developed by introducing another point mutation, H114Y, to OxyR-RD. HyPer3 gains an expanded dynamic range compared to HyPer and faster kinetics than HyPer2.[41] The red version of HyPer, HyPerRed, was designed by replacing the cpYFP with cpmApple.[42] Unlike HyPer, HyPer2, and HyPer3, HyPerRed is an intensiometric indicator whose emission increases by ~ 2-fold upon oxidation by H_2O_2.[42] Because HyPers are pH-sensitive, a pH control SypHer was also developed.[104] By introducing a point mutation C199S, SypHer is insensitive to H_2O_2 but shows the same pH sensitivity as HyPer.[104]

HyPer7, the most updated version of the HyPer family, was developed by inserting cpGFP into an OxyR-RD from *Neisseria meningitidis (N. meningitidis)*.[43] HyPer7 is 15- to 17- fold brighter than HyPer3, and its ratiometric readout (F_{500}/F_{400}) is stable within the physiological pH range. Compared to the previous HyPer indicators, HyPer7 can respond to a relatively low concentration range of H_2O_2, and the response is much more rapid.[43] The minimum H_2O_2 concentration needed for a ratiometric increase of 0.1 is approximately 1 μM for HyPer and HyPer3 but only 0.03 μM for HyPer7. The reaction rate of HyPer7 with H_2O_2 is ~ 60 and 86 times faster than those of HyPer and HyPer3.[43]

1.3.4.3 NeonOxIrr and TriPer

Like HyPer family indicators, NeonOxIrr was constructed by fusing a cpmNeonGreen to the truncated OxyR from *E.coli*.[98, 105] NeonOxIrr displayed 5.9-fold higher brightness, 15-fold faster oxidation rate, and 7.6-fold longer reduction half-time than HyPer3.[98] Additionally, NeonOxIrr has demonstrated a 2.3-fold dynamic range in response to H_2O_2 with higher stability within the pH range of 5.5-7.5.[98] The slow reduction rate of NeonOxIrr can help integrate signals over time; on the other hand, it makes NeonOxIrr unsuitable for real-time monitoring of fast H_2O_2 dynamics.[98]

HyPer is inadequate to sense H_2O_2 in the thiol-oxidizing ER environment due to its low redox potential. In HyPer, C199 of OxyR reacts with H_2O_2 to form a sulfenic acid, which C208 further attacks to form a disulfide bond. The disulfide bond would be continuously formed in the presence of the ER protein disulfide isomerases (PDIs), depleting all reduced HyPer.[106] By replacing Ala187 in OxyR with Cys, a tri-Cys indicator, TriPer, was generated.[99] It is speculated that the presence of this additional cysteine creates a diversionary disulfide, C187-C208, keeping a fraction of C199 in its reduced form. Thus, a fraction of the C199 thiolate could still react with H_2O_2 to form a sulfenic acid intermediate, which could be further converted into a low-fluorescence state when excited at 488 nm. As a result, the ER-expressed TriPer responded to H_2O_2, while Hyper did not show any response under the same condition.[99]

1.3.4.4 OxyFRET and PerFRET

Two novel FRET-based indicators, OxyFRET and PerFRET, were built to measure H_2O_2 generated by NADPH-dependent oxidase (NOX) in live cells.[100] Both indicators have a H_2O_2-sensitive domain inserted between Cerulean[54] and Venus.[77] The sensory domains in OxyFRET are

N- and C- terminal cysteine-rich domains of Yap1 (nCRD and cCRD), while PerFRET contains Orp1 and Yap1 cCRD.[107] Upon oxidation by H_2O_2, the catalytic cysteine of Orp1 or nCRD forms a disulfide bridge with the cCRD of the Yap1,[108] altering the effective FRET distance between the CFP and YFP (**Figure 1.1F**). Interestingly, the F_{535}/F_{480} emission ratios of OxyFRET and PerFRET change in opposite directions: oxidation of OxyFRET increases its F_{535}/F_{480} emission ratio while the F_{535}/F_{480} emission ratio of PerFRET decreases under the same condition.[100] The oxidation of these indicators is rapid and reversible; their ratiometric readouts are relatively insensitive to pH changes. However, these indicators lack complete *in vitro* characterizations because it has been challenging to purify them.[100]

1.3.4.5 Peroxiredoxin-2 (Prx2)-based FRET indicator

The exceptionally active cysteine at the N-terminus of human Prx2 can form a disulfide bond with a second cysteine residue located on an adjacent Prx2 monomer, leading to a covalently linked dimer.[101] Prx2 reacts with H_2O_2 faster than other sensing domains such as Orp1 and OxyR, making it more kinetically favored.[101] Based on this mechanism, a fluorescent FRET indicator was developed for monitoring trace H_2O_2 fluctuations. Prx2 was placed between Clover,[73] a GFP, and mRuby2,[73] an RFP (**Figure 1.1F**). This FRET FP pair was chosen because it was reported to have a higher dynamic range than conventional CFP-YFP FRET pairs.[73] The resultant Prx2-based indicator is ultrasensitive to the femtomolar-level change of H_2O_2 concentrations.[101]

1.3.5 GERIs for pyridine dinucleotides

Pyridine dinucleotides are essential for maintaining cellular redox homeostasis. In particular, NADPH provides the reducing power and neutralizes ROS through the glutathione and

Trx antioxidant pathways. In addition to its role in protecting cells against oxidative stress, NADPH also serves as the substrate for NADPH oxidases to generate ROS. NADH is another cellular reducing molecule, although, in most organisms, NADH's function is primarily metabolic. NADH is the primary electron donor for mitochondrial ATP synthesis, and ROS is generated in this process as by-products. NADH and NADPH are linked through their oxidation products, NAD^+ and $NADP^+$, since NAD^+ kinase (NAK),[109] a well-known enzyme, can convert NAD^+ into $NADP^+$, which is further reduced into NADPH through the pentose phosphate pathway. MESH1 (Metazoan SpoT Homologue 1)[110] was recently reported as a cytosolic NADPH phosphatase in mammalian cells, and MESH1 converts cellular NADPH into NADP to promote ferroptosis under stress conditions. Below we discuss a few examples of GERIs that can sense the NADPH and NADH redox couples (**Table 1.3**).

Table 1.3 Representative GERIS for NADPH and the NADH redox couple.

GERIs	Targets	λ_{ex} (nm)	λ_{em} (nm)	K_d[a]	Signal	Sensory Domain	Recommended pH control
LigA-cpVenus[111]	NAD^+	405/480	530	65 μM	cpVenus	DNA ligase	cpVenus
FiNad[112]	NAD^+/(ATP+ADP) ratio	500	518	14 μM to 1.3 mM	cpYFP	T-Rex	mCherry-cpYFP
Frex[113]	NADH	421/500	518	3.7μM	cpYFP	B-Rex	cpYFP
FrexH[113]	NADH	421/500	518	40 nM	cpYFP	B-Rex	cpYFP
Peredox[88]	NADH/NAD^+ ratio	400	510	<5 nM for NADH	cpT-Sapphire	T-Rex	pH resistant
RexYFP[114]	NAD^+/NADH ratio	490	516	180 nM for NADH	cpYFP	T-Rex	SypHer
Apollo-$NADP^+$[115]	$NADP^+$	485	535	0.1~20 μM	HomoFRET	G6PD	pH resistant
NADPSor[116]	$NADP^+$	440	478/526	2 mM	FRET	KPR	pH resistant
SoNar[44]	NAD^+/NADH ratio	420	485	5 μM for NAD^+ 0.2 μM for NADH	cpYFP	T-Rex	cpYFP
iNaps[117]	NADPH	420/500	515	2-120 μM	cpYFP	T-Rex	iNapC

[a] K_d: dissociation constant

1.3.5.1 LigA-cpVenus

LigA-cpVenus is an NAD^+ indicator derived from a bacterial DNA ligase, which contains a bipartite NAD^+-binding domain.[111, 118] A cpVenus[77] was inserted between the two subdomains (**Figure 1.1D**). The apparent K_d of LigA-cpVenus to NAD^+ is ~ 65 μM.[111] The binding of NAD^+ results in a decrease of fluorescence in a dose-dependent manner with excitation at 488 nm (F_{488}), whereas the fluorescence with excitation at 405 nm (F_{405}) remains unchanged.[111] Thus, an excitation-ratiometric readout (F_{488}/F_{405}) can be used to normalize sensor expression levels. Tests against other nucleotides and NAD^+ precursors show that the probe is specific to NAD^+.[111] LigA-cpVenus is susceptible to pH change, but the pH influences can be corrected using cpVenus due to their similar pH profiles.[111]

1.3.5.2 FiNad

FiNad is another GERI for NAD^+. A cpYFP was inserted between F189 and L190 of the *Thermus aquaticus* Rex (T-Rex) monomer through short peptide linkers (**Figure 1.1D**).[112] FiNad's fluorescence increases ~ 7-fold after binding with NAD^+. It also responds to NADPH, but the response range is far above the physiological concentration of cytosolic and nuclear NADPH.[112] ATP or ADP affects the affinity of FiNad to NAD^+, and the K_d of FiNad to NAD^+ ranges from ~14 μM to 1.3 mM, depending on the concentrations of ATP or ADP. Thus, FiNad is actually an indicator for the NAD^+/AXP ratio, in which AXP is the total pool of ATP and ADP.[112] FiNad has been genetically fused to mCherry,[80] and the resultant mCherry-FiNad chimera allows a ratiometric readout of NAD^+ dynamics. The green fluorescence of mCherry-FiNad excited at 485 nm is pH-sensitive, whereas the red fluorescence excited at 590 nm is relatively insensitive to pH

changes. When using mCherry-FiNad in conditions with pH fluctuations, a mCherry-cpYFP fusion protein should be used in parallel for correction.[112]

1.3.5.3 Frex and FrexH

Frex and FrexH are GERIs for monitoring NADH dynamics. They were designed by inserting a cpYFP between a complete *Bacillus subtilis* Rex (B-Rex) monomer and B-Rex's NADH-binding domain (**Figure 1.1D**).[113] Both indicators displayed similar spectral properties as cpYFP with two excitation peaks at 421 and 500 nm and a single emission peak at 518 nm.[113] Frex exhibits a 9-fold fluorescence increase upon binding with NADH, while FrexH displays a change in the opposite direction, ~ 3-fold fluorescence turn-off. In addition, both of them showed high selectivity toward NADH. The K_d of FrexH to NADH is ~ 40 nM, 10-fold lower than that of Frex (~ 3.7 μM).[113] Due to their pH responses similar to cpYFP, the pH interference can be corrected by using cpYFP in parallel experiments.

1.3.5.4 Peredox

Peredox was constructed by integrating a pH-resistant GFP, T-Sapphire,[83] between two subunits of a T-Rex tandem dimer. It is an indicator for NADH/NAD^+ ratio because its affinity for NADH effectively decreases with increasing NAD^+ concentration.[88] Due to its pH resistance, the fluorescence of Peredox is not affected by pH changes. However, the competitive binding with NAD^+ or NADH varies substantially with pH. Peredox provides intensiometric readouts with a single excitation peak at 400 nm and an emission peak at 510 nm, but it has been fused with mCherry[80] or mCitrine,[55] for ratiometric reading.[88, 119] One limitation of Peredox is its exceptionally high affinity to NADH, making it easily saturated in some cellular compartments.[88]

1.3.5.5 RexYFP

RexYFP was made by integrating cpYFP into the loop of one subunit of T-Rex, between the nucleotide and DNA binding domain (**Figure 1.1D**).[114] The molecular weight of RexYFP is 1.5- to 2-fold smaller than Frex and Peredox. NADH binding leads to a fluorescence decrease with 490 nm excitation and a fluorescence increase with 340 nm excitation.[114] When tested against various NADH analogs, RexYFP responded to both NADH and NADPH. Thus, it is hard to exclude the NADPH interference when using RexYFP in living cells. Although NAD^+ does not elicit fluorescence change of RexYFP, it can compete with NADH for binding to RexYFP.[114] Due to the greater concentration of NAD^+ than NADH in live cells, RexRFP should be considered as an indicator for the NAD^+/NADH.[114] Since RexYFP is pH-sensitive, SypHer,[104] a pH indicator with a cpYFP chromophore, was used to correct pH-related artifacts.[114]

1.3.5.6 Apollo-$NADP^+$

Apollo-$NADP^+$ is based on homo-FRET, which uses the same FP as both the donor and acceptor.[115] Homo-FRET decreases steady-state fluorescence anisotropy.[120] Glucose-6-phosphate dehydrogenase(G6PD) is an inactive monomer in the absence of $NADP^+$. In the presence of high amounts of $NADP^+$, it turns into an active homodimer.[121] Taking advantage of this dimerization mechanism, Apollo-$NADP^+$ was made by sandwiching a catalytically inactive human G6PD between two copies of Venus, a YFP.[77] $NADP^+$ binds Apollo-$NADP^+$ at an affinity similar to that of the wild-type G6PD, triggering dimerization and fluorescence anisotropy decrease.[115] The probe does not respond to other metabolites, including NADPH, NAD^+, NADH, and ATP. Apollo-$NADP^+$ is a reversible, pH-resistant indicator compatible with many other indicators. The limitation of this indicator is its relatively small (15-20%) dynamic range.[115]

1.3.5.7 NADPsor

$NADP^+$ can bind ketopantoate reductase (KPR) as a cofactor.[122] Hence, NADPSor was generated by inserting the binding element from KPR between a CFP-YFP FRET pair.[116] The binding of $NADP^+$ triggers a conformational change of KPR from a relatively closed form to an open state. This structural rearrangement distances the two fluorophores and lowers the FRET efficiency.[116] Thus, the indicator displays an $NADP^+$ concentration-dependent decrease in FRET, indicated by a lower fluorescence emission ratio (F_{526}/F_{478}) at 526 and 478 nm. NADPsor is specific to $NADP^+$ with a detection limit of ~1 µM and does not respond to other $NADP^+$-like metabolites.[116]

1.3.5.8 SoNar

SoNar, one of the most promising indicators for monitoring the live-cell NAD^+/NADH ratio, was constructed based on a truncated T-Rex.[44] NADH-bound T-Rex exhibits an open conformation while NAD^+-bound T-Rex shows a closed conformation. Integration of cpYFP into the surface loop of T-Rex couples the NADH/NAD^+ binding-induced conformational change with cpYFP's spectral characteristics, enabling SoNar to provide an excitation-ratiometric readout (**Figure 1.1D**).[44] SoNar has two excitation peaks at 420 and 485 nm (F_{420}/F_{485}). Binding to NADH increases the excitation ratios (F_{420}/F_{485}) while binding to NAD^+ decreases the ratio, resulting in a maximal 15-fold fluorescence change *in vitro*.[44, 123] The apparent K_d of SoNar for NAD^+ and NADH is ~ 5 µM and ~ 0.2 µM, respectively, far below the intracellular NAD^+ and NADH concentrations, making SoNar a good reporter for the NAD^+/NADH ratio without being affected by the total NAD(H) pool. [44, 124, 125] SoNar responds rapidly even to subtle differences in cellular

NAD^+/NADH.[123] As a cpYFP-based indicator, the pH effect of SoNar can be corrected using a cpYFP in parallel.

1.3.5.9 iNap indicators

iNap indicators (iNaps) were NADPH sensors developed from SoNar. Mutations were introduced to convert T-Rex from an NADH binder to an NADPH binder.[117] The resultant iNap variants (named iNap1, iNap2, iNap3, and iNap4) have apparent NADPH affinities ranging from 2 μM to 120 μM. iNaps have two excitation peaks at ~420 nm and ~500 nm and one emission peak at 515 nm.[117] NADPH binding leads to a ~3.5-fold increase in fluorescence excitation at 420 nm and a ~2.5-fold decrease of fluorescence excitation at 485 nm, rendering a ~ 900% excitation-ratiometric change.[117] As iNaps can give ratiometric readouts, iNaps can be targeted to different cellular compartments to measure the NADPH levels. They have also been applied to measure the change of NADPH levels in cells under oxidative stress.[117] A pH control, iNapc, was created by introducing four mutations into the binding domain to abolish ligand-binding.[117]

1.3.6 GERIs for molecular oxygen (O_2)

The d(UnaG-mOrange) fusion protein for hypoxia and reoxygenation (dUnOHR),[126] is an indicator consists of an oxygen-independent FP, UnaG,[79] and an oxygen-dependent orange FP, mOrange.[80] Under hypoxia, only the fluorescence of UnaG is detectable, while the fluorescence of mOrange is undetectable. Following reoxygenation, the mOrange chromophore matures, and its fluorescence becomes detectable while UnaG fluorescence decreases due to FRET from UnaG to mOrange.[126] FluBO[127] is another similar indicator based on FRET between YFP and the oxygen-independent flavin-binding fluorescent protein (FbFP).[128] The presence of oxygen leads to YFP

chromophore maturation and efficient FRET to FbFP. In the absence of oxygen, the chromophore of YFP is not formed, and there is no FRET.[127] Both dUnOHR and FluBO are based on irreversible oxygen-dependent chromophore maturation, so their responses are irreversible and slow. Additionally, UnaG and FbFP require bilirubin and flavin mononucleotide as cofactors for fluorescence, leading to inaccurate outputs when these cofactors' levels are limited.[129]

ProCY, developed by our research group, is also a FRET-based indicator responsive to oxygen levels.[130] Hypoxia-inducible factor (HIF-1α) is a transcription factor regulated by prolyl hydroxylase domain enzymes (PHDs) in an oxygen-dependent manner. Under normal oxygen levels, PHDs can use oxygen to hydroxylate the conserved proline (Pro564) of HIF-1α. As a result, hydroxylated HIF-1α subsequently binds to von Hippel-Lindau (VHL), leading to subsequent polyubiquitination and proteasomal degradation of HIF-1α. Under hypoxia, HIF-1α is stabilized due to the reduced activity of PHDs.[131-133] ProCY was generated by inserting a 22-amino-acid proline-containing peptide (556-577) from HIF-1α and a 10-kDa binding domain of VHL between an ECFP and a yellow FP (YPet).[134] The HIF-1α derived peptide and the VHL domain were connected by a 21-aa GS rich linker. The interaction between HIF-1α peptide and the VHL domain under different oxygen levels would result in a conformational change that affects distance, orientations, and subsequently, the FRET efficiency between ECFP and YPet (**Figure 1.1F**).[130] ProCY shows a dynamic range of 168% with the FRET ratio change from 2.95 to 1.76 upon proline hydroxylation, making it a reliable tool for monitoring hypoxia.[130]

1.3.7 GERIs for Methionine sulfoxide (MetO)

Methionine can be converted to the R- or S-diastereomers of methionine sulfoxide (MetO) by different oxidants when reacted with ROS.[135] Methionine sulfoxide reductases A (MSRA) and

B (MSRB) are the specific enzymes of the S- and R-diastereomers of MetO.[136, 137] Reduction of the MetO-containing substrate in MSRA/MSRB can lead to a stable disulfide bond between an MSR and a corresponding Trx in the fusion chimera and thus trigger conformational changes (**Figure 1.1D**). Based on this mechanism, two indicators, MetSOx and MetROx, were developed by sandwiching cpYFP between MSRA/MSRB and Trx, enabling the detection for S and R-forms of MetO, respectively.[138] Reduced recombinant MetSOx shows two excitation peaks at 425 and 505 nm and a single emission peak at ~ 515 nm. Upon reaction with MetO, there is a noticeable increase in fluorescence emission with excitation at 505 nm but not with excitation at 425 nm.[138] Similarly, reduced MetROx displays two excitation peaks at 410 and 500 nm and a single emission peak at ~ 515 nm. Reaction with MetO results in a turn-on fluorescence change with excitation at 410 nm and a turn-off change with excitation at 500 nm.[138]

1.3.8 GERIs for Peroxynitrite ($ONOO^-$)

Peroxynitrite ($ONOO^-$) is a highly reactive RNS formed from a diffusion-controlled reaction of superoxide and nitric oxide.[139, 140] Boronate-containing small molecules[141, 142] have been developed as indicators for $ONOO^-$, although they often cross-react with other ROS such as H_2O_2 and HOCl.[141, 143] Our group used a genetic code expansion technology to introduce an ncAA, *p*-boronophenylalanine (*p*BoF), into the chromophores of cpGFPs, and further performed protein engineering on the scaffolds to modulate the reactivity of the introduced new functional group (**Figure 1.1E**). Using a circularly permutated sfGFP (cpsGFP),[69] we derived pnGFP, with a single excitation peak at 484 nm and a single emission peak at 508 nm.[46] The indicator switches from a nearly dark state to a fluorescent state after treatment of nanomolar level of $ONOO^-$ while showing no visible response to other redox-active molecules at physiologically relevant concentrations.[46]

By identifying an appropriate tRNA/aminoacyl-tRNA synthetase pair for mammalian cells, the probe was expressed in mammalian cells to image $ONOO^-$ with minimal interference from other reductants or oxidants.[46] Recently, we reported a second-generation $ONOO^-$ indicator, pnGFP-Ultra, engineered via structure-guided reactivity screening.[48] pnGFP-Ultra displays a remarkable ~110-fold fluorescence enhancement in response to $ONOO^-$. It presents faster chromophore maturation, greater brightness and selectivity, and a larger dynamic range than pnGFP.[48] With an optimized ncAA incorporation system, the expression level of pnGFP-Ultra in HEK 293T cells has been drastically improved. pnGFP-Ultra has been demonstrated to be a robust tool for $ONOO^-$ detection in activated macrophages and primary mouse glia.[48]

In another recent study, the ncAA, thyronine (Thy), was introduced into the chromophores of sfGFP or cpsGFP.[144] The incorporation of Thy led to non-fluorescent proteins, the fluorescence of which could be activated by $ONOO^-$ in a concentration- and time-dependent manners.[144] Despite the initial promise, these Thy-based indicators need further improvement for brightness, sensitivity, specificity, and detection limits.

1.3.9 GERIs for Hydrogen sulfide (H_2S)

Hydrogen sulfide (H_2S) is a weak reducing agent. Although it may directly neutralize highly reactive ROS and RNS, H_2S executes its antioxidant activity primarily through other indirect pathways. H_2S was shown to induce S-sulfhydration of specific cysteine residues in proteins,[145] upregulate reduced glutathione and Trx1,[146, 147] enhance antioxidative enzymes such as superoxide dismutase (SOD),[148] promote the biosynthesis of antioxidative enzymes,[149] and inhibit mitochondrial free radical production.[150] To develop a selective GERI for H_2S, H_2S-reactive ncAA, *p*-azidophenylalanine (*p*AzF) was introduced into the chromophores of a cpGFP

(**Figure 1.1D**). The full-length protein, named cpGFP-Tyr66*p*AzF, was generated in live cells by co-expressing corresponding tRNA/aminoacyl-tRNA synthetase pairs.[45] Treatment with H_2S resulted in specific and rapid fluorescence enhancement.[45] A significantly enhanced version of the H_2S indicator, hsGFP, was later developed based on cpsGFP.[47] The chromophore-forming Tyr in cpsGFP was replaced with *p*AzF, followed by optimization of N- and C- terminal residues close to the chromophore. The addition of H_2S to hsGFP decreases the absorbance peak at 391 nm with an accompanying increase at 452 nm.[47] hsGFP is superior to cpGFP-*p*AzF in many aspects. Due to the superfolder mutations in hsGFP, the hsGFP indicator shows much-improved folding and maturation. Additionally, the product of hsGFP upon reaction with H_2S is ~ 9-fold brighter than the product of cpGFP-Tyr66*p*AzF. After incubation with 100 µM H_2S, the fluorescence of hsGFP increases by ~ 5.5-fold, whereas the fluorescence change of cpGFP-Tyr66*p*AzF is only ~ 0.6-fold.[47] It was also demonstrated that hsGFP could be readily targeted to various subcellular domains to detect H_2S effectively.[47] Because hsGFP is an intensiometric indicator, its intensity is sensitive to protein expression levels and instrumental setups. To create a ratiometric H_2S indicator, hsGFP was fused to EBFP2.[75] In the resultant hsFRET indicator, the reaction product of hsGFP and H_2S acts as a FRET acceptor to EBFP2. Upon reaction, the green-to-blue emission ratio of hsFRET increases from 0.62 to 1.73.[151]

1.3.10 GERIs for organic hydroperoxides (OHPs).

Organic hydroperoxides (OHPs) induce more sustained cellular stress than H_2O_2.[152] While a number GERIs for H_2O_2 have been developed, to our knowledge, OHser (Organic Hydroperoxide Sensor) remains the only indicator for OHPs.[152] OHser was generated by inserting cpVenus,[77] a circularly permuted form of a YFP variant, into Xc-OhrR,[153] a transcriptional regulator controlling

OHP detoxification in the soil bacterium *Xanthomonas campestris* (Xc).[152, 153] Upon oxidation by OHPs, two intersubunit disulfide bonds are formed, breaking the α5 helix in OhrR into two distinct helices connected by a loop. This helix-to-loop conversion results in a significant conformational change, leading to the fluorescence change of cpVenus (**Figure 1.1C**).[152] OHser displays a 2-fold response to cumene hydroperoxide (CHP) and *tert*-butyl hydroperoxide, but almost no response to H_2O_2. It is sensitive to pH changes, so cpVenus should be used in parallel as a control.[152]

1.3.11 GERIs for Nitric Oxide (NO)

Nitric oxide (NO) is a crucial gasotransmitter. In addition to its well-known role in inactivating cyclic guanosine monophosphate (cGMP)-dependent signaling pathways,[154] NO can execute its biological functions through $ONOO^-$, which is made from a diffusion-controlled combination of NO and superoxide, or through *S*-nitrosylation (-SNO), a crucial post-translational modification of sulfhydryl residues in proteins.[155] An amplifier-coupled fluorescent indicator for NO, namely NOA-1, was created by individually fusing the α- and β-subunits of the NO receptor protein sGC with a genetically encoded cGMP indicator named CGY.[156, 157] Upon binding with NO, the spontaneously formed sGCα-CGY/sGCβ-CGY heterodimer can generate cGMP from GTP at a ~ 400-fold faster speed. The generated cGMP binds to CGY to cause a fluorescence change, showing as a ratiometric readout.[156, 157] Another family of NO indicators is geNOps.[158] A bacteria-derived NO-binding domain, GAF,[159] was fused with various FPs to generate chimeras. The addition of NOC-7, a potent NO donor,[160] quickly reduces the fluorescence of geNOps by ~7-18%. There is a linear correlation between the NO concentration and NO-induced fluorescence quenching, and the response is fully reversible.[158] However, geNOps require high levels of Fe^{2+}

for its expression, and it is often needed to soak geNOp-expressing cells with a Fe^{2+} booster solution before imaging. This is an obvious limitation of these geNOp indicators.[158]

1.4 Selected applications of GERIs

Redox-active molecules, such as Trx, Grx, and H_2O_2, are essential for normal cell functions. For example, EGF promotes RTK autophosphorylation and activation, which further triggers cell proliferation and differentiation through the ERK kinase pathway.[161] NOX, activated by EGF, induces H_2O_2 production to deactivate tyrosine phosphatases through cysteine sulfenylation (Cys-SOH), thereby augmenting the EGF signal transduction through RTKs.[3] Furthermore, H_2O_2 has been shown to directly enhance the kinase activity of EGF receptor (EGFR) by sulfenylation of EGFR's catalytic cysteine.[162] Production of H_2O_2 by NOX is, in fact, essential for ERK activation and cell spread.[163] On the other hand, the GSH and Trx antioxidant systems can reduce sulfenic cysteines back to thiolates, terminating EGF signaling.[3, 6] Combining TrxRFP with Grx-roGFP2 reveals that EGF indeed increases the oxidation of both Trx and GSH/GSSG.[36]

Dysregulation of redox signaling can cause oxidative stress, which shifts cells towards disease states.[164] Antioxidants have been explored to reduce oxidative stress and boost antioxidant defense, but dietary antioxidants have failed to yield consistent and satisfactory clinical outcomes.[165] Some studies have shown that certain nutritional antioxidants can even increase cancer progression by downregulating the expression of antioxidant genes.[166] Also, unsuccessful treatment of neurodegenerative diseases with generic antioxidants indicates that some levels of oxidation may be needed for normal signaling and neurogenesis.[167, 168] Because redox signaling is tissue-dependent and spatially regulated, generic antioxidants may not be effective for disease treatment. Meanwhile, a recent study has shown that an organelle-specific NOX inhibitor can

substantially reduce airway inflammation and slow down viral replication.[165, 169] Therefore, the spatial information of redox signaling in diseases would be crucial for developing effective antioxidant treatments. GERIs provide a convenient means to access the spatiotemporal information of redox signaling, thus offering opportunities to better understand diseases and develop new treatments (**Figure 1.2**). Here, we discuss several examples, which applied GERIs to studies related to oxidative signaling and diseases.

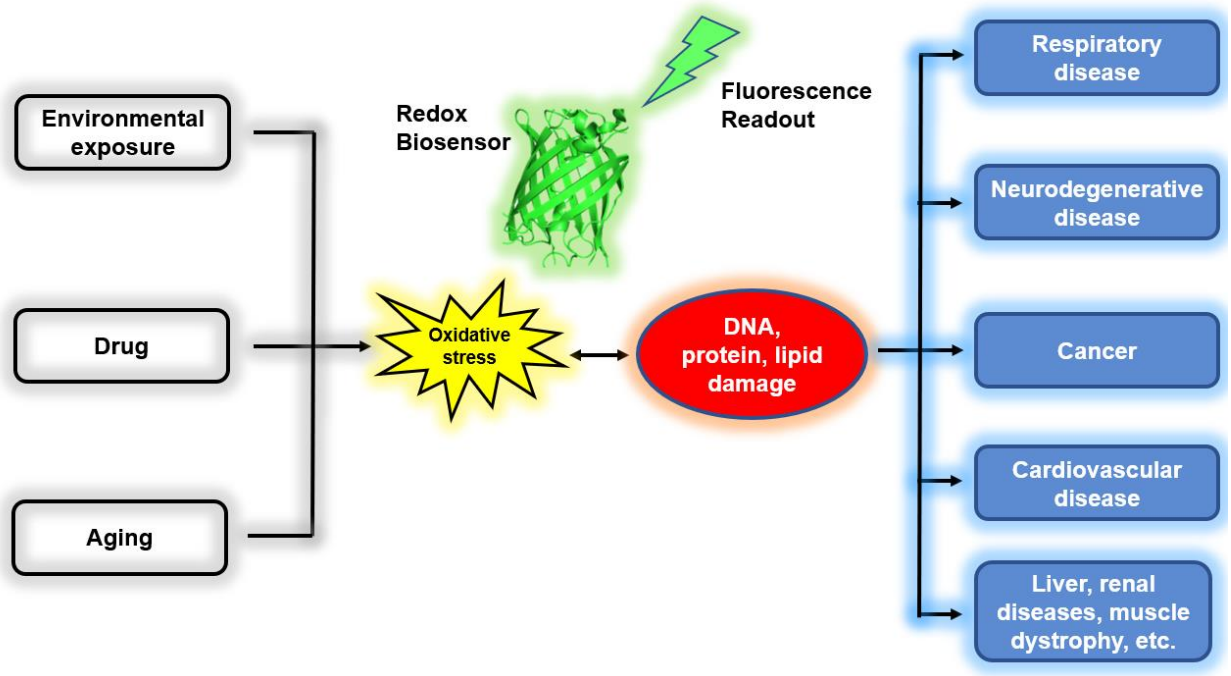

Figure 1.2 Acute and chronic oxidative stress induced by various factors can lead to a large variety of diseases.

Environmental exposure to toxins, drugs, and aging can result in elevated oxidative stress. Unregulated oxidative stress can cause cellular damage through DNA, protein, lipid damages, which exacerbate oxidative stress and contribute to the initiation and progression of diseases.

1.4.1 Using GERIs to study ROS signaling

The number of available GERIs was relatively limited in the first decade of this century. An early study combined roGFP1 with SOD expression and showed that the H_2O_2 level was elevated during cancer progression.[170] Another study combined roGFP1 with small molecule dyes, revealing that mitochondrial inhibition in neurons generates superoxide, H_2O_2, and free radicals and causes neuronal oxidation.[171]

After the H_2O_2-specific sensor HyPer was developed, the H_2O_2 level can be closely monitored. In one example, HyPer was used to evaluate the roles of H_2O_2 in *C. elegans* development.[172] The HyPer biosensor revealed that endogenous H_2O_2 levels were elevated during the early larval stage but rapidly decreased in the reproductive and fertile phases.[172] Moreover, the sensor provided an adequate spatial resolution to show the strongest fluorescence signal in the head region.[172] Although the underlying mechanism needs further studies, the available results strongly suggest that the accumulation of H_2O_2 is tissue-dependent.

Similarly, a transgenic *Xenopus* line expressing HyPer also exhibited a fluorescence increase during fertile phase.[173] HyPer combined with a red genetically encoded fluorescent calcium biosensor, R-GECO,[72] revealed that peroxide production correlates with the Ca^{2+} influx in mitochondria after fertilization.[173] Inhibition of the mitochondrial calcium uniporter (MCU) diminishes the production of peroxide, and the peroxide production quickly recovers after the removal of the MCU inhibitor.[173] Further studies showed that the cell cycle in the embryos' early cleavage stages was regulated through mitochondrial ROS oscillation. Inhibition of mitochondrial ROS production results in cell-cycle arrest, and the Cdc25C phosphatase may be a key regulator during the process.[173]

The role of redox signaling in regenerative processes has also been increasingly studied. HyPer was used to map ROS production during vertebrate tail regeneration in *Xenopus* tadpoles. Several *X. laevis* transgenic lines were developed to express HyPer ubiquitously. After tail amputation, a remarkable increase in intracellular H_2O_2 was detected using HyPer, and such high intracellular H_2O_2 concentrations are maintained throughout the entire tail regeneration process.[174]

HyPer has also been used to visualize H_2O_2 production caused by photodynamic therapy.[175] Interestingly, in drug-resistant cancer cells, ROS levels are often low due to the upregulation of antioxidant defences such as GSH, demonstrating the vital role of redox molecules in cancer progression and treatment.[176] H_2O_2 is a trigger for the expression of pro-metastatic and proangiogenic factors. Using HyPer, Satoka and Hara-Chikuma show that aquaporin-3 (AQP3) imports the extracellular peroxide produced by NOX2, and the increase of intracellular peroxide favors cancer cell migration.[177, 178]

GERIs are valuable tools for revealing redox transients in subcellular compartments. roGFP2 has been targeted to the cytosol or mitochondria to assess the oxidative stress in the murine lung.[179] The sensor showed that lung hyperoxia, which refers to the state of having excess oxygen, causes over-oxidation of the mitochondria but not the cytosol in neonatal alveolar cells. Oxidative stress subsequently induces NOX expression and cell death.[179] While hyperoxia can cause cytotoxicity in the lung, some levels of oxidation are essential for regulating its normal function. By using roGFP2, Desireddi et al. were able to show that oxidation induced by hypoxia, which refers to the state of having inadequate oxygen, triggers Ca^{2+} import to promote pulmonary vasoconstriction.[180]

GERIs have been applied to studying redox signaling in neurodegenerative diseases, such as Alzheimer's disease (AD). Amyloid β (Aβ) aggregation is associated with AD. To investigate

the onset of Aβ neurotoxicity, the researchers expressed cytosolic roGFP2-Orp1 or Grx1-roGFP2 in the Aβ fruit fly models to monitor the H_2O_2 levels and the redox potential of GSH (E_{GSH}) in parallel.[181] Increased cytosolic E_{GSH} was observed in neurons upon onset of Aβ aggregation, suggesting that E_{GSH} is the driving force for the Aβ-mediated neurotoxicity in AD.[181] More specifically, this redox change was only observed in neurons but not in glial cells, implying that neurons are susceptible to Aβ-regulated redox stress.[181] The study performed in *Drosophila* Aβ aggregation models suggested that glutathione redox potential plays a pivotal role in AD. In another study, roGFP2 was targeted to mitochondria in neurodegenerative or mitochondrial encephalomyopathy *Drosophila* models with ATPase deficiency or electron transport chain (ETC) deficiency. roGFP2 revealed an elevated oxidation state at a later age in diseased fly models with reduced lifespan and increased degeneration.[182] Moreover, mitochondria-targeted antioxidants improved locomotor function in early pathogenesis and extended the fly longevity, indicating the involvement of oxidative stress in the disease progression.[182]

Grx1-roGFP2 has been used to study transgenic amyotrophic lateral sclerosis (ALS) and spinal cord injury in mice models. In physiological conditions, mitochondrial contraction, a process in neurons that protects mitochondria from acute stress, is accompanied by reversible redox changes.[183] Grx1-roGFP2 revealed that mitochondrial contraction is preceded by transient mild mitochondrial oxidation caused by stressors.[183] Next, the membrane depolarization through potassium (K^+) or sodium ion (Na^+) fluxes further reduces membrane potential, consequently increasing the mitochondrial matrix's pH and accelerating the ETC.[183] The ETC generates ROS, which oxidizes the mitochondria to activate the uncoupling proteins (UCPs), dissipating the proton gradient to protect mitochondria from prolonged damage.[183] In the ALS and spinal cord injury

models, mitochondria in neurons do not experience contraction. Thus, mitochondrial oxidation in these neurons becomes persistent, causing permanent mitochondrial permeability.[183]

roGFP1 has also been expressed in cultured rat hippocampal neurons or organotypic slices for monitoring the alteration of neuronal redox states during mitochondrial inhibition and neuronal stimulation. Neuronal stimulation by K^+ consistently increases the oxidation of neurons, while neuronal stimulation by glutamate can increase or decrease oxidation depending on the glutamate levels.[171] In another study, the cytosolic or mitochondria-localized roGFP1 was stably expressed in transgenic mice under the Thy1 promoter to ensure cell-type-specific expression in excitatory neurons.[184] Neuron activation by either electrical stimulation or K^+-mediated depolarization altered the neuronal redox states indicated by roGFP1.[184] The inhibition of the mitochondrial respiratory chain in acute brain slices shifts roGFP1 to a more oxidized state.[184] In these examples, roGFP1 provided a robust ratiometric readout for neuronal oxidation state unaffected by pH changes.[171]

GERIs have been utilized to investigate the role of redox in cardiac dysfunction. For example, D-amino acid oxidase (DAAO), a protein that can produce H_2O_2 from the oxidation of D-amino acids, was used as a chemogenetic tool to induce H_2O_2 production. At the same time, HyPer was fused with DAAO to monitor H_2O_2 production.[185] Using the cardiac troponin T (cTnT) promoter, the fusion protein, HyPer-DAAO, was specifically targeted to the rat heart to induce H_2O_2 production. HyPer revealed that DAAO stably expressed in the rat heart induced H_2O_2 production when supplementing D-alanine.[185] Rats with H_2O_2 generation showed cardiac dysfunction such as systolic dysfunction (reduced heart contraction) and dilated cardiomyopathy (weakened and enlarged heart muscle) without any signs of fibrotic remodeling.[185] Although overexpression of redox-active enzymes was observed in rat hearts, GSH concentration was

lowered while the overall glutathione (GSH/GSSG) concentration was elevated, indicating the presence of oxidative stress in the heart.[185]

1.4.2 Using GERIs to decipher drug-induced oxidative toxicity

GERIs have been applied in high-throughput drug screening to evaluate the oxidative toxicity of various drugs and drug candidates. SoNar, an indicator for the ratio of NAD^+/NADH, was used to screen > 5500 metabolism-perturbing anticancer drug candidates for cytotoxicity.[44] In the study, SoNar was stably expressed in a human lung cancer cell line, H1299, and the effect of the drug candidates on the cytosolic NAD^+/NADH redox states was then assessed. Interestingly, most compounds decreasing the cellular NAD^+/NADH ratio showed no or minimal impact on cell toxicity. In contrast, a significant fraction of the compounds that increased the ratio presented apparent cell toxicity. A protein kinase B (Akt) inhibitor KP372-1, which increased the NAD^+/NADH ratio, exhibited the most potent cell cytotoxicity at the nanomolar concentration range. Furthermore, a collective use of SoNar, HyPer, and roGFP revealed that KP372-1 is an NAD(P)H dehydrogenase quinone 1 regulator, which mediates the NAD(P)H-dependent redox cycling.[44, 186] This compound thus kills cancer cells by generating ROS. Using roUnaG, a later study further confirmed this finding that KP372-1 exerts its anticancer function by creating severe oxidative stress.[187]

In another study, stable cancer cell lines expressing mitochondrial-localized roGFP2(mt-roGFP) and nuclear H2B-mCherry were utilized as tools for high-throughput drug screening.[188] Mt-roGFP was explicitly used to screen for drugs capable of perturbing mitochondrial redox because mitochondrial oxidation is a marker for cytotoxicity. H2B-mCherry was used as a control to mark nuclear structures. A library of cancer drugs was successfully screened through high-

throughput imaging and segmentation of pre- or post-drug-treated cells.[188] The study demonstrated that cisplatin, a chemotherapy medication, can cause mitochondrial damage and cytotoxicity. Moreover, a later study used HyPer2 to further demonstrate that cisplatin could generate H_2O_2 in a time- and dose-dependent manner in cancer cells.[189] Thus, GERIs have provided a promising way to visualize drug-induced toxicity due to their ease of use, adaptability for different cell types, and compatibility with high-throughput screening.

1.4.3 Using GERIs to decipher age-induced oxidative toxicity

Aging increases the risk for many diseases as well as morbidity and mortality from diseases.[190] ROS accumulation and the depletion of other endogenous redox-active molecules such as NAD^+ have been associated with aging.[191, 192] For example, mCherry-FiNad showed a decline of NAD^+ level as mice age.[112] Model animals with compromised antioxidant defense systems often exhibit features of premature aging such as mitochondrial dysfunction and DNA damage.[193]

Using Grx1-roGFP2 and roGFP2-Orp1, Albrecht et al. found that the aging-dependent oxidation in *Drosophila* was restricted to particular regions (e.g., midgut enterocytes), and the redox states of H_2O_2 and Grx were not coupled.[194] Interestingly, higher levels of H_2O_2 were observed in *Drosophila* with longer lifespans.[194] In another study using *C. elegans*, the H_2O_2 level, measured by HyPer, increases as aging occurs.[195] A restricted diet could artificially extend the lifespan of *C. elegans* and delay aging-dependent oxidation.[195] A recent study has further elucidated the relationship between cellular redox states and *C. elegans* aging using Grx1-roGFP2. An elevated oxidation level in the early developmental state is associated with a longer lifespan.[196] The study showed that redox signaling could lower the trimethylation of lysine 4 in histone H3

(H3K4me3), resulting in increased stress resistance and more reduced cellular states at a later timepoint.[196]

Similarly, experiments in yeasts have shown aging-dependent oxidation. Both the H_2O_2 level measured by roGFP2-Orp1 and the redox potential of the cytosolic GSH/GSSG pool measured by Grx1-roGFP2 increase as yeasts age in aerobic conditions.[197] However, although the H_2O_2 level is still associated with the replicative lifespan of yeasts under anaerobic conditions, the cytoplasmic GSH/GSSG redox system does not seem to play a role in lifespan.[197]

1.4.4 Using GERIs to decipher environmental exposure-induced oxidative toxicity

It is well recognized that the environment is a critical contributing factor to human health. Exposure to toxic environmental substances, such as heavy metals, pollutants, and chemicals, can cause oxidative stress, skewing the cellular redox balance and elevating ROS levels. For example, iron, copper, and chromium can generate free radicals through Fenton chemistry, while cadmium can cause oxidative stress by inhibiting redox enzymes and depleting glutathione.[198] Subsequently, when the level of ROS exceeds the antioxidant capacity, it can lead to tissue and DNA damage.[199] Cellular and DNA damage further increases ROS levels through inflammatory response, leading to cytotoxicity and even cancer.[200]

roGFP2 has been applied in *E. coli* to study the level of oxidative stress resulted from H_2O_2, menadione, sodium selenite, zinc pyrithione, and other heavy metals.[201] Interestingly, the heavy metals have resulted in oxidation increases smaller than other chemical stressors in the bacterial system.[201] In another study, a redox biosensor created by immobilizing roGFP2-expressing *E. coli* in a *k*-carrageenan matrix was applied to study metalloid-induced oxidative stress.[202] Oxidative stress, indicated by a rapid excitation increase of roGFP2 at 400 nm and an excitation decrease at

490 nm, was observed after the exposure to metalloids.[202] Arsenite and selenite are two representative metalloid pollutants in the aquatic environment, and they can enter the human body after bioaccumulation. Both can cause cell cytotoxicity by inducing oxidative stress.[202] This immobilized redox biosensor showed concentration-dependent fluorescence change in response to both arsenite and selenite metalloids. However, different limits of detection (LODs) were observed, which may be explained by different cytotoxicity levels of these two types of metalloids.[202]

1.5 Conclusions and outlook

ROS are typical examples of "the dose makes the poison" – a toxicological phenomenon discovered by Paracelsus in 1538.[203] When ROS are generated at low levels, they carry out crucial signaling functions. However, when exceeding the physiological level, ROS can cause toxicity and even irreversible damages. ROS concentrations largely contribute to the level of oxidative toxicity, but the spatiotemporal regulation of various redox molecules is now found to play an equally important role. This review article summarized a selected panel of GERIs, which form a toolkit for studying redox signaling dynamics in various biological systems. When applying these indicators in studies, it is necessary to consider different parameters, including the probe sensitivity, specificity, detection limit, and dynamic range. In addition, artifact-inducing factors, such as pH, temperature, and interactions with interfering ions, should also be excluded using appropriate controls. Moreover, it should be taken into account that overexpression of GERIs in cells may result in buffering effects, limiting the magnitude of redox changes in response to stimuli. In many cases, the selection of the most suitable GERI depends on the particular research question, but as a general rule, GERIs with appropriate midpoint redox potentials should be selected to ensure their

proper functions. Sometimes, a head-by-head comparison may be needed to identify the best GERI for a particular application.

While GERIs specific for Grx, Trx, and H_2O_2 have been developed, indicators specific for other redox-active molecules are still in high demand. ROS such as superoxide and hydroxyl radicals exhibit unique toxicity, but the detection of these radicals is difficult due to their short lifetime. Having probes specific for them would be advantageous for understanding ROS-induced toxicity as these radicals can directly damage DNA, react with protein, or modify lipid functions. Other redox enzymes such as Ero1 (ER oxidoreductase 1) and PDI are critical for oxidative protein folding,[204] unfolded protein response (UPR),[205] and cell apoptosis. GERIs specific to these redox enzymes are currently lacking but needed.

In general, FPs with higher brightness and more robust folding and chromophore maturation should be more amenable to redox-sensitive modifications and sensor engineering. Also, indicators derived from FPs with better photophysical properties are more likely to inherit these favorable features. With the appearance of more and more FPs possessing improved properties, it would be desirable to develop GERIs based on these new FPs. For example, the development of mScarlet, a red FP with better maturation, brightness, and photostability, may lead to the generation of better, red fluorescent redox indicators.[206] GERIs with new colors, especially those with longer excitation and emission wavelengths, would benefit redox studies in living organisms. First, illuminating cells with longer wavelengths can lower cytotoxicity. Second, the 'optical window' of tissues is also in the far-red and near-infrared spectral range in which efficient endogenous absorbers are lacking.[207] GERIs based on far-red and near-infrared FPs will likely become available, resulting in better tissue and animal imaging tools. Moreover, the development

of GERIs in various colors can provide multi-color imaging tools to unravel the interplay and crosstalk between different signaling pathways.

GERIs in imaging modalities other than fluorescence would also be valuable tools. Recent studies have generated a panel of luciferase-luciferin pairs independent of the ATP cofactor,[208-213] resulting in a platform for further developments of ATP-independent, bioluminescent GERIs. These efforts will significantly facilitate our understanding of redox processes under opaque tissue because bioluminescence imaging can reach deeper than fluorescence imaging.

The advances in GERIs will continue to accelerate our understanding of redox signaling, which can, in turn, lead to the development of new indicators. The application of these new tools would further expand our knowledge. As more is known, intervention strategies may be developed to restore cellular redox balance and treat diseases.

There are continuous needs for advanced imaging techniques and/or indicators with better photostability, brightness, and dynamic range. Currently, wide-field or confocal microscopy is often used for imaging redox signals in living systems. Super-resolution imaging could be an exciting new tool for investigating redox signaling with better spatial resolution. In one example, super-solution imaging of cellular redox was demonstrated using HyPer2 and stimulated emission depletion(STED) microscopy.[214] However, super-resolution methods such as STED and photo-activated localization microscopy (PALM or STORM) require high light doses, resulting in substantial photobleaching and cytotoxicity.[215] Other super-resolution methods, such as structured illumination microscopy (SIM)[216] and super-resolution radial fluctuations (SRRF)[217], cause less photobleaching and may be promising for imaging various GERIs. With advances in both microscopy and indicators, the spatiotemporal regulation of redox signaling and oxidative toxicity can be better understood in the future.

1.6 References

1. D'Autréaux, B.; Toledano, M. B., ROS as signalling molecules: mechanisms that generate specificity in ROS homeostasis. *Nat. Rev. Mol. Cell Biol.* **2007,** *8* (10), 813-824.
2. Valko, M.; Rhodes, C.; Moncol, J.; Izakovic, M.; Mazur, M., Free radicals, metals and antioxidants in oxidative stress-induced cancer. *Chem.-Biol. Interact.* **2006,** *160* (1), 1-40.
3. Schieber, M.; Chandel, N. S., ROS function in redox signaling and oxidative stress. *Curr. Biol.* **2014,** *24* (10), R453-R462.
4. Dickinson, B. C.; Chang, C. J., Chemistry and biology of reactive oxygen species in signaling or stress responses. *Nat. Chem. Biol.* **2011,** *7* (8), 504.
5. Beckman, J. S.; Koppenol, W. H., Nitric oxide, superoxide, and peroxynitrite: the good, the bad, and ugly. *Am. J. Physiol. Cell Physiol.* **1996,** *271* (5), C1424-C1437.
6. Lee, S.-R.; Kwon, K.-S.; Kim, S.-R.; Rhee, S. G., Reversible inactivation of protein-tyrosine phosphatase 1B in A431 cells stimulated with epidermal growth factor. *J. Biol. Chem.* **1998,** *273* (25), 15366-15372.
7. To, E. E.; Vlahos, R.; Luong, R.; Halls, M. L.; Reading, P. C.; King, P. T.; Chan, C.; Drummond, G. R.; Sobey, C. G.; Broughton, B. R., Endosomal NOX2 oxidase exacerbates virus pathogenicity and is a target for antiviral therapy. *Nat. Commun.* **2017,** *8* (1), 1-17.
8. Ischiropoulos, H.; Zhu, L.; Beckman, J. S., Peroxynitrite formation from macrophage-derived nitric oxide. *Arch. Biochem. Biophys.* **1992,** *298* (2), 446-451.
9. Kruk, J.; Aboul-Enein, H. Y.; Kładna, A.; Bowser, J. E., Oxidative stress in biological systems and its relation with pathophysiological functions: the effect of physical activity on cellular redox homeostasis. *Free Radic. Res.* **2019,** *53* (5), 497-521.
10. Cherubini, A.; Ruggiero, C.; Polidori, M. C.; Mecocci, P., Potential markers of oxidative stress in stroke. *Free Radic. Biol. Med.* **2005,** *39* (7), 841-852.
11. Srinivas, U. S.; Tan, B. W.; Vellayappan, B. A.; Jeyasekharan, A. D., ROS and the DNA damage response in cancer. *Redox Biol.* **2019,** *25*, 101084.
12. Leutner, S.; Eckert, A.; Müller, W., ROS generation, lipid peroxidation and antioxidant enzyme activities in the aging brain. *J. Neural Transm.* **2001,** *108* (8-9), 955-967.
13. Luceri, C.; Bigagli, E.; Femia, A. P.; Caderni, G.; Giovannelli, L.; Lodovici, M., Aging related changes in circulating reactive oxygen species (ROS) and protein carbonyls are indicative of liver oxidative injury. *Toxicol. Rep.* **2018,** *5*, 141-145.
14. Lee, I.-T.; Yang, C.-M., Role of NADPH oxidase/ROS in pro-inflammatory mediators-induced airway and pulmonary diseases. *Biochem. Pharmacol.* **2012,** *84* (5), 581-590.
15. Ozbek, E., Induction of oxidative stress in kidney. *Int. J. Nephrol.* **2012,** *2012*.
16. Pacher, P.; Beckman, J. S.; Liaudet, L., Nitric oxide and peroxynitrite in health and disease. *Physiol. Rev.* **2007,** *87* (1), 315-424.

17. Beckman, J. S., Understanding peroxynitrite biochemistry and its potential for treating human diseases. *Arch. Biochem. Biophys.* **2009,** *484* (2), 114.
18. Suzen, S.; Gurer-Orhan, H.; Saso, L., Detection of reactive oxygen and nitrogen species by electron paramagnetic resonance (EPR) technique. *Molecules* **2017,** *22* (1), 181.
19. Agarwal, A.; Allamaneni, S. S.; Said, T. M., Chemiluminescence technique for measuring reactive oxygen species. *Reprod. Biomed. Online* **2004,** *9* (4), 466-468.
20. Jiao, X.; Li, Y.; Niu, J.; Xie, X.; Wang, X.; Tang, B., Small-molecule fluorescent probes for imaging and detection of reactive oxygen, nitrogen, and sulfur species in biological systems. *Anal. Chem.* **2018,** *90* (1), 533-555.
21. Dickinson, B. C.; Srikun, D.; Chang, C. J., Mitochondrial-targeted fluorescent probes for reactive oxygen species. *Curr. Opin. Chem. Biol.* **2010,** *14* (1), 50-56.
22. Lou, Z.; Li, P.; Han, K., Redox-responsive fluorescent probes with different design strategies. *Acc. Chem. Res.* **2015,** *48* (5), 1358-1368.
23. Lü, R., Reaction-based small-molecule fluorescent probes for dynamic detection of ROS and transient redox changes in living cells and small animals. *J. Mol. Cell. Cardiol.* **2017,** *110*, 96-108.
24. Bai, X.; Ng, K. K.-H.; Hu, J. J.; Ye, S.; Yang, D., Small-molecule-based fluorescent sensors for selective detection of reactive oxygen species in biological systems. *Annu. Rev. Biochem.* **2019,** *88*, 605-633.
25. Ren, W.; Ai, H.-W., Genetically encoded fluorescent redox probes. *Sensors* **2013,** *13* (11), 15422-15433.
26. Schwarzlander, M.; Dick, T. P.; Meyer, A. J.; Morgan, B., Dissecting Redox Biology Using Fluorescent Protein Sensors. *Antioxid. Redox Signal.* **2016,** *24* (13), 680-712.
27. Meyer, A. J.; Dick, T. P., Fluorescent protein-based redox probes. *Antioxid. Redox Signal.* **2010,** *13* (5), 621-650.
28. Lukyanov, K. A.; Belousov, V. V., Genetically encoded fluorescent redox sensors. *Biochim. Biophys. Acta* **2014,** *1840* (2), 745-756.
29. Kostyuk, A. I.; Kokova, A. D.; Podgorny, O. V.; Kelmanson, I. V.; Fetisova, E. S.; Belousov, V. V.; Bilan, D. S., Genetically Encoded Tools for Research of Cell Signaling and Metabolism under Brain Hypoxia. *Antioxidants* **2020,** *9* (6), 516.
30. Tsien, R. Y., The Green Fluorescent Protein. *Annu. Rev. Biochem.* **1998,** *67* (1), 509-544.
31. Hanson, G. T.; Aggeler, R.; Oglesbee, D.; Cannon, M.; Capaldi, R. A.; Tsien, R. Y.; Remington, S. J., Investigating mitochondrial redox potential with redox-sensitive green fluorescent protein indicators. *J. Biol. Chem.* **2004,** *279* (13), 13044-13053.
32. Østergaard, H.; Tachibana, C.; Winther, J. R., Monitoring disulfide bond formation in the eukaryotic cytosol. *J. Cell Biol.* **2004,** *166* (3), 337-345.
33. Fan, Y.; Chen, Z.; Ai, H. W., Monitoring redox dynamics in living cells with a redox-sensitive red fluorescent protein. *Anal. Chem.* **2015,** *87* (5), 2802-2810.
34. Fan, Y.; Ai, H. W., Development of redox-sensitive red fluorescent proteins for imaging redox dynamics in cellular compartments. *Anal. Bioanal. Chem.* **2016,** *408* (11), 2901-2911.

35. Gutscher, M.; Pauleau, A. L.; Marty, L.; Brach, T.; Wabnitz, G. H.; Samstag, Y.; Meyer, A. J.; Dick, T. P., Real-time imaging of the intracellular glutathione redox potential. *Nat. Methods* **2008,** *5* (6), 553-559.
36. Fan, Y.; Makar, M.; Wang, M. X.; Ai, H.-w., Monitoring thioredoxin redox with a genetically encoded red fluorescent biosensor. *Nat. Chem. Biol.* **2017,** *13* (9), 1045.
37. Gutscher, M.; Sobotta, M. C.; Wabnitz, G. H.; Ballikaya, S.; Meyer, A. J.; Samstag, Y.; Dick, T. P., Proximity-based protein thiol oxidation by H2O2-scavenging peroxidases. *J. Biol. Chem.* **2009,** *284* (46), 31532-31540.
38. Baird, G. S.; Zacharias, D. A.; Tsien, R. Y., Circular permutation and receptor insertion within green fluorescent proteins. *Proc. Natl. Acad. Sci. U.S.A.* **1999,** *96* (20), 11241-11246.
39. Belousov, V. V.; Fradkov, A. F.; Lukyanov, K. A.; Staroverov, D. B.; Shakhbazov, K. S.; Terskikh, A. V.; Lukyanov, S., Genetically encoded fluorescent indicator for intracellular hydrogen peroxide. *Nat. Methods* **2006,** *3* (4), 281-286.
40. Markvicheva, K. N.; Bilan, D. S.; Mishina, N. M.; Gorokhovatsky, A. Y.; Vinokurov, L. M.; Lukyanov, S.; Belousov, V. V., A genetically encoded sensor for H_2O_2 with expanded dynamic range. *Biorg. Med. Chem.* **2011,** *19* (3), 1079-1084.
41. Bilan, D. S.; Pase, L.; Joosen, L.; Gorokhovatsky, A. Y.; Ermakova, Y. G.; Gadella, T. W.; Grabher, C.; Schultz, C.; Lukyanov, S.; Belousov, V. V., HyPer-3: a genetically encoded H_2O_2 probe with improved performance for ratiometric and fluorescence lifetime imaging. *ACS Chem. Biol.* **2013,** *8* (3), 535-542.
42. Ermakova, Y. G.; Bilan, D. S.; Matlashov, M. E.; Mishina, N. M.; Markvicheva, K. N.; Subach, O. M.; Subach, F. V.; Bogeski, I.; Hoth, M.; Enikolopov, G., Red fluorescent genetically encoded indicator for intracellular hydrogen peroxide. *Nat. Commun.* **2014,** *5* (1), 1-9.
43. Pak, V. V.; Ezerina, D.; Lyublinskaya, O. G.; Pedre, B.; Tyurin-Kuzmin, P. A.; Mishina, N. M.; Thauvin, M.; Young, D.; Wahni, K.; Martinez Gache, S. A.; Demidovich, A. D.; Ermakova, Y. G.; Maslova, Y. D.; Shokhina, A. G.; Eroglu, E.; Bilan, D. S.; Bogeski, I.; Michel, T.; Vriz, S.; Messens, J.; Belousov, V. V., Ultrasensitive Genetically Encoded Indicator for Hydrogen Peroxide Identifies Roles for the Oxidant in Cell Migration and Mitochondrial Function. *Cell Metab.* **2020,** *31* (3), 642-653 e646.
44. Zhao, Y.; Hu, Q.; Cheng, F.; Su, N.; Wang, A.; Zou, Y.; Hu, H.; Chen, X.; Zhou, H. M.; Huang, X.; Yang, K.; Zhu, Q.; Wang, X.; Yi, J.; Zhu, L.; Qian, X.; Chen, L.; Tang, Y.; Loscalzo, J.; Yang, Y., SoNar, a Highly Responsive NAD+/NADH Sensor, Allows High-Throughput Metabolic Screening of Anti-tumor Agents. *Cell Metab.* **2015,** *21* (5), 777-789.
45. Chen, S.; Chen, Z. J.; Ren, W.; Ai, H. W., Reaction-based genetically encoded fluorescent hydrogen sulfide sensors. *J. Am. Chem. Soc.* **2012,** *134* (23), 9589-9592.
46. Chen, Z. J.; Ren, W.; Wright, Q. E.; Ai, H. W., Genetically encoded fluorescent probe for the selective detection of peroxynitrite. *J. Am. Chem. Soc.* **2013,** *135* (40), 14940-14943.

47. Chen, Z. J.; Ai, H. W., A highly responsive and selective fluorescent probe for imaging physiological hydrogen sulfide. *Biochemistry* **2014,** *53* (37), 5966-5974.
48. Chen, Z.; Zhang, S.; Li, X.; Ai, H. W., A high-performance genetically encoded fluorescent biosensor for imaging physiological peroxynitrite. *Cell Chem. Biol.* **2021**, DOI:https://doi.org/10.1016/j.chembiol.2021.01.013
49. Clegg, R., Fluorescence resonance energy transfer. In *Fluorescence imaging spectroscopy and microscopy*, X.F. Wang and B. Herman, editors. John Wiley & Sons Inc., New York. **1996,** Vol. 137, 179-251.
50. Sekar, R. B.; Periasamy, A., Fluorescence resonance energy transfer (FRET) microscopy imaging of live cell protein localizations. *J. Cell Biol.* **2003,** *160* (5), 629-633.
51. Carlson, H. J.; Campbell, R. E., Genetically encoded FRET-based biosensors for multiparameter fluorescence imaging. *Curr. Opin. Biotechnol.* **2009,** *20* (1), 19-27.
52. Kolossov, V. L.; Spring, B. Q.; Clegg, R. M.; Henry, J. J.; Sokolowski, A.; Kenis, P. J.; Gaskins, H. R., Development of a high-dynamic range, GFP-based FRET probe sensitive to oxidative microenvironments. *Exp. Biol. Med.* **2011,** *236* (6), 681-691.
53. Moye-Rowley, W.; Harshman, K.; Parker, C., Yeast YAP1 encodes a novel form of the jun family of transcriptional activator proteins. *Genes Dev.* **1989,** *3* (3), 283-292.
54. Rizzo, M. A.; Springer, G. H.; Granada, B.; Piston, D. W., An improved cyan fluorescent protein variant useful for FRET. *Nat. Biotechnol.* **2004,** *22* (4), 445-449.
55. Griesbeck, O.; Baird, G. S.; Campbell, R. E.; Zacharias, D. A.; Tsien, R. Y., Reducing the environmental sensitivity of yellow fluorescent protein: mechanism and applications. *J. Biol. Chem.* **2001,** *276* (31), 29188-29194.
56. Yano, T.; Oku, M.; Akeyama, N.; Itoyama, A.; Yurimoto, H.; Kuge, S.; Fujiki, Y.; Sakai, Y., A novel fluorescent sensor protein for visualization of redox states in the cytoplasm and in peroxisomes. *Mol. Cell. Biol.* **2010,** *30* (15), 3758-3766.
57. Ostergaard, H.; Henriksen, A.; Hansen, F. G.; Winther, J. R., Shedding light on disulfide bond formation: engineering a redox switch in green fluorescent protein. *EMBO J.* **2001,** *20* (21), 5853-5862.
58. Elsliger, M.-A.; Wachter, R. M.; Hanson, G. T.; Kallio, K.; Remington, S. J., Structural and spectral response of green fluorescent protein variants to changes in pH. *Biochemistry* **1999,** *38* (17), 5296-5301.
59. Wachter, R. M.; Remington, S. J., Sensitivity of the yellow variant of green fluorescent protein to halides and nitrate. *Curr. Biol.* **1999,** *9* (17), R628-R629.
60. Dooley, C. T.; Dore, T. M.; Hanson, G. T.; Jackson, W. C.; Remington, S. J.; Tsien, R. Y., Imaging dynamic redox changes in mammalian cells with green fluorescent protein indicators. *J. Biol. Chem.* **2004,** *279* (21), 22284-22293.
61. Lohman, J. R.; Remington, S. J., Development of a family of redox-sensitive green fluorescent protein indicators for use in relatively oxidizing subcellular environments. *Biochemistry* **2008,** *47* (33), 8678-8688.

62. Aller, I.; Rouhier, N.; Meyer, A. J., Development of roGFP2-derived redox probes for measurement of the glutathione redox potential in the cytosol of severely glutathione-deficient rml1 seedlings. *Front. Plant Sci.* **2013,** *4*, 506.
63. Pédelacq, J.-D.; Cabantous, S.; Tran, T.; Terwilliger, T. C.; Waldo, G. S., Engineering and characterization of a superfolder green fluorescent protein. *Nat. Biotechnol.* **2006,** *24* (1), 79-88.
64. Hoseki, J.; Oishi, A.; Fujimura, T.; Sakai, Y., Development of a stable ERroGFP variant suitable for monitoring redox dynamics in the ER. *Biosci. Rep.* **2016,** *36* (2).
65. Norcross, S.; Trull, K. J.; Snaider, J.; Doan, S.; Tat, K.; Huang, L.; Tantama, M., Extending roGFP Emission via FRET Relay Enables Simultaneous Dual Compartment Ratiometric Redox Imaging in Live Cells. *ACS Sens.* **2017,** *2* (11), 1721.
66. Shaner, N. C.; Lin, M. Z.; McKeown, M. R.; Steinbach, P. A.; Hazelwood, K. L.; Davidson, M. W.; Tsien, R. Y., Improving the photostability of bright monomeric orange and red fluorescent proteins. *Nat. Methods* **2008,** *5* (6), 545.
67. Zhao, Y.; Araki, S.; Wu, J.; Teramoto, T.; Chang, Y. F.; Nakano, M.; Abdelfattah, A. S.; Fujiwara, M.; Ishihara, T.; Nagai, T.; Campbell, R. E., An Expanded Palette of Genetically Encoded Ca2+ Indicators. *Science* **2011,** *333* (6051), 1888-1891.
68. Piattoni, C. V.; Sardi, F.; Klein, F.; Pantano, S.; Bollati-Fogolin, M.; Comini, M., New red-shifted fluorescent biosensor for monitoring intracellular redox changes. *Free Radic. Biol. Med.* **2019,** *134*, 545-554.
69. Lam, A. J.; St-Pierre, F.; Gong, Y.; Marshall, J. D.; Cranfill, P. J.; Baird, M. A.; McKeown, M. R.; Wiedenmann, J.; Davidson, M. W.; Schnitzer, M. J., Improving FRET dynamic range with bright green and red fluorescent proteins. *Nat. Methods* **2012,** *9* (10), 1005-1012.
70. Sugiura, K.; Nagai, T.; Nakano, M.; Ichinose, H.; Nakabayashi, T.; Ohta, N.; Hisabori, T., Redox sensor proteins for highly sensitive direct imaging of intracellular redox state. *Biochem. Biophys. Res. Commun.* **2015,** *457* (3), 242-248.
71. Tomosugi, W.; Matsuda, T.; Tani, T.; Nemoto, T.; Kotera, I.; Saito, K.; Horikawa, K.; Nagai, T., An ultramarine fluorescent protein with increased photostability and pH insensitivity. *Nat. Methods* **2009,** *6* (5), 351-353.
72. Ai, H.-w.; Shaner, N. C.; Cheng, Z.; Tsien, R. Y.; Campbell, R. E., Exploration of new chromophore structures leads to the identification of improved blue fluorescent proteins. *Biochemistry* **2007,** *46* (20), 5904-5910.
73. Goedhart, J.; Van Weeren, L.; Hink, M. A.; Vischer, N. O.; Jalink, K.; Gadella, T. W., Bright cyan fluorescent protein variants identified by fluorescence lifetime screening. *Nat. Methods* **2010,** *7* (2), 137-139.
74. Nagai, T.; Ibata, K.; Park, E. S.; Kubota, M.; Mikoshiba, K.; Miyawaki, A., A variant of yellow fluorescent protein with fast and efficient maturation for cell-biological applications. *Nat. Biotechnol.* **2002,** *20* (1), 87-90.
75. Sugiura, K.; Tanaka, H.; Kurisu, G.; Wakabayashi, K.-i.; Hisabori, T., Multicolor redox sensor proteins can visualize redox changes in various compartments of the living cell. *Biochim. Biophys. Acta Gen. Subj .* **2019,** *1863* (6), 1098-1107.

76. Shitashima, Y.; Shimozawa, T.; Kumagai, A.; Miyawaki, A.; Asahi, T., Two distinct fluorescence states of the ligand-induced green fluorescent protein UnaG. *Biophys. J.* **2017,** *113* (12), 2805-2814.
77. Kumagai, A.; Ando, R.; Miyatake, H.; Greimel, P.; Kobayashi, T.; Hirabayashi, Y.; Shimogori, T.; Miyawaki, A., A Bilirubin-Inducible Fluorescent Protein from Eel Muscle. *Cell* **2013,** *153* (7), 1602-1611.
78. Hu, H.; Wang, A.; Huang, L.; Zou, Y.; Gu, Y.; Chen, X.; Zhao, Y.; Yang, Y., Monitoring cellular redox state under hypoxia using a fluorescent sensor based on eel fluorescent protein. *Free Radic. Biol. Med.* **2018,** *120*, 255-265.
79. Shaner, N. C.; Campbell, R. E.; Steinbach, P. A.; Giepmans, B. N.; Palmer, A. E.; Tsien, R. Y., Improved monomeric red, orange and yellow fluorescent proteins derived from Discosoma sp. red fluorescent protein. *Nat. Biotechnol.* **2004,** *22* (12), 1567-1572.
80. Prasher, D. C.; Eckenrode, V. K.; Ward, W. W.; Prendergast, F. G.; Cormier, M. J., Primary structure of the Aequorea victoria green-fluorescent protein. *Gene* **1992,** *111* (2), 229-233.
81. Cormack, B. P.; Valdivia, R. H.; Falkow, S., FACS-optimized mutants of the green fluorescent protein (GFP). *Gene* **1996,** *173* (1), 33-38.
82. Zapata-Hommer, O.; Griesbeck, O., Efficiently folding and circularly permuted variants of the Sapphire mutant of GFP. *BMC Biotechnol.* **2003,** *3* (1), 1-6.
83. Sugiura, K.; Mihara, S.; Fu, N.; Hisabori, T., Real-time monitoring of the in vivo redox state transition using the ratiometric redox state sensor protein FROG/B. *Proc. Natl. Acad. Sci. U.S.A.* **2020,** *117* (27), 16019-16026.
84. Björnberg, O.; Østergaard, H.; Winther, J. R., Mechanistic insight provided by glutaredoxin within a fusion to redox-sensitive yellow fluorescent protein. *Biochemistry* **2006,** *45* (7), 2362-2371.
85. Håkansson, K. O.; Winther, J. R., Structure of glutaredoxin Grx1p C30S mutant from yeast. *Acta Crystallogr. Sect. D. Biol. Crystallogr.* **2007,** *63* (3), 288-294.
86. Gallogly, M. M.; Starke, D. W.; Mieyal, J. J., Mechanistic and kinetic details of catalysis of thiol-disulfide exchange by glutaredoxins and potential mechanisms of regulation. *Antioxid. Redox Signal.* **2009,** *11* (5), 1059-1081.
87. Shokhina, A. G.; Kostyuk, A. I.; Ermakova, Y. G.; Panova, A. S.; Staroverov, D. B.; Egorov, E. S.; Baranov, M. S.; van Belle, G. J.; Katschinski, D. M.; Belousov, V. V.; Bilan, D. S., Red fluorescent redox-sensitive biosensor Grx1-roCherry. *Redox Biol.* **2019,** *21*, 101071.
88. Hung, Y. P.; Albeck, J. G.; Tantama, M.; Yellen, G., Imaging cytosolic NADH-NAD(+) redox state with a genetically encoded fluorescent biosensor. *Cell Metab.* **2011,** *14* (4), 545-554.
89. Sadhu, S. S.; Callegari, E.; Zhao, Y.; Guan, X.; Seefeldt, T., Evaluation of a dithiocarbamate derivative as an inhibitor of human glutaredoxin-1. *J. Enzyme Inhib. Med. Chem.* **2013,** *28* (3), 456-462.
90. Laurent, T. C.; Moore, E. C.; Reichard, P., Enzymatic Synthesis of Deoxyribonucleotides: IV. Isolation and characterization of thioredoxin, the hydrogen donor from Escherichia Coli B. *J. Biol. Chem.* **1964,** *239* (10), 3436-3444.

91. Lee, S.; Kim, S. M.; Lee, R. T., Thioredoxin and thioredoxin target proteins: from molecular mechanisms to functional significance. *Antioxid. Redox Signal.* **2013,** *18* (10), 1165-1207.
92. Du, Y.; Zhang, H.; Zhang, X.; Lu, J.; Holmgren, A., Thioredoxin 1 is inactivated due to oxidation induced by peroxiredoxin under oxidative stress and reactivated by the glutaredoxin system. *J. Biol. Chem.* **2013,** *288* (45), 32241-32247.
93. Roder, C.; Thomson, M. J., Auranofin: repurposing an old drug for a golden new age. *Drugs in R&D* **2015,** *15* (1), 13-20.
94. Sugiura, K.; Yokochi, Y.; Fu, N.; Fukaya, Y.; Yoshida, K.; Mihara, S.; Hisabori, T., The thioredoxin (Trx) redox state sensor protein can visualize Trx activities in the light/dark response in chloroplasts. *J. Biol. Chem.* **2019,** *294* (32), 12091-12098.
95. Forman, H. J.; Maiorino, M.; Ursini, F., Signaling functions of reactive oxygen species. *Biochemistry* **2010,** *49* (5), 835-842.
96. Delaunay, A.; Pflieger, D.; Barrault, M.-B.; Vinh, J.; Toledano, M. B., A thiol peroxidase is an H_2O_2 receptor and redox-transducer in gene activation. *Cell* **2002,** *111* (4), 471-481.
97. Morgan, B.; Van Laer, K.; Owusu, T. N.; Ezeriņa, D.; Pastor-Flores, D.; Amponsah, P. S.; Tursch, A.; Dick, T. P., Real-time monitoring of basal H 2 O 2 levels with peroxiredoxin-based probes. *Nat. Chem. Biol.* **2016,** *12* (6), 437-443.
98. Carmona, M.; de Cubas, L.; Bautista, E.; Moral-Blanch, M.; Medraño-Fernández, I.; Sitia, R.; Boronat, S.; Ayté, J.; Hidalgo, E., Monitoring cytosolic H_2O_2 fluctuations arising from altered plasma membrane gradients or from mitochondrial activity. *Nat. Commun.* **2019,** *10* (1), 1-13.
99. Choi, H.-J.; Kim, S.-J.; Mukhopadhyay, P.; Cho, S.; Woo, J.-R.; Storz, G.; Ryu, S.-E., Structural basis of the redox switch in the OxyR transcription factor. *Cell* **2001,** *105* (1), 103-113.
100. Matlashov, M. E.; Bogdanova, Y. A.; Ermakova, G. V.; Mishina, N. M.; Ermakova, Y. G.; Nikitin, E. S.; Balaban, P. M.; Okabe, S.; Lukyanov, S.; Enikolopov, G., Fluorescent ratiometric pH indicator SypHer2: Applications in neuroscience and regenerative biology. *Biochim. Biophys. Acta Gen. Subj.* **2015,** *1850* (11), 2318-2328.
101. Subach, O. M.; Kunitsyna, T. A.; Mineyeva, O. A.; Lazutkin, A. A.; Bezryadnov, D. V.; Barykina, N. V.; Piatkevich, K. D.; Ermakova, Y. G.; Bilan, D. S.; Belousov, V. V., Slowly reducible genetically encoded green fluorescent indicator for In Vivo and Ex Vivo visualization of hydrogen peroxide. *Int. J. Mol. Sci.* **2019,** *20* (13), 3138.
102. Shaner, N. C.; Lambert, G. G.; Chammas, A.; Ni, Y.; Cranfill, P. J.; Baird, M. A.; Sell, B. R.; Allen, J. R.; Day, R. N.; Israelsson, M., A bright monomeric green fluorescent protein derived from Branchiostoma lanceolatum. *Nat. Methods* **2013,** *10* (5), 407-409.
103. Mehmeti, I.; Lortz, S.; Lenzen, S., The H2O2-sensitive HyPer protein targeted to the endoplasmic reticulum as a mirror of the oxidizing thiol–disulfide milieu. *Free Radic. Biol. Med.* **2012,** *53* (7), 1451-1458.
104. Melo, E. P.; Lopes, C.; Gollwitzer, P.; Lortz, S.; Lenzen, S.; Mehmeti, I.; Kaminski, C. F.; Ron, D.; Avezov, E., TriPer, an optical probe tuned to the

endoplasmic reticulum tracks changes in luminal H_2O_2. *BMC Biol.* **2017,** *15* (1), 24.
105. Enyedi, B.; Zana, M.; Donkó, A.; Geiszt, M., Spatial and temporal analysis of NADPH oxidase-generated hydrogen peroxide signals by novel fluorescent reporter proteins. *Antioxid. Redox Signal.* **2013,** *19* (6), 523-534.
106. Wood, M. J.; Storz, G.; Tjandra, N., Structural basis for redox regulation of Yap1 transcription factor localization. *Nature* **2004,** *430* (7002), 917-921.
107. Ma, L.-H.; Takanishi, C. L.; Wood, M. J., Molecular mechanism of oxidative stress perception by the Orp1 protein. *J. Biol. Chem.* **2007,** *282* (43), 31429-31436.
108. Langford, T. F.; Huang, B. K.; Lim, J. B.; Moon, S. J.; Sikes, H. D., Monitoring the action of redox-directed cancer therapeutics using a human peroxiredoxin-2-based probe. *Nat. Commun.* **2018,** *9* (1), 3145.
109. Tedeschi, P. M.; Bansal, N.; Kerrigan, J. E.; Abali, E. E.; Scotto, K. W.; Bertino, J. R., NAD+ kinase as a therapeutic target in cancer. *Clin. Cancer Res.* **2016,** *22* (21), 5189-5195.
110. Ding, C.-K. C.; Rose, J.; Sun, T.; Wu, J.; Chen, P.-H.; Lin, C.-C.; Yang, W.-H.; Chen, K.-Y.; Lee, H.; Xu, E., MESH1 is a cytosolic NADPH phosphatase that regulates ferroptosis. *Nat. Metab.* **2020,** *2* (3), 270-277.
111. Cambronne, X. A.; Stewart, M. L.; Kim, D.; Jones-Brunette, A. M.; Morgan, R. K.; Farrens, D. L.; Cohen, M. S.; Goodman, R. H., Biosensor reveals multiple sources for mitochondrial NAD^+. *Science* **2016,** *352* (6292), 1474-1477.
112. Gajiwala, K. S.; Pinko, C., Structural rearrangement accompanying NAD^+ synthesis within a bacterial DNA ligase crystal. *Structure* **2004,** *12* (8), 1449-1459.
113. Zou, Y.; Wang, A.; Huang, L.; Zhu, X.; Hu, Q.; Zhang, Y.; Chen, X.; Li, F.; Wang, Q.; Wang, H.; Liu, R.; Zuo, F.; Li, T.; Yao, J.; Qian, Y.; Shi, M.; Yue, X.; Chen, W.; Zhang, Z.; Wang, C.; Zhou, Y.; Zhu, L.; Ju, Z.; Loscalzo, J.; Yang, Y.; Zhao, Y., Illuminating NAD^+ Metabolism in Live Cells and In Vivo Using a Genetically Encoded Fluorescent Sensor. *Dev. Cell* **2020,** *53* (2), 240-252 e247.
114. Zhao, Y.; Jin, J.; Hu, Q.; Zhou, H. M.; Yi, J.; Yu, Z.; Xu, L.; Wang, X.; Yang, Y.; Loscalzo, J., Genetically encoded fluorescent sensors for intracellular NADH detection. *Cell Metab.* **2011,** *14* (4), 555-566.
115. Hung, Y. P.; Yellen, G., Live-cell imaging of cytosolic NADH–NAD^+ redox state using a genetically encoded fluorescent biosensor. In *Fluorescent protein-based biosensors*, Springer: 2014; pp 83-95.
116. Bilan, D. S.; Matlashov, M. E.; Gorokhovatsky, A. Y.; Schultz, C.; Enikolopov, G.; Belousov, V. V., Genetically encoded fluorescent indicator for imaging NAD^+/NADH ratio changes in different cellular compartments. *Biochim. Biophys. Acta* **2014,** *1840* (3), 951-957.
117. Cameron, W. D.; Bui, C. V.; Hutchinson, A.; Loppnau, P.; Graslund, S.; Rocheleau, J. V., Apollo-NADP(+): a spectrally tunable family of genetically encoded sensors for $NADP^+$. *Nat. Methods* **2016,** *13* (4), 352-358.
118. Jares-Erijman, E. A.; Jovin, T. M., FRET imaging. *Nat. Biotechnol.* **2003,** *21* (11), 1387-1395.

119. Kanji, M. I.; Toews, M.; Carper, W., Glucose-6-phosphate dehydrogenase. Purification and partial characterization. *J. Biol. Chem.* **1976,** *251* (8), 2255-2257.
120. Lobley, C. M.; Ciulli, A.; Whitney, H. M.; Williams, G.; Smith, A. G.; Abell, C.; Blundell, T. L., The crystal structure of Escherichia coli ketopantoate reductase with $NADP^+$ bound. *Biochemistry* **2005,** *44* (25), 8930-8939.
121. Zhao, F. L.; Zhang, C.; Zhang, C.; Tang, Y.; Ye, B. C., A genetically encoded biosensor for in vitro and in vivo detection of $NADP^+$. *Biosens. Bioelectron.* **2016,** *77*, 901-906.
122. Zhao, Y.; Yang, Y., Real-time and high-throughput analysis of mitochondrial metabolic states in living cells using genetically encoded $NAD^{+/}$NADH sensors. *Free Radic. Biol. Med.* **2016,** *100*, 43-52.
123. Yu, Q.; Heikal, A. A., Two-photon autofluorescence dynamics imaging reveals sensitivity of intracellular NADH concentration and conformation to cell physiology at the single-cell level. *J. Photochem. Photobiol. B: Biol.* **2009,** *95* (1), 46-57.
124. Yamada, K.; Hara, N.; Shibata, T.; Osago, H.; Tsuchiya, M., The simultaneous measurement of nicotinamide adenine dinucleotide and related compounds by liquid chromatography/electrospray ionization tandem mass spectrometry. *Anal. Biochem.* **2006,** *352* (2), 282-285.
125. Tao, R.; Zhao, Y.; Chu, H.; Wang, A.; Zhu, J.; Chen, X.; Zou, Y.; Shi, M.; Liu, R.; Su, N.; Du, J.; Zhou, H. M.; Zhu, L.; Qian, X.; Liu, H.; Loscalzo, J.; Yang, Y., Genetically encoded fluorescent sensors reveal dynamic regulation of NADPH metabolism. *Nat. Methods* **2017,** *14* (7), 720-728.
126. Erapaneedi, R.; Belousov, V. V.; Schafers, M.; Kiefer, F., A novel family of fluorescent hypoxia sensors reveal strong heterogeneity in tumor hypoxia at the cellular level. *EMBO J.* **2016,** *35* (1), 102-113.
127. Potzkei, J.; Kunze, M.; Drepper, T.; Gensch, T.; Jaeger, K.-E.; Büchs, J., Real-time determination of intracellular oxygen in bacteria using a genetically encoded FRET-based biosensor. *BMC Biol.* **2012,** *10* (1), 28.
128. Wingen, M.; Potzkei, J.; Endres, S.; Casini, G.; Rupprecht, C.; Fahlke, C.; Krauss, U.; Jaeger, K.-E.; Drepper, T.; Gensch, T., The photophysics of LOV-based fluorescent proteins–new tools for cell biology. *Photochem. Photobiol. Sci.* **2014,** *13* (6), 875-883.
129. Weits, D. A.; van Dongen, J. T.; Licausi, F., Molecular oxygen as a signaling component in plant development. *New Phytol.* **2020**.
130. Youssef, S.; Ren, W.; Ai, H.-w., A genetically encoded FRET sensor for hypoxia and prolyl hydroxylases. *ACS Chem. Biol.* **2016,** *11* (9), 2492-2498.
131. Ivan, M.; Kondo, K.; Yang, H.; Kim, W.; Valiando, J.; Ohh, M.; Salic, A.; Asara, J. M.; Lane, W. S.; Kaelin Jr, W. G., HIFα targeted for VHL-mediated destruction by proline hydroxylation: implications for O2 sensing. *Science* **2001,** *292* (5516), 464-468.
132. Semenza, G. L., Hydroxylation of HIF-1: oxygen sensing at the molecular level. *Physiology* **2004,** *19* (4), 176-182.
133. Van Molle, I.; Thomann, A.; Buckley, D. L.; So, E. C.; Lang, S.; Crews, C. M.; Ciulli, A., Dissecting fragment-based lead discovery at the von Hippel-Lindau

protein: hypoxia inducible factor 1α protein-protein interface. *Chem. Biol.* **2012,** *19* (10), 1300-1312.
134. Nguyen, A. W.; Daugherty, P. S., Evolutionary optimization of fluorescent proteins for intracellular FRET. *Nat. Biotechnol.* **2005,** *23* (3), 355-360.
135. Sharov, V. S.; Ferrington, D. A.; Squier, T. C.; Schöneich, C., Diastereoselective reduction of protein-bound methionine sulfoxide by methionine sulfoxide reductase. *FEBS Lett.* **1999,** *455* (3), 247-250.
136. Brot, N.; Weissbach, L.; Werth, J.; Weissbach, H., Enzymatic reduction of protein-bound methionine sulfoxide. *Proc. Natl. Acad. Sci. U.S.A.* **1981,** *78* (4), 2155-2158.
137. Grimaud, R.; Ezraty, B.; Mitchell, J. K.; Lafitte, D.; Briand, C.; Derrick, P. J.; Barras, F., Repair of oxidized proteins: identification of a new methionine sulfoxide reductase. *J. Biol. Chem.* **2001,** *276* (52), 48915-48920.
138. Tarrago, L.; Peterfi, Z.; Lee, B. C.; Michel, T.; Gladyshev, V. N., Monitoring methionine sulfoxide with stereospecific mechanism-based fluorescent sensors. *Nat. Chem. Biol.* **2015,** *11* (5), 332-338.
139. Radi, R., Peroxynitrite, a stealthy biological oxidant. *J. Biol. Chem.* **2013,** *288* (37), 26464-26472.
140. Beckman, J. S., Oxidative damage and tyrosine nitration from peroxynitrite. *Chem. Res. Toxicol.* **1996,** *9* (5), 836-844.
141. Sikora, A.; Zielonka, J.; Lopez, M.; Joseph, J.; Kalyanaraman, B., Direct oxidation of boronates by peroxynitrite: mechanism and implications in fluorescence imaging of peroxynitrite. *Free Radic. Biol. Med.* **2009,** *47* (10), 1401-1407.
142. Sedgwick, A. C.; Sun, X.; Kim, G.; Yoon, J.; Bull, S. D.; James, T. D., Boronate based fluorescence (ESIPT) probe for peroxynitrite. *Chem. Commun.* **2016,** *52* (83), 12350-12352.
143. Zielonka, J.; Sikora, A.; Hardy, M.; Joseph, J.; Dranka, B. P.; Kalyanaraman, B., Boronate probes as diagnostic tools for real time monitoring of peroxynitrite and hydroperoxides. *Chem. Res. Toxicol.* **2012,** *25* (9), 1793-1799.
144. Li, S.; Yang, B.; Kobayashi, T.; Yu, B.; Liu, J.; Wang, L., Genetically encoding thyronine for fluorescent detection of peroxynitrite. *Biorg. Med. Chem.* **2020,** *28* (18), 115665.
145. Mustafa, A. K.; Gadalla, M. M.; Sen, N.; Kim, S.; Mu, W.; Gazi, S. K.; Barrow, R. K.; Yang, G.; Wang, R.; Snyder, S. H., H2S signals through protein S-sulfhydration. *Sci. Signal.* **2009,** *2* (96), ra72.
146. Kimura, H., Physiological role of hydrogen sulfide and polysulfide in the central nervous system. *Neurochem. Int.* **2013,** *63* (5), 492-497.
147. Nicholson, C. K.; Lambert, J. P.; Molkentin, J. D.; Sadoshima, J.; Calvert, J. W., Thioredoxin 1 is essential for sodium sulfide–mediated cardioprotection in the setting of heart failure. *Arterioscler. Thromb. Vasc. Biol.* **2013,** *33* (4), 744-751.
148. Searcy, D. G.; Whitehead, J. P.; Maroney, M. J., Interaction of Cu, Zn superoxide dismutase with hydrogen sulfide. *Arch. Biochem. Biophys.* **1995,** *318* (2), 251-263.
149. Yang, G.; Zhao, K.; Ju, Y.; Mani, S.; Cao, Q.; Puukila, S.; Khaper, N.; Wu, L.; Wang, R., Hydrogen sulfide protects against cellular senescence via S-

sulfhydration of Keap1 and activation of Nrf2. *Antioxid. Redox Signal.* **2013,** *18* (15), 1906-1919.
150. Xie, Z.-Z.; Liu, Y.; Bian, J.-S., Hydrogen sulfide and cellular redox homeostasis. *Oxid. Med. Cell. Longev.* **2016,** *2016*.
151. Youssef, S.; Zhang, S.; Ai, H.-w., A genetically encoded, ratiometric fluorescent biosensor for hydrogen sulfide. *ACS Sens.* **2019,** *4* (6), 1626-1632.
152. Simen Zhao, B.; Liang, Y.; Song, Y.; Zheng, C.; Hao, Z.; Chen, P. R., A highly selective fluorescent probe for visualization of organic hydroperoxides in living cells. *J. Am. Chem. Soc.* **2010,** *132* (48), 17065-17067.
153. Sukchawalit, R.; Loprasert, S.; Atichartpongkul, S.; Mongkolsuk, S., Complex Regulation of the Organic Hydroperoxide Resistance Gene (ohr) from XanthomonasInvolves OhrR, a Novel Organic Peroxide-Inducible Negative Regulator, and Posttranscriptional Modifications. *J. Bacteriol.* **2001,** *183* (15), 4405-4412.
154. Schlossmann, J.; Feil, R.; Hofmann, F., Signaling through NO and cGMP-dependent protein kinases. *Ann. Med.* **2003,** *35* (1), 21-27.
155. Kadlec, M.; Ros-Santaella, J. L.; Pintus, E., The Roles of NO and H_2S in Sperm Biology: Recent Advances and New Perspectives. *Int. J. Mol. Sci.* **2020,** *21* (6), 2174.
156. Sato, M.; Hida, N.; Umezawa, Y., Imaging the nanomolar range of nitric oxide with an amplifier-coupled fluorescent indicator in living cells. *Proc. Natl. Acad. Sci. U.S.A.* **2005,** *102* (41), 14515-14520.
157. Sato, M.; Hida, N.; Ozawa, T.; Umezawa, Y., Fluorescent indicators for cyclic GMP based on cyclic GMP-dependent protein kinase Iα and green fluorescent proteins. *Anal. Chem.* **2000,** *72* (24), 5918-5924.
158. Eroglu, E.; Gottschalk, B.; Charoensin, S.; Blass, S.; Bischof, H.; Rost, R.; Madreiter-Sokolowski, C. T.; Pelzmann, B.; Bernhart, E.; Sattler, W.; Hallstrom, S.; Malinski, T.; Waldeck-Weiermair, M.; Graier, W. F.; Malli, R., Development of novel FP-based probes for live-cell imaging of nitric oxide dynamics. *Nat. Commun.* **2016,** *7*, 10623.
159. Bush, M.; Ghosh, T.; Tucker, N.; Zhang, X.; Dixon, R., Transcriptional regulation by the dedicated nitric oxide sensor, NorR: a route towards NO detoxification. *Biochem. Soc. Trans.* **2011,** *39* (1), 289-293.
160. Hrabie, J. A.; Klose, J. R.; Wink, D. A.; Keefer, L. K., New nitric oxide-releasing zwitterions derived from polyamines. *J. Org. Chem.* **1993,** *58* (6), 1472-1476.
161. Sun, Y.; Liu, W.-Z.; Liu, T.; Feng, X.; Yang, N.; Zhou, H.-F., Signaling pathway of MAPK/ERK in cell proliferation, differentiation, migration, senescence and apoptosis. *J. Recept. Signal Transduct.* **2015,** *35* (6), 600-604.
162. Paulsen, C. E.; Truong, T. H.; Garcia, F. J.; Homann, A.; Gupta, V.; Leonard, S. E.; Carroll, K. S., Peroxide-dependent sulfenylation of the EGFR catalytic site enhances kinase activity. *Nat. Chem. Biol.* **2012,** *8* (1), 57.
163. Flinder, L. I.; Timofeeva, O. A.; Rosseland, C. M.; Wierød, L.; Huitfeldt, H. S.; Skarpen, E., EGF-induced ERK-activation downstream of FAK requires rac1-NADPH oxidase. *J. Cell. Physiol.* **2011,** *226* (9), 2267-2278.

164. Boukhenouna, S.; Wilson, M. A.; Bahmed, K.; Kosmider, B., Reactive Oxygen Species in Chronic Obstructive Pulmonary Disease. *Oxid. Med. Cell. Longev.* **2018,** *2018*, 1-9.
165. Selemidis, S., Targeting reactive oxygen species for respiratory infection: Fact or fancy? *Respirology* **2018**.
166. Sayin, V. I.; Ibrahim, M. X.; Larsson, E.; Nilsson, J. A.; Lindahl, P.; Bergo, M. O., Antioxidants Accelerate Lung Cancer Progression in Mice. *Sci. Transl. Med.* **2014,** *6* (221), 221ra215-221ra215.
167. Leuner, K.; Schütt, T.; Kurz, C.; Eckert, S. H.; Schiller, C.; Occhipinti, A.; Mai, S.; Jendrach, M.; Eckert, G. P.; Kruse, S. E., Mitochondrion-derived reactive oxygen species lead to enhanced amyloid beta formation. *Antioxid. Redox Signal.* **2012,** *16* (12), 1421-1433.
168. Shelat, P. B.; Chalimoniuk, M.; Wang, J. H.; Strosznajder, J. B.; Lee, J. C.; Sun, A. Y.; Simonyi, A.; Sun, G. Y., Amyloid beta peptide and NMDA induce ROS from NADPH oxidase and AA release from cytosolic phospholipase A2 in cortical neurons. *J. Neurochem.* **2008,** *106* (1), 45-55.
169. Harrison, I. P.; Vinh, A.; Johnson, I. R. D.; Luong, R.; Drummond, G. R.; Sobey, C. G.; Tiganis, T.; Williams, E. D.; O'Leary, J. J.; Brooks, D. A.; Selemidis, S., NOX2 oxidase expressed in endosomes promotes cell proliferation and prostate tumour development. *Oncotarget* **2018,** *9* (83), 35378-35393.
170. Hempel, N.; Ye, H.; Abessi, B.; Mian, B.; Melendez, J., Altered redox status accompanies progression to metastatic human bladder cancer. *Free Radic. Biol. Med.* **2009,** *46* (1), 42-50.
171. Funke, F.; Gerich, F. J.; Müller, M., Dynamic, semi-quantitative imaging of intracellular ROS levels and redox status in rat hippocampal neurons. *NeuroImage* **2011,** *54* (4), 2590-2602.
172. Knoefler, D.; Thamsen, M.; Koniczek, M.; Niemuth, N. J.; Diederich, A.-K.; Jakob, U., Quantitative in vivo redox sensors uncover oxidative stress as an early event in life. *Mol. Cell* **2012,** *47* (5), 767-776.
173. Han, Y.; Ishibashi, S.; Iglesias-Gonzalez, J.; Chen, Y.; Love, N. R.; Amaya, E., Ca2+-induced mitochondrial ROS regulate the early embryonic cell cycle. *Cell Rep.* **2018,** *22* (1), 218-231.
174. Love, N. R.; Chen, Y.; Ishibashi, S.; Kritsiligkou, P.; Lea, R.; Koh, Y.; Gallop, J. L.; Dorey, K.; Amaya, E., Amputation-induced reactive oxygen species are required for successful Xenopus tadpole tail regeneration. *Nat. Cell Biol.* **2013,** *15* (2), 222-228.
175. Brilkina, A. A.; Peskova, N. N.; Dudenkova, V. V.; Gorokhova, A. A.; Sokolova, E. A.; Balalaeva, I. V., Monitoring of hydrogen peroxide production under photodynamic treatment using protein sensor HyPer. *J. Photochem. Photobiol. B: Biol.* **2018,** *178*, 296-301.
176. Benhar, M.; Engelberg, D.; Levitzki, A., ROS, stress-activated kinases and stress signaling in cancer. *EMBO Rep.* **2002,** *3* (5), 420-425.
177. Kimura, S.; Waszczak, C.; Hunter, K.; Wrzaczek, M., Bound by fate: the role of reactive oxygen species in receptor-like kinase signaling. *Plant Cell* **2017,** *29* (4), 638-654.

178. Satooka, H.; Hara-Chikuma, M., Aquaporin-3 controls breast cancer cell migration by regulating hydrogen peroxide transport and its downstream cell signaling. *Mol. Cell. Biol.* **2016,** *36* (7), 1206-1218.
179. Berkelhamer, S. K.; Kim, G. A.; Radder, J. E.; Wedgwood, S.; Czech, L.; Steinhorn, R. H.; Schumacker, P. T., Developmental differences in hyperoxia-induced oxidative stress and cellular responses in the murine lung. *Free Radic. Biol. Med.* **2013,** *61*, 51-60.
180. Desireddi, J. R.; Farrow, K. N.; Marks, J. D.; Waypa, G. B.; Schumacker, P. T., Hypoxia increases ROS signaling and cytosolic Ca2+ in pulmonary artery smooth muscle cells of mouse lungs slices. *Antioxid. Redox Signal.* **2010,** *12* (5), 595-602.
181. Stapper, Z. A.; Jahn, T. R., Changes in glutathione redox potential are linked to Aβ42-induced neurotoxicity. *Cell Rep.* **2018,** *24* (7), 1696-1703.
182. Liu, Z.; Celotto, A. M.; Romero, G.; Wipf, P.; Palladino, M. J., Genetically encoded redox sensor identifies the role of ROS in degenerative and mitochondrial disease pathogenesis. *Neurobiol. Dis.* **2012,** *45* (1), 362-368.
183. Breckwoldt, M. O.; Pfister, F. M.; Bradley, P. M.; Marinković, P.; Williams, P. R.; Brill, M. S.; Plomer, B.; Schmalz, A.; St Clair, D. K.; Naumann, R., Multiparametric optical analysis of mitochondrial redox signals during neuronal physiology and pathology in vivo. *Nat. Med.* **2014,** *20* (5), 555-560.
184. Wagener, K. C.; Kolbrink, B.; Dietrich, K.; Kizina, K. M.; Terwitte, L. S.; Kempkes, B.; Bao, G.; Müller, M., Redox indicator mice stably expressing genetically encoded neuronal roGFP: versatile tools to decipher subcellular redox dynamics in neuropathophysiology. *Antioxid. Redox Signal.* **2016,** *25* (1), 41-58.
185. Steinhorn, B.; Sorrentino, A.; Badole, S.; Bogdanova, Y.; Belousov, V.; Michel, T., Chemogenetic generation of hydrogen peroxide in the heart induces severe cardiac dysfunction. *Nat. Commun.* **2018,** *9* (1), 1-10.
186. Zhao, Y.; Zhang, Z.; Zou, Y.; Yang, Y., Visualization of nicotine adenine dinucleotide redox homeostasis with genetically encoded fluorescent sensors. *Antioxid. Redox Signal.* **2018,** *28* (3), 213-229.
187. Li, L.; Zhang, C.; Wang, P.; Wang, A.; Zhou, J.; Chen, G.; Xu, J.; Yang, Y.; Zhao, Y.; Zhang, S., Imaging the redox states of live cells with the time-resolved fluorescence of genetically encoded biosensors. *Anal. Chem.* **2019,** *91* (6), 3869-3876.
188. Chandrasekharan, A.; Varadarajan, S. N.; Lekshmi, A.; Lupitha, S. S.; Darvin, P.; Chandrasekhar, L.; Pillai, P. R.; Santhoshkumar, T.; Pillai, M. R., A high-throughput real-time in vitro assay using mitochondrial targeted roGFP for screening of drugs targeting mitochondria. *Redox Biol.* **2019,** *20*, 379-389.
189. Nerush, A.; Shchukina, K.; Balalaeva, I.; Orlova, A., Hydrogen peroxide in the reactions of cancer cells to cisplatin. *Biochim. Biophys. Acta Gen. Subj.* **2019,** *1863* (4), 692-702.
190. Lennicke, C.; Cochemé, H. M., Redox signalling and ageing: insights from Drosophila. *Biochem. Soc. Trans.* **2020,** *48* (2), 367-377.
191. Covarrubias, A. J.; Kale, A.; Perrone, R.; Lopez-Dominguez, J. A.; Pisco, A. O.; Kasler, H. G.; Schmidt, M. S.; Heckenbach, I.; Kwok, R.; Wiley, C. D.,

Senescent cells promote tissue NAD+ decline during ageing via the activation of CD38+ macrophages. *Nat. Metab.* **2020,** *2* (11), 1265-1283.
192. Chini, C. C.; Peclat, T. R.; Warner, G. M.; Kashyap, S.; Espindola-Netto, J. M.; de Oliveira, G. C.; Gomez, L. S.; Hogan, K. A.; Tarragó, M. G.; Puranik, A. S., CD38 ecto-enzyme in immune cells is induced during aging and regulates NAD+ and NMN levels. *Nat. Metab.* **2020,** *2* (11), 1284-1304.
193. Davalli, P.; Mitic, T.; Caporali, A.; Lauriola, A.; D'Arca, D., ROS, Cell Senescence, and Novel Molecular Mechanisms in Aging and Age-Related Diseases. *Oxid. Med. Cell. Longev.* **2016,** *2016*, 1-18.
194. Simone; Ana; Großhans, J.; Aurelio; Tobias, In Vivo Mapping of Hydrogen Peroxide and Oxidized Glutathione Reveals Chemical and Regional Specificity of Redox Homeostasis. *Cell Metab.* **2011,** *14* (6), 819-829.
195. Back, P.; De Vos, W. H.; Depuydt, G. G.; Matthijssens, F.; Vanfleteren, J. R.; Braeckman, B. P., Exploring real-time in vivo redox biology of developing and aging Caenorhabditis elegans. *Free Radic. Biol. Med.* **2012,** *52* (5), 850-859.
196. Bazopoulou, D.; Knoefler, D.; Zheng, Y.; Ulrich, K.; Oleson, B. J.; Xie, L.; Kim, M.; Kaufmann, A.; Lee, Y.-T.; Dou, Y., Developmental ROS individualizes organismal stress resistance and lifespan. *Nature* **2019,** *576* (7786), 301-305.
197. Knieß, R. A.; Mayer, M. P., The oxidation state of the cytoplasmic glutathione redox system does not correlate with replicative lifespan in yeast. *NPJ Aging Mech. Dis.* **2016,** *2*, 16028.
198. Madejczyk, M. S.; Baer, C. E.; Dennis, W. E.; Minarchick, V. C.; Leonard, S. S.; Jackson, D. A.; Stallings, J. D.; Lewis, J. A., Temporal changes in rat liver gene expression after acute cadmium and chromium exposure. *PLoS One* **2015,** *10* (5), e0127327.
199. Cooke, M. S.; Evans, M. D.; Dizdaroglu, M.; Lunec, J., Oxidative DNA damage: mechanisms, mutation, and disease. *FASEB J.* **2003,** *17* (10), 1195-1214.
200. Rowe, L. A.; Degtyareva, N.; Doetsch, P. W., DNA damage-induced reactive oxygen species (ROS) stress response in Saccharomyces cerevisiae. *Free Radic. Biol. Med.* **2008,** *45* (8), 1167-1177.
201. Arias-Barreiro, C. R.; Okazaki, K.; Koutsaftis, A.; Inayat-Hussain, S. H.; Tani, A.; Katsuhara, M.; Kimbara, K.; Mori, I. C., A bacterial biosensor for oxidative stress using the constitutively expressed redox-sensitive protein roGFP2. *Sensors* **2010,** *10* (7), 6290-6306.
202. Ooi, L.; Heng, L. Y.; Mori, I. C., A high-throughput oxidative stress biosensor based on Escherichia coli roGFP2 cells immobilized in a k-carrageenan matrix. *Sensors* **2015,** *15* (2), 2354-2368.
203. Paracelsus, T., Die dritte Defension wegen des Schreibens der neuen Rezepte. *Septem Defensiones* **1965,** *1538*, 508-513.
204. Shergalis, A. G.; Hu, S.; Bankhead III, A.; Neamati, N., Role of the ERO1-PDI interaction in oxidative protein folding and disease. *Pharmacol. Ther.* **2020,** *210*, 107525.
205. Yu, J.; Li, T.; Liu, Y.; Wang, X.; Zhang, J.; Wang, X. e.; Shi, G.; Lou, J.; Wang, L.; Wang, C. c., Phosphorylation switches protein disulfide isomerase activity to maintain proteostasis and attenuate ER stress. *EMBO J.* **2020,** *39* (10), e103841.

206. Bindels, D. S.; Haarbosch, L.; Van Weeren, L.; Postma, M.; Wiese, K. E.; Mastop, M.; Aumonier, S.; Gotthard, G.; Royant, A.; Hink, M. A., mScarlet: a bright monomeric red fluorescent protein for cellular imaging. *Nat. Methods* **2017,** *14* (1), 53-56.
207. Duan, Y.; Liu, B., Recent advances of optical imaging in the second near-infrared window. *Adv. Mater.* **2018,** *30* (47), 1802394.
208. Hall, M. P.; Unch, J.; Binkowski, B. F.; Valley, M. P.; Butler, B. L.; Wood, M. G.; Otto, P.; Zimmerman, K.; Vidugiris, G.; Machleidt, T.; Robers, M. B.; Benink, H. A.; Eggers, C. T.; Slater, M. R.; Meisenheimer, P. L.; Klaubert, D. H.; Fan, F.; Encell, L. P.; Wood, K. V., Engineered luciferase reporter from a deep sea shrimp utilizing a novel imidazopyrazinone substrate. *ACS Chem. Biol.* 2012, *7* (11), 1848-1857.
209. Yeh, H. W.; Ai, H. W., Development and Applications of Bioluminescent and Chemiluminescent Reporters and Biosensors. *Annu. Rev. Anal. Chem.* **2019,** *12*, 129-150.
210. Yeh, H. W.; Karmach, O.; Ji, A.; Carter, D.; Martins-Green, M. M.; Ai, H. W., Red-shifted luciferase-luciferin pairs for enhanced bioluminescence imaging. *Nat. Methods* **2017,** *14* (10), 971-974.
211. Yeh, H. W.; Wu, T.; Chen, M.; Ai, H., Identification of Factors Complicating Bioluminescence Imaging. *Biochemistry* **2019,** *58* (12), 1689-1697.
212. Yeh, H. W.; Xiong, Y.; Wu, T.; Chen, M.; Ji, A.; Li, X.; Ai, H., ATP-Independent Bioluminescent Reporter Variants To Improve in Vivo Imaging. *ACS Chem. Biol.* **2019,** *14* (5), 959-965.
213. Chu, J.; Oh, Y.; Sens, A.; Ataie, N.; Dana, H.; Macklin, J. J.; Laviv, T.; Welf, E. S.; Dean, K. M.; Zhang, F.; Kim, B. B.; Tang, C. T.; Hu, M.; Baird, M. A.; Davidson, M. W.; Kay, M. A.; Fiolka, R.; Yasuda, R.; Kim, D. S.; Ng, H. L.; Lin, M. Z., A bright cyan-excitable orange fluorescent protein facilitates dual-emission microscopy and enhances bioluminescence imaging in vivo. *Nat. Biotechnol.* **2016,** *34* (7), 760-767.
214. Mishina, N. M.; Mishin, A. S.; Belyaev, Y.; Bogdanova, E. A.; Lukyanov, S.; Schultz, C.; Belousov, V. V., Live-cell STED microscopy with genetically encoded biosensor. *Nano Lett.* **2015,** *15* (5), 2928-2932.
215. Achimovich, A. M.; Ai, H.; Gahlmann, A., Enabling technologies in super-resolution fluorescence microscopy: reporters, labeling, and methods of measurement. *Curr. Opin. Struct. Biol.* **2019,** *58*, 224-232.
216. Heintzmann, R.; Huser, T., Super-Resolution Structured Illumination Microscopy. *Chem. Rev.* **2017,** *117* (23), 13890-13908.
217. Gustafsson, N.; Culley, S.; Ashdown, G.; Owen, D. M.; Pereira, P. M.; Henriques, R., Fast live-cell conventional fluorophore nanoscopy with ImageJ through super-resolution radial fluctuations. *Nat. Commun.* **2016,** *7*, 12471.

Chapter 2 Improved red fluorescent redox indicators for monitoring cytosolic and mitochondrial thioredoxin redox dynamics

This chapter is converted from a published paper: Pang, Yu, Hao Zhang, and Hui-wang Ai. "Improved Red Fluorescent Redox Indicators for Monitoring Cytosolic and Mitochondrial Thioredoxin Redox Dynamics." Biochemistry 61, no. 5 (2022): 377-384. Contributions of each author are Yu Pang developed TrxRFP2 and MtrxRFP2. Hao Zhang and Yu Pang characterized TrxRFP2. Yu Pang characterized MtrxRFP2. Hao Zhang performed structural modeling. Yu Pang analyzed data and prepared the figures. Hao Zhang and Yu Pang wrote the manuscript. Hui-wang Ai supervised research and revised the manuscript.

2.1 Abstract

Thioredoxin (Trx) is one of the major thiol-dependent antioxidants in living systems. The study of Trx functions in redox biology was impeded by the lack of practical tools to track Trx redox dynamics in live cells. Our previous work developed TrxRFP1, the first genetically encoded fluorescent indicator for Trx redox. In this work, we report an improved fluorescent indicator, TrxRFP2, for tracking the redox of Trx1, which is primarily cytosolic and nuclear. Furthermore, because mitochondria specifically express Trx2, we have created a new genetically encoded fluorescent indicator, MtrxRFP2, for the redox of mitochondrial Trx. We characterized MtrxRFP2 as a purified protein and used subcellularly localized MtrxRFP2 to image mitochondrial redox changes in live cells.

2.2 Introduction

Thioredoxin (Trx) is a family of redox-active proteins that play vital roles in cellular redox homeostasis.[1, 2] While imbalanced cellular homeostasis can cause oxidative stress, Trx can defend against the stress by actively regulating many cellular functional activities, such as transcription, deoxyribonucleotides synthesis, cell proliferation, and apoptosis.[2-4] Trx serves as a key regulator in cellular function, and dysfunction of Trx redox activities can lead to diseases. For example, alterations in Trx activities are found in various neurological disorders,[5] while overactivation of Trx reductase (TrxR), a Trx regulator, is often observed in cancer proliferation and metastasis.[4, 6] Moreover, Trx may impact viral infection. For example, the reaction between Trx secreted from $CD4^+$ T cells and the redox-active D2 disulfide of CD4 is essential for the entry of HIV-1 into susceptible cells.[7] In this context, Trx and TrxR have emerged as promising therapeutic targets for cancer, viral infection, and neurodegenerative diseases.[4-8]

The typical Trx system contains Trx, TrxR, and nicotinamide adenine dinucleotide phosphate (NADPH). The electrons are first transferred from NADPH to Trx through TrxR.[9] Reduced Trx subsequently neutralizes reactive oxygen species (ROS) via peroxiredoxins or induces the reduction of many other oxidized proteins while getting itself oxidized in the process.[9, 10] Mammalian Trx antioxidant system includes two major members, the cytosolic Trx1[11] and the mitochondrial Trx2,[12] each with a corresponding reductase, TrxR1 and TrxR2, respectively. Both Trx1 and Trx2 are 12-kDa redox enzymes with a conserved redox-active Cys-Gly-Pro-Cys motif.[13] Trx1 and Trx2 are primarily localized to different subcellular organelles for spatial control of redox signaling. Trx1 is mainly responsible for regulating the redox signaling in the cytosol and nucleus, while Trx2 regulates the mitochondrial redox.[1] Because mitochondria are the primary cellular

sources of ROS, inhibition of mitochondrial Trx2 and TrxR2 can remarkably decrease the capacity of cells to scavenge ROS.[14]

Despite their essential roles in redox biology, the research tools for tracing Trx redox dynamics remain inadequate. Prevalent approaches, including Western blotting,[15] immunohistochemistry,[16] and mass spectrometry[17] have been widely utilized to study the redox status of Trx1. These methods, which only provide endpoint measurements, are incapable of providing spatiotemporal resolution of redox signals in live cells. Moreover, the time-consuming procedures, including cell lysis and sample preparation, might generate ROS, resulting in artifacts. In the past two decades or so, fluorescent protein (FP)-based indicators have appeared as promising tools for real-time tracking of redox molecules due to their genetic encodability, excellent specificity, and superior capability to provide spatiotemporal information with outstanding signal-to-noise ratios.[18-22] For example, Gutscher et al. genetically fused glutaredoxin-1 (Grx1) to the N-terminus of redox-active green fluorescent protein (roGFP2) to generate Grx1-roGFP2, a fluorescent protein-based biosensor for detecting endogenous glutathione dynamics in live cells.[23] Similar strategy to fuse human Trx1 (hTrx1) with roGFP2 did not yield any effective redox-sensing biosensor.[23] Previously, our group developed the first genetically encoded fluorescent biosensor, TrxRFP1, that can detect the dynamic redox status of Trx in live mammalian cells by fusing hTrx1 with redox-active RFP (rxRFP1). In contrast with roGFP2, which bears the active cysteine residues at the surface of the β-barrel of a green FP (GFP), rxRFP1 has two active cysteines at the N- and C- termini of a circularly permutated red FP (cpRFP).[24-26] In TrxRFP1, Trx1 was placed in proximity to rxRFP1 through a 30-amino-acid Gly-Ser-rich linker. Because of the spatial proximity, the redox status of the active cysteines in Trx1 is kinetically coupled with the redox state of rxRFP1. Such coupling allows TrxRFP1 to monitor the redox status of Trx1.[24]

In this work, we performed directed evolution with TrxRFP1 using an enzymatic reaction-based screening strategy. We developed an enhanced Trx fluorescent biosensor, TrxRFP2, which maintains the specificity but displays higher responsiveness than TrxRFP1 in live mammalian cells. In parallel, we developed a Trx2-specific red fluorescent redox indicator, MtrxRFP2, by generating and optimizing the redox relay between human Trx2 and rxRFP1.1.[27] We localized MtrxRFP2 to the mitochondria of living cells for detecting Trx2 redox.

2.3 Methods and Materials

2.3.1 Engineering of TrxRFP2

Directed evolution was used to improve the responsiveness of TrxRFP1.[24] Briefly, oligos pBAD-F and pBAD-R (**Table 2.1**) were used to amplify the TrxRFP1 gene in a pBAD/His B vector under an error-prone PCR (EP-PCR) condition. The resultant product was cloned into pBAD/His B predigested with Xho I and Hind III using Gibson Assembly.[28] The resulting library was used to transform E. coli DH10B cells via electroporation. Cells were plated on LB agar plates supplemented with 100 μg/mL ampicillin and 0.02% (w/v) L-arabinose. After incubation at 37 °C overnight, the plates were imaged using a customized imaging system equipped with a Dolan-Jenner Mi-LED Fiber Optic light source, appropriate excitation and emission filters in Thorlabs motorized filter wheels, and a QSI 628 CCD camera. Bacterial colonies with medium to high fluorescence were selected and cultured in 96-well deep-well plates containing 2×YT medium supplemented with 100 μg/ml ampicillin and 0.2% (w/v) L-arabinose. Cells were cultured at 30 °C, 250 r.p.m for 24 h and then at 16 °C for additional 48 h. Bacteria cells were then pelleted at 3000×g for 15 minutes and lysed using Bacterial Protein Extraction Reagents (B-PER). Fluorescence responses of cell lysates were measured on a BioTek Synergy Mx Microplate Reader. Fluorescence intensities were quantified and compared between an oxidized state (lysates treated with 10 μM peroxiredoxin TPx1 and 100 μM H_2O_2) and a reduced state (lysates treated with 10 μM TrxR1 and 200 μM NADPH). Two clones with high brightness and the greatest responsiveness were selected for DNA extraction. Their mixture was used as the template for the next round of EP-PCR. A total of seven rounds of directed evolution were performed to derive TrxRFP2.

Table 2.1 Oligonucleotides used in this work.

PCR Primers	**Sequence (5′→3′)**
pBAD-Mtrx-F1	ataaggatccgagctcgagcacaacctttaatatccaggatgga
pBAD-Mtrx-R1	gccaatcagcttcttcaggaag
pBAD-Mtrx-F2	cttcctgaagaagctgattggcggtggatccggtggcgg
pBAD-Mtrx-R2	tccgccaaaacagccaagcttttaagccacacttttgcacctttggtcacgcgtagcct
pcDNA3-TrxRFP2-F	ctatagggagacccaagcttgccgccaccatgggaggttctcatcatca
pcDNA3-TrxRFP2-R	cactatagaatagggccctctagattaagcctgactggagcac
pCS2-Mito-F	atccattcgttgggggataccggtcatcatcatcatcatcatggtatggc
pCS2-Mito-R1	taatacgactcactatagttctagaggctcgagttaagcctgactggagcacc
pCS2-Mito-R2	aatacgactcactatagttctagaggctcgagttaagccacacttttgcacct

2.3.2 Protein purification and comparison of TrxRFP1 and TrxRFP2

Oligos pET-TrxRFP-F and pET-TrxRFP-R (**Table 2.1**) were used to amplify TrxRFP1 or TrxRFP2 gene fragment from plasmid pBAD-TrxRFP1 or pBAD-TrxRFP2, respectively. Each amplified fragment was inserted into a pET28a vector predigested with BamH I and Xho I via Gibson Assembly.[28] The products were used to transform E. coli DH10B cells. Plasmids were prepared, confirmed by Sanger sequencing, and used to transform BL21(DE3) competent cells. A single E. coli colony was selected for inoculating 5 mL 2×YT medium supplemented with 50 μg/mL kanamycin. After overnight cultured at 250 r.p.m and 37 °C, the culture was used to inoculate 500 mL of 2×YT medium with 50 μg/mL kanamycin. Cells were cultured at 37 °C and 250 r.p.m until the optical density at 600 nm (OD_{600}) reached 0.8. Next, 1 mM IPTG was added to induce protein expression at 16 °C for 72 h. Proteins were purified using Ni-NTA agarose beads, and next, subjected to size-exclusion chromatography with 1× phosphate-buffered saline (PBS, pH 7.4) as the eluent. Protein concentrations were determined using an alkali denaturation method.[29] The prepared proteins were initially in the fully oxidized state due to the existence of oxygen in the air. To monitor reduction kinetics, oxidized proteins (1 μM) were reduced with 10 μM TrxR1 and 200 μM NADPH in 1× PBS (pH 7.4) at room temperature. To monitor oxidation kinetics, the freshly prepared proteins (20 μM) were first reduced with 100 molar equivalents of dithiothreitol (DTT) in an argon-filled anaerobic chamber at room temperature overnight; next, the reduced proteins were immediately diluted 100 times with 1× PBS (pH 7.4) and oxidized by the addition of 20 μM TPx1 and 200 μM H_2O_2 at room temperature. Both human TPx1 and TrxR1 were recombinantly expressed and purified from E. coli. For technical convenience, the selenocysteine residue in TrxR1 was mutated to cysteine. Kinetic traces were monitored at room temperature using the BioTek Synergy Mx Microplate Reader with excitation and emission

wavelengths set at 560 and 610 nm, respectively. The intensity values were subtracted for the background intensity of 1× PBS and then fitted for monoexponential decay (one phase decay) or pseudo-first order association (one phase association) using the equations preset in Graphpad Prism 9.

2.3.3 Modeling of TrxRFP2 with ColabFold

ColabFold,[30] which combines AlphaFold2 with MMseqs,[31, 32] was used to predict the 3-dimensional structure of TrxRFP2. Default settings were used. The program generated five structures ranked by pTMscores for each sequence input. The one with the best pTMscore was used to create illustrations and compared with the crystal structure of Trx (PDB:3TRX). Structural presentations were prepared in PyMOL.

2.3.4 Engineering of MtrxRFP2

Oligos pBAD-Mtrx-F1 and pBAD-Mtrx-R1 (**Table 2.1**) were used to amplify the human Trx2 gene using a gBlocks Gene Fragment ordered from Integrated DNA Technologies (IDT). Next, oligos pBAD-Mtrx-F2 and pBAD-Mtrx-R2 were used to amplify a Gly-Ser-rich linker and mutate the C-terminal residues of rxRFP1 from pBAD-TrxRFP1.[24] The C-terminus of rxRFP1 was mutated to that of rxRFP1.1 for a lower mid-point redox potential suited for the mitochondrial redox environment.[27] These two fragments were assembled in an overlap PCR reaction using pBAD-Mtrx-F1 and pBAD-Mtrx-R2 as the amplification primers. The resultant PCR product was inserted into a pBAD/His B vector predigested with Xho I and Hind III using Gibson Assembly.[28] The product was used to transform cells as described above. The plasmid was isolated and confirmed with Sanger sequencing.

2.3.5 Protein purification and *in vitro* characterization of MtrxRFP2

The plasmid pBAD-MtrxRFP2 was used to transform E.coli DH10B cells, and a single colony was used to inoculate 5 mL 2×YT medium supplemented with 100 μg/mL ampicillin. After shaking overnight at 250 r.p.m and 37 °C, the culture was diluted with 500 mL of 2×YT medium containing 100 μg/mL ampicillin. OD600 was monitored, and 0.2% (w/v) L-arabinose was added to induce protein expression when OD600 reached 0.6. Expression was conducted at 30 °C for 24 h and then at 16 °C for another 72 h. The protein was purified using Ni-NTA agarose beads and size-exclusion chromatography as described above. An alkali denaturation method was used to determine the protein concentration.[29] To examine the indicator's specificity, freshly prepared proteins (1 μM) were incubated with the indicated chemicals or enzymes at room temperature for 10 minutes, and fluorescence with 570 nm excitation and 600 nm emission was measured using the BioTek Synergy Mx Microplate Reader. Human TrxR2 used in these assays was recombinantly expressed and purified from E. coli, and the selenocysteine residue was mutated to cysteine.

2.3.6 Construction of mammalian expression plasmids

Oligos pcDNA3-TrxRFP2-F and pcDNA3-TrxRFP2-R (**Table 2.1**) were used to amplify the TrxRFP2 gene from pBAD-TrxRFP2. The resultant product was inserted into a pcDNA3 vector predigested with Hind III and Xba I via Gibson Assembly.[28] To construct plasmids for mitochondrial expression, the TrxRFP1 (or MtrxRFP2) gene was amplified with oligos pCS2-Mito-F and pCS2-Mito-R1 (or pCS2-Mito-R2) (**Table 2.1**) from the corresponding pBAD bacterial expression plasmids. The PCR products were inserted between Age I and Xba I of a compatible pCS2+ vector, which contains tandem mitochondrial targeting signals derived from cytochrome c oxidase subunit VIII.

2.3.7 Mammalian cell culture, transfection, and live-cell imaging

HEK (human embryonic kidney) 293T and HeLa cells were cultured and transfected as previously described.[24] At 72 h post-transfection, cells in DPBS supplemented with 1 mM Ca^{2+}, 1 mM Mg^{2+} were imaged using a Leica DMi8 inverted microscope equipped with a Leica EL6000 light source, a TRITC filter cube (545/25 nm bandpass excitation and 605/70-nm bandpass emission), and a Photometrics Prime 95B sCMOS camera. To study the time-lapse responses of the transfected cells, auranofin (15 μM) was added to the abovementioned imaging buffer, and images were acquired at the indicated intervals. To test the reversibility of the indicators in live cells, additional DTT (10 mM) was added to cells that were pre-treated with auranofin (15 μM). Images were analyzed using the ImageJ[33] software. Background subtraction was performed by setting the rolling ball radius to 50 pixels. Cells were randomly selected, and the intensity means for regions of interest were extracted for further analysis. Fluorescence intensities at different time points (F) were normalized to the value at t = 0 min (F_0), and the F/F_0 ratios were plotted against time.

2.4 Results and Discussion

2.4.1 Engineering and structural modeling of TrxRFP2, an enhanced TrxRFP1 variant

TrxRFP1 is a genetic fusion of hTrx1 and rxRFP1 via a 30-amino-acid Gly-Ser-rich linker.[24] Despite the initial probe being adequate for detecting the redox changes of Trx both *in vitro* and in live mammalian cells, its responsiveness was not fully optimized. Therefore, we performed seven rounds of error-prone PCR-based directed evolution on TrxRFP1. To screen for candidates with better redox-indued fluorescence response, colonies from each library with

medium to high fluorescence were selected, and crude protein extracts were screened for redox-induced responsiveness. We carried out enzyme-based assays in 96-well plates. TPx1 and H_2O_2 were used to oxidize the proteins, while TrxR1 and NADPH were used to induce reduction. Fluorescence intensities at the two states were quantified, and intensity ratios were derived. After screening ~20,000 individual colonies on LB agar plates and testing ~700 clones as cell lysates, we identified a promising mutant showing a larger fluorescence response than the parental TrxRFP1. This mutant, named TrxRFP2 (**Figure 2.1A**), contains five mutations from TrxRFP1 (A18T, E56G, A66T, N93D, D248V). We compared the reduction and oxidation of TrxRFP1 and TrxRFP2 using enzyme-based assays. Recombinant TrxR1 and NADPH were used to reduce the oxidized proteins, while recombinant peroxiredoxin TPx1 and H_2O_2 were used to oxidize the reduced proteins. Within the first 60 s, the magnitudes of changes caused by reduction were ~3.0-fold and ~4.2-fold for TrxRFP1 and TrxRFP2, respectively, while the oxidation reactions caused fluorescence increases by ~3.5-fold and ~4.5-fold, respectively (**Figure 2.1BC**). The residual oxygen in the reaction systems (e.g., pre-dissolved in the buffers or from the air during the measurements) may impact the fluorescence changes and account for the discrepancies in the response magnitudes during reduction and oxidation. Nevertheless, TrxRFP1 and TrxRFP2 were compared in parallel during these experiments. We fitted the fluorescence responses using a monoexponential decay or pseudo-first order association model. The half-time ($t_{0.5}$) for TrxRFP2 reduction was determined to be 5.1 s while $t_{0.5}$ for TrxRFP1 reduction was 8.8 s. As for the oxidation kinetics, $t_{0.5}$ values were 3.9 and 6.8 s for TrxRFP2 and TrxRFP1, respectively. In both reduction and oxidation assays, TrxRFP2 showed faster kinetics and a more significant response magnitude than TrxRFP1.

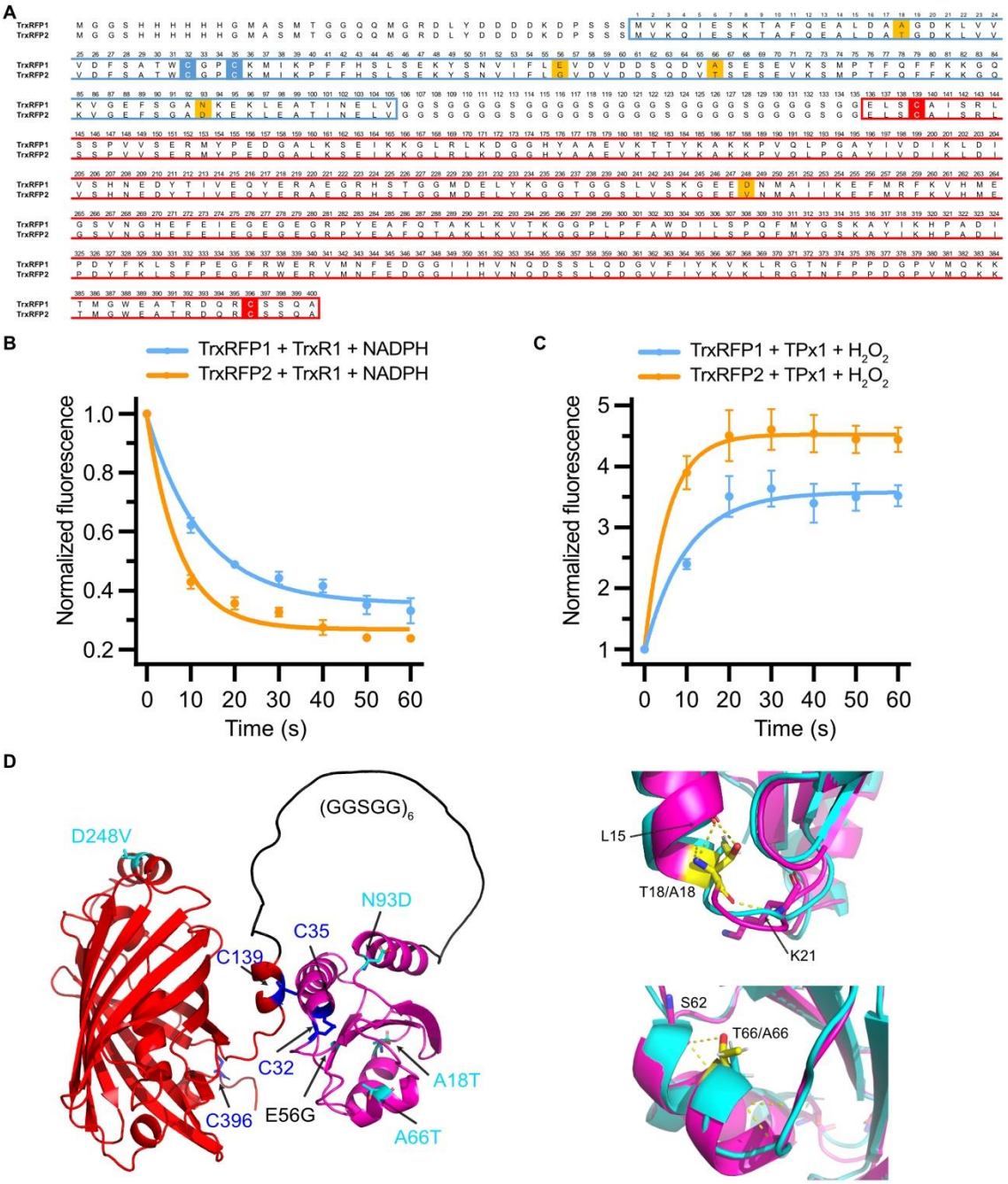

Figure 2.1 Mutations and *in vitro* response kinetics of TrxRFP2.

(**A**) Primary sequence alignment of TrxRFP1 and TrxRFP2. Residues mutated in TrxRFP2 via directed evolution from TrxRFP1 are shaded in orange. The active-site cysteine residues in human thioredoxin1 (hTrx1) are shaded in blue. The sequences derived from hTrx1 and rxRFP1 are highlighted in blue and red boxes. The key cysteine residues in the rxRFP1 portion for reversible disulfide formation are shaded in red. The unnumbered N-terminal residues (including the His_6 tag) were derived from the pBAD/His B vector. (**BC**) Comparison of oxidized (B) or reduced (C) TrxRFP1 and TrxRFP2 in response to enzymatic reduction (10 μM TrxR1 + 200 μM NADPH)

and oxidation (20 μM TPx1 + 200 μM H_2O_2). Fluorescence intensities were normalized to the values at t = 0 min. Data represent mean ± SD of three technical repeats. (**D**) TrxRFP2 structural model built with ColabFold (AlphaFold2 using MMseqs2). Left panel: the overall 3-dimensional model highlighting mutations (cyan), key cysteine residues (blue), and the interdomain floppy linker (black). Right panels: local structures of the TrxRFP2 model (magenta) overlaid with the Trx1 crystal structure (PDB: 3TRX) (cyan), highlighting newly formed H-bonds near A18T (top) and A66T (bottom) mutations.

Recently, artificial intelligence and deep learning have been successfully used to predict 3-dimensional protein structures. AlphaFold2, one of the most advanced computational tools, is known for its impressive accuracy.[31] We used ColabFold,[30] which runs a simplified version of AlphaFold2 by using a fast MMseqs2[32] search in the input feature generation stage, to predict the structures of TrxRFP2. Five structures ranked by pTMscores (a computed parameter reflecting the global modeling accuracy) were provided by the program. Among these structures, the folding of the individual hTrx1 and rxRFP1 domains is almost identical, but the relative position of the two domains varies. Within three of the five structures (including the one with the best pTMscore shown in **Figure 2.1D**), the reactive cysteines in hTrx1 and rxRFP1 are closely positioned, likely promoting the kinetic disulfide exchange between them. TrxRFP2 is different from TrxRFP1 with five mutations. Although it is hard to pinpoint the contributions of each mutation to the enhanced response kinetics of TrxRFP2, we speculate that the A18T and A66T mutations introduce additional H-bonds into the hTrx1 fold (**Figure 2.1D**), thereby enhancing thermostability and potentially affecting the redox reactions. In addition, E56G and N93D are close to the reactive cysteines, possibly affecting local structural flexibility and the electrostatic environment. The D248V mutation is within the rxRFP1 fold, and it seems to stabilize a short α-helix. Further studies are needed to better delineate the roles of these mutations.

2.4.2 Chemical-induced redox response of TrxRFPs in HEK 293T cells

We next directly compared TrxRFP2 with TrxRFP1 in live mammalian cells. Both indicators were transiently expressed in human embryonic kidney (HEK) 293T cells. Fluorescent responses induced by oxidation-stimulating chemicals were examined. Auranofin is a selective TrxR inhibitor.[34] TrxRFP1 and TrxRFP2-expressing cells presented a notable fluorescent increase

when treated with 15 μM auranofin (**Figure 2.2AB**). Moreover, cells expressing TrxRFP2 showed a more noticeable fluorescence increase, and the improvement of the dynamic range was ~1.75-fold (**Figure 2.2A-C**). Of note, the auranofin treatment did not interrupt intracellular pH, as shown previously.[24] No significant change was observed in both TrxRFP1- and TrxRFP2-expressing cells treated with a low-nanomolar concentration of 2-AAPA, a glutathione-reductase inhibitor (**Figure 2.2C**).[35] Similarly, no apparent fluorescent responses were caused in both groups of cells after 16-h incubation with 20 μM dimethyl fumarate (DMF),[36] a GSH redox reagent involved in GSH synthesis and GSH reductase upregulation (**Figure 2.2C**). The data suggest that both TrxRFP1 and TrxRFP2 do not respond to chemicals specifically disturbing the glutathione antioxidant system and are specific indicators for the redox of the Trx system. Furthermore, TrxRFP2-expressing cells pre-treated with auranofin reacted quickly with the further added reductant, DTT, confirming the reversibility of TrxRFP2 in live mammalian cells (**Figure 2.2D**). We speculate that several reasons may collectively contribute to the improved performance of TrxRFP2 relative to TrxRFP1 in live cells. In addition to the increased response magnitude and kinetics observed in the previously presented biochemical assays, the mutations in TrxRFP2 may enhance its folding, resulting in a larger portion of proteins in live cells responsive to the auranofin treatment.

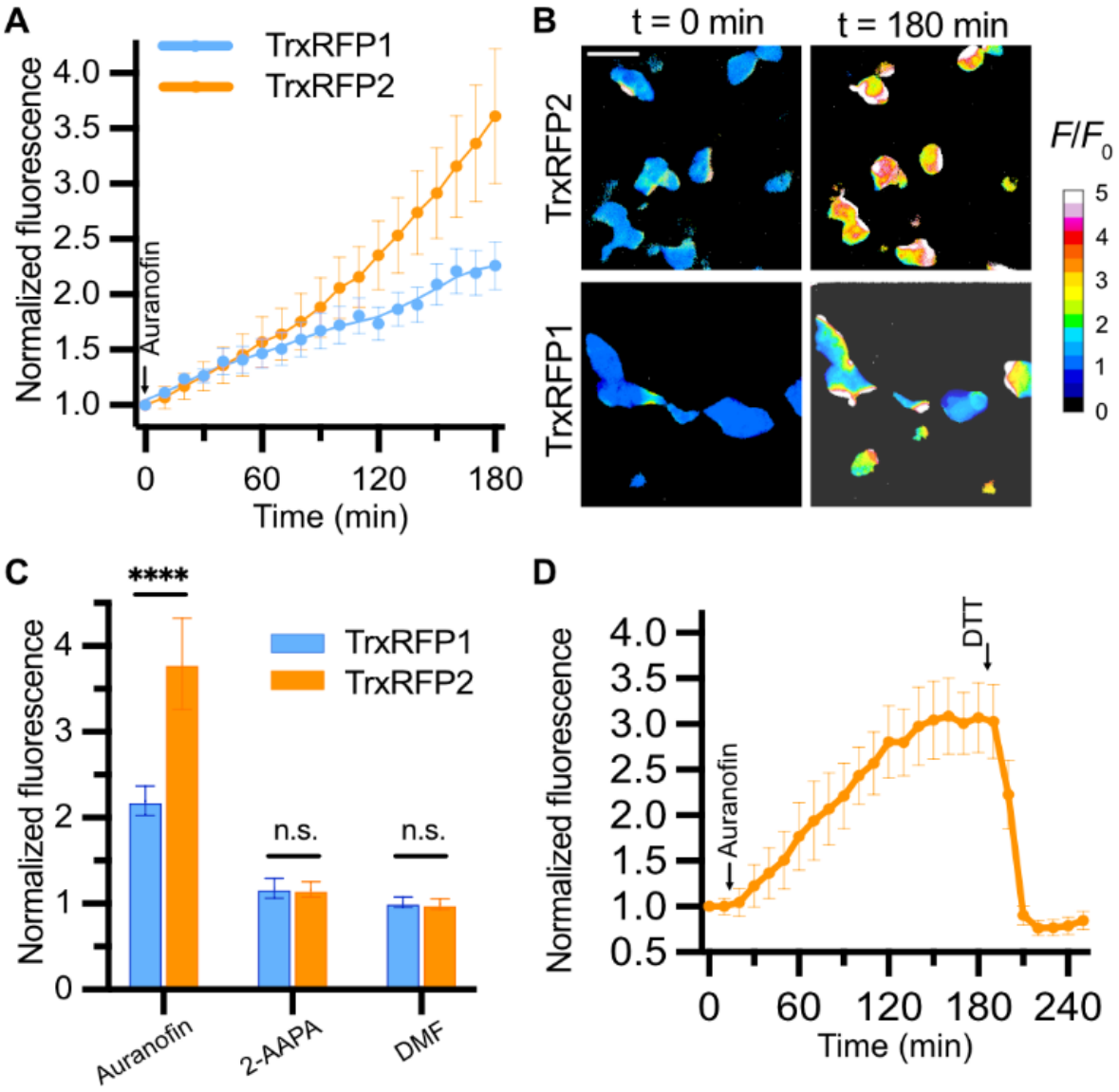

Figure 2.2 TrxRFPs in HEK 293T cells in response to oxidation-stimulating chemicals.

(**A**) Time course of the responses of HEK 293T cells expressing TrxRFP1 (blue) or TrxRFP2 (orange) to auranofin (15 μM). Fluorescence intensities were normalized to the values of each cell at t = 0 min. Data represent mean ± SD of 15 cells from three technical repeats. (**B**) Time-lapse pseudocolored fluorescence images (F/F_0) of HEK 293T cells expressing TrxRFP1 or TrxRFP2 treated with 15 μM auranofin. Scale bar, 50 μm. (**C**) Comparison of fluorescence responses of TrxRFP1 (blue bar) and TrxRFP2 (orange bar). Cells were treated with auranofin (15 μM), 2-AAPA (100 nM), or DMF (20 μM) for 180 min. Fluorescence intensities were normalized to the values at t = 0 min in their corresponding groups. Data represent mean ± SD of 12 cells from three

technical repeats. *P* values were determined by two-way ANOVA with Šidák's multiple comparisons test (****$P < 0.0001$; n.s, not significant, $P > 0.05$). (**D**) Sequential responses of TrxRFP2 in HEK 293T to auranofin (15 μM) and DTT (10 mM). Fluorescence intensities were normalized to the values at $t = 0$ min. Data represent mean ± SD of 9 cells from three technical repeats.

2.4.3 Development of MtrxRFP2, an indicator for the redox of mitochondrial Trx2

Trx1 and TrxR1 are primarily cytosolic. In contrast, Trx2 and TrxR2 are found in the mitochondria of mammalian cells. We previously fused TrxRFP1 to a mitochondrial targeting sequence (MTS) and successfully used Mito-TrxRFP1 to monitor compartmentalized Trx oxidation. Although the result suggests that the mitochondrial Trx system can cross-react with Trx1 in TrxRFP1, such reaction is likely not kinetically optimal. Using a sensor design strategy similar to TrxRFP1, we genetically linked rxRFP1.1, which has a redox potential suitable for mitochondria, to human Trx2, through a 30-amino-acid Gly-Ser-rich linker. We hypothesized that within this configuration, the redox change of active Cys residues (C31 and C34) in Trx2 could be coupled to the redox status of the inserted active cysteine pair at the C- and N-termini of rxRFP1.1. Such disulfide exchange reaction could be kinetically preferred due to the close distance between Trx2 and rxRFP1.1 in the fusion construct. As a result, the fluorescence of rxRFP1.1 becomes an indicator for the Trx2 redox status. We named the TrxR2 and rxRFP1.1 fusion construct MtrxRFP2 and purified the protein for further characterization. The freshly purified MtrxRFP2, which was oxidized by air, presented identical excitation and emission peaks at 575 nm and 600 nm as rxRFP1.1 (**Figure 2.3A**). Dithiothreitol (DTT) reduced MtrxRFP2 quickly, leading to a 3.5-fold fluorescence decrease (**Figure 2.3A**). Oxidized MtrxRFP2 showed minimal response to H_2O_2 and GSH at millimolar concentrations (**Figure 2.3B**). In addition, MtrxRFP2 in the oxidized state showed a robust, ~ 3.3-fold fluorescence decrease upon the addition of our purified TrxR2 with NADPH as the co-factor (**Figure 2.3B**).

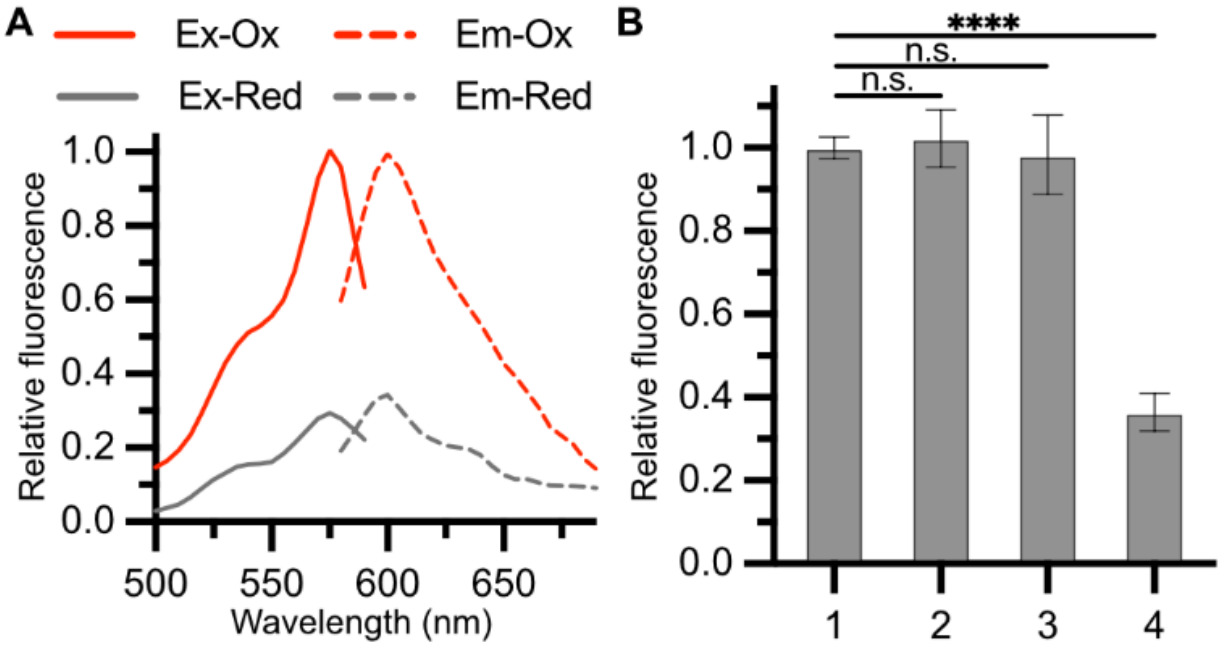

Figure 2.3 In vitro characterization of purified MtrxRFP2.

(**A**) Excitation (solid line) and emission (dot line) spectra of MtrxRFP2 in oxidized (red) and reduced (grey) states. (**B**) Fluorescence responses of MtrxRFP2 post 10-min incubation with: 1, PBS; 2, 1 mM H_2O_2; 3, 1 mM GSH; 4, 20 µM purified TrxR2 + 400 µM NADPH. Data represent mean ± SD of three technical repeats. *P* values were determined by one-way ANOVA with Dunnett's multiple comparisons test (****$P < 0.0001$; n.s, not significant, $P > 0.05$).

2.4.4 Chemical-induced Trx redox changes in the mitochondria of mammalian cells

We next subcellularly localized TrxRFP1 and MtrxRFP2 to the mitochondria to monitor Trx redox changes. A tandem MTS was appended to the N-terminus of TrxRFP1 or MtrxRFP2 (**Figure 2.4A).** Expressing the constructs led to the successful localization of these probes in the mitochondrial compartment of cultured human cervical cancer HeLa cells. When treating the cells expressing mitochondrial TrxRFP1 or MtrxRFP2 with auranofin, the fluorescence intensity increased gradually within the monitored 30-min period. In comparison, mitochondrial MtrxRFP2 presented a more robust fluorescence increase than mitochondrial TrxRFP1 (F/F_0, 140% versus 120%) and faster kinetics (**Figure 2.4BC**). These results indicate that MtrxRFP2 is a better indicator than TrxRFP1 for monitoring Trx2 redox dynamic changes in the mitochondria of mammalian cells. This property could result from the mitochondrial-specific sensory domain Trx2 and the fused RFP1.1, which are equipped with a redox potential more suitable for the mitochondria environment. In addition, we examined the reversibility of mitochondrial MtrxRFP2 in HEK 293T cells. Fast reversed responses to DTT were observed in cells pre-oxidized with auranofin (**Figure 2.4D**).

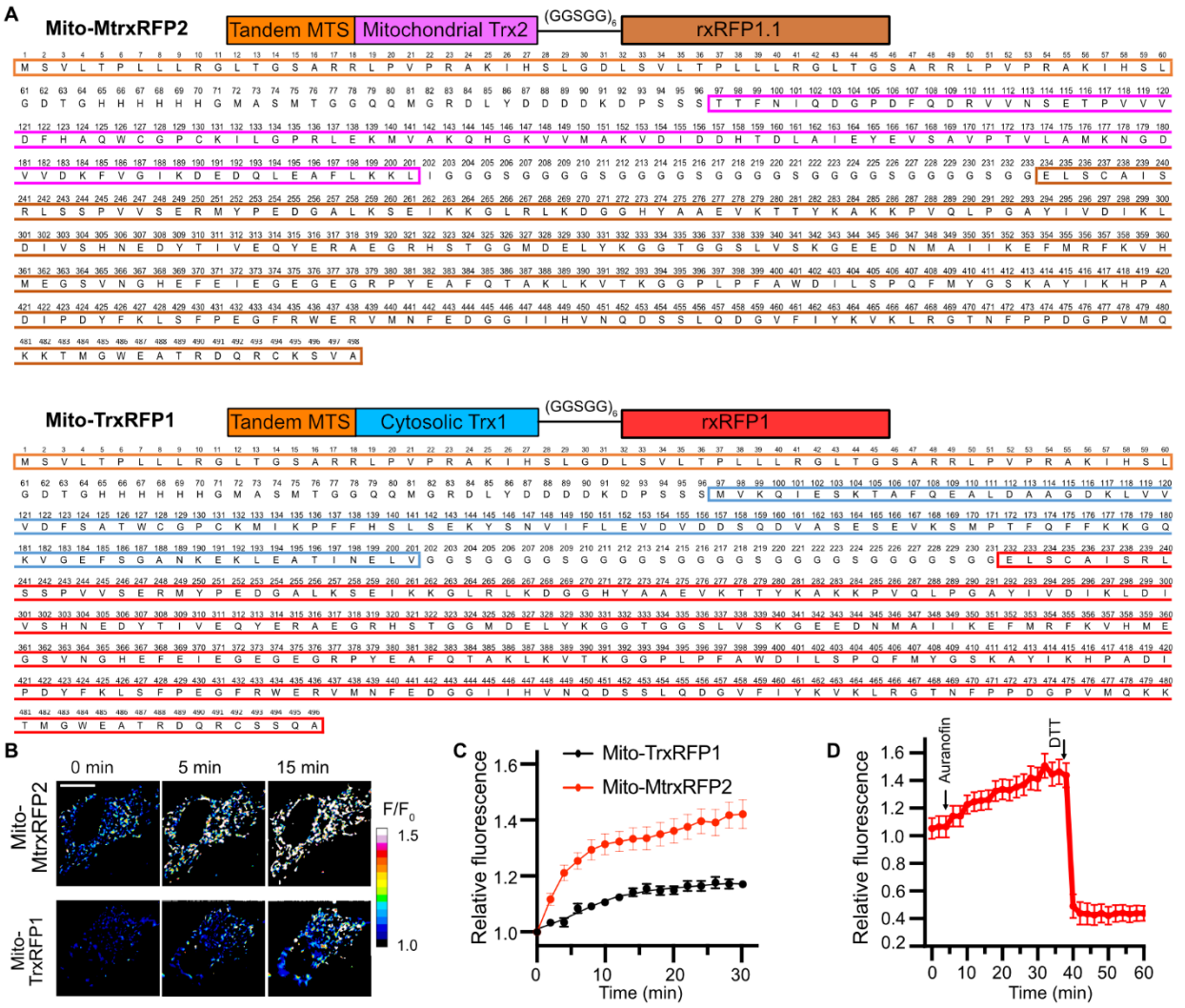

Figure 2.4 Sequences and fluorescence response of mitochondrially localized MtrxRFP2 and TrxRFP1 in mammalian cells.

(**A**) Domain arrangements and primary sequences of mitochondrial MtrxRFP2 and TrxRFP1. Top: Mito-MtrxRFP2 highlighting the tandem MTS (orange box) and fragments derived from hTrx2 (magenta box) and rxRFP1.1 (crimson box). Bottom: Mito-TrxRFP1 highlighting the tandem MTS (orange box) and fragments derived from hTrx1 (cyan box) and rxRFP1 (red box). (**B**) Time-lapse pseudocolored fluorescence images (F/F_0) of HeLa cells expressing mitochondrial TrxRFP1 or MtrxRFP2 treated with 15 μM auranofin. Scale bar, 20 μm. (**C**) Time course of Mito-TrxRFP1 or Mito-MtrxRFP2 fluorescence in HeLa cells treated with auranofin (15 μM). Fluorescence intensities were normalized to the values of each cell at t = 0 min. Data represent mean ± SD of 15 cells from three technical repeats. (**D**) Time course responses of MtrxRFP2 in HEK 293T to auranofin (15 μM) and DTT (10 mM). Fluorescence intensities were normalized to the values of each cell at t = 0 min. Data represent mean ± SD of 10 cells from three technical repeats.

2.5 Conclusion

Trx, as a thiol-dependent antioxidant protein, is essential for redox signaling and has been linked to many pathological processes. We previously reported the first genetically encoded biosensor, TrxRFP1. Based on our previous work, we have developed an improved indicator, TrxRFP2, via random mutagenesis and enzyme-based screening. Compared to TrxRFP1, TrxRFP2 showed improved response kinetics and a greater fluorescence response to TrxR inhibition in mammalian cells without appreciable cross-reaction to the GSH system. Due to its specificity and improved dynamic range, TrxRFP2 is a better indicator for redox biology studies.

MtrxRFP2 was created by linking a redox-sensitive rxRFP1.1 and mitochondrial Trx (Trx2). The proximity forced by the linker in the fusion construct indeed facilitated the disulfide exchange between rxRFP1.1 and Trx2. MtrxRFP2 displayed a ~ 3.5-fold dynamic range. We compared subcellularly localized MtrxRFP2 to TrxRFP1 for monitoring mitochondrial Trx redox changes. MtrxRFP2-expressing cells showed larger and faster responses upon auranofin treatment than TrxRFP1-expressing cells. Thus, although mitochondrially localized TrxRFP1 can detect the dynamics of mitochondrial Trx redox, MtrxRFP2 derived from Trx2 is a more robust indicator for monitoring Trx redox dynamics in mitochondria.

2.6 Reference

1. Lu, J.; Holmgren, A., The thioredoxin antioxidant system. *Free Radic. Biol. Med.* **2014,** *66*, 75-87.
2. Powis, G.; Montfort, W. R., Properties and biological activities of thioredoxins. *Annu. Rev. Biophys. Biomol. Struct.* **2001,** *30* (1), 421-455.
3. Holmgren, A.; Sengupta, R., The use of thiols by ribonucleotide reductase. *Free Radic. Biol. Med.* **2010,** *49* (11), 1617-1628.
4. Bian, M.; Fan, R.; Zhao, S.; Liu, W., Targeting the Thioredoxin System as a Strategy for Cancer Therapy: Miniperspective. *J. Med. Chem.* **2019,** *62* (16), 7309-7321.
5. Ren, X.; Zou, L.; Zhang, X.; Branco, V.; Wang, J.; Carvalho, C.; Holmgren, A.; Lu, J., Redox signaling mediated by thioredoxin and glutathione systems in the central nervous system. *Antioxid. Redox Signal.* **2017,** *27* (13), 989-1010.
6. Holmgren, A.; Lu, J., Thioredoxin and thioredoxin reductase: current research with special reference to human disease. *Biochem. Biophys. Res. Commun.* **2010,** *396* (1), 120-124.
7. Matthias, L. J.; Yam, P. T.; Jiang, X.-M.; Vandegraaff, N.; Li, P.; Poumbourios, P.; Donoghue, N.; Hogg, P. J., Disulfide exchange in domain 2 of CD4 is required for entry of HIV-1. *Nat. Immunol.* **2002,** *3* (8), 727-732.
8. Benhar, M.; Shytaj, I. L.; Stamler, J. S.; Savarino, A., Dual targeting of the thioredoxin and glutathione systems in cancer and HIV. *J. Clin. Investig.* **2016,** *126* (5), 1630-1639.
9. Holmgren, A., Thioredoxin. *Annu. Rev. Biochem.* **1985,** *54* (1), 237-271.
10. Nakamura, H.; Nakamura, K.; Yodoi, J., Redox regulation of cellular activation. *Annu. Rev. Immunol.* **1997,** *15* (1), 351-369.
11. Taniguchi, Y.; Taniguchi-Ueda, Y.; Mori, K.; Yodoi, J., A novel promoter sequence is involved in the oxidative stress-induced expression of the adult T-cell leukemia-derived factor (ADF)/human thioredoxin (Trx) gene. *Nucleic Acids Res.* **1996,** *24* (14), 2746-2752.
12. Spyrou, G.; Enmark, E.; Miranda-Vizuete, A.; Gustafsson, J.-Å., Cloning and expression of a novel mammalian thioredoxin. *J. Biol. Chem.* **1997,** *272* (5), 2936-2941.
13. Weichsel, A.; Gasdaska, J. R.; Powis, G.; Montfort, W. R., Crystal structures of reduced, oxidized, and mutated human thioredoxins: evidence for a regulatory homodimer. *Structure* **1996,** *4* (6), 735-751.
14. Starkov, A. A.; Andreyev, A. Y.; Zhang, S. F.; Starkova, N. N.; Korneeva, M.; Syromyatnikov, M.; Popov, V. N., Scavenging of H_2O_2 by mouse brain mitochondria. *J. Bioenerg. Biomembr.* **2014,** *46* (6), 471-477.
15. Ungerstedt, J.; Du, Y.; Zhang, H.; Nair, D.; Holmgren, A., In vivo redox state of human thioredoxin and redox shift by the histone deacetylase inhibitor suberoylanilide hydroxamic acid (SAHA). *Free Radic. Biol. Med.* **2012,** *53* (11), 2002-2007.
16. Huang, Q.; Zhou, H. J.; Zhang, H.; Huang, Y.; Hinojosa-Kirschenbaum, F.; Fan, P.; Yao, L.; Belardinelli, L.; Tellides, G.; Giordano, F. J., Thioredoxin-2 inhibits mitochondrial reactive oxygen species generation and apoptosis stress kinase-1 activity to maintain cardiac function. *Circulation* **2015,** *131* (12), 1082-1097.

17. Hägglund, P.; Bunkenborg, J.; Maeda, K.; Svensson, B., Identification of thioredoxin disulfide targets using a quantitative proteomics approach based on isotope-coded affinity tags. *J. Proteome Res.* **2008,** *7* (12), 5270-5276.
18. Ueno, T.; Nagano, T., Fluorescent probes for sensing and imaging. *Nat. Methods* **2011,** *8* (8), 642-645.
19. Dooley, C. T.; Dore, T. M.; Hanson, G. T.; Jackson, W. C.; Remington, S. J.; Tsien, R. Y., Imaging dynamic redox changes in mammalian cells with green fluorescent protein indicators. *J. Biol. Chem.* **2004,** *279* (21), 22284-93.
20. Ostergaard, H.; Henriksen, A.; Hansen, F. G.; Winther, J. R., Shedding light on disulfide bond formation: engineering a redox switch in green fluorescent protein. *EMBO J.* **2001,** *20* (21), 5853-62.
21. Lukyanov, K. A.; Belousov, V. V., Genetically encoded fluorescent redox sensors. *Biochim Biophys Acta Gen Subj* **2014,** *1840* (2), 745-56.
22. Pang, Y.; Zhang, H.; Ai, H.-w., Genetically Encoded Fluorescent Redox Indicators for Unveiling Redox Signaling and Oxidative Toxicity. *Chem. Res. Toxicol.* **2021,** *34* (8), 1826-1845.
23. Gutscher, M.; Pauleau, A. L.; Marty, L.; Brach, T.; Wabnitz, G. H.; Samstag, Y.; Meyer, A. J.; Dick, T. P., Real-time imaging of the intracellular glutathione redox potential. *Nat. Methods* **2008,** *5* (6), 553-9.
24. Fan, Y.; Makar, M.; Wang, M. X.; Ai, H. W., Monitoring thioredoxin redox with a genetically encoded red fluorescent biosensor. *Nat. Chem. Biol.* **2017,** *13* (9), 1045-1052.
25. Fan, Y.; Chen, Z.; Ai, H. W., Monitoring redox dynamics in living cells with a redox-sensitive red fluorescent protein. *Anal. Chem.* **2015,** *87* (5), 2802-10.
26. Hanson, G. T.; Aggeler, R.; Oglesbee, D.; Cannon, M.; Capaldi, R. A.; Tsien, R. Y.; Remington, S. J., Investigating mitochondrial redox potential with redox-sensitive green fluorescent protein indicators. *J. Biol. Chem.* **2004,** *279* (13), 13044-53.
27. Fan, Y.; Ai, H. W., Development of redox-sensitive red fluorescent proteins for imaging redox dynamics in cellular compartments. *Anal. Bioanal. Chem.* **2016,** *408* (11), 2901-11.
28. Gibson, D. G.; Young, L.; Chuang, R. Y.; Venter, J. C.; Hutchison, C. A., 3rd; Smith, H. O., Enzymatic assembly of DNA molecules up to several hundred kilobases. *Nat. Methods* **2009,** *6* (5), 343-5.
29. Wu, T.; Pang, Y.; Ai, H. W., Circularly Permuted Far-Red Fluorescent Proteins. *Biosensors* **2021,** *11* (11), 438.
30. Mirdita, M.; Schütze, K.; Moriwaki, Y.; Heo, L.; Ovchinnikov, S.; Steinegger, M., ColabFold-Making protein folding accessible to all. **2021**.
31. Jumper, J.; Evans, R.; Pritzel, A.; Green, T.; Figurnov, M.; Ronneberger, O.; Tunyasuvunakool, K.; Bates, R.; Žídek, A.; Potapenko, A., Highly accurate protein structure prediction with AlphaFold. *Nature* **2021,** *596* (7873), 583-589.
32. Steinegger, M.; Söding, J., MMseqs2 enables sensitive protein sequence searching for the analysis of massive data sets. *Nat. Biotechnol.* **2017,** *35* (11), 1026-1028.
33. Schindelin, J.; Arganda-Carreras, I.; Frise, E.; Kaynig, V.; Longair, M.; Pietzsch, T.; Preibisch, S.; Rueden, C.; Saalfeld, S.; Schmid, B., Fiji: an open-source platform for biological-image analysis. *Nat. Methods* **2012,** *9* (7), 676-682.

34. Zhang, X.; Selvaraju, K.; Saei, A. A.; D'Arcy, P.; Zubarev, R. A.; Arnér, E. S.; Linder, S., Repurposing of auranofin: Thioredoxin reductase remains a primary target of the drug. *Biochimie* **2019,** *162*, 46-54.
35. Seefeldt, T.; Zhao, Y.; Chen, W.; Raza, A. S.; Carlson, L.; Herman, J.; Stoebner, A.; Hanson, S.; Foll, R.; Guan, X., Characterization of a novel dithiocarbamate glutathione reductase inhibitor and its use as a tool to modulate intracellular glutathione. *J. Biol. Chem.* **2009,** *284* (5), 2729-2737.
36. Hoffmann, C.; Dietrich, M.; Herrmann, A.-K.; Schacht, T.; Albrecht, P.; Methner, A., Dimethyl fumarate induces glutathione recycling by upregulation of glutathione reductase. *Oxid. Med. Cell. Longev.* **2017,** *2017*.

Chapter 3 Development, Characterization, and Structural Analysis of a Genetically Encoded Red Fluorescent Peroxynitrite Biosensor

This chapter is converted from a manuscript accepted by the journal of "ACS Chemical Biology". The author list are Yu Pang, Mian Huang, Yichong Fan, Hsien-Wei Yeh, Ying Xiong, Ho Leung Ng,* and Hui-wang Ai*. Author contributions are H.A. and H.L.N. conceived and supervised the project. Y.P. Y.F. and Y.X. engineered the biosensor, prepared proteins, and characterized the biosensor and related variants. M.H. solved the crystal structures and performed computational modeling. H.W.Y. and J.F.E. carried out the ^{11}B-NMR experiment. H.A., Y.P., M.H., and H.L.N wrote the manuscript. The two authors (Y.P. and M.H.) contributed equally to this work.

3.1 Abstract

Boronic acid-containing fluorescent molecules have been widely used to sense hydrogen peroxide and peroxynitrite, which are important reactive oxygen and nitrogen species in biological systems. However, it has been challenging to gain specificity. Our previous studies developed genetically encoded, green fluorescent peroxynitrite biosensors by genetically incorporating a boronic acid-containing noncanonical amino acid (ncAA), *p*-boronophenylalanine (*p*BoF), into the chromophore of circularly permuted green fluorescent proteins (cpGFPs). In this work, we introduced *p*BoF to amino acid residues spatially close to the chromophore of an enhanced circularly permuted red fluorescent protein (ecpApple). Our effort has resulted in two responsive ecpApple mutants: one be-stows reactivity toward both peroxynitrite and hydrogen peroxide, while the other, namely pnRFP, is a selective red fluorescent peroxynitrite biosensor. We characterized pnRFP in vitro and in live mammalian cells. We further studied the structure and

sensing mechanism of pnRFP using X-ray crystallography, ^{11}B-NMR, and computational methods. The boron atom in pnRFP adopts an sp^2-hybridization geometry in a hydrophobic pocket, and the reaction of pnRFP with peroxynitrite generates a product with a twisted chromophore, corroborating the observed "turn-off" fluores-cence response. Thus, this study extends the color palette of genetically encoded peroxynitrite biosensors, provides insight into the response mechanism of the new biosensor, and demonstrates the versatility of using protein scaffolds to modulate chemoreactivity.

3.2 Introduction

Peroxynitrite ($ONOO^-$) is a highly reactive molecule formed by the reaction between nitric oxide (•NO) and superoxide anion ($O_2^{\bullet-}$) via a diffusion-controlled process.[1, 2] The decomposition of peroxynitrite can further produce secondary radicals.[3, 4]In biological systems, peroxynitrite and its derived radicals act through direct or radical-mediated oxidation and nitration of biomolecules.[5-8] In particular, tyrosine nitration, which is the most representative post-translational protein modification caused by peroxynitrite, has been considered a maker of nitrosative stress.[9] Peroxynitrite is thus recognized as an important pathogenic mediator for various diseases, such as cardiovascular diseases, neurodegeneration, inflammation, and cancer.[10-12] Additionally, low levels of peroxynitrite may play signaling roles.[13, 14] Furthermore, peroxynitrite has been identified as a potent cytotoxic effector of macrophages, and due to its cell permeability, macrophage-induced peroxynitrite can kill surrounding target cells or invading pathogens.[15, 16]

To better understand the pathophysiology of peroxynitrite and develop related therapies, it is crucial to track peroxynitrite in living systems.[17] However, this is challenging due to peroxynitrite's high reactivity, low steady-state concentration, and complex diffusion and reaction

pathways in the cellular milieu. Fluorescent sensors have emerged as a promising approach for peroxynitrite detection, as they are sensitive, provide good signal-to-background ratios, and can be used with widely available fluorescence microscopy platforms.[18-21] However, these sensors often exhibit cross-reactivity with other reactive oxygen and nitrogen species (ROS/RNS), such as hydroxyl radical (•OH), hypochlorite (ClO^-), and hydrogen peroxide (H_2O_2). Developing specific sensors for peroxynitrite remains a highly sought-after goal.

Fluorescent molecules containing boronic acid have been commonly used for detecting hydrogen peroxide and peroxynitrite.[22-24] However, it is difficult to differentiate between the two using these molecules, because although arylboronic acid reacts with peroxynitrite more rapidly than hydrogen peroxide, hydrogen peroxide is more prevalent and abundant in biological systems. To address this issue, previous studies have created several boronic acid-based sensors that utilize N-B interactions to convert boronic acid into an sp^3-hybridized boron species, which reduces reactivity with hydrogen peroxide and increases specificity for peroxynitrite.[19,25-27] In particular, we previously created genetically encoded fluorescent peroxynitrite sensors, such as pnGFP and pnGFP-Ultra, by introducing a noncanonical amino acid (ncAA), *p*-boronophenylalanine (*p*BoF), into the chromophores of circularly permuted fluorescent proteins (cpFPs).[25-27] We utilized a genetic code expansion technology,[28-32] which involves the expression of an engineered orthogonal tRNA and aminoacyl-tRNA synthetase pair, to incorporate ncAAs into proteins in a site-specific manner. cpFPs were employed in our studies due to their more accessible chromophores than fluorescent proteins (FPs) in the wild-type topology.[24,33] The peroxynitrite-induced oxidation of boronic acid-derived chromophores generates tyrosine-derived phenolate chromophores (**Figure 3.1A**), resulting in drastic fluorescence turn-on responses. The genetic encodability of these sensors makes them compatible with directed evolution for response and specificity

optimization,[27] and it further allows for convenient dissemination and broad adaptation. In addition, signal sequences can be used to readily express the sensors in subcellular localizations.[33] Mechanistic studies suggest that the boron atoms in these sensors were converted to be sp^3-hybridized due to the N-B interaction with a nearby histidine residue through a polarized water bridge, leading to high specificity that can differentiate peroxynitrite from hydrogen peroxide.[26]

Herein, we present the development, characterization, and structural analysis of a genetically encoded red fluorescent peroxynitrite biosensor (pnRFP), which specifically detects peroxynitrite *in vitro* and in mammalian cells. Instead of incorporating *p*BoF into the chromophore of a circularly permuted red fluorescent protein (cpRFP), we replaced residues near the chromophore with *p*BoF, allowing modulation of chromophore fluorescence through the boronic acid oxidation reaction (**Figure 3.1B**). In addition, we studied the structures of pnRFP and relevant mutants using biophysical and computational methods, gaining insight into the response mechanism of this new sensor.

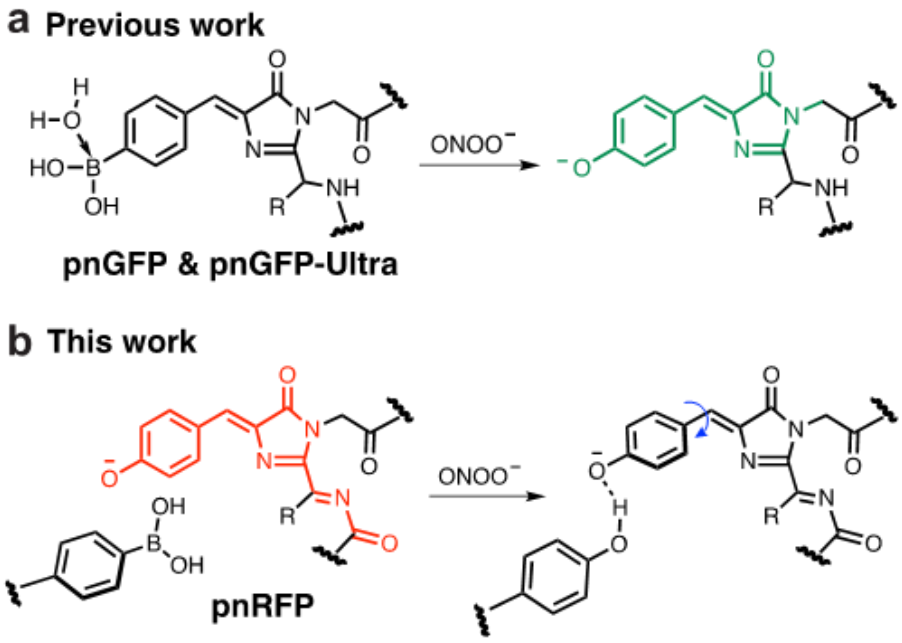

Figure 3.1 Mechanisms of protein-based, noncanonical amino acid (ncAA)-containing peroxynitrite biosensors

(**A**) **Previous work (pnGFP and pnGFP-Ultra):** *p*BoF was introduced to the chromophore of pnGFP or pnGFP-Ultra, which could further react with peroxynitrite to form a tyrosine-derived chromophore for enhanced fluorescence. (**B**) **This work (pnRFP):** *p*BoF is introduced to an amino acid residue in proximity to the chromophore, and the reaction of *p*BoF with peroxynitrite forms a tyrosine residue, which reduces fluorescence by bending the chromophore via hydrogen bonding.

3.3 Methods and Materials

3.3.1 Sources of Key Reagents

The amino acid *p*-borono-DL-phenylalanine (*p*BoF) was purchased from Synthonix (Wake Forest, NC). Synthetic DNA oligos were purchased from Integrated DNA Technologies (Coralville, IA). Restriction endonucleases or other molecular biology reagents were purchased from Thermo Fisher Scientific (Waltham, MA) or New England Biolabs (Ipswich, MA). Plasmid pCMV-R-GECO1 (Addgene plasmid # 32444) and pAcBac3 were gifts from Robert E. Campbell (University of Alberta) and Abhishek Chatterjee (Boston College), respectively.[34, 35]

3.3.2 Mutagenesis and Biosensor Engineering

The generation of ecpApple from R-GECO1 was described elsewhere.[36] Next, overlap extension polymerase chain reactions (PCRs) were used to introduce the TAG amber codon to specific residue positions of ecpApple. To introduce the TAG codon to residue 14, oligos ecpApple-S14TAG-F and cpRFP_R (**Table 3.2**) were first used to amplify a fragment from ecpApple; next, oligos cpRFP_F and cpRFP_R were used to further amplify and extend the fragment recovered from the previous reaction. The PCR product was then digested with Hind III and Xho I and ligated with a predigested, compatible pBAD vector. To introduce the TAG codon to residue 30, oligos cpRFP_F and ecpApple-K30TAG-R, and ecpApple-K30TAG-F and cpRFP_R were used in two separate PCRs to amplify two separate fragments from ecpApple. The two fragments were used as templates in an overlap extension PCR with oligos cpRFP_F and cpRFP_R. The full-length product was generated, digested with Hind III and Xho I, and inserted into a pBAD vector. A similar procedure was used to derive other ecpApple mutants, and the

sequences of the corresponding oligos are presented in **Table 3.2**. Ligation products were used to transform *Escherichia coli* (*E. coli*) DH10B competent cell, which was next plated on LB agar plates supplemented with ampicillin (100 μg/mL). Plasmids were minipreped from liquid cell culture inoculated with single colonies, and the sequences of the variants were confirmed with Sanger Sequencing (Eurofins Genomics, Louisville, KY).

3.3.3 Protein Purification and Characterization

The pBAD plasmid harboring the gene of each ecpApple mutant was used along with the pEvol-*p*BoF plasmid[37,38] to co-transform *E. coli* DH10B cells, which were next grown on LB agar plates supplemented with ampicillin (100 μg/mL), chloramphenicol (50 μg/mL), and L-arabinose (0.02% w/v) at 37 °C overnight. A single colony was used to inoculate 2 × YT liquid culture with 100 μg/mL ampicillin and 50 μg/mL chloramphenicol. After growth overnight at 37 °C and 250 rpm, the saturated cell culture was diluted 100-fold with 2 × YT with 100 μg/mL ampicillin and 50 μg/mL chloramphenicol. When the optical density at 600 nm (OD_{600}) reached 0.6, 0.2% (w/v) L-arabinose and 2 mM racemic *p*BoF were added. Cells were grown at 30°C, 250 rpm for another 48 h, before being harvested by centrifugation and lysed by sonication. His-tagged proteins were purified using Pierce Ni-NTA agarose beads according to the manufacturer's instructions. The buffer was switched to 1× phosphate-buffered saline (PBS, pH 7.4) via dialysis, and protein concentrations were determined with Bradford assays. The preparation of other redox-active species was performed as described,[25] and 1× PBS was used to dilute proteins and reagents. To record the fluorescence excitation spectra, the emission wavelength was set at 620 nm, and the excitation was scanned from 450 to 600 nm. To record the emission spectra, the excitation was set at 540 nm, and the emission was scanned from 560 to 700 nm. Other intensity measurements

typically used 560 nm excitation and 610 nm emission. To examine responses to various redox-active chemicals, protein stock solutions were diluted with 1× PBS to gain a final concentration of 1 μM. Individual redox-active molecules (5 μL) were added to proteins (95 μL) in individual wells of a 96-well plate sitting on ice. The mixtures were moved to room temperature and incubated for 20 min before fluorescence recording. To examine time-dependent responses, 95 μL of the protein in 1× PBS was mixed with 5 μL of each reagent, and the kinetics was monitored at room temperature for 1 h. To test concentration-dependent responses, the pnRFP protein was mixed with peroxynitrite or SIN-1 at the indicated concentrations in individual wells of a black 96-well plate. The mixtures were incubated at room temperature for 1 h before end-point measurements were performed. All fluorescence signals were recorded with a monochromator-based BioTek Synergy Mx Microplate Reader.

3.3.4 Mammalian Expression and Live-Cell Imaging

To construct mammalian expression plasmids, oligos pnRFP_F and pnRFP_R were used to amplify the gene fragment of pnRFP or pnRFP-B30Y from corresponding pBAD plasmids. The resultant PCR product was digested with Hind III and Apa I and inserted into a predigested pMAH-POLY plasmid. The resultant pMAH-pnRFP (Addgene plasmid # 201679) or pMAH-pnRFP-B30Y (Addgene plasmid # 201823) plasmid was used along with pMAH-POLY-eRF1(E55D) to co-transfect HEK 293T cells by following a described procedure.[26] The *p*BoF amino acid was added to the cell culture medium to a final concentration of 2 mM at 18 h after transfection. Next, the culture was kept in a 37 °C, 5% CO_2 incubator for another 48 h, before being transferred into a fresh medium with no *p*BoF. Cells were imaged 16 h later in Dulbecco's phosphate-buffered saline (DPBS) supplemented with 1 mM Ca^{2+} and Mg^{2+} on a Leica DMi8 inverted fluorescence

microscope. To express pnRFP in mouse RAW 264.7 macrophage cells, oligos pBac3-F and pBac3-R were used to amplify the gene from pMAH-pnRFP, and the PCR product was inserted into a compatible pAcBac3 vector predigested with Xho I and EcoR I, resulting in pAcBAC3-POLY-pnRFP (Addgene plasmid # 201680). The control plasmid pAcBAC3-POLY- pnRFP-B30Y was created similarly. RAW 264.7 cells were cultured in Dulbecco's modified Eagle medium (DMEM) with GlutaMAX (Gibco) supplemented with 10% fetal bovine serum (FBS). The pAcBAC3 (3 μg) plasmid was used to transfect RAW 264.7 cells by mixing the DNA with 6 μg of X-tremeGENE HP DNA Transfection Reagent (Roche) according to the manufacturer's instruction. At 20 h after transfection, 1 mM *p*BoF was added dropwise. After another 24 h, the *p*BoF-containing medium was replaced with fresh DMEM with GlutaMAX and 10% FBS but no *p*BoF. After *p*BoF depletion, RAW 264.7 cells were incubated with 1 μg/mL LPS and 100 ng/mL IFN-γ for 15 h. Next, the culture medium was replaced with a HEPES-buffered Hank's Balanced Salt Solution (HBSS), and cells were treated with 100 nM/mL PMA and imaged on a Leica DMi8 inverted fluorescence microscope. A Leica EL6000 light source, a TRITC filter cube (545/25 nm bandpass excitation and 605/70 nm bandpass emission), and a Photometrics Prime 95B sCMOS camera were used for the imaging experiments.

3.3.5 Protein Crystallization and Structure Determination

The purified pnRFP (22 mg/mL) in 20 mM Tris (pH 8.0) was crystallized by sitting-drop method with vapor diffusion against the crystallization reagent (0.1 M Na_2HPO_4: citric acid pH 4.2, 40% (v/v) PEG 400). A liquid drop at pH 6.0 was prepared by mixing 0.6 μL of protein solution with 0.6 μL of the crystallization reagent. It was equilibrated against 400 μL of the crystallization reagent to accomplish crystallization. To obtain high-quality crystals, microseeding

was applied under the same crystallization condition. The mutant pnRFP-B30Y was crystallized at 8 mg/mL under the same process mentioned above without microseeding operation. X-ray diffraction data for the pnRFP crystal was collected by the SIBYLS beamline of the Advanced Light Source at Lawrence Berkeley National Lab, and the pnRFP-K30Y crystal was collected by the beamline 23-ID-D of the Argonne Photon Source, Chicago. Both data were processed by X-ray Detector Software (XDS)[39] and reduced by POINTLESS[40], AIMLESS[41] and TRUNCATE[42] in the CCP4 suite. Molecular replacement was applied to the reduced data with Phaser[43] for building structure models. The models were then refined by Coot 0.8.9-pre EL[44] and Refmac5.[45] Crystal structures of pnRFP and pnRFP-B30Y were performed via the PyMOL Molecular Graphics System, Version 1.8 Schrödinger, LLC. The protein-ligand 2D interaction diagrams were built via LigPlot+ version 1.4.5.[46] The RMSD between the structures was calculated by YASARA.[47]

3.3.6 ^{11}B-NMR Characterization

The pnRFP protein was purified as described above, concentrated using Amicon Ultra Centrifugal Filter Units (3000 Da cutoff), and exchanged into 20 mM phosphate (pH 7.4, D_2O (v): H_2O (v) = 1:1) to final concentrations of 15.6 mg/mL. The ^{11}B NMR spectra were acquired on a Varian VNMRS 600 spectrometer operating at 192.439 MHz using a 5 mm AutoXDB probe. Samples were placed in quartz NMR tubes. The protein spectra were collected with single pulse excitation (45-degree pulses were used, 90-degree pulse width = 13 μs). The sweep width was 200 ppm and the total acquisition time was 24 h (scan = 1.4 million, delay before pulse = 10 ms, single FID acquisition time = 52 ms). To further remove background signal, back linear prediction within the MestReNova software was used (Method = Toeplitz, COEF = 32, Base points = 256, from 0

to 46). Data were then processed in the normal manner with 100 Hz line broadening applied. Chemical shifts were referenced to external 15% boron trifluoride etherate in $CDCl_3$ ($BF_3 \cdot Et_2O$, δ = 0 ppm). For standard comparisons, we recorded ^{11}B NMR spectra for both phenylboronic acid (20 mM) in the 20 mM phosphate buffer (pH 7.4, D_2O (v): H_2O (v) = 1:1), and phenylboronic acid (20 mM) in 1N NaOH aqueous solution (D_2O (v): H_2O (v) = 1:1).

3.3.7 Computational Modelling

The crystal structure of pnRFP was used as a template. At position 30, BoF was substituted by Lys with an extended side-chain conformation toward the phenyl ring of NRQ. At position 14, Ser was substituted by BoF. BoF was adjusted in Coot to adopt a conformation with the side chain buried in the barrel. The homology model was further conformationally adjusted by MD simulations The model was then subjected to a 131-ns length MD simulation with the AMBER14 force field in YASARA version 19.12.14.L.64. The system was performed with explicit solvent in a cube box with a 60.83-Å side length, containing 6,437 water molecules. The default parameter settings were used in the MD run with the pressure at 1 bar, a temperature of 298 K, pH 7.4, 1-fs time steps, and snapshots taken at every 100-ps interval. The trajectory was analyzed, and the simulated model was considered in the equilibrium state. The partial atomic charges assigned to boron and other atoms were calculated by the AM1 semi-empirical methods.[48]

3.4 Results

3.4.1 Engineering of pnRFP

To expand the color palette of genetically encoded peroxynitrite biosensors, we sought to introduce *p*BoF into cpRFPs. We selected cpmApple, a cpRFP variant previously used in the

development of other biosensors,[34, 49] as the starting scaffold. Next, we used error-prone polymerase chain reactions (EP-PCRs) to randomize cpmApple. Screening the libraries for increased brightness at 37 °C led to the identification of an enhanced cpmApple mutant (ecpApple), which is three mutations (S9G, E135K, and M206V) away from cpmApple (**Figure 3.2**).[36] Next, taking inspiration from pnGFP and pnGFP-Ultra, we introduced *p*BoF to the chromophore-forming tyrosine residue of ecpApple via genetic code expansion. The codon of residue 176 of ecpApple was mutated to TAG (amber codon), and an amber suppression plasmid, pEvol-*p*BoF, which expresses orthogonal, *p*BoF-specific tRNA and aminoacyl-tRNA synthetase in *E. coli*, was used to incorporate *p*BoF in response to the amber codon.[37, 38] Unfortunately, our prepared protein (ecpApple-Y176B) did not show robust fluorescence responses to peroxynitrite. After mixing peroxynitrite with ecpApple-Y176B, we observed a very slow development of red fluorescence. Because the chromophore maturation of red fluorescent proteins (RFPs) has to undergo a more complex process than green fluorescent proteins (GFPs),[50] we reasoned that the introduction of *p*BoF to residue 176 of ecpApple disrupted the formation of a mature chromophore. We further performed random mutagenesis on ecpApple-Y176B but were unable to identify any improved mutants.

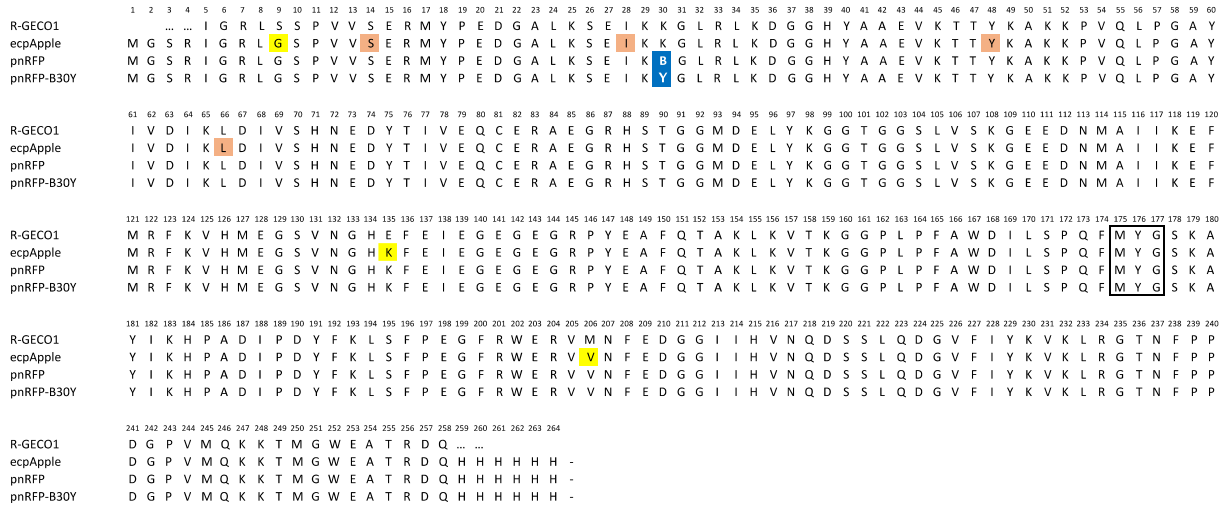

Figure 3.2 Sequence alignment of pnRFP with several relevant variants.

Shaded in yellow are mutations in ecpApple obtained through directed evolution from the circularly permuted RFP fragment in R-GECO1. Shaded in blue is residue 30 in pnRFP or pnRFP-B30Y, and B denotes *p*BoF. Shaded in orange are other residues in ecpApple examined for the genetic incorporation of *p*BoF in this study. Highlighted in the black box are residues 175-177, which are responsible for the formation of the chromophore in each protein.

Because the fluorescence of FP chromophores is sensitive to the surrounding environment, we next investigated the possibility of replacing residues near the chromophore of ecpApple with *p*BoF. We selected residues 14, 28, 30, 48 and 66 (**Figure 3.3A**) and introduced *p*BoF to each of these residues. The variants were expressed and purified from *E. coli* and tested for fluorescence responses to 100 μM peroxynitrite (**Figure 3.4A**). To our delight, two of these variants, including ecpApple-S14B and ecpApple-K30B, showed turn-on and turn-off responses, respectively. The results suggest that the peroxynitrite-induced oxidation of the two residues, which are spatially close to the phenolate of the chromophore (**Figure 3.3B**), can modulate the fluorescence of the chromophore.

We further tested ecpApple-S14B and ecpApple-K30B in response to hydrogen peroxide. The fluorescence of ecpApple-S14B was sensitive to micromolar hydrogen peroxide, and 100 μM hydrogen peroxide increased the fluorescence of ecpApple-S14B similarly to 100 μM peroxynitrite (**Figure 3.5**). In contrast, the fluorescence of ecpApple-K30B was unaffected by 1 mM hydrogen peroxide (**Figure 3.4B**). Due to the selectivity of ecpApple-K30B toward peroxynitrite, we named this mutant "pnRFP". Furthermore, we constructed a pnRFP-B30Y mutant (equivalent to ecpApple-K30Y, **Figure 3.2**), which is the expected major oxidation product of pnRFP (**Figure 3.1A**). pnRFP-B30Y was unresponsive to peroxynitrite (**Figure 3.4A**), confirming that the quenching of pnRFP by peroxynitrite was indeed caused by the reaction between the *p*BoF30 residue and peroxynitrite.

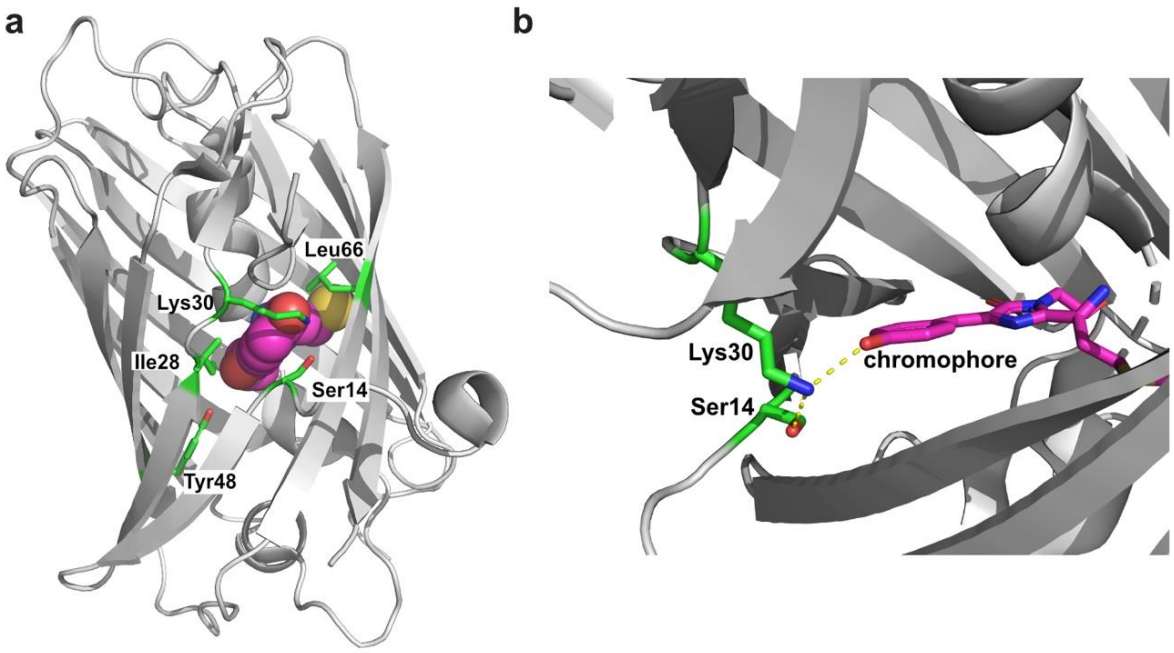

Figure 3.3 Illustration of residues in cpmApple targeted for site-specific incorporation of *p*BoF.

(**A**) Presented in green sticks are residues 14, 28, 30, 48, and 66. The chromophore is shown in magenta balls. (**B**) A detailed illustration of residues 14 and 30 (green sticks) in relation to the chromophore (magenta sticks). H-bonds between them are presented as yellow dashes. These graphs were generated based on the X-ray crystal structure of R-GECO1 (Protein Data Bank (PDB) entry 4I2Y).

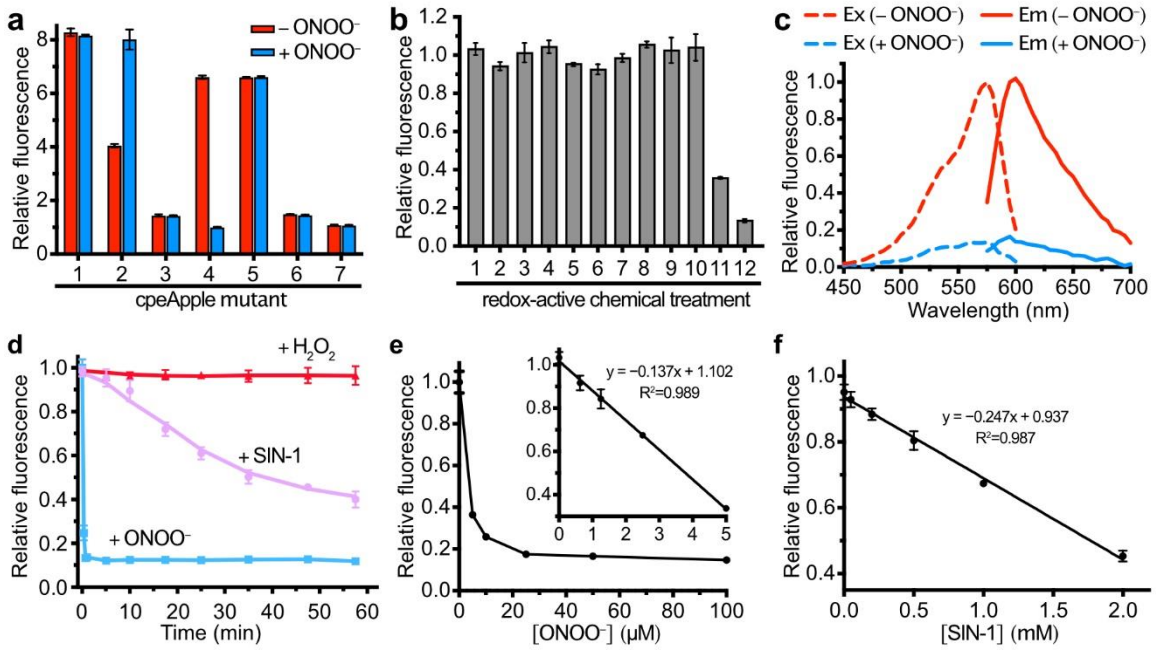

Figure 3.4 ***In vitro*** **characterization of pnRFP and relevant mutants.**

(**A**) Relative fluorescence intensities of pnRFP and other relevant variants (1, ecpApple; 2, ecpApple-S14B; 3, ecpApple-I28B; 4, pnRFP (*a.k.a.* ecpApple-K30B); 5, ecpApple-Y48B; 6, ecpApple-L66B; and 7, pnRFP-B30Y (*a.k.a.* ecpApple-K30Y) before (red) and after (blue) treatment with 100 μM peroxynitrite. (**B**) Fluorescence responses of pnRFP after 20-min incubation with a series of redox-active chemicals: 1, PBS; 2, 5 mM GSH; 3, 5 mM L-cysteine; 4, 1 mM DTT; 5, 1 mM H_2O_2; 6, 300 μM $O_2^{\bullet-}$; 7, 100 μM NaHS (H_2S donor); 8, 100 μM ClO^-; 9, 1 mM Fe^{2+} + 100 μM H_2O_2 (generation of •OH); 10, 5 mM GSSG; 11, 5 μM $ONOO^-$; 12, 100 μM $ONOO^-$. (**C**) Excitation (dash line) and emission (solid line) spectra of pnRFP before (red) and after (blue) reaction with 100 μM $ONOO^-$. (**D**) Time-dependent responses of pnRFP to 100 μM $ONOO^-$ (blue), 10 mM SIN-1 (magenta), and 100 μM H_2O_2 (red). (**E**) Dose-dependent response of pnRFP (1 μM) to $ONOO^-$ at indicated concentrations. (**F**) Dose-dependent response of pnRFP (1 μM) to SIN-1 at indicated concentrations. The incubation was 1 h at room temperature. Represented spectra are shown in panel c, and data in all other panels are presented as mean ± s.d. of triplicates.

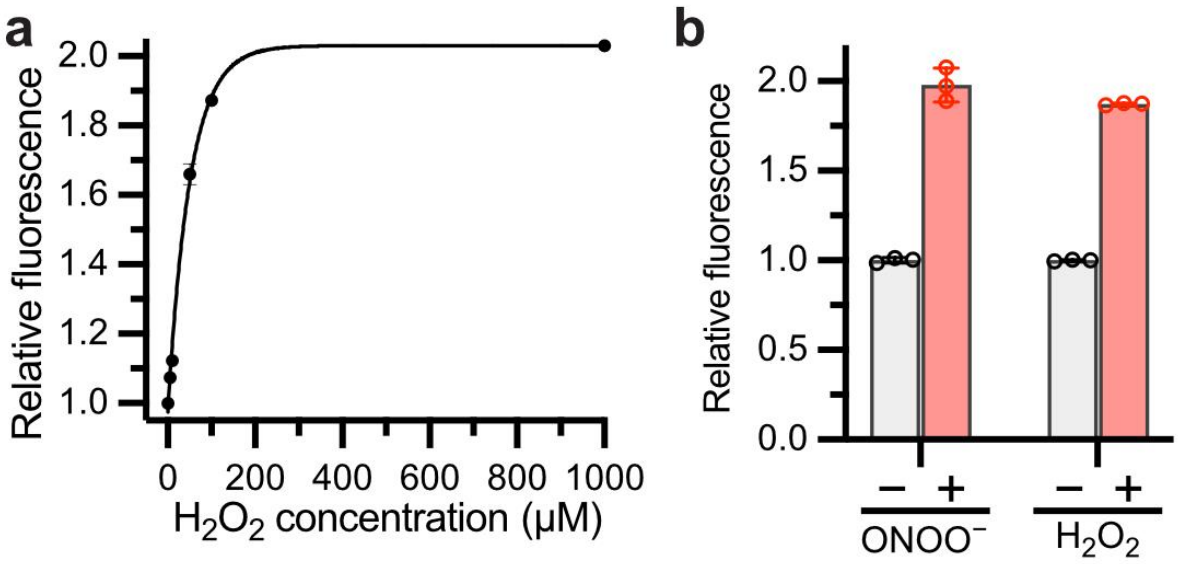

Figure 3.5 Fluorescence responses of ecpApple-S14B.

(**A**) Fluorescence increases of ecpApple-S14B after incubation with the indicated concentrations of hydrogen peroxide for 20 min, showing the sensitivity of ecpApple-S14B to micromolar hydrogen peroxide. (**B**) Comparison of the responses of ecpApple-S14B to 100 μM peroxynitrite or 100 μM hydrogen peroxide. Data are presented as mean ± s.d. of three technical replicates.

3.4.2 Further Characterization of pnRFP *In Vitro*

We examined the specificity of pnRFP against an expanded panel of redox-active molecules involved in cellular redox signaling. At physiologically relevant concentrations, only peroxynitrite caused notable fluorescence changes (**Figure 3.4B**), further confirming that pnRFP is a specific peroxynitrite sensor. pnRFP emitted strong red fluorescence with the excitation and emission peaks at 572 and 594 nm, respectively (**Figure 3.4C**). After reacting with peroxynitrite, its fluorescence decreased by about 5-fold. The reaction between pnRFP and peroxynitrite completed quickly, while a prolonged incubation of pnRFP with hydrogen peroxide did not cause notable fluorescence changes (**Figure 3.4D**). In addition, the incubation of pnRFP with SIN-1 (3-morpholinosydnonimine), a slow peroxynitrite-releasing molecule,[51] led to a time-dependent fluorescence decrease (**Figure 3.4D**). Furthermore, we mixed pnRFP with various concentrations of peroxynitrite or SIN-1, and the induced fluorescence changes were concentration-dependent (**Figure 3.4 E, F**). In particular, pnRFP was quite sensitive to peroxynitrite, and the response was saturated by ~5 μM peroxynitrite. A linear response was observed in the low micromolar concentration range (< 5 μM) with a limit of detection (LOD) of ~225 nM. The linear response range of pnRFP for SIN-1 was in the low millimolar range (< 2 mM). Collectively, the results suggest that pnRFP is a specific and sensitive red fluorescent peroxynitrite sensor.

3.4.3 Use of pnRFP to Image Peroxynitrite in Live Mammalian Cells

To examine whether pnRFP could image peroxynitrite in mammalian cells, we co-transfected human embryonic kidney (HEK) 293T cells with our constructed mammalian expression plasmid pMAH-pnRFP (**Figure 3.6A**), in addition to pMAH-POLY-eRF1(E55D) which expresses an orthogonal tRNA and aminoacyl-tRNA synthetase pair and a translation

release factor mutant for efficient genetic encoding of *p*BoF in mammalian cells (**Figure 3.6B**).[25, 27]

Cells were treated with the peroxynitrite donor SIN-1, and the fluorescence of pnRFP-expressing cells decreased as peroxynitrite was generated, causing a 22% ($\Delta F/F_0$) fluorescence decay within the monitoring period (**Figure 3.7A-C**). pnRFP-B30Y, whose fluorescence is insensitive to peroxynitrite, was expressed as a negative control. HEK 293T cells expressing pnRFP-B30Y showed negligible fluorescence changes under the SIN-1 treatment. Next, we expressed pnRFP in mouse RAW 264.7 macrophage cells. A plasmid (pAcBAC3-POLY-pnRFP, **Figure 3.6C**) containing the genes for pnRFP, the engineered aminoacyl-tRNA synthetase, and 20 copies of the amber suppression tRNA was used to boost protein expression.[35] After transfection and pnRFP expression, RAW 264.7 cells were pre-treated with lipopolysaccharide (LPS) and interferon-γ (IFN-γ) to induce the expression of nitric oxide synthase. Next, phorbol 12-myristate 13-acetate (PMA) was added to activate NADPH oxidase, and cells were imaged simultaneously. We observed a 20% ($\Delta F/F_0$) fluorescence turn-off response in these activated pnRFP-expressing cells, while cells expressing the negative control, pnRFP-B30Y, showed no obvious fluorescence change (**Figure 3.7D-F**). Collectively, these results confirm that pnRFP is a reliable biosensor for monitoring chemically induced and physiologically relevant peroxynitrite generation in live mammalian cells.

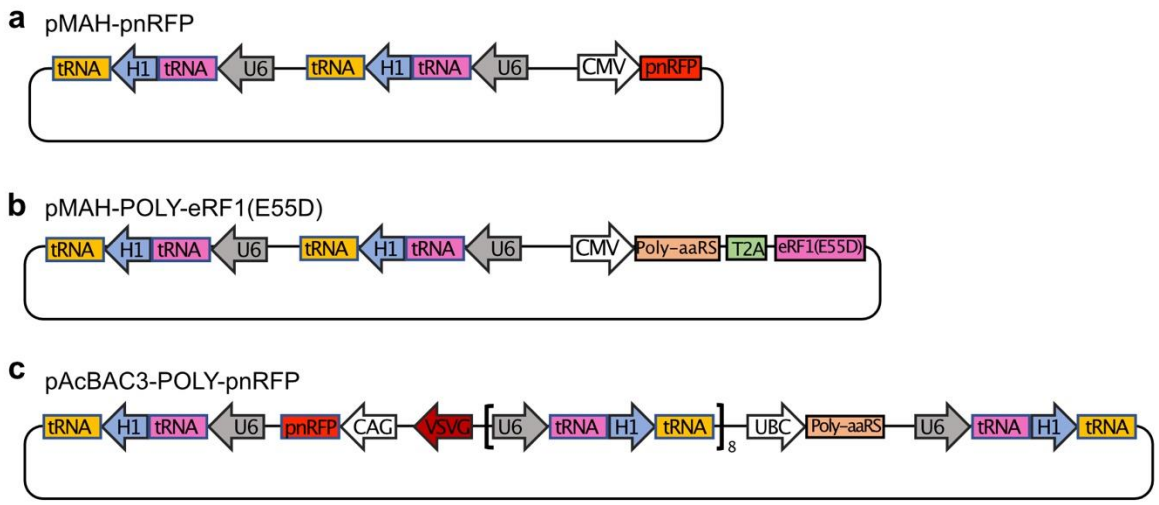

Figure 3.6 Illustration of main genetic elements of the indicated plasmids.

(A) Plasmid maps for pMAH-pnRFP (**a**), pMAH-POLY-eRF1(E55D) (**B**), and pAcBAC3-POLY-pnRFP (**C**). H1 and U6 are promoters to drive the expression of the amber suppression tRNAs. CMV, CAG and UBC are promoters to drive the expression of the orthogonal aminoacyl-tRNA synthetase (Poly-aaRS), the pnRFP sensor, or a release factor mutant (eRF1(E55D)) that competes with endogenous eRF1 to reduce amber codon termination. pAcBAC3 was initially designed for packing baculovirus, but this study uses it as a plasmid vector for transient transfection.

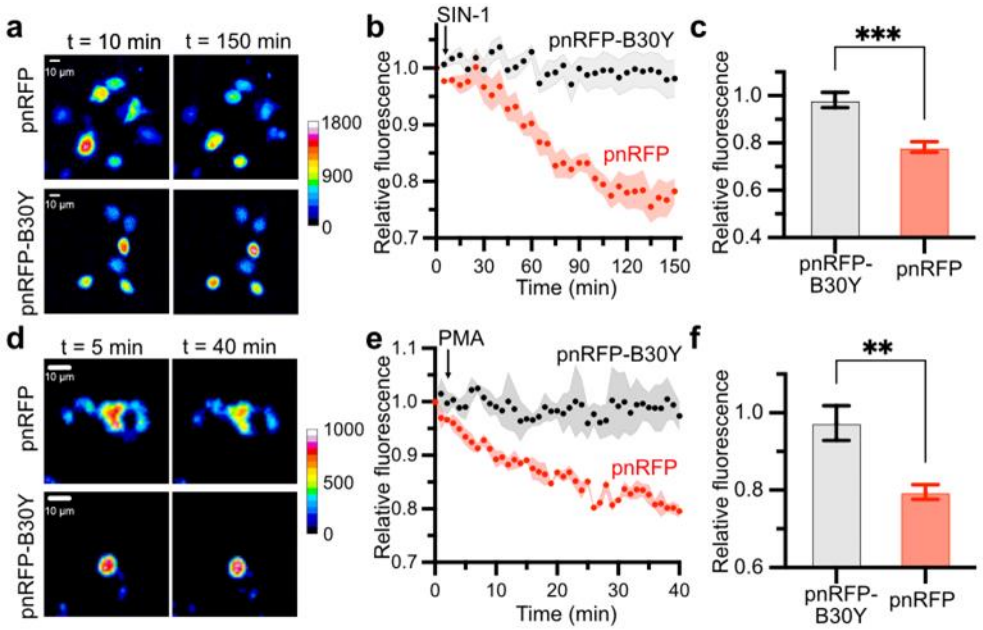

Figure 3.7 Imaging peroxynitrite in mammalian cells using pnRFP

(**A**) Representative pseudocolored fluorescence images of pnRFP- or pnRFP-B30Y-expressing HEK 293T cells in response to SIN-1 (1 mM). Images were taken at 10 and 150 min. Scale bar, 10 μm. (**B**) Time-lapse quantitation of fluorescence changes of HEK 293T cells expressing either pnRFP (red) or pnRFP-B30Y (black) in response to SIN-1. Intensities were normalized to the fluorescence signal of each cell at $t = 0$ min. The arrow indicates the time point for SIN-1 addition. (**C**) Comparison of total intensity changes for HEK 293T cells expressing pnRFP (red) or pnRFP-B30Y (black). Data represent mean ± s.e.m. of nine cells from three technical repeats in each group (***$P < 0.001$, unpaired two-tailed *t*-test). (**D**) Representative pseudocolored fluorescence images of pnRFP- or pnRFP-B30Y-expressing RAW 264.7 cells in response to PMA (100 nM/mL). Images were taken at 5- and 40-min. Scale bar, 10 μm. (**E**) Time-lapse quantitation of fluorescence changes of RAW 264.7 cells expressing either pnRFP (red) or pnRFP-B30Y (black) in response to treatment of PMA followed 15 h incubation in LPS/IFN γ. Intensities were normalized to the fluorescence signal of each cell at $t = 0$ min. The arrow indicates the time point for PMA addition. (**F**) Comparison of total intensity changes for RAW 264.7 cells expressing pnRFP (red) or pnRFP-B30Y (black). Data represent mean ± s.e.m. of three cells from three technical repeats (**$P < 0.01$, unpaired two-tailed *t*-test).

3.4.4 Structural and Mechanistic Analysis

To gain more insights into the sensing mechanism of pnRFP, we obtained the monomeric crystal structure of pnRFP (**PDB 7LQO**) to a 2.10-Å resolution through X-ray crystallography (**Table 3.1**). The structure displayed the typical architecture of an FP, in which a chromophore was surrounded by an 11-β-strand barrel (**Figure 3.8A**). In the crystal structure, the chromophore (denoted as NRQ176) formed from M175, Y176, and G177 (**Figure 3.2**) perfectly fitted in the 2Fo-Fc electron density map, indicating a clear *cis* conformation (**Figure 3.9**). Its approximately planar conformation was stabilized by the joint effects of hydrogen bonds and hydrophobic interactions (**Figure 3.8B**). Two carbonyl oxygen atoms on the backbone and the imidazole ring of NRQ176 contacted with Q173, K179, R204, Q218, and S220 via direct or water-mediated hydrogen bonds. In the meantime, other surrounding residues, including *p*BoF30, hydrophobically interacted with NRQ176.

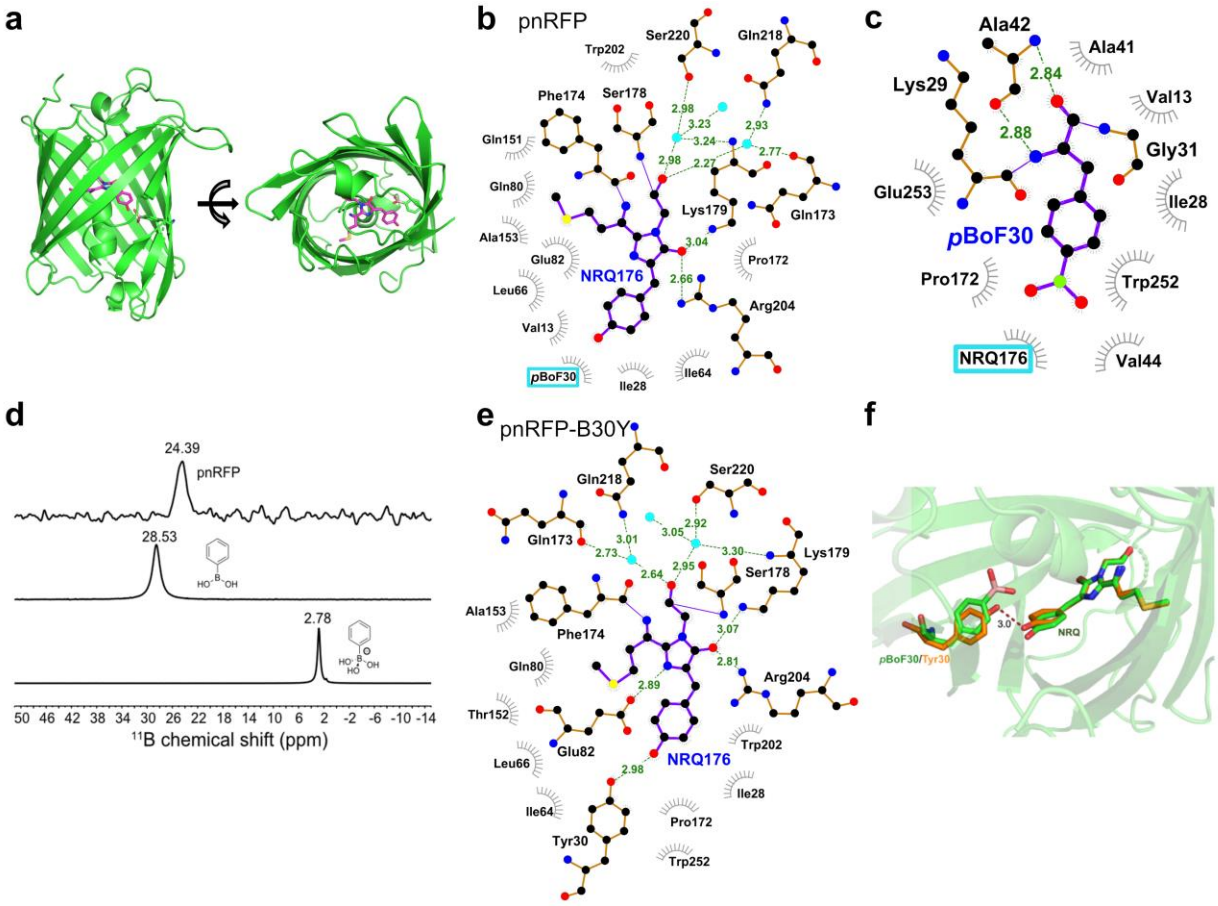

Figure 3.8 Structural analysis of pnRFP.

(**A**) Side (left) and top (right) views of the X-ray crystal structure of pnRFP at a 2.10 Å resolution (**PDB 7LQO**). (**B**) Interactions of the chromophore (NRQ176, purple) of pnRFP with surrounding residues through hydrogen bonds (green dash lines) and hydrophobic effects (red scattered lines). The conformation of the phenolic ring of the chromophore is stabilized by hydrophobic interactions with the surrounding residues, including *p*BoF30. (**C**) Interactions of *p*BoF30 in pnRFP with surrounding residues through hydrogen bonds (green dash lines) and hydrophobic effects (red scattered lines). (**D**) ^{11}B-NMR spectra (from top to bottom: pnRFP, phenylboronic acid, and phenylboronic acid in 1 M NaOH), confirming an sp^2-hybridized boron atom in pnRFP. (**E**) Interactions of the chromophore (NRQ176, purple) of the pnRFP-B30Y mutant (1.95 Å resolution, PDB ID 7LUG) with the surrounding residues, showing new hydrogen bonds including one between the phenolic ring of the chromophore and Tyr30. (**F**) Overlay of the structures of pnRFP (green) and the pnRFP-B30Y mutant (orange), highlighting out-of-plane distortion of the chromophore in pnRFP-B30Y.

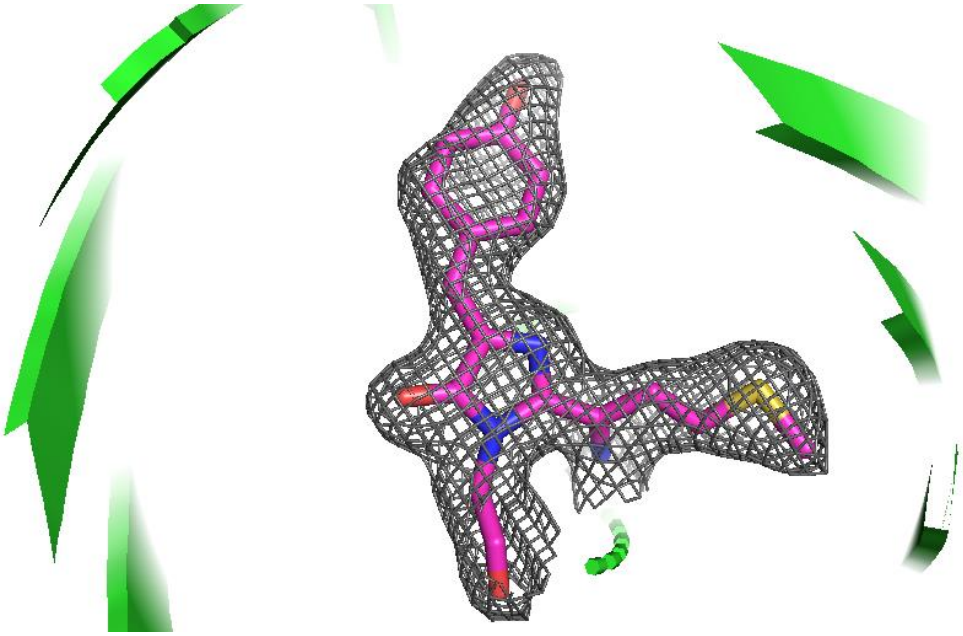

Figure 3.9 Fitting of the chromophore of pnRFP in the 2Fo-Fc electron density map at 1.0σ.

The chromophore adopts a clear *cis* conformation.

Table 3.1 X-ray crystallography data collection and structure refinement statistics.

	pnRFP PDB 7LQO	pnRFP-B30Y PDB 7LUG
Data collection		
Space group	C121	C121
Unit cell dimensions		
a, b, c (Å)	84.20, 34.57, 88.81	84.28, 34.11, 89.22
A, β, γ (°)	90.00, 110.90, 90.00	90.00, 110.79, 90.00
Resolution range (Å)	41.81 - 2.10 (2.16 - 2.10)	41.85 - 1.95 (2.00 - 1.95)
Total reflections	50624 (2135)	62455 (4587)
Unique reflections	13553 (831)	17539 (1245)
Completeness (%)	94.9 (70.3)	99.2 (99.5)
I/δ (I)	13.3 (1.78)	10.8 (2.57)
R_{merge} (%)	0.052 (0.433)	0.058 (0.445)
CC(1/2)	0.998 (0.805)	0.998 (0.814)
Refinement		
Resolution range (Å)	41.81 – 2.10	41.85 – 1.95
No. of Reflections	12873	16652
No. of non-hydrogen atoms	1933	1903
No. of waters	51	65
R_{work}/ R_{free}	0.188/0.254	0.189/0.212
RMS bond length (Å)	0.0080	0.0050
RMS bond angles (°)	1.571	1.531
Average B value ($Å^2$)	38.0	34.0
Ramachandran plot		
Favored (%)	97.79	99.11
Allowed (%)	2.21	0.89
Outliers (%)	0.00	0.00

The conformation of *p*BoF30 was described by the 2Fo-Fc electron density map at 1.0 σ (**Figure 3.10A**). To further confirm the conformation of the dihydroxyl boron portion, we replaced *p*BoF with Phe in the model by Coot[44] and recalculated electron density maps by Refmac5.[45] The positive Fo-Fc difference density appeared in the map (shown as an orange meshed bubble in **Figure 3.10B**), suggesting that we initially assigned the correct pose to *p*BoF30. The boron atom in pnRFP seemed to be sp^2-hybridized, and the backbone of *p*BoF30 was stabilized through hydrogen bonding to A42, while the conformation of the benzene ring and the slightly twisted boronic acid head appeared to be an outcome of the hydrophobic interaction with the chromophore (NRQ176) and other residues (**Figure 3.8C**).

We further performed ^{11}B-NMR spectroscopy to confirm that the sp^2-hybridized boron in pnRFP was not an artifact caused by crystallization. The recorded spectrum of the purified pnRFP protein displayed a single peak at 24.39 ppm (**Figure 3.8D**). We also recorded the ^{11}B-NMR spectra of phenylboronic acid and phenylboronic acid in 1 M NaOH. A single sharp peak of sp^2-hybridized boron (free phenylboronic acid) was observed at 28.53 ppm, while sp^3-hybridized boron (phenyl boronate anion) showed a peak at 2.78 ppm. Thus, the ^{11}B-NMR spectra also support that the boron atom in pnRFP is sp^2-hybridized, corroborating the X-ray crystallography result.

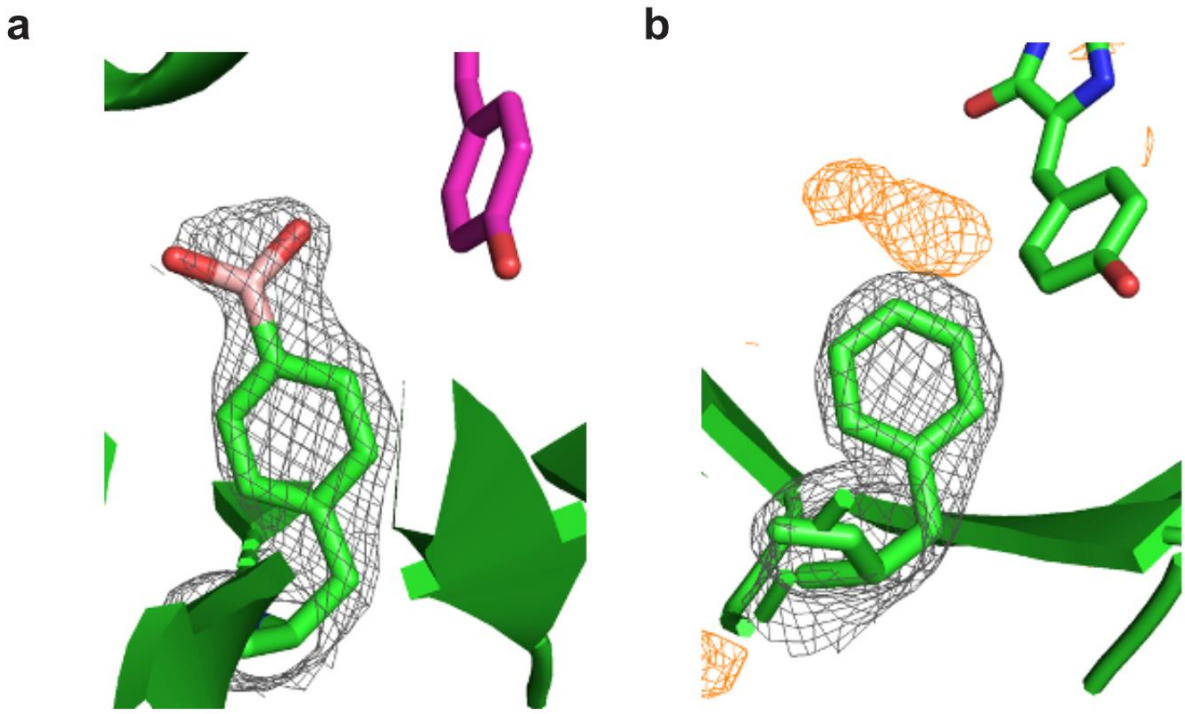

Figure 3.10 Conformation analysis of *p*BoF30 in pnRFP

(**A**) The 2Fo-Fc electron density map (grey mesh) well describes *p*BoF30 at 1.0 σ. (**B**) After substituting *p*BoF with Phe, a positive Fo-Fc difference electron density map (orange) was shown on the top of Phe at 3.0 σ, demonstrating a missing portion of the residue.

Next, we crystalized pnRFP-B30Y (*a.k.a*. ecpApple-K30Y; see **Figure 3.2**), which is the expected major oxidation product of pnRFP. The crystallization condition was identical to that used for pnRFP. The structure of pnRFP-B30Y, which was refined to a 1.95-Å resolution (**PDB 7LUG**), could superimpose on pnRFP with a 0.75 Å RMSD across Ca carbon atoms, showing a high degree of conformational similarity between the two proteins. In pnRFP-B30Y, two carbonyl oxygen atoms of the chromophore (NRQ176) connected to the surrounding residues through an almost identical hydrogen bonding network (**Figure 3.8E**). Meanwhile, two additional hydrogen bonds were formed between Y30 and the oxygen on the phenolic ring of the chromophore, and between Q82 and a nitrogen atom on the imidazole ring of the chromophore (**Figure 3.8E**). Three hydrogen bonds on the imidazole ring could limit the dynamics of the chromophore in space, while the phenolic rings of Y30 and the chromophore shifted closer to each other due to the new hydrogen bond between them. The combined forces disfavored the maintenance of the co-planar conformation of the chromophore. Subsequently, the bending of the chromophore (**Figure 3.8F**) reduced the conjugation effect through the π system, thereby leading to the diminished fluorescence of pnRFP-B30Y compared to pnRFP. Together, the structural results explain how peroxynitrite turns off the fluorescence of pnRFP.

Finally, we built a homology model for ecpApple-S14B, which was responsive to both peroxynitrite and hydrogen peroxide (**Figure 3.5**). We used the pnRFP structure (**PDB 7LQO**) as the scaffold and substituted *p*BoF30 with K with an extended side-chain conformation toward the phenolic ring of the chromophore. We also substituted S14 with *p*BoF in Coot[44] with the side chain buried in the β-barrel. Next, the model was then subjected to a 131-ns length molecular dynamics (MD) simulation with the AMBER14 force field in YASARA (**Figure 3.11**).[47, 52] The average model indicated the dominant conformations of residues during the simulation, so we used it for

further analysis. In this model (**Figure 3.12**), ecpApple-S14B well maintained a typical β-barrel structure resembling other FPs. Also, *p*BoF14 π-stacks with the phenolic ring of the chromophore, and K30 interacts with the backbone of *p*BoF14 through a hydrogen bond. E82 further interacts with the hydroxyl group of *p*BoF14 through hydrogen bonding. Compared with *p*BoF30 in pnRFP (**Figure 3.8C**), the boronic acid-head group of *p*BoF14 in ecpApple-S14B stays in a more hydrophilic pocket (**Figure 3.12** and **Figure 3.13**), which favors the polarization of the group. Moreover, the negative charge carried by E82 drives electrons to move from *p*BoF14 to E82 through the hydrogen bond. We further used the AM1 semi-empirical method in YASARA to assign charges to the boron atoms, and the charges of the boron atoms in pnRFP and ecpApple-S14B were +0.3562 and +0.4998, respectively, supporting that that boron in pnRFP is less positively charged. Since the oxidation of phenylboronic acid started with the nucleophilic attack by anionic species (*e.g.*, $ONOO^-$ or HOO^-),[26] the result is aligned with the observed, much-reduced reactivity of pnRFP, compared to ecpApple-S14B, with HOO^-. Meanwhile, because $ONOO^-$ is more electronegative than HOO^-, $ONOO^-$ can still retain good reactivity with pnRFP. Overall, the modeling results further confirm that protein scaffolds can offer unique local environments to modulate the reactivity of boronic acid.

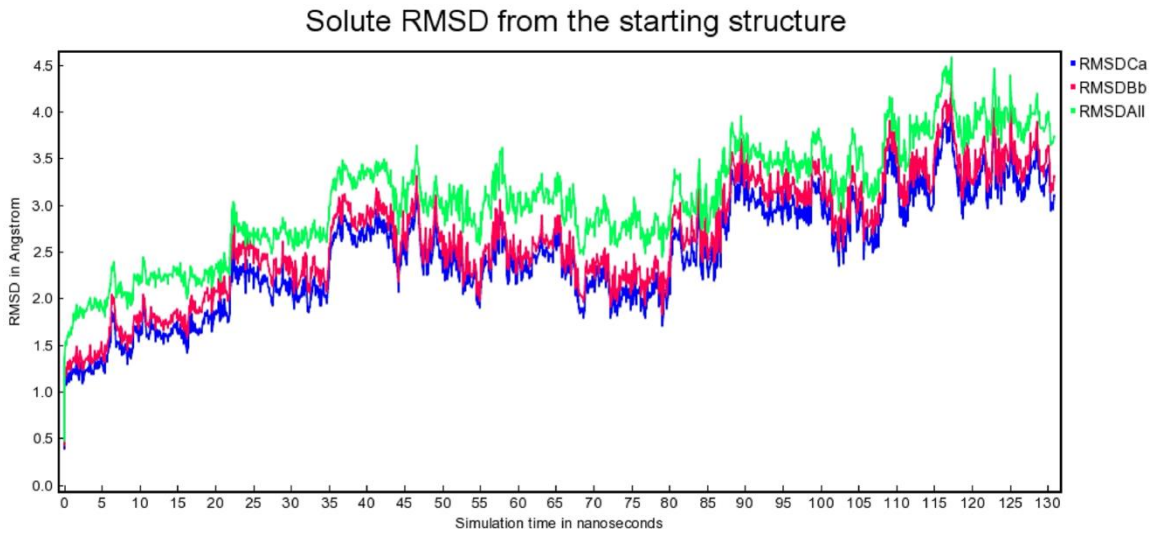

Figure 3.11 MD simulation trajectory of ecpApple-S14B under the AMBER14 force field in YASARA.

The trajectory indicates that the simulated model was in the equilibrium state.

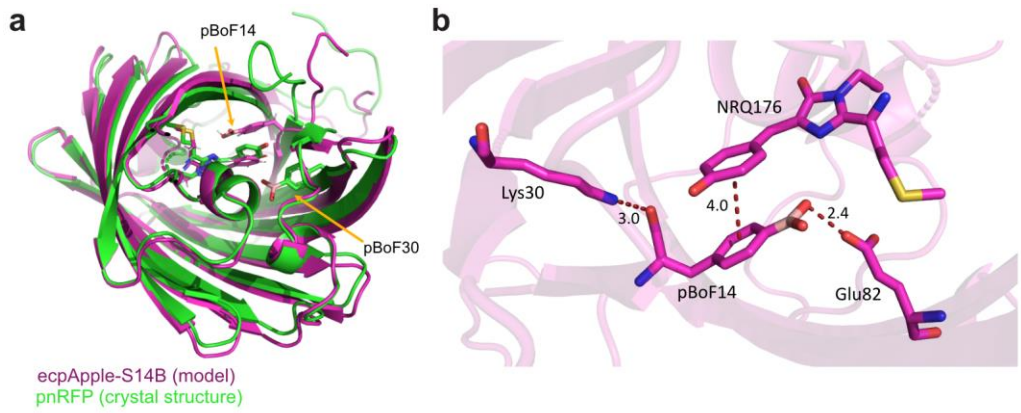

Figure 3.12 Computational modeling of ecpApple-S14B.

(**A**) Overlay of the pnRFP crystal structure (green) and the model structure of ecpApple-S14B (magenta), highlighting the locations of *p*BoF30 and *p*BoF14 in relation to the chromophores. (**B**) Model structure of ecpApple-S14B, highlighting interactions (hydrogen bonds and π-π stacking) with *p*BoF14.

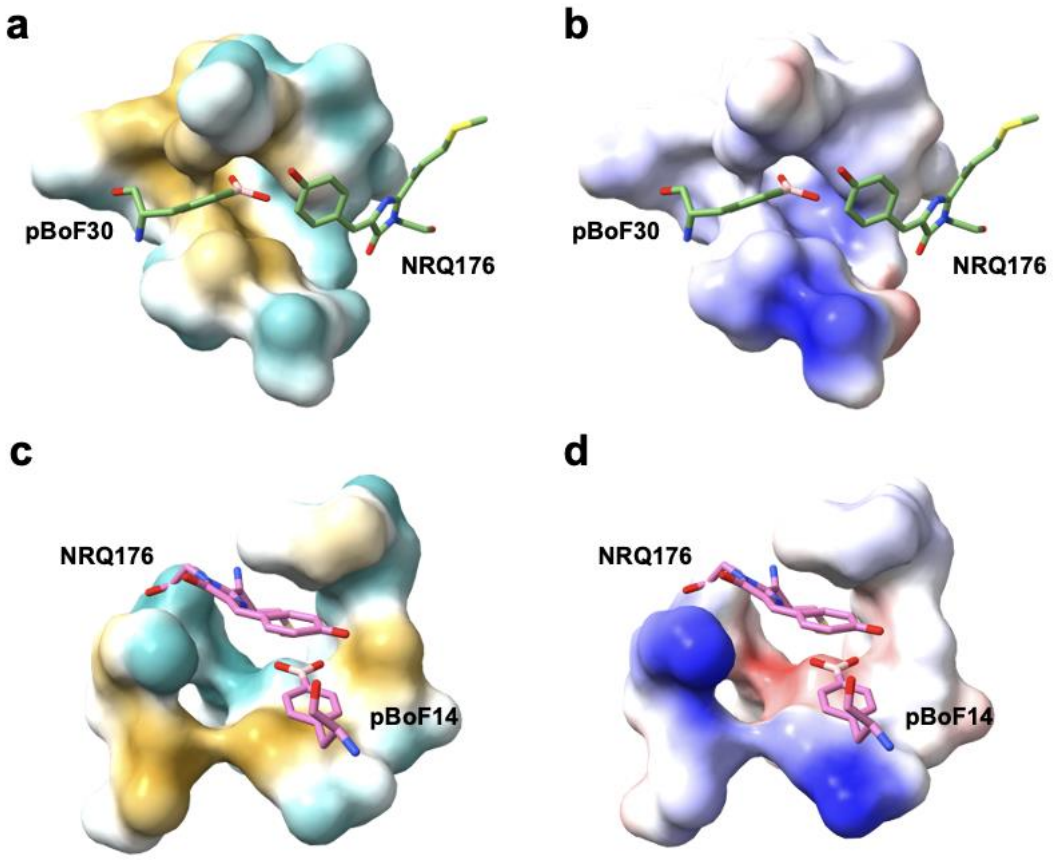

Figure 3.13 Hydrophobicity and electrostatic potentials of residues surrounding *p*BoF in pnRFP (A, B) and ecpApple-S14B (C, D).

In panels a and c, hydrophobicity surface was mapped according to the hydrophobicity scale of Kyte and Doolittle[53] and colored from cyan for the most hydrophilic, to white, to deep sand for the most hydrophobic. In panels b and d, electrostatic potentials of the surrounding residues were calculated by Coulomb's law[54], and the surface was colored with the calculated values from blue for the most positive potential, to white, to red for the most negative potential. Compared with *p*BoF30 in pnRFP, the boronic acid-head group of *p*BoF14 in ecpApple-S14B is in a more hydrophilic and more negatively charged environment. The surface coloring and visualization of the models were achieved with ChimeraX[55].

3.5 Discussion

Starting from a cpRFP mutant, we developed a genetically encoded red fluorescent peroxynitrite biosensor (pnRFP) by site-specifically introducing a boronic acid-containing ncAA into a residue close to the chromophore. This effort expands not only the color of genetically

encoded peroxynitrite biosensors from green to red but also how ncAA-base FP biosensors could be designed. In addition to directly using ncAAs to modify the chromophores of FPs [33, 56-58], modifying chromophore-surrounding residues with ncAAs has now proven to be another viable strategy for developing ncAA-base FP biosensors.

pnRFP were discovered from site-directed mutagenesis of a cpRFP mutant derived from the Ca^{2+} sensor, R-GECO1.[34] We introduced *p*BoF to several residues around the chromophore and gained responsive mutants at two locations (residues 14 and 30). This observation is not surprising, since these two residues have strong effects on the fluorescence of the chromophore. The crystal structure of R-GECO1 at the Ca^{2+}-bound state was solved previously (**PDB 4I2Y**).[59] The K78 residue of R-GECO1 (equivalent to residue 30 in ecpApple or pnRFP) forms an ionic interaction with the phenolated oxygen of the chromophore, while S62 (equivalent to residue 14 in ecpApple or pnRFP) further stabilizes this interaction via a hydrogen bond (**Figure 3.3B**).

In pnRFP-B30Y, a hydrogen bond is formed between Y30 and the phenolated oxygen of the chromophore. A similar hydrogen bond exists between K78 and the chromophore of R-GECO1 at the Ca^{2+}-bound state. However, the location of Y30 of pnRFP-B30Y has been shifted from that of K78 in R-GECO1 (**Figure 3.14**). The outcome is that K78 helps to maintain a largely co-planar conformation of the chromophore of R-GECO1, while Y30 contributes to bending the chromophore of pnRFP-B30Y. Therefore, R-GECO1 at the Ca^{2+}-bound state is quite fluorescent, while pnRFP-B30Y shows reduced fluorescence.

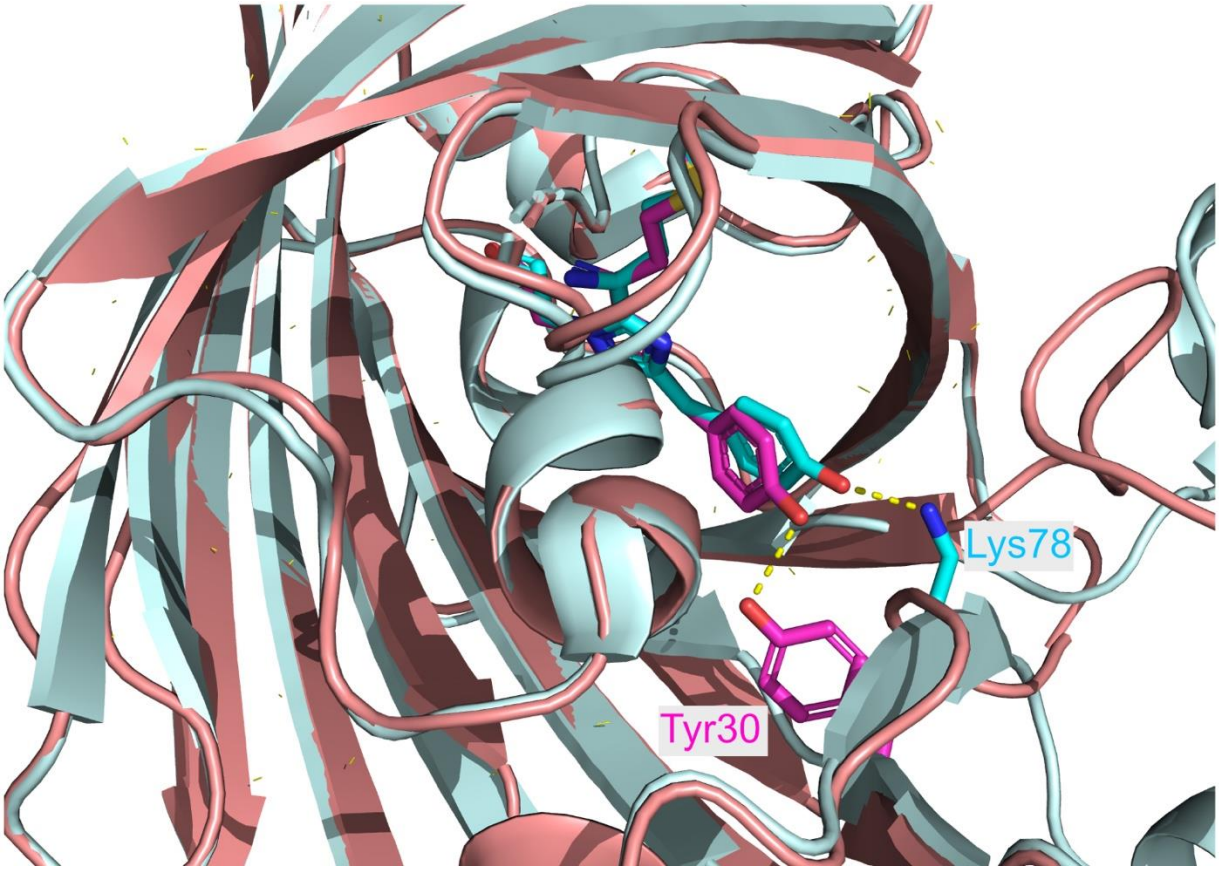

Figure 3.14 Overlay of the crystal structures of R-GECO1 (cyan) and pnRFP-B30Y (pink/magenta).

The locations of Lys78 of R-GECO1 and Tyr30 of pnRFP-B30Y in relation to the chromophores are highlighted.

Normally, arylboronic acid can be oxidized by both hydrogen peroxide and peroxynitrite to generate the phenol product. Previous studies used N-B interactions to generate sp^3-hybridized boron species for enhanced specificity toward peroxynitrite.[19, 25-27] This study derived pnRFP, which still has an sp^2-hybridized boron atom, as confirmed by the X-ray crystal structure and ^{11}B-NMR spectra (**Figure 3.8**). Although further research is still needed to pinpoint the mechanism, our results here indicate that hydrophobicity and hydrogen bonding patterns in the local environment and the charge distribution of the boron atom may be factors contributing to the high specificity of pnRFP. Collectively, pnRFP and ecpApple-S14B, as well as pnGFP and pnGFP-Ultra, offer a series of examples that demonstrate the versatility of using protein scaffolds to tune chemoselectivity.

Peroxynitrite reacts rapidly with carbon dioxide (CO_2) to form nitrosoperoxycarbonate ($ONOOCO_2^-$),[50] which may be a competitive pathway for the reaction between peroxynitrite and the pnRFP sensor. In this study, we imaged live cells in either PBS (which does not contain HCO_3^-) or HBSS (which contains 4 mM HCO_3^-) and observed peroxynitrite-induced fluorescence changes of pnRFP. These results are consistent with a previous study on the reaction between peroxynitrite and a synthetic boronate,[51] indicating that while CO_2 or HCO_3^- may negatively affect the response of the pnRFP sensor, the boronic acid-containing sensor still displays adequate reactivity to detect peroxynitrite even in the presence of millimolar HCO_3^-.

This study has several limitations regarding its methodology and results. First, predicting the outcome of replacing residues near the chromophore is a challenging task. Several ecpApple mutants tested in this study, except for pnRFP and ecpApple-S14B, were found to be nonresponsive. Furthermore, ecpApple-S14B exhibited turn-on responses to both peroxynitrite and hydrogen peroxide, while pnRFP showed a specific turn-off response to peroxynitrite. These

results could not be rationally predicted beforehand. It is also worth noting that pnRFP is a turn-off sensor, which makes it more susceptible to artifacts than fluorescence turn-on sensors. We recommend future users to carefully control the photobleaching factor and use the negative control (pnRFP-B30Y) in parallel.

In summary, we have developed a genetically encoded red fluorescent peroxynitrite biosensor and characterized it *in vitro* and for imaging chemically induced and physiologically relevant peroxynitrite generation in live mammalian cells. We further used structural, biophysical, and computational methods to study the response mechanism of this new sensor. Our results may provide inspiration to further biosensor development and the turning of chemoreactivity.

Table 3.2 The sequences of oligos used in this work.

Oligo Name	Sequence (5′→3′)
cpRFP_F	GGAATTAACCATGGGCTCGAGAATAGGTCGGCTGGGCTCA
cpRFP_R	TCCGCCAAAACAGCCAAGCTTAATGATGGTGGTGATGGTG
ecpApple-S14TAG-F	ATAGGTCGGCTGGGCTCACCCGTAGTTTAGGAGCGGATGT ACCCCGAGG
ecpApple-I28TAG-F	GCGAGTAGAAGAAGGGGCTGAGGCTGAA
ecpApple-I28TAG-R	CAGCCCCTTCTTCTACTCGCTCTTCAG
ecpApple-K30TAG-F	GCGAGATCAAGTAGGGGCTGAGGCTGAA
ecpApple-K30TAG-R	CAGCCCCTACTTGATCTCGCTCTTCA
ecpApple-Y48TAG-F	CCTAGAAGGCCAAGAAGCCCGTGCAGCTGCCCGGC
ecpApple-Y48TAG-R	GGGCTTCTTGGCCTTCTAGGTGGTCTTGAC
ecpApple-L66TAG-F	ATCAAGTAGGACATCGTGTCCCACAAC
ecpApple-L66TAG-R	GTGGGACACGATGTCCTACTTGATGTCGACGATGTA
ecpApple-Y176TAG-F	TCCCCTCAGTTCATGTAGGGCTCCAAGGCCTACATT
ecpApple-Y176TAG-R	GGAGCCCTACATGAACTGAGGGGACAGGATGTC
pnRFP_F	CCAGGTCCAACTGCACGGAAGCTTGCCACCATGGATAGGT CGGCTGGGCTC
pnRFP_R	TCAGCGGGTTTAAACGGGCCCTTAATGATGGTGGTGATGG TGTTGGTCACGCGTAGCC
pBac3-F	GGAGGCCACCATGGGCTCGAGAATAGGTCGGCTGGGCTC A
pBac3-R	TCGACTTAACGCGTTGAATTCATGCATTTAATGATGGTGGT

3.6 References

1. Radi, R., Peroxynitrite, a stealthy biological oxidant. *J. Biol. Chem.* 2013, *288* (37), 26464-26472.
2. Beckman, J. S.; Koppenol, W. H., Nitric oxide, superoxide, and peroxynitrite: The good, the bad, and the ugly. *American Journal of Physiology-Cell Physiology* **1996,** *271* (5), C1424-C1437.
3. Szabó, C.; Ischiropoulos, H.; Radi, R., Peroxynitrite: biochemistry, pathophysiology and development of therapeutics. *Nature reviews Drug discovery* **2007,** *6* (8), 662-680.
4. Beckman, J. S.; Beckman, T. W.; Chen, J.; Marshall, P. A.; Freeman, B. A., Apparent hydroxyl radical production by peroxynitrite: implications for endothelial injury from nitric oxide and superoxide. *Proc. Natl. Acad. Sci. U. S. A.* **1990,** *87* (4), 1620-4.
5. Radi, R., Protein tyrosine nitration: biochemical mechanisms and structural basis of functional effects. *Acc. Chem. Res.* **2013,** *46* (2), 550-559.
6. Alvarez, B.; Ferrer-Sueta, G.; Freeman, B. A.; Radi, R., Kinetics of peroxynitrite reaction with amino acids and human serum albumin. *J. Biol. Chem.* **1999,** *274* (2), 842-848.
7. Rubbo, H.; Radi, R.; Trujillo, M.; Telleri, R.; Kalyanaraman, B.; Barnes, S.; Kirk, M.; Freeman, B. A., Nitric oxide regulation of superoxide and peroxynitrite-dependent lipid peroxidation. Formation of novel nitrogen-containing oxidized lipid derivatives. *J. Biol. Chem.* **1994,** *269* (42), 26066-26075.
8. Kennett, E. C.; Davies, M. J., Glycosaminoglycans are fragmented by hydroxyl, carbonate, and nitrogen dioxide radicals in a site-selective manner: implications for peroxynitrite-mediated damage at sites of inflammation. *Free Radical Biology and Medicine* **2009,** *47* (4), 389-400.
9. Monteiro, H. P.; Arai, R. J.; Travassos, L. R., Protein tyrosine phosphorylation and protein tyrosine nitration in redox signaling. *Antioxid. Redox Signal.* **2008,** *10* (5), 843-890.
10. Félétou, M.; Vanhoutte, P. M., Endothelial dysfunction: a multifaceted disorder (the Wiggers Award Lecture). *American Journal of Physiology-Heart and Circulatory Physiology* **2006,** *291* (3), H985-H1002.
11. Baillet, A.; Chanteperdrix, V.; Trocmé, C.; Casez, P.; Garrel, C.; Besson, G., The role of oxidative stress in amyotrophic lateral sclerosis and Parkinson's disease. *Neurochem. Res.* **2010,** *35* (10), 1530-1537.
12. Pacher, P.; Beckman, J. S.; Liaudet, L., Nitric oxide and peroxynitrite in health and disease. *Physiol. Rev.* **2007,** *87* (1), 315-424.
13. Mallozzi, C.; Di Stasi, M. A.; Minetti, M., Peroxynitrite-dependent activation of src tyrosine kinases lyn and hck in erythrocytes is under mechanistically different pathways of redox control. *Free Radic. Biol. Med.* **2001,** *30* (10), 1108-17.
14. Klotz, L. O.; Schroeder, P.; Sies, H., Peroxynitrite signaling: receptor tyrosine kinases and activation of stress-responsive pathways. *Free Radic. Biol. Med.* **2002,** *33* (6), 737-43.
15. Prolo, C.; Álvarez, M. N.; Radi, R., Peroxynitrite, a potent macrophage-derived oxidizing cytotoxin to combat invading pathogens. *BioFactors* **2014,** *40* (2), 215-225.

16. Marla, S. S.; Lee, J.; Groves, J. T., Peroxynitrite rapidly permeates phospholipid membranes. *Proc. Natl. Acad. Sci. U.S.A.* **1997,** *94* (26), 14243-14248.
17. Chen, X.; Chen, H.; Deng, R.; Shen, J., Pros and cons of current approaches for detecting peroxynitrite and their applications. *Biomed J* **2014,** *37* (3), 120-6.
18. Peng, T.; Wong, N. K.; Chen, X.; Chan, Y. K.; Ho, D. H.; Sun, Z.; Hu, J. J.; Shen, J.; El-Nezami, H.; Yang, D., Molecular imaging of peroxynitrite with HKGreen-4 in live cells and tissues. *J. Am. Chem. Soc.* **2014,** *136* (33), 11728-34.
19. Sun, X.; Xu, Q.; Kim, G.; Flower, S. E.; Lowe, J. P.; Yoon, J.; Fossey, J. S.; Qian, X.; Bull, S. D.; James, T. D., A water-soluble boronate-based fluorescent probe for the selective detection of peroxynitrite and imaging in living cells. *Chemical Science* **2014,** *5* (9), 3368-3373.
20. Chen, Z.; Truong, T. M.; Ai, H. W., Development of Fluorescent Probes for the Detection of Peroxynitrite. In *Peroxynitrite Detection in Biological Media: Challenges and Advances*, 2015; p 186.
21. Ambikapathi, G.; Kempahanumakkagari, S. K.; Lamani, B. R.; Shivanna, D. K.; Maregowda, H. B.; Gupta, A.; Malingappa, P., Bioimaging of Peroxynitrite in MCF-7 Cells by a New Fluorescent Probe Rhodamine B Phenyl Hydrazide. *Journal of Fluorescence* **2013,** *23* (4), 705-712.
22. Zielonka, J.; Sikora, A.; Hardy, M.; Joseph, J.; Dranka, B. P.; Kalyanaraman, B., Boronate probes as diagnostic tools for real time monitoring of peroxynitrite and hydroperoxides. *Chem. Res. Toxicol.* **2012,** *25* (9), 1793-9.
23. Lippert, A. R.; De Bittner, G. C. V.; Chang, C. J., Boronate Oxidation as a Bioorthogonal Reaction Approach for Studying the Chemistry of Hydrogen Peroxide in Living Systems. *Acc. Chem. Res.* **2011,** *44* (9), 793-804.
24. Wang, F.; Niu, W.; Guo, J. T.; Schultz, P. G., Unnatural Amino Acid Mutagenesis of Fluorescent Proteins. *Angew Chem Int Edit* **2012,** *51* (40), 10132-10135.
25. Chen, Z. J.; Ren, W.; Wright, Q. E.; Ai, H. W., Genetically encoded fluorescent probe for the selective detection of peroxynitrite. *J. Am. Chem. Soc.* **2013,** *135* (40), 14940-3.
26. Chen, Z. J.; Tian, Z.; Kallio, K.; Oleson, A. L.; Ji, A.; Borchardt, D.; Jiang, D. E.; Remington, S. J.; Ai, H. W., The N-B Interaction through a Water Bridge: Understanding the Chemoselectivity of a Fluorescent Protein Based Probe for Peroxynitrite. *J. Am. Chem. Soc.* **2016,** *138* (14), 4900-7.
27. Chen, Z.; Zhang, S.; Li, X.; Ai, H. W., A high-performance genetically encoded fluorescent biosensor for imaging physiological peroxynitrite. *Cell Chem Biol* **2021,** *28* (11), 1542-1553.
28. Liu, C. C.; Schultz, P. G., Adding new chemistries to the genetic code. *Annu Rev Biochem* **2010,** *79*, 413-44.
29. Diercks, C. S.; Dik, D. A.; Schultz, P. G., Adding new chemistries to the central dogma of molecular biology. *Chem* **2021,** *7* (11), 2883-2895.
30. Chin, J. W., Expanding and reprogramming the genetic code. *Nature* **2017,** *550* (7674), 53-60.
31. Shandell, M. A.; Tan, Z.; Cornish, V. W., Genetic Code Expansion: A Brief History and Perspective. *Biochemistry* **2021,** *60* (46), 3455-3469.
32. Schultz, P., Expanding the genetic code. *Protein Sci.* **2023,** *32* (1), e4488.

33. Chen, S.; Chen, Z. J.; Ren, W.; Ai, H. W., Reaction-based genetically encoded fluorescent hydrogen sulfide sensors. *J. Am. Chem. Soc.* **2012,** *134* (23), 9589-92.
34. Zhao, Y.; Araki, S.; Wu, J.; Teramoto, T.; Chang, Y. F.; Nakano, M.; Abdelfattah, A. S.; Fujiwara, M.; Ishihara, T.; Nagai, T.; Campbell, R. E., An expanded palette of genetically encoded Ca^{2+} indicators. *Science* **2011,** *333* (6051), 1888-91.
35. Zheng, Y.; Lewis, T. L., Jr.; Igo, P.; Polleux, F.; Chatterjee, A., Virus-Enabled Optimization and Delivery of the Genetic Machinery for Efficient Unnatural Amino Acid Mutagenesis in Mammalian Cells and Tissues. *ACS Synth Biol* **2017,** *6* (1), 13-18.
36. Zhang, J.; Li, Z.; Pang, Y.; Fan, Y.; Ai, H. W., Genetically Encoded Boronolectin as a Specific Red Fluorescent UDP-GlcNAc Sensor. *bioRxiv* **2023**, DOI: 10.1101/2023.03.01.530644.
37. Young, T. S.; Ahmad, I.; Yin, J. A.; Schultz, P. G., An enhanced system for unnatural amino acid mutagenesis in E. coli. *J. Mol. Biol.* **2010,** *395* (2), 361-74.
38. Brustad, E.; Bushey, M. L.; Lee, J. W.; Groff, D.; Liu, W.; Schultz, P. G., A genetically encoded boronate-containing amino acid. *Angew. Chem. Int. Ed. Engl.* **2008,** *47* (43), 8220-3.
39. Kabsch, W., Xds. *Acta Crystallogr. Sect. D. Biol. Crystallogr.* **2010,** *66* (2), 125-132.
40. Evans, P. R., An introduction to data reduction: space-group determination, scaling and intensity statistics. *Acta Crystallogr. D Biol. Crystallogr.* **2011,** *67* (Pt 4), 282-92.
41. Evans, P. R.; Murshudov, G. N., How good are my data and what is the resolution? *Acta Crystallogr. D Biol. Crystallogr.* **2013,** *69* (Pt 7), 1204-14.
42. French, S.; Wilson, K., On the treatment of negative intensity observations. *Acta Crystallographica Section A: Crystal Physics, Diffraction, Theoretical and General Crystallography* **1978,** *34* (4), 517-525.
43. McCoy, A. J.; Grosse-Kunstleve, R. W.; Adams, P. D.; Winn, M. D.; Storoni, L. C.; Read, R. J., Phaser crystallographic software. *J. Appl. Crystallogr.* **2007,** *40* (4), 658-674.
44. Emsley, P.; Cowtan, K., Coot: model-building tools for molecular graphics. *Acta Crystallogr. Sect. D. Biol. Crystallogr.* **2004,** *60* (12), 2126-2132.
45. Murshudov, G. N.; Skubák, P.; Lebedev, A. A.; Pannu, N. S.; Steiner, R. A.; Nicholls, R. A.; Winn, M. D.; Long, F.; Vagin, A. A., REFMAC5 for the refinement of macromolecular crystal structures. *Acta Crystallogr. Sect. D. Biol. Crystallogr.* **2011,** *67* (4), 355-367.
46. Laskowski, R. A.; Swindells, M. B., LigPlot+: multiple ligand-protein interaction diagrams for drug discovery. *J. Chem. Inf. Model.* **2011,** *51* (10), 2778-86.
47. Krieger, E.; Koraimann, G.; Vriend, G., Increasing the precision of comparative models with YASARA NOVA—a self-parameterizing force field. *Proteins: Structure, Function, and Bioinformatics* **2002,** *47* (3), 393-402.
48. Dewar, M. J. S.; Zoebisch, E. G.; Healy, E. F.; Stewart, J. J. P., Development and use of quantum mechanical molecular models. 76. AM1: a new general purpose quantum mechanical molecular model. *J. Am. Chem. Soc.* **1985,** *107* (13), 3902-3909.
49. Fan, Y.; Chen, Z.; Ai, H. W., Monitoring redox dynamics in living cells with a redox-sensitive red fluorescent protein. *Anal. Chem.* **2015,** *87*, 2802-2810.

50. Miyawaki, A.; Shcherbakova, D. M.; Verkhusha, V. V., Red fluorescent proteins: chromophore formation and cellular applications. *Curr. Opin. Struct. Biol.* **2012,** *22* (5), 679-88.
51. Martin-Romero, F. J.; Gutierrez-Martin, Y.; Henao, F.; Gutierrez-Merino, C., Fluorescence measurements of steady state peroxynitrite production upon SIN-1 decomposition: NADH versus dihydrodichlorofluorescein and dihydrorhodamine 123. *J Fluoresc* **2004,** *14* (1), 17-23.
52. Maier, J. A.; Martinez, C.; Kasavajhala, K.; Wickstrom, L.; Hauser, K. E.; Simmerling, C., ff14SB: Improving the Accuracy of Protein Side Chain and Backbone Parameters from ff99SB. *J. Chem. Theory Comput.* **2015,** *11* (8), 3696-713.
53. Kyte, J.; Doolittle, R. F., A simple method for displaying the hydropathic character of a protein. *J. Mol. Biol.* **1982,** *157* (1), 105-132.
54. The detail on Coulomb's law applied in the calculation is presented on the following website: https://www.cgl.ucsf.edu/chimera/data/downloads/1.8/docs/ContributedSoftware/coulombic/coulombic.html.
55. Pettersen, E. F.; Goddard, T. D.; Huang, C. C.; Meng, E. C.; Couch, G. S.; Croll, T. I.; Morris, J. H.; Ferrin, T. E., UCSF ChimeraX: Structure visualization for researchers, educators, and developers. *Protein Sci.* **2021,** *30* (1), 70-82.
56. Niu, W.; Guo, J., Expanding the chemistry of fluorescent protein biosensors through genetic incorporation of unnatural amino acids. *Mol. Biosyst.* **2013,** *9* (12), 2961-70.
57. Liu, X.; Li, J.; Hu, C.; Zhou, Q.; Zhang, W.; Hu, M.; Zhou, J.; Wang, J., Significant expansion of the fluorescent protein chromophore through the genetic incorporation of a metal-chelating unnatural amino acid. *Angew. Chem. Int. Ed. Engl.* **2013,** *52* (18), 4805-9.
58. Zhang, S.; Ai, H. W., A general strategy to red-shift green fluorescent protein-based biosensors. *Nat. Chem. Biol.* **2020**, DOI: 10.1038/s41589-020-0641-7.
59. Akerboom, J.; Carreras Calderón, N.; Tian, L.; Wabnig, S.; Prigge, M.; Tolö, J.; Gordus, A.; Orger, M. B.; Severi, K. E.; Macklin, J. J., Genetically encoded calcium indicators for multi-color neural activity imaging and combination with optogenetics. *Front. Mol. Neurosci.* **2013,** *6*, 2.
60. Denicola, A.; Freeman, B. A.; Trujillo, M.; Radi, R., Peroxynitrite reaction with carbon dioxide/bicarbonate: kinetics and influence on peroxynitrite-mediated oxidations. *Arch Biochem Biophys* **1996,** *333* (1), 49-58.
61. Sikora, A.; Zielonka, J.; Lopez, M.; Joseph, J.; Kalyanaraman, B., Direct oxidation of boronates by peroxynitrite: mechanism and implications in fluorescence imaging of peroxynitrite. *Free Radic. Biol. Med.* **2009,** *47* (10), 1401-7.

Chapter 4 SHRIMP: A Circularly Permutated mScarlet-based Genetically Encoded Hydrogen Peroxide Red Fluorescent Indicator with High Brightness and Minimal Photoactivation

The work described in this chapter includes collaborative efforts from Yiyu Zhang and Jing Zhang. Author contributions are Yu Pang engineered cpmScarlet and SHRIMP biosensor, performed in-vitro characterizations, mammalian cell response in HEK 293T, RAW 264.7, initial photophysical property experiments, islet STZ stimulation and two-color cell imaging. Yiyu Zhang and Yu Pang performed islet STZ stimulation. Jing Zhang provided cell culture for experiments and imaged the two-color co-expression of Gcamp6 and SHRIMP in HEK 293T cells.

4.1 Abstract

Hydrogen peroxide (H_2O_2) is involved in not only the modulation of redox signaling but also the regulation of other physiological behaviors and it is closely related with the onset and progression of many diseases. Genetically encoded redox indicators (GERIs) based on single fluorescent protein (FP) are valuable tools for tracking spatiotemporal dynamics of H_2O_2 production and consumption. While most GERIs are based on green fluorescent protein (GFP), which causes higher autofluorescence and increased cytotoxicity, several circularly permutated red FP-based red GERIs have been developed to expand the spectrum to the red section of visible spectrum. Among RFPs, mScarlet-I was reported with fast maturation, great brightness and better photostability. Here, we described the development of the first cpmScarlet-based hydrogen peroxide redox indicator with minimal photoactivation (SHRIMP). SHRIMP showed an excitation and emission peak at 570 nm and 595 nm, respectively, and exhibited maximal 5-fold fluorescence

intensity “turn-off” upon oxidation by H_2O_2. We tested SHRIMP in live-cell imaging with either exogenous addition of H_2O_2 or under physiological stimulation towards macrophage. Besides, SHRIMP presented good brightness and minimal photoactivation, confirming its utility for multi-color imaging. Moreover, SHRIMP displayed good brightness in isolated mouse islets and can respond to chemical-induced H_2O_2 generation. Last, SHRIMP was co-expressed with green calcium indicator in mammalian cells for multiparameter imaging.

4.2 Introduction

Reactive oxygen species (ROS), the potent oxidants with an unpaired electron, have been widely recognized for playing an indispensable role of cellular metabolism. When generated near basal levels, ROS are involved in various metabolic processes, and the overproduction of ROS has been implicated in diseases ranging from cardiovascular diseases to cancer to neurological disorders.[1-4]

Hydrogen peroxide (H_2O_2) is generated from the dismutation of superoxide anion (O_2^-) by superoxide dismutase (SOD).[5] As the most long-lived ROS, it mediates the redox signaling through oxidizing redox sensitive cysteine residues of target protein. Oxidation of thiols leads to formation of disulfide bonds and sulfenic acids, which can subsequently cause the conformational and activity change of the target proteins.[6] Due to its good stability and capability to diffuse within or between cells, H_2O_2 is identified as a second messenger involved in insulin signaling, growth factor-induced signaling cascades and protein kinase regulation.[7-9] It participates in many physiological processes, such as cell differentiation, proliferation and survival. On the other hands, H_2O_2 is also considered as toxic metabolic byproduct since high levels of H_2O_2 can cause cell cycle arrest or even apoptosis.[10] Whether H_2O_2 exerts a beneficial or harmful effects on living system

highly depends on the cellular context, its local concentration and the exposure time.[11, 12] For example, intracellular H_2O_2 concentration increase only ~100 nM during muscle contractions and failure of this redox-mediated adaption contributes to loss of skeletal muscle during aging process.[13] Therefore, it is of great importance to monitor H_2O_2 signals in different cellular compartments under various biological scenarios.

Genetically-encoded FP-based redox indicators (GEFRIs) are indispensable tools that provide chances to monitor the real-time dynamics of redox signaling in diverse biological system.[14] Most GEFRIs are built upon GFP or YFP.[15-21] Both GFP and YFP are short wavelength emitters, which can generate excessive phototoxicity in the biological samples due to the generation of endogenous free radicals.[22] Besides, the short wavelength lasers limit the application for deep tissue imaging and preclude their applicability for multi-color imaging. Therefore, expanding the color palette of GEFRIs is of great importance to overcome these limitations.

The first red fluorescent genetically encoded redox probe, HyperRed[23], is built by fusing H_2O_2 sensory domain OxyR with circularly permutated mApple[24] (cpmApple). Our group previously developed a series of cpmApple-based GEFRIs for monitoring redox status in live cells and different subcellular compartments.[25-28] The red fluorescent protein mRuby2[29] and mCherry[30] have also been used to design redox indicators.[31, 32] All these monomeric RFPs (mRFPs) were adapted from RFP homologs of corals and other *Anthozoa* species, which tend to form obligate tetramers/oligomers.[33] The monomerization of some RFPs lead to the loss of brightness compared to their tetramer ancestors. For example, mRuby2[29] and mCherry[30] exhibited relatively dim fluorescence with quantum yield below 50%. Some indicators based on cpmApple have been reported to present blue-light photoactivation, which may introduce artifacts during long-term

optical imaging.[34] Other drawbacks include incomplete or partial green maturation and a residual tendency to dimerize.[35]

Instead of evolving from tetrameric RFP analogs, the brightest available RFP mScarlet-I was developed from a synthetic gene template based on mCherry and multiple other natural RFPs. It outperforms other RFPs with much greater brightness, favorable maturation rate and good photostability,[36] making it an optimal mRFP for sensor development. With its great brightness, mScarlet has been used as fluorescent reporter, together with CRISPR-Cas9 technology, for developing Zebrafish line (RedEfish)[37] or human induced pluripotent stem cell line (NES-mScarlet hiPSCs).[38] A pH-sensitive red indicator based on wildtype mScarlet-I (pHmScarlet) have been engineered and used to monitor fusion pore formation during exocytosis.[39] A FRET pair of mScarlet-derived GFP (mWatermelon) and mScarlet-I have also been reported. This FRET pair was engineered to different biosensors for the detection of diverse biological signaling.[40] In another work, mScarlet was converted to large Stokes shift FP (LSSmScarlet) and utilized for dual-color two-photon imaging and super-resolution STED imaging in cultured mammalian cells.[41]

In all above-mentioned cases, mScarlet-I has been treated as an individual entity that maintained intact tertiary structure to protect the chromophore. Circular permutation of FPs has markedly expanded the utility of FPs, enabling the development of diverse genetically encoded sensors.[21, 42-44] In a cpFP, the new N- and C- termini are created in proximity to the chromophore while the original termini connected with a linker. Since the chromophore is exposed to the exterior environment, circular permutants are more susceptible to the environment change than the native proteins.[45, 46] One of the typical strategies for designing genetically-encoded redox fluorescent biosensor is to fuse the cpFP with a redox-active sensory domain so that the fluorescence readout

can be modulated through the interaction between redox sensor domain and the corresponding analytes.[28]

In this work, we first engineered a circularly permutated mScarlet-I (cpmScarlet), which maintained its autocatalytic fluorescence with excitation and emission peak at 570 nm and 595 nm. We then fused H_2O_2 regulatory domain OxyR to the N- and C- termini of the cpmScarlet scaffold and optimized the length and composition of the linker connecting the sensory domain and cpmScarlet. Through further random mutagenesis and screening, we identified a circularly permutated mScarlet-based genetically encoded hydrogen peroxide red fluorescent indicator with high brightness and minimal photoactivation (SHRIMP), that exhibited maximal 5-fold fluorescence "turn-off" when fully oxidized compared to the reduced state at pH 7.4. We performed thorough *in-vitro* characterization of SHRIMP and then investigated its photophysical characteristics. SHRIMP has also been expressed in different living mammalian cell lines to monitor real-time H_2O_2 dynamics. In addition, SHRIMP showed good brightness and response in tissue-level samples and great incompatibility with genetically encoded indicator of other colors for multiparameter imaging. To our knowledge, this is the first genetically-encoded redox biosensor based on cpmScarlet.

4.3 Methos and Materials

4.3.1 Library construction and screening of circularly-permutated mScarlet

The fragment 146-232 of cpmScarlet-I was amplified from plasmid pBad-mScarlet-I using Taq DNA Polymerase with cpmScarlet-2NNK-F1 and cpmScarlet-R1 primers. The fragment 1-145 was amplified from plasmid pBad-mScarlet-I using cpmScarlet-F2 and cpmScarlet-NNK-R2 primers. The oligonucleotide primers were designed to add 2 × "NNK" codon to the N-terminus

of fragment 146-232, one 1 × "NNK" codon to the C-terminus of fragment 1-145, and the nucleotides encoding a Gly- and Ser-rich floppy linker between C-terminus of the 146-232 fragment and the N-terminus of 1-145 fragment. Next, two fragments were assembled by overlap polymerase chain reaction (PCR) with cpmScarlet-2NNK-G-F and cpmScarlet-NNK-G-R primers to add Xho I and Hind III restriction sites. The overlap PCR product was then digested with Xho I and Hind III and inserted into a predigested pBAD/HisB vector via ligation. The ligation product was transformed to *E. coli* DH10β cells and the culture was plated on LB agar plates supplemented with 100 mg/mL ampicillin and 0.02% (w/v) L-arabinose. After incubation for 24 hrs at 37°C, colonies were screened for bright red fluorescence under a customized bacterial colony imaging system. The system was composed of a Dolan-Jenner Mi-LED Fiber Optic light source, excitation and emission filters in Thorlabs motorized filter wheels, and a QSI 628 CCD camera. Mutants with relatively high brightness were inoculated in 0.5 mL 2 × YT supplemented with 100 μg/mL ampicillin and 0.02% (w/v) L-arabinose in a 96-well deep-well bacterial culture plate to obtain crude proteins. Cells were grown at 37 °C, 250 rpm until OD_{600} reached 0.8, and then transferred to 16°C, 250 rpm for another 48 h. The 96-well culture plate was then centrifuged at 4150 × g for 15 min and 300 μL of Bacterial Protein Extraction Reagents (B-PER, Pierce) was added to lyse the pellets in each well. The fluorescent intensity of each cell lysate was recorded using a BioTek Synergy Mx Microplate Reader. The mutant with good brightness and corresponding excitation/emission spectrum was confirmed by Sanger sequencing. For comparing the brightness of the cpmScarlet mutant with ecpmApple mutant, each plasmid was transformed to *E. cloni* 10G cells and the culture was plated on 2 × YT agar plates supplemented with 100 mg/mL ampicillin and 0.02% (w/v) L-arabinose at 37 °C for overnight incubation. The colonies were imaged with abovementioned imaging system with excitation 550-30 nm and emission 645-75nm.

4.3.2 Engineering and library screening of SHRIMP

To insert cpmScarlet between two OxyR domains, cpmScarlet was amplified from its corresponding pBAD vector by using oligos OxyR-cpmScarlet-F1 and OxyR-cpmScarlet-R1 (Table S1). These oligos were designed to add 2 × NNK degenerate codon to both N and C-term of cpmScarlet. Two OxyR sensory domains were amplified from pBAD-HyPerRed with oligo pairs OxyR-N-F, OxyR-N-R and OxyR-C-F, OxyR-C-R separately. Amplified cpmScarlet and two OxyR domains were assembled into a compatible pBAD/His B vector by Gibson assembly. The assembly product was transformed into *E. coli* DH10β cells and then plated on LB agar plates supplemented with appropriate antibiotic and 0.02% (w/v) L-arabinose. Bright colonies were selected under abovementioned colony imaging system and inoculated into 500 μL 2 × YT with 100 μg/mL ampicillin in two 96-well deep-well plates. After overnight growth at 37 °C, 250 rpm, 500 uL 2 × YT supplemented with 100 μg/mL ampicillin and 0.4% (w/v) L-arabinose was added to the overnight cell culture. Next, the plates were moved to 16°C with shaking at 250 rpm for 3 days to express the protein. The cell culture was spin down at 4150 × g for 20 min to obtain the cell pellet. To get the bacteria crude lysates, 300 μL of Bacterial Protein Extraction Reagents (B-PER, Pierce) was added each well and the plates were incubated with gentle shaking on ice for 1hr. The plates were centrifuged at 3500 × g, 4°C for 20 min and supernatant was used to test the H_2O_2 response. The fluorescent intensity of each cell lysate with or without adding H_2O_2 was recorded using a BioTek Synergy Mx Microplate Reader with excitation at 570 nm and emission at 600 nm. The variant showed maximal fluorescence dynamic change was selected as template for directed evolution. Two rounds of random mutagenesis, based on error-prone PCR using oligos pBAD-F/R, were performed and library was screened as abovementioned. The clone presented bright red fluorescence with maximal fluorescence change was chosen for in-vitro characterization.

The negative control, SHRIMP-N, was constructed by mutating active Cys at the 199 site to Ser (C199S) to abolish the activity of OxyR sensor domain.

4.3.3 Protein purification and in-vitro characterization

To express ecpApple and cpmScarlet, the plasmid pBAD-ecpApple/pBAD-cpmScarlet was transformed to *E. cloni* 10G cells and then plated on 2 × YT agar plates supplemented with 100 mg/mL ampicillin and 0.02% (w/v) L-arabinose for overnight incubation at 37 °C. Single colony was selected to start a 2 mL 2 × YT starter culture at 37 °C overnight shaking at 225 rpm. The next day, the 2 mL saturated starter culture was diluted into 200 mL 2 × YT and 0.2 % (w/v) L-arabinose was added to the 200 mL culture to induce the protein expression when OD_{600} reached around ~0.6. The protein was expressed under 37°C with shaking at 225 rpm for 24 hrs and 1 mL cell culture was lysed with B-PER to measure the brightness and spectrum. The rest of the culture was incubated to express the protein at 16 °C for another 48 hrs and cell pellet was harvested for protein purification. Bacterial cells were centrifuged at 4500 × g for 20 min and the pellet was resuspended in 1 × PBS buffer (pH 7.4). The bacteria resuspension was lysed by sonication and the lysed supernatant was collected by centrifugation at 12000 × g for 30 min at 4 °C. The clear supernatant was applied to Ni-NTA agarose beads (Pierce) for purification according to the manufacturer's instructions. The purified protein was buffer exchange with MilliporeSigma™ Amicon™ Ultra-15 Centrifugal Filter Units (10,000 Da molecular weight cutoff) and then used for photophysical properties measurements.

SHRIMP was amplified from corresponding pcDNA3 construct and Gibson assembly [47] into a compatible pET28a vector tagged with His_6. The plasmid with sequencing confirmation was used to transform BL21(DE) competent cells, which were then plated on a 2 × YT agar plate

supplemented with 50 μg/mL kanamycin. The plate was incubated at 37 °C overnight (~18 hrs) and a single colony was selected and inoculated into 5 mL of liquid 2 × YT medium supplemented with 50 μg/mL kanamycin. After shaking at 250 rpm, 37 °C overnight, the starter culture was next diluted 100-fold into 500 mL 2 × YT supplemented with 50 μg/mL kanamycin. When the optical density at 600 nm (OD_{600}) reached 0.8, 1 mM IPTG was added into the medium to induce the protein expression. The bacteria culture was shaken at 16 °C and 250 rpm for 96 hrs. The cell culture was harvested and protein was purified as abovementioned. The protein eluate was further applied to size exclusion column and then concentrated by using Amicon Ultra Centrifugal Filter Units (10,000 Da molecular weight cutoff). The purified protein was aliquoted as small fraction and stored at -80 °C.

Purified protein was diluted in 1 × PBS to a final concentration of 500 nM for excitation and emission spectra scanning. The emission wavelength was set at 615 nm, and the excitation spectra was scanned from 450 to 595 nm. To record emission spectra, the excitation wavelength was fixed at 555 nm and the emission spectra was scanned from 575 nm to 700 nm. mScarlet-I (Φ = 0.54) (Bindels et al., 2017) was selected as the reference to determine the quantum yield of purified SHRIMP and HyperRed. Purified protein was diluted to a series of different concentrations in 1× PBS and emission spectra in the range of 560 nm-700 nm were recorded with an interval of 5 nm. The quantum yield (QY) was determined as previously described.[48]. The absorption spectra were scanned from 520 nm to 700 nm to determine extinction coefficient (EC). To determine the dose-response performance towards different concentrations of H_2O_2, 1 mM DTT was first added to fully reduced the protein (10 μM). Next, the reduced protein was diluted 1000-fold and incubated with H_2O_2 (100 – 1000 nM) at RT. The fluorescence intensities (ex. 570 nm and em. 600 nm) of each group were measured on a BioTek Synergy Mx Microplate Reader.

To test the specificity of SHRIMP, the fully reduced protein was incubated with different oxidants according to a previous publication.[49] The fluorescence of each group was recorded as abovementioned. A series of buffer containing 200mM citric acid and 200 mM boric acid, with pH ranging from 3 to 10, were prepared for pH titration. 5 μL purified protein (500 nM) was mixed with 95 μL buffer and fluorescence intensity of each sample was recorded. The fluorescence value was plotted against pH values to determine apparent pK_a.

4.3.4 Demonstration of H_2O_2 redox response in HEK 293T cells

To construct SHRIMP into mammalian cell expression vector pcDNA3, oligos pcDNA3-SHRIMP-F and pcDNA3-SHRIMP-R (**Table S1**) were used to amplify the SHRIMP insert from pET-SHRIMP plasmid. The pcDNA3-SHRIMP-N was prepared by mutating Cys at 199 to Ser through overlap PCR. The amplified insert was inserted with the compatible pcDNA3 vector via Gibson Assembly. HEK (human embryonic kidney) 293T were cultured and transfected with 3 μg of plasmid pcDNA3-SHRIMP evenly mixed with 9 μg PEI following manufacture's instruction. After 24 hrs post-transfection, cells were imaged with DPBS (1 mM Ca^{2+}, 1 mM Mg^{2+}) under a Leica DMi8 inverted microscope equipped with a Leica EL6000 light source and a Photometrics Prime 95B sCMOS camera. TRITC filter cube with 545/25-nm bandpass excitation and 605/70-nm bandpass emission was applied to illuminate the cells. H_2O_2 (150 μM) was added externally to the transfected cells in the imaging buffer and images were acquired at the certain intervals to monitor the time-lapse responses. Images were analyzed using the ImageJ [50] software. The mean fluorescence intensity for ROI (regions of interest) of randomly selected cells were analyzed. The ratios of fluorescence intensities at different time points (F_t) versus the value at t = 0 min (F_0) were plotted against time.

Table 4.1 Sequence of primers for cloning.

Primers	Sequence (5'- 3')
cpmScarlet-2NNK-F1	ataggtcggctgggctcacccgtannknnkgagcggttgtaccccgag
cpmScarlet-R1	cgcccttgctcaccagactcccgcctgtacctcccttgtacagctcgtccatgc
cpmScarlet-F2	gacgagctgtacaagggaggtacaggcgggagtctggtgagcaagggcgaggcag
cpmScarlet-NNK-R2	ggtgatggtgttggtcacgmnncgcttcccagcccattgtc
cpmScarlet-2NNK-G-F	gaattaaccatgggctcgagaataggtcggctgggctcac
cpmScarlet-2NNK-G-R	ccgccaaaacagccaagcttaatgatggtggtgatggtgttggtcacg
pcDNA3-SHRIMP-F	atgacgataaggatccgagctcgagagccaccatggagatggcg
pcDNA3-SHRIMP-R	gacactatagaatagggccctctagattaaaccgcctgttttaaaactttatcga
pAAV-insulin-F	aaggatcccgccaccatggcgagccagcagggc
pAAV-insulin-R	ggttgattatcgataagcttttaaaccgcctgttttaaaacttt
OxyR-cpmScarlet-F1	tgcgcgatcaggcaatgcccnnknnkgagcggttgtaccccgagga
OxyR-cpmScarlet-R1	ccggcttcaaaacagaaacccacmnnmnncgcttcccagcccattgtctt
OxyR-N-F	atgacgataaggatccgagctcgagagccaccatggagatggcg
OxyR-N-R	gggcattgcctgatcgcgca
OxyR-C-F	gtgggtttctgttttgaagccgg
OxyR-C-R	tccgccaaaacagccaagcttttaaaccgcctgttttaaaactttatcga
pBAD-F	atgacgataaggatccgagctcgag
pBAD-R	ctcatccgccaaaacagccaagctttta

4.3.5 Photophysical properties characterization of SHRIMP

For photoactivation comparison, HEK 293T cells expressing SHRIMP or HyPerRed were illuminated with laser light switching between consecutive 8s of 532 nm with 50% power intensity (0.107 W/cm^2) and 2s of a 405 nm with 80% power intensity (0.162 W/cm^2) under the abovementioned Leica microscope platform with SPE-II spectral confocal module.

For regular photobleaching characterizations, HEK 293T cells transiently transfected with SHRIMP or HyPerRed were stimulated with consecutive TRITC filter with 10% power intensity (0.091 W/cm^2) laser light under wide-field condition and 532 nm with 8% power intensity (0.004 W/cm^2) under confocal module condition respectively.

In both photophysical properties characterizations, the mean fluorescence intensity at certain time points (F_t) of randomly circled single cell were normalized to the fluorescence intensity at time t = 0 min (F_0). The F_t/F_0 ratio was plotted against time. The laser intensity at the focal plane was measured with a digital optical power meter (Thorlabs, #PM100D) equipped with a microscope slide photodiode power sensor (Thorlabs, #S170C). According to the formula $\pi \cdot (0.5 \cdot D_{FOV})^2$, the illumination area was calculated 0.3445 mm^2.

4.3.6 Construction AAV plasmids and preparation of Adeno-Associated Viruses (AAVs)

To construct plasmids for packing adeno-associated virus for expression in islet clusters, the SHRIMP (or SHRIMP-N) insert gene was amplified with oligos pAAV-insulin-F and pAAV-insulin-R (**Table S1**) from the corresponding pcDNA3 mammalian cell expression plasmids. The pAAV vector, which contains insulin promoter, was digested with Nhe I and Hind III. The resultant PCR insert was assembled into predigested pAAV-insulin vector by Gibson Assembly. Plasmids were sent for Sanger sequencing confirmation.

To pack AAV of SHRIMP (or SHRIMP-N), pAdDeltaF6 (Addgene #112867) and pAAV2/9n (Addgene #112865) gifts from James M. Wilson, were used as our AAV packing plasmids. pAAV-insulin-SHRIMP/SHRIMP-N were co-transfected with pAdDeltaF6 and pAAV2/9n into HEK 293T cell line to pack virus. Protocol by Rego et al. [51] was used for AAV packing and purification. AAV was titrated with quantitative PCR (qPCR) by following a protocol from Addgene. The AAV titers were in the range of 1×10^{13} to 1×10^{14} vg/mL. AAVs were aliquoted and stored in -80 ℃ for long term usage.

4.3.7 Imaging redox response in activated macrophages

RAW 264.7 cells were cultured in Dulbecco's Modified Eagle Medium (DMEM) supplemented with 10% FBS at 37 ℃ with 5% CO_2. When cells reached ~60% confluency, 3 μg of plasmid pcDNA3-SHRIMP/SHRIMP-N was mixed with 6 μg X-tremeGENE™ HP DNA Transfection Reagent (Roche) as manufacturer's instruction. The DNA-lipid complexes were added directly into the medium of cells and incubated at 37 ℃ with 5% CO_2. Cells were imaged in Hank's balanced salt solution (HBSS) after 24 hrs post transfection. 2 μM phorbol myristate acetate (PMA) was added dropwise to the cells in imaging buffer. Fluorescence change within certain interval was recorded with abovementioned Leica microscope platform. The fluorescence response was analyzed with ImageJ as previously described.

4.3.8 Mouse pancreatic islets isolation and AAV transduction

Mouse pancreatic islets were isolated from the pancreata of C57BL/6 mice (Jackson Laboratory, MA) at age of 10-12 weeks. Islets were cultured according to the established protocol [52]. In brief, 0.375 mg/mL of Collagenase P (Roche Applied Science, IN) were injected into the

pancreata for digestion at 37 °C for 15 min. A discontinuous Ficoll gradient (Mediatech, VA) was used to further purify the islets. Next, purified islets were cultured in RPMI 1640 containing 10% fetal bovine serum (Hyclone Inc., MA) and 1% penicillin/streptomycin (Mediatech, VA) at 37°C under 5% CO_2.

For AAV transduction, islets were pre-treated with 0.05% trypsin in 37°C for 2 min and immediately transferred into abovementioned RPMI 1640 medium to stop trypsinization. Around 50 islets were handpicked into a well of 96-well-plate with 100 µl RPMI 1640 medium. 5 µL AAV (titer of 1×10^{13} to 1×10^{14} vg/mL) were added to each well (estimated multiplicity of infection (MOI) ~100,000 vg/cell). After 20 hrs incubation at 37°C with 5% CO_2, cells together with medium in 96-well plates were transferred into 24-well plate containing 1 mL complete medium. Medium was changed every 2 days and islets were imaged after 3 days.

4.3.9 Imaging redox response in chemical stimulated Islet

Islets were transduced with AAV-SHRIMP (or AAV-SHRIMP-N) as previously described. For imaging, islets were transferred into Krebs-Ringer Modified Buffer (KRB, 135 mM NaCl, 5 mM KCl, 1 mM $MgSO_4$, 0.4 mM K_2HPO_4, 1 mM $CaCl_2$, 5.5 mM Glucose and 20 mM HEPES). Different concentrations of H_2O_2 were added externally to SHRIMP/SHRIMP-N transduced islets to stimulate redox response. For monitoring the redox response caused by streptozotocin (STZ)-stimulation, 6 mM STZ was added to the islets and images were acquired at indicated interval. Image data was analyzed as abovementioned.

4.3.10 Dual-color imaging of H_2O_2 and Ca^{2+} in mammalian cell culture

The plasmids pcDNA3-cyto-GCaMP6m (1.5 μg) and mitochondria-localized pCS-MLS-SHRIMP/SHRIMP-N (1.5 μg) were transiently co-transfected into HEK 293T cells. The cells were imaged in HBSS buffer after 48 hrs transfection under the abovementioned Leica DMi8 inverted microscope system. The Leica SPE-II spectral confocal module was used to determine cellular localization of GCaMP6m and SHRIMP. The green fluorescence was acquired with a 488-nm laser and the emission was scanned from 510-565 nm. The red fluorescence was collected with a 532 nm laser and emission was collected from 600-665 nm. Time-lapse experiments were carried out under the wide-field condition. The 10 μM Thapsigargin (TG) was added to stimulate the cells post 10 min imaging. The FITC filter cube with 470/40-nm bandpass excitation and 525/50-nm bandpass emission was applied to illuminate GCaMP6m and TRITC filter cube with 545/25-nm bandpass excitation and 605/70-nm bandpass emission was applied to illuminate the SHRIMP. Time-lapse imaging was sequentially acquired between the two channels. Images were analyzed as previously described. Fluorescence signals at a certain timepoint (F_t) of each channel was normalized to basal intensity levels (F_0) at t = 0 upon stimulation.

4.4 Results

4.4.1 Engineering and Screening of SHRIMP

The natural mScarlet-I was split between the 146th and 147th amino acid, which lie in close proximity to the chromophore. The original N- and C- termini of mScarlet-I were fused with a Gly-Ser-rich peptide linker (GGSGGT), and the sites 146 and 147 turn to the new termini. Degenerate codons (NNKs) were added to the new termini to build saturated mutagenesis library

for screening (**Figure 4.1A**). The colonies with faster onset of fluorescence after overnight incubation at 37 °C were selected for expression. Upon the expression of protein, the *E. coli* lysate was screened for brightness of red fluorescence by using a BioTek™ Synergy™ Microplate Reader. The brightest clone was selected and sent for sequencing confirmation (**Figure 4.1A**). The resultant cpmScarlet exhibits an excitation peak at 570 nm and an emission peak at 595 nm (**Figure 4.1C**), which are close to the wild-type mScarlet-I (Ex: 569 nm, Em: 593 nm). In addition, the cell lysate of cpmScarlet presents better brightness, ~5-fold greater brightness, and better fluorescence spectrum than ecpApple[53] (**Figure 4.1B**) after 37 °C overnight protein induction. We also compared the photophysical properties of cpmScarlet and ecpApple. The EC of ecpApple is 46,924 M^{-1} cm^{-1} and QY is 0.03, while the EC of cpmScarlet is 31,546 M^{-1} cm^{-1} and QY is 0.31 Collectively, the brightness of purified cpmScarlet is ~6-fold higher than ecpApple (**Table 4.2**).

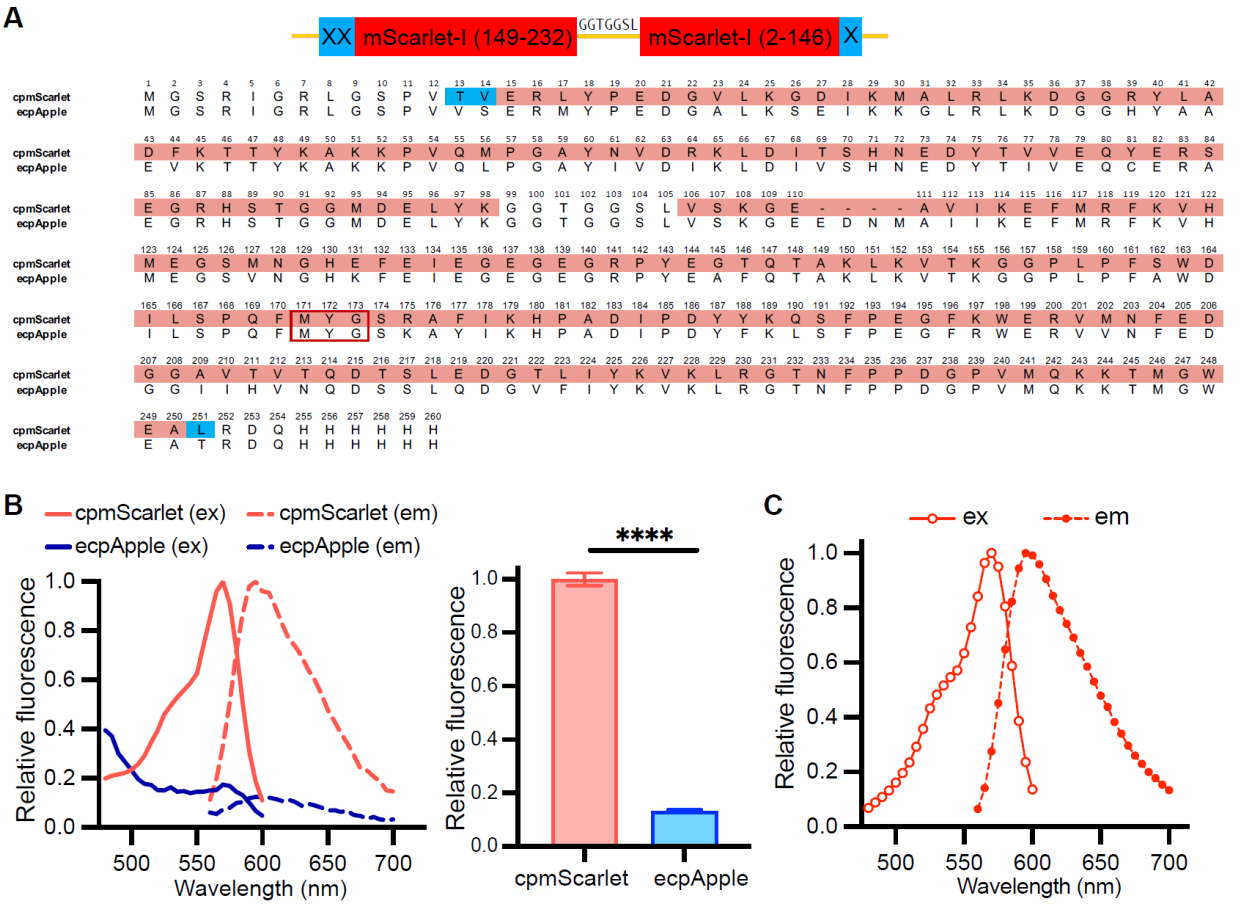

Figure 4.1 Sequence and fluorescence spectrum of cpmScarlet.

(A) Schematic presentation of cpmScarlet library design and sequence alignment of ecpApple and cpmScarlet. X represents NNK, N: any base, K: G or T. Two fragments of cpmScarlet are connected through a GGTGGSL linker. Residues in this figure are numbered according to the cpmScarlet sequence. The detailed sequences for pBAD-His B vector are not shown. **(B)** Left panel: comparison of fluorescence spectrum of ecpApple and cpmScarlet from cell lysate. Right panel: emission peak intensity comparison of ecpApple and cpmScarlet cell lysate. **(C)** Fluorescence spectrum of purified cpmScarlet (Ex-570 nm, Em-595 nm).

Next, we replaced cpmApple in HyPerRed with cpmScarlet (15-250) and kept the same linker length, 3 amino acids on each side, between sensory domain OxyR and cpmScarlet. The two amino acids closest to the N- and C-termini of cpmScarlet were adapted to degenerate codon to build the initial library for screening (**Figure 4.2A**). An initial mutant (SHRIMP 0.1) presented ~2.9-fold of fluorescence decrease towards 500 μM externally added H_2O_2 was selected for further engineering. Since SHRIMP 0.1 showed relatively dim red fluorescence and required to express under 16°C, we performed random mutagenesis to enhance its maturation and brightness. Two rounds of error-prone PCR-based random mutagenesis were conducted and the selected colonies were incubated under room temperature for expression (**Figure 4.2A**). A variant, containing the linkers Pro-Gly-Thr and Gly-Gly-Val, showed maximal ~5-fold of fluorescence change against added H_2O_2. Compared to SHRIMP 0.1, it gained 3 mutations (A363T, A404T, K495M) during the evolution process (**Figure 4.2B**). This clone was named SHRIMP and selected for further characterization.

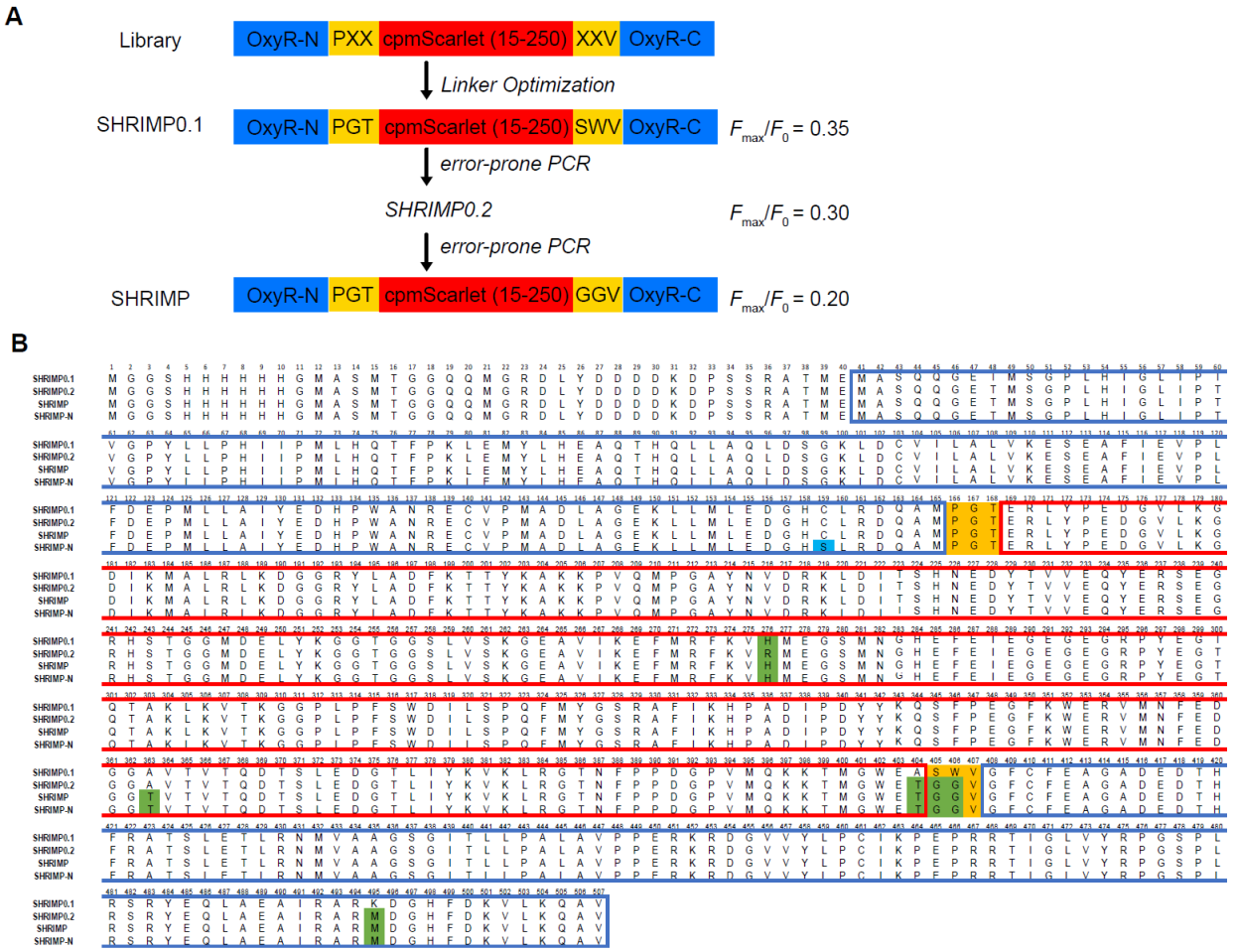

Figure 4.2 Engineering and evolution process of SHRIMP.

(A) Workflow showing the library design and development of SHRIMP. **(B)** Sequence alignments of different SHRIMP mutants and the negative control SHRIMP-N. X represents NNK, N: any base, K: G or T. H_2O_2 sensory domain OxyR is boxed in blue, cpmScarlet (15-250) is boxed in red. OxyR and cpmScarlet are connected through 3-amino-acid linkers (residues highlighted in orange). Mutations obtained during evolution are highlighted in green. The detailed sequences for pBAD-His B vector are not shown.

4.4.2 Protein Expression and *in vitro* Characterization of SHRIMP

We next performed in vitro characterization of SHRIMP. Purified SHRIMP presented an excitation and emission peak at 570 nm and 595 nm respectively. Fluorescence intensity presented a maximal 5-fold decrease upon adding 1000 μM H_2O_2 (**Figure 4.3B**). The emission spectrum indicated that the fluorescence intensity decreased against H_2O_2 in a dose-dependent manner (**Figure 4.3C**). To test SHRIMP specificity, we measured fluorescence change in the presence of other redox-active molecules, including reactive nitrogen species (NO•), major targets of ROS (cysteine/homocysteine) and other ROS (•OH/GSSG). Significant declined fluorescence intensity was only observed in presence of H_2O_2 (**Figure 4.3D**), suggesting that SHRIMP can detect H_2O_2 with good specificity. To construct a negative control (SHRIMP-N), we mutated the critical active Cysteine residue 199 involved in H_2O_2 redox response, to Serine. When adding the same concentration of H_2O_2 to purified protein, SHRIMP displayed fluorescence decrease towards H_2O_2 (EC_{50} ~ 294 nM) while SHRIMP-N did not show significant fluorescence response (**Figure 4.3F**). To exclude the artifacts from pH, we also compared the pH response of SHRIMP and the negative control SHRIMP-N within pH range from 3-10, which cover the physiological pH range. SHRIMP and SHRIMP-N presented similar response to different pH, with pKa of 7.49 and 7.10 respectively. Both mutants showed minimal fluorescence change within physiological pH range 7 - 7.5 (**Figure 4.3E**), indicating that the pH artifacts can be excluded by using SHRIMP-N to perform experiments parallelly with SHRIMP. We further measured quantum yield, using mScarlet-I as reference, and extinction coefficient of SHRIMP to evaluate its brightness. The quantum yield of SHRIMP remained as 0.32 under both redox states. Extinction coefficient changed from 127,784 to 25,557 when fully oxidized by H_2O_2, leading to a maximal 5-fold of brightness change (**Table 4.2**). Compared to HyPerRed, the brighter state (reduced state) of SHRIMP presents ~ 4.0-fold

higher brightness than the brighter state (oxidized state) of HyPerRed. The dimmer (oxidized) state of SHRIMP shows ~ 1.5-fold higher brightness than the brightness of reduced sate of HyPerRed (**Table 4.2**). Taken together, in vitro characterizations indicated that SHRIMP exhibited great brightness, excellent sensitivity and good selectivity against H_2O_2, making it a favorable tool to study H_2O_2-related redox biological questions.

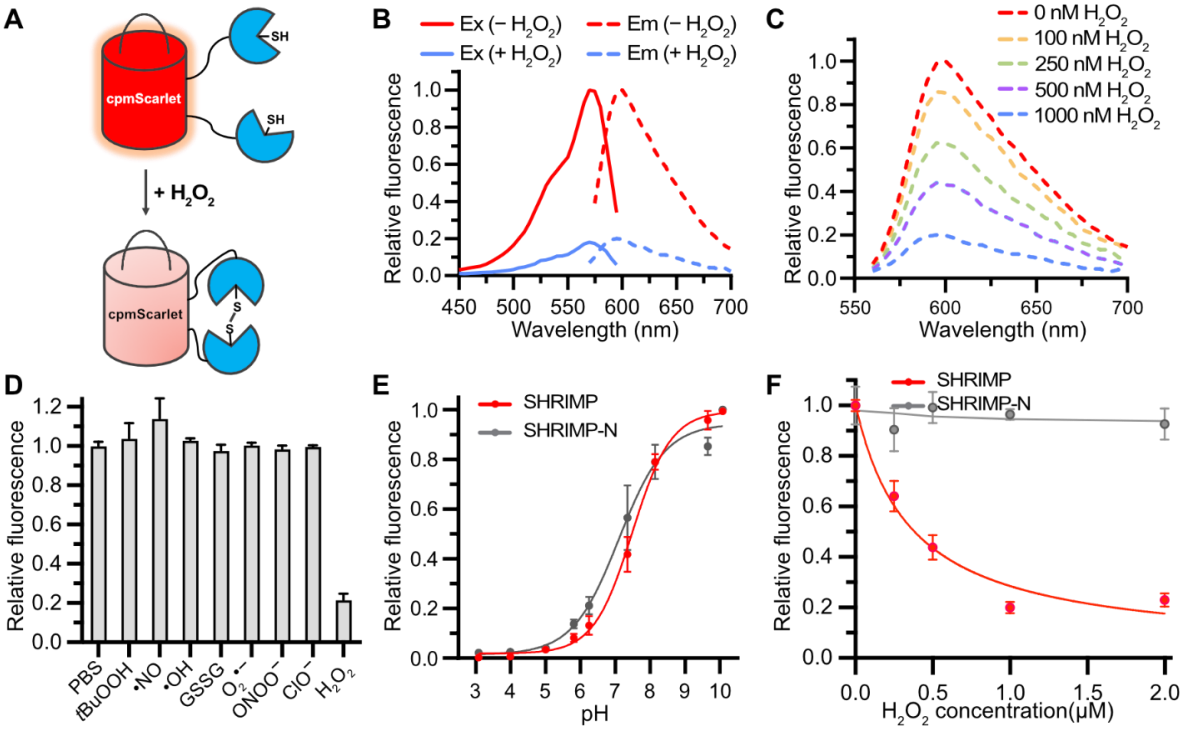

Figure 4.3 Design and in vitro characterization of SHRIMP biosensor.

(A) Schematic representation of SHRIMP sensor design. **(B)** Excitation (solid line) and emission (dot line) spectra of oxidized (blue) and reduced (red) purified SHRIMP. **(C)** Emission spectrum against different concentrations of H_2O_2. **(D)** Selectivity assay of SHRIMP towards various redox molecules. **(E)** The pH profile of purified SHRIMP and SHRIMP-N. (**F**) Fluorescence response of purified SHRIMP and SHRIMP-N against different concentrations of H_2O_2.

Table 4.2 Photophysical properties of the indicated cpRFPs and red fluorescent H_2O_2 sensors.

	λ_{ex} (nm)	λ_{em} (nm)	ε (M^{-1} cm^{-1})	ϕ	Brightness[a]
cpmScarlet	570	595	31,546	0.31	9.79
ecpApple	570	600	46,924	0.03	1.60
SHRIMP	oxidized				
	570	600	25,557	0.32	8.18
	reduced				
	570	600	127,784	0.32	40.89
HyPerRed	oxidized				
	575	605	38,148	0.27	10.30
	reduced				
	575	605	19,074	0.27	5.33

[a] The intrinsic brightness is defined as the product of ε and ϕ.

4.4.3 H_2O_2 dynamic imaging in mammalian cell culture

To assess the performance of SHRIMP in culturing mammalian cells, we generated mammalian cell expressing plasmid of pcDNA3-SHRIMP and the corresponding control pcDNA3-SHRIMP-N. Expressed in HEK 293T cells, SHRIMP manifested ~ 3.3-fold of fluorescence decrease in the presence of 150 μM exogenous H_2O_2 while the fluorescence change of SHRIMP-N was negligible (**Figure 4.4A-C**). SHRIMP utilized the same OxyR sensory domain as HyPerRed with several mutations obtained through the evolutions. Its fluorescence dynamic change was 65% greater than that of HyPerRed (~2-fold)[23] towards the same concentration of external H_2O_2.

To assess the applicability of SHRIMP in physiological milieu, we further expressed SHRIMP in mouse RAW 264.7 macrophage, which was reported to release ROS during phagocytosis or activated with a wide range of stimuli. [54, 55] It has long been recognized that H_2O_2 was generated during phagocyte respiratory burst via the nicotinamide adenine dinucleotide phosphate reduced (NADPH) oxidase and elevated H_2O_2 contributes to pathogens killing and digestion. [56] SHRIMP or SHRIMP-N was transfected in mouse RAW 264.7 macrophage for 24 hrs. Post 24-hrs expression, phorbol myristate acetate (PMA), protein kinase C agonists, [57] was added to the cells to activate NADPH-oxidase to release H_2O_2. [58] The cells expressing SHRIMP showed ~30% fluorescence "turn-off" upon PMA stimulation. Parallelly, we expressed SHRIMP-N in RAW 264.7 cells and the fluorescence change of cells bearing SHRIMP-N is negligible (**Figure 4.4D-F**). Taken together, these results indicated that SHRIMP can be a reliable tool to monitor both external H_2O_2 and physiological-related H_2O_2 generation in different mammalian cell systems.

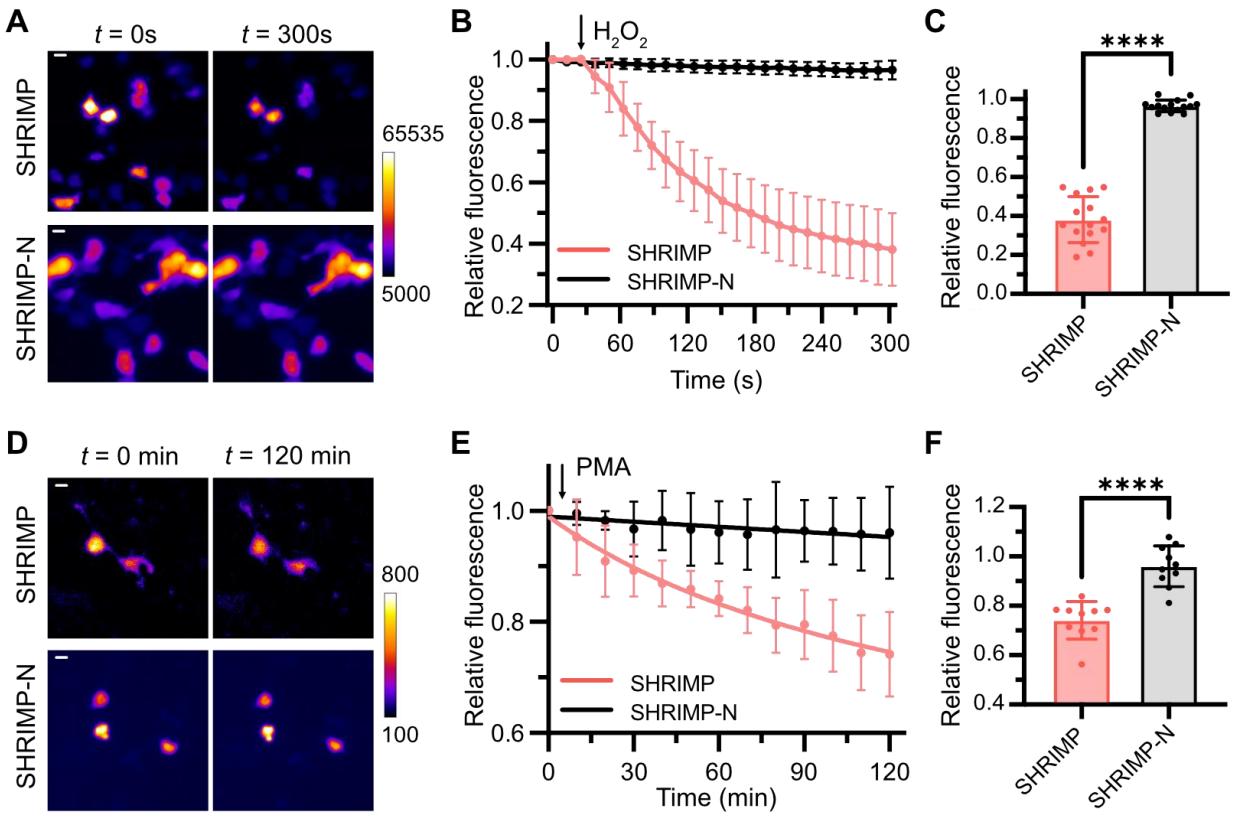

Figure 4.4 Imaging of SHRIMP response in mammalian cells.

(A) Representative pseudocolored fluorescence images of HEK 293T cells expressing SHRIMP/SHRIMP-N response to H_2O_2. Images were taken at 0 and 300 sec. **(B)** Time-lapse responses of HEK 293T cells expressing SHRIMP (red) or SHRIMP-N (black) to externally added 150 µM H_2O_2. **(C)** Comparison of total intensity changes for HEK 293T cells expressing SHRIMP (red) or SHRIMP-N (black) (****P < 0.0001, unpaired two-tailed t-test). Data represent mean ± SD of 15 cells from three technical repeats in each group. Arrow indicates the time point for H_2O_2 addition. **(D)** Representative pseudocolored fluorescence images of macrophages expressing SHRIMP/SHRIMP-N. Images were taken at 0- and 120-min. **(E)** Time-lapse responses of PMA-activated macrophage expressing SHRIMP (red) or SHRIMP-N (black). **(F)** Total fluorescence intensity comparison of activated macrophages with SHRIMP (red) or SHRIMP-N (black). Data represent mean ± SD of 10 cells from three technical repeats. (**** indicate P < 0.0001). Arrow indicates the time point for PMA addition. Scale bar: 10 µm.

4.4.4 Photophysical Properties Characterization of SHRIMP biosensor

To further look into the photophysical properties of SHRIMP, we illuminated the protein under different laser conditions. HEK 293T cells expressing SHRIMP and HyPerRed were cultured and imaged in the glass-bottom dish via 40 × oil objective lens. When illuminated under 10% intensity with TRITC filter (0.091 W/cm^2), HyPerRed displayed ~ 8% fluorescence increases while SHRIMP showed ~ 20% fluorescence decrease within a certain period of time (500 s) (**Figure 4.9A**). Similarly, under the 8% intensity illumination at 532 nm (0.004 W/cm^2), HyPerRed presented ~0.02 % photobleaching while SHRIMP presented ~ 0.05% photobleaching (**Figure 4.9B**).

As to photoactivation, illuminating HyPerRed with 405 nm laser (0.162 W/cm^2) for 2 s led to maximal ~10 % fluorescence increases as detected with 532 nm illumination (**Figure 4.5B**). The intense violet laser illumination resulted in a fluorescence increase ranging from 2% to 10% (**Figure 4.5B**). The photoactivation effect was accumulative and showed a maximal ~1.3-fold of fluorescence increase of baseline (**Figure 4.5B**). In contrast, this photoactivation effect was not detected in SHRIMP-expressing cells under the same illumination condition (**Figure 4.5A**), indicating that SHRIMP might be a more ideal biosensor in combination for multi-channel imaging.

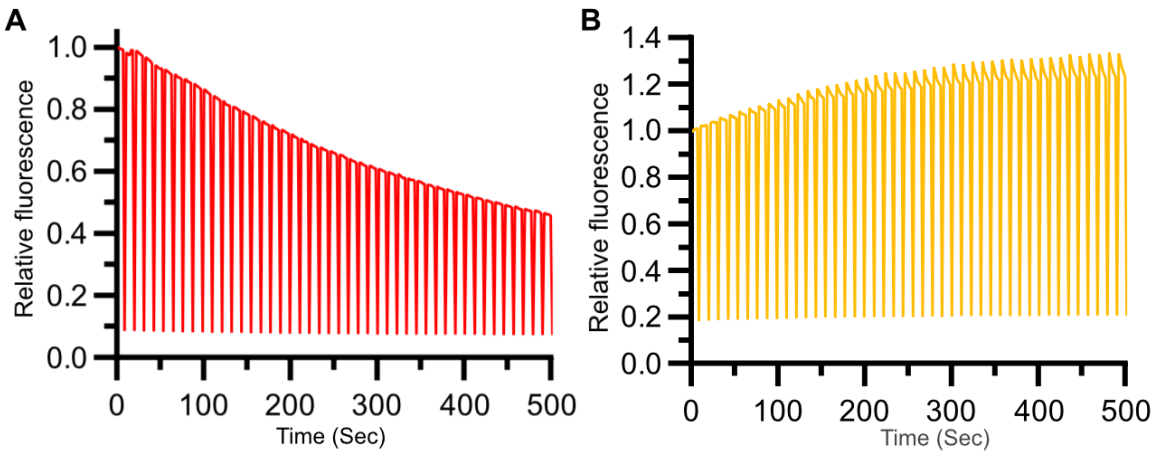

Figure 4.5 Photophysical characteristics of SHRIMP and HyPerRed in mammalian cell culture.

(A) Representative SHRIMP fluorescence changes to switching between illumination 5s with a 532 nm 50% intensity (0.107 W/cm^2) laser and 2 s with a 405 nm 80% intensity (0.162 W/cm^2) laser. **(B)** Representative HyperRed fluorescence changes to switching between illumination 5s with a 532 nm 50% intensity (0.107 W/cm^2) laser and 2 s with a 405 nm 80% intensity (0.162 W/cm^2) laser. Representative data from three independent technical repeats were shown.

4.4.5 Imaging of redox dynamics in chemical stimulated Islet

First, we added H_2O_2 at different concentrations (5, 25 and 100 μM) to prompt the redox response in SHRIMP-expressing islets. The fluorescence intensity of SHRIMP exhibited a concentration-dependent decrease with a maximal 2.5-fold of dynamic change. The response showed a Kd of 12 μM and was saturated at 100 μM H_2O_2. Meanwhile, SHRIMP-N did not show obvious response towards the addition of 100 μM H_2O_2 (**Figure 4.6**). Next, we further assessed the performance of SHRIMP in islets under physiological-related stimulation. Streptozotocin (STZ) (2-deoxy-2-(3-methyl-3-nitrosourea)-1-D-glucopyranose) is a cytotoxic glucose and N-acetyl glucosamine (GlcNAc) analogue, which has been used as a chemotherapeutics alkylating agent to treat metastasizing pancreatic islet cell tumors.[59] STZ was found to increase the activity of xanthine oxidase to generate superoxide, which will subsequently form hydrogen peroxide and hydroxyl radicals.[60] Generation of hydrogen peroxide has been studied in pancreatic islets of C57BL/6 mice with multiple low doses STZ induced diabetes. [61] Here, we expressed SHRIMP in isolated pancreatic cells of C57BL/6 mice to test if it can monitor the H_2O_2 generation during STZ stimulation. AAV transduced pancreatic cells were transferred into imaging buffer KRB for STZ stimulation. In the presence of 6 mM STZ, the fluorescence intensity of SHRIMP displayed a 38% decrease from the basal level within 1hr. In contrast, the fluorescence intensity decreased only around 12% without STZ addition. Parallel experiments were performed on pancreatic cells expressing negative control, SHRIMP-N. The fluorescence intensity in the control group exhibited similar decrease level (~12%) as SHRIMP group without STZ (**Figure 4.7A and 4.7B**). The marked fluorescence decreases in SHRIMP group, compared to different control groups, indicated ~1.5-fold elevations of H_2O_2 levels in STZ-mediated pancreatic islet (**Figure 4.7C**). Collectively,

these data suggested that SHRIMP can be applied to stimulated tissue for monitoring H_2O_2 dynamic change.

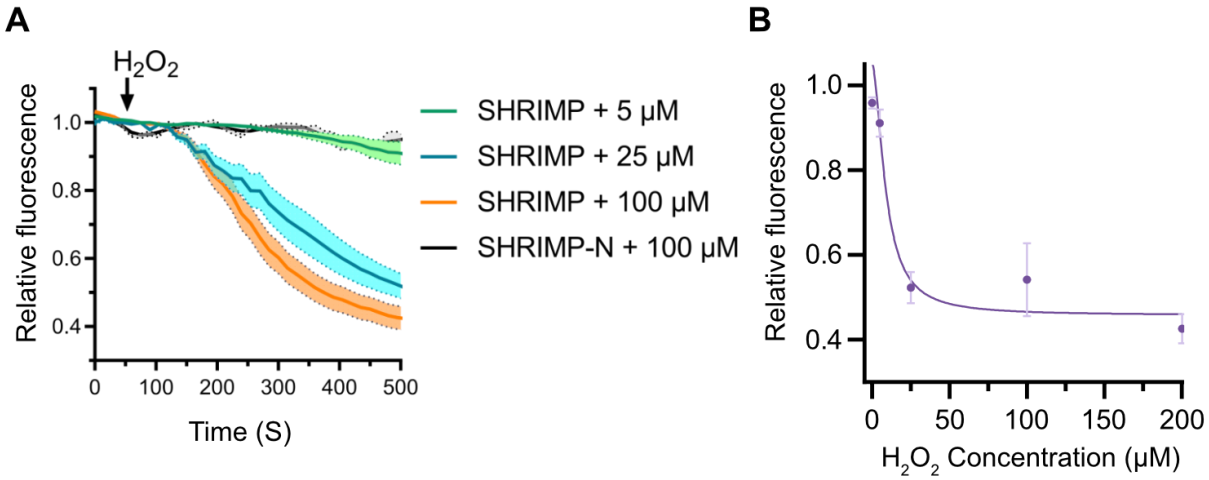

Figure 4.6 Imaging of SHRIMP (SHRIMP-N) transduced islets response to external H_2O_2.

(A) Time-lapse fluorescence changes of islets transduced with SHRIMP (SHRIMP-N) to different concentrations of externally added H2O2. (B) Fluorescence signal changes of SHRIMP against concentrations of H2O2.

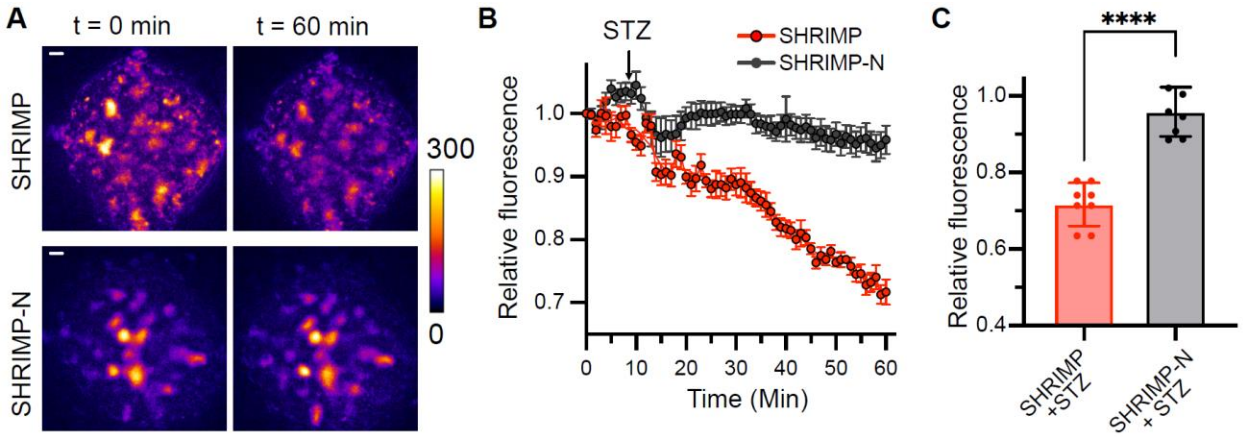

Figure 4.7 Detection of hydrogen peroxide generation in Streptozotocin (STZ) mediated mouse pancreatic islets.

(A) Representative pseudocolored real-time fluorescence images of islet expressing SHRIMP/SHRIMP-N. Images were taken at 0- and 60-min upon 6 mM STZ stimulation. **(B)** Time-lapse responses of islets expressing SHRIMP (red) or SHRIMP-N (black) upon STZ treatment. **(C)** Fluorescence intensity comparison of STZ-treated islets with SHRIMP (red) or SHRIMP-N (black) expression. Data represent mean ± s.e.m. from three technical repeats. (**** indicate $P < 0.0001$). Arrow indicates the time point for STZ treatment. Scale bar: 10 μm.

4.4.6 Dual-color imaging of Ca^{2+} signaling and H_2O_2 dynamics in different subcellular compartment of HEK 293T cells

To assess the compatibility of SHRIMP for dual-color imaging, we co-expressed SHRIMP with GCAMP6 in the mitochondria and cytosol of HEK293T respectively (**Figure 4.8A**). The effect of Ca^{2+} load on ROS generation in mitochondria are controversial from different studies, ranging from increase to significant decrease to no significant impact [62-64].

Thapsigargin (TG), as an inhibitor of sarco/endoplasmic reticulum Ca^{2+}- ATPase (SERCA), inhibiting the Ca^{2+} pumping from the cytoplasm into the sarcoplasmic reticulum (SR) lumen and the endoplasmic reticulum (ER) [65]. When treating the cells with 15 μM TG, the green fluorescence of GCAMP6 displayed an increase in response to TG-treatment in the cytosol (**Figure 4.8BC**). Meanwhile, the red fluorescence of SHRIMP decreased during monitoring time, indicating a simultaneous increase in H_2O_2 generation in mitochondria (**Figure 4.8DE**). In contrast, the fluorescence of negative control SHRIMP-N was negligible (**Figure 4.8E**). These results support the applicability of SHRIMP for multicolor/multiparameter imaging in combination with other indicators.

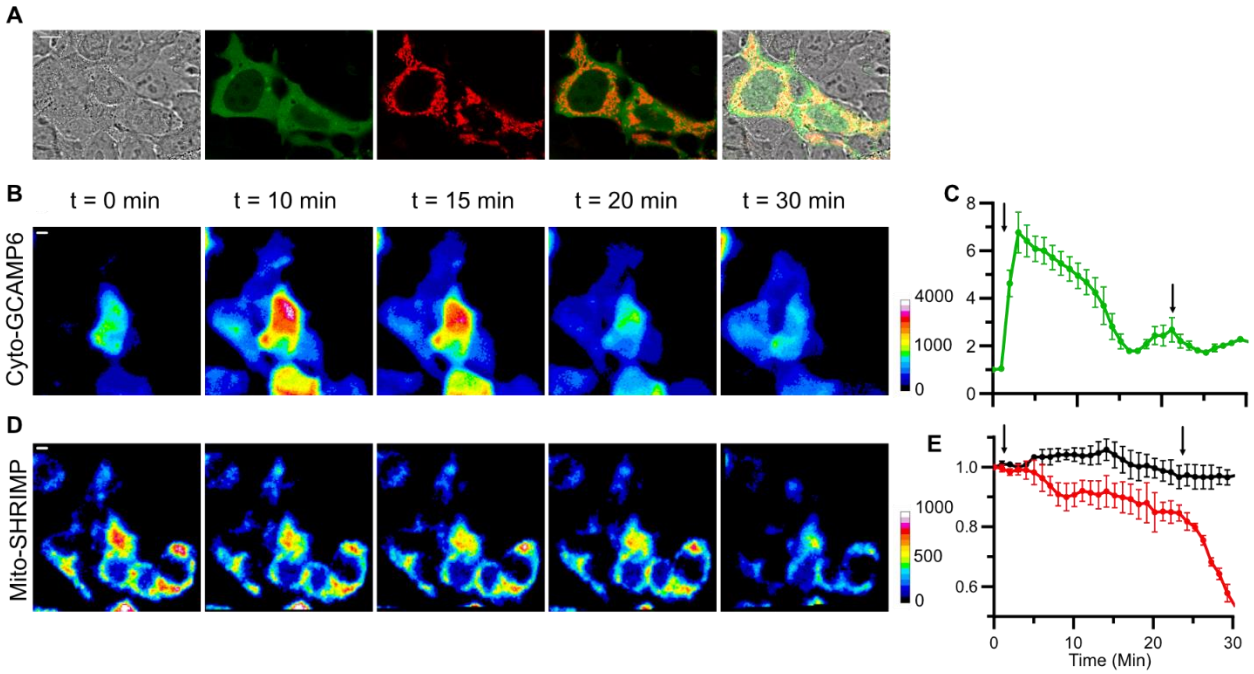

Figure 4.8 Multicolor imaging of Ca2+ and H2O2 signaling in HEK 293T cells.

(A) Co-expression of Cyto-GCAMP6 and Mito-SHRIMP in HEK 293T cells. **(B)** Representative pseudocolored real-time fluorescence images of GCAMP6-expressing HEK 293T cells. **(C)** Time-lapse Ca^{2+} responses of GCAMP6 expressed in cytosol. **(D)** Representative pseudocolored real-time fluorescence images of SHRIMP-(red)/SHRIMP-N (black)-expressing HEK 293T cells. Data represent mean ± S.E.M from three technical repeats. Arrow indicates the time point for Thapsigargin (TG) treatment.

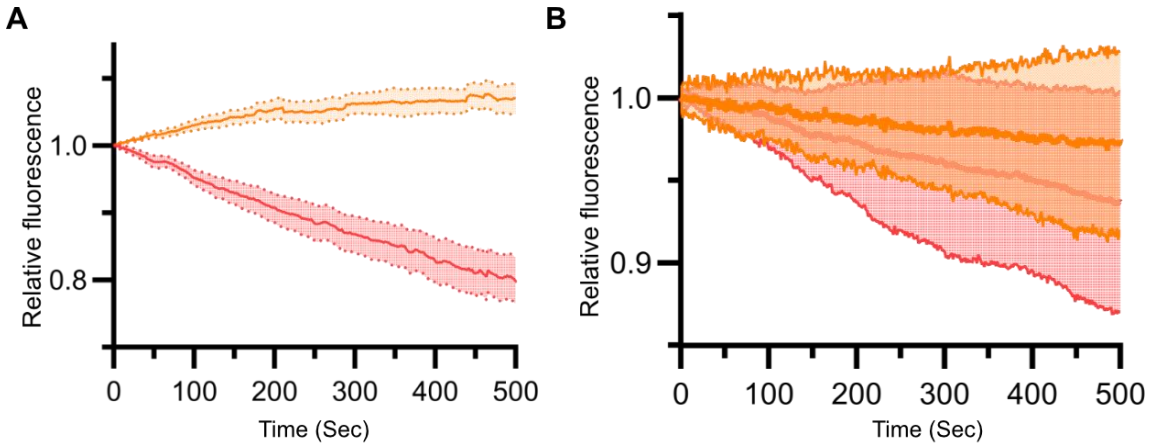

Figure 4.9 Photostability of SHRIMP and HyPerRed in mammalian cells.

(**A & B**) Time-course fluorescence photobleaching pattern of SHRIMP (red) or HyperRed (orange) with excitation (A) at TRITC filter 10% intensity. (0.091 W/cm^2) (B) at 532 nm 8% intensity (0.004 W/cm^2) under confocal module.

4.5 Discussions

In this work, we first generated a mScarlet-based circularly permutated RFP scaffold, cpmScarlet, which displays similar excitation and emission peak as its parental RFP. Due to the lack of crystal structure of mScarlet, we chose to align the DNA sequence of mScarlet-I to mApple. Learning from the design strategy from cpmApple, we decided to create the new termini at the A146 and E147. Meanwhile, we extended linker sequences, adapted from our previous reporters rxRFPs, on both newly-created N- and C-termini. Through random mutagenesis and directed evolution, we identified a variant maintained the autocatalytic red fluorescence with good brightness and maturation rate at 37°C.

Next, we attached two flanking sensory domains OxyR, the *E. coli* H_2O_2-activated transcription factor, to the N- and C-termini of cpmScarlet. Both sides contained three amino acids linker length between the OxyR and cpmScarlet. Most variants from the initial library display poor maturation rate under 37°C and only expressed weak red fluorescence when incubated at 16°C. We further performed several rounds of directed evolution and step-wise increased the library expression temperature gradually, from 16°C to room temperature to 30°C, to screen for variants with better maturation rate and protein folding. As a result, we identified a variant showing good brightness and "turn-off" fluorescence change towards H_2O_2. On the other hand, we also attempted to select relatively dim variant to see if they showed any "turn-on" fluorescence change against H_2O_2. However, none of these variants display detectable fluorescence response to H_2O_2. We speculated that the dim fluorescence indicates the poor maturation and protein folding of the FP, which may lead to the disfunction of the biosensor. It is possible that the cpmScarlet-based biosensors with good brightness are reaching the saturation level of brightness, building a barrier to develop biosensors with fluorescence increase in response to H_2O_2.

One of the reported drawbacks of DsRed-derived RFP,[66] mApple, is blue-light photoactivation behavior. The cpmApple-based Ca^{2+} indicator R-GECO series present apparent photoactivation with blue or green light illumination, which demanding extra caution to be taken to exclude the artifacts from the real response when integrated with channelrhodopsin-based optogenetics.[34, 35, 67] Here, we also assessed the photoactivation properties of HyPerRed, a redox biosensor adapted from cpmApple, and SHRIMP. Under high intensity blue laser illumination, SHRIMP does not show detectable photoactivation while HyPerRed exhibits notable photoactivation behavior, which may result from the photophysical property of the FP template cpmApple. Although these effects may be minimized by reducing blue-light intensity, SHRIMP provides an alternative to overcome this limitation and could be a more robust tool for in vivo study in combination with green/blue illumination biosensors.

We also, for the first time, circularly permutated mScarlet to a cpFP scaffold and use it as readout modality to create a genetically encoded redox biosensor. With similar circular permutation sites as cpmApple, our hydrogen peroxide biosensor SHRIMP demonstrates that the fluorescence intensity of cpmScarlet is sensitive to the fused protein changes on its N- and C-termini. For prospects, cpmScarlet can be a potential feasible template to construct single-FP GEFIs. The most direct example is to fuse CaM and M13 with cpmScarlet to build a Ca^{2+} indicator with minimized photoactivation.

Besides single-FP GEFIs, cpmScarlet is also appealing for FRET sensor development, serving as a donor or acceptor. FRET efficiency can be affected by the distance or the relative orientation of dipole moments between acceptor and donor FPs, which can be modulated through the utility of cpFPs.[68] cpFP variants, such as cpVenus and cpTFP1, have been optimized to develop FRET Ca^{2+} or kinase biosensors.[69-73] However, all of these utilization are based on the canonical

CFP-YFP FRET pair, which has apparent limitation such as short-wavelength excitation-induced phototoxicity, autofluorescence and biological sample scattering, photobleaching properties of YFPs and spectral cross-talk. [29, 74] Thus, GFP-RFP FRET pair could potentially overcome these limitations. Both mScarlet and mScarlet-I have been explored to use as acceptor in FRET biosensors. [40, 75, 76] We believe that cpmScarlet will be a valuable asset, as a donor or acceptor, for developing new FRET biosensors.

In summary, we first circularly permutated the brightest RFP to create a cpmScarlet, which then became the fluorescence readout modality of a genetically encoded red fluorescent hydrogen peroxide biosensor (SHRIMP). We characterized it *in vitro*, in cultured mammalian cells and in biological tissues for imaging chemically induced and physiologically relevant hydrogen peroxide generation. SHRIMP has also been demonstrated for multichannel imaging with green calcium indicator in mammalian cells. This work provides insights for expanding usage of new cpFP variant for further development of GERIs, which is expected to enable new studies in various signaling or pathological conditions.

4.6 Reference

1. Dickinson, B. C.; Chang, C. J., Chemistry and biology of reactive oxygen species in signaling or stress responses. *Nat. Chem. Biol.* **2011,** *7* (8), 504-11.
2. Valko, M.; Rhodes, C.; Moncol, J.; Izakovic, M.; Mazur, M., Free radicals, metals and antioxidants in oxidative stress-induced cancer. *Chemico-biological interactions* **2006,** *160* (1), 1-40.
3. Barnham, K. J.; Masters, C. L.; Bush, A. I., Neurodegenerative diseases and oxidative stress. *Nature reviews Drug discovery* **2004,** *3* (3), 205-214.
4. Liguori, I.; Russo, G.; Curcio, F.; Bulli, G.; Aran, L.; Della-Morte, D.; Gargiulo, G.; Testa, G.; Cacciatore, F.; Bonaduce, D., Oxidative stress, aging, and diseases. *Clin. Interv. Aging* **2018,** *13*, 757.
5. Lambeth, J. D., NOX enzymes and the biology of reactive oxygen. *Nature Reviews Immunology* **2004,** *4* (3), 181-189.
6. Antelmann, H.; Helmann, J. D., Thiol-based redox switches and gene regulation. *Antioxid. Redox Signal.* **2011,** *14* (6), 1049-1063.
7. Tiganis, T., Reactive oxygen species and insulin resistance: the good, the bad and the ugly. *Trends Pharmacol. Sci.* **2011,** *32* (2), 82-89.
8. Bae, Y. S.; Kang, S. W.; Seo, M. S.; Baines, I. C.; Tekle, E.; Chock, P. B.; Rhee, S. G., Epidermal growth factor (EGF)-induced generation of hydrogen peroxide: role in EGF receptor-mediated tyrosine phosphorylation. *J. Biol. Chem.* **1997,** *272* (1), 217-221.
9. Corcoran, A.; Cotter, T. G., Redox regulation of protein kinases. *The FEBS journal* **2013,** *280* (9), 1944-1965.
10. Lennicke, C.; Rahn, J.; Lichtenfels, R.; Wessjohann, L. A.; Seliger, B., Hydrogen peroxide–production, fate and role in redox signaling of tumor cells. *Cell Communication and Signaling* **2015,** *13* (1), 1-19.
11. Schieber, M.; Chandel, N. S., ROS function in redox signaling and oxidative stress. *Curr. Biol.* **2014,** *24* (10), R453-R462.
12. Holmström, K. M.; Finkel, T., Cellular mechanisms and physiological consequences of redox-dependent signalling. *Nat. Rev. Mol. Cell Biol.* **2014,** *15* (6), 411-421.
13. Jackson, M. J., Control of reactive oxygen species production in contracting skeletal muscle. *Antioxid. Redox Signal.* **2011,** *15* (9), 2477-2486.
14. Pang, Y.; Zhang, H.; Ai, H.-w., Genetically Encoded Fluorescent Redox Indicators for Unveiling Redox Signaling and Oxidative Toxicity. *Chem. Res. Toxicol.* **2021,** *34* (8), 1826-1845.
15. Hanson, G. T.; Aggeler, R.; Oglesbee, D.; Cannon, M.; Capaldi, R. A.; Tsien, R. Y.; Remington, S. J., Investigating mitochondrial redox potential with redox-sensitive green fluorescent protein indicators. *J. Biol. Chem.* **2004,** *279* (13), 13044-53.
16. Ostergaard, H.; Henriksen, A.; Hansen, F. G.; Winther, J. R., Shedding light on disulfide bond formation: engineering a redox switch in green fluorescent protein. *EMBO J.* **2001,** *20* (21), 5853-62.
17. Dooley, C. T.; Dore, T. M.; Hanson, G. T.; Jackson, W. C.; Remington, S. J.; Tsien, R. Y., Imaging dynamic redox changes in mammalian cells with green fluorescent protein indicators. *J. Biol. Chem.* **2004,** *279* (21), 22284-93.

18. Gutscher, M.; Pauleau, A. L.; Marty, L.; Brach, T.; Wabnitz, G. H.; Samstag, Y.; Meyer, A. J.; Dick, T. P., Real-time imaging of the intracellular glutathione redox potential. *Nat. Methods* **2008,** *5* (6), 553-9.
19. Belousov, V. V.; Fradkov, A. F.; Lukyanov, K. A.; Staroverov, D. B.; Shakhbazov, K. S.; Terskikh, A. V.; Lukyanov, S., Genetically encoded fluorescent indicator for intracellular hydrogen peroxide. *Nat. Methods* **2006,** *3* (4), 281-6.
20. Markvicheva, K. N.; Bilan, D. S.; Mishina, N. M.; Gorokhovatsky, A. Y.; Vinokurov, L. M.; Lukyanov, S.; Belousov, V. V., A genetically encoded sensor for H2O2 with expanded dynamic range. *Biorg. Med. Chem.* **2011,** *19* (3), 1079-1084.
21. Bilan, D. S.; Pase, L.; Joosen, L.; Gorokhovatsky, A. Y.; Ermakova, Y. G.; Gadella, T. W.; Grabher, C.; Schultz, C.; Lukyanov, S.; Belousov, V. V., HyPer-3: a genetically encoded H(2)O(2) probe with improved performance for ratiometric and fluorescence lifetime imaging. *ACS Chem. Biol.* **2013,** *8* (3), 535-42.
22. Icha, J.; Weber, M.; Waters, J. C.; Norden, C., Phototoxicity in live fluorescence microscopy, and how to avoid it. *Bioessays* **2017,** *39* (8), 1700003.
23. Ermakova, Y. G.; Bilan, D. S.; Matlashov, M. E.; Mishina, N. M.; Markvicheva, K. N.; Subach, O. M.; Subach, F. V.; Bogeski, I.; Hoth, M.; Enikolopov, G.; Belousov, V. V., Red fluorescent genetically encoded indicator for intracellular hydrogen peroxide. *Nat Commun* **2014,** *5*, 5222.
24. Shaner, N. C.; Lin, M. Z.; McKeown, M. R.; Steinbach, P. A.; Hazelwood, K. L.; Davidson, M. W.; Tsien, R. Y., Improving the photostability of bright monomeric orange and red fluorescent proteins. *Nat. Methods* **2008,** *5* (6), 545.
25. Fan, Y.; Chen, Z.; Ai, H. W., Monitoring redox dynamics in living cells with a redox-sensitive red fluorescent protein. *Anal. Chem.* **2015,** *87* (5), 2802-10.
26. Fan, Y.; Ai, H. W., Development of redox-sensitive red fluorescent proteins for imaging redox dynamics in cellular compartments. *Anal. Bioanal. Chem.* **2016,** *408* (11), 2901-11.
27. Fan, Y.; Makar, M.; Wang, M. X.; Ai, H. W., Monitoring thioredoxin redox with a genetically encoded red fluorescent biosensor. *Nat. Chem. Biol.* **2017,** *13* (9), 1045-1052.
28. Pang, Y.; Zhang, H.; Ai, H.-w., Improved Red Fluorescent Redox Indicators for Monitoring Cytosolic and Mitochondrial Thioredoxin Redox Dynamics. *Biochemistry* **2022,** *61* (5), 377-384.
29. Lam, A. J.; St-Pierre, F.; Gong, Y.; Marshall, J. D.; Cranfill, P. J.; Baird, M. A.; McKeown, M. R.; Wiedenmann, J.; Davidson, M. W.; Schnitzer, M. J., Improving FRET dynamic range with bright green and red fluorescent proteins. *Nat. Methods* **2012,** *9* (10), 1005-1012.
30. Shaner, N. C.; Campbell, R. E.; Steinbach, P. A.; Giepmans, B. N.; Palmer, A. E.; Tsien, R. Y., Improved monomeric red, orange and yellow fluorescent proteins derived from Discosoma sp. red fluorescent protein. *Nat. Biotechnol.* **2004,** *22* (12), 1567-72.
31. Piattoni, C. V.; Sardi, F.; Klein, F.; Pantano, S.; Bollati-Fogolin, M.; Comini, M., New red-shifted fluorescent biosensor for monitoring intracellular redox changes. *Free Radic. Biol. Med.* **2019,** *134*, 545-554.
32. Shokhina, A. G.; Kostyuk, A. I.; Ermakova, Y. G.; Panova, A. S.; Staroverov, D. B.; Egorov, E. S.; Baranov, M. S.; van Belle, G. J.; Katschinski, D. M.; Belousov,

V. V.; Bilan, D. S., Red fluorescent redox-sensitive biosensor Grx1-roCherry. *Redox Biol* **2019,** *21*, 101071.
33. Chudakov, D. M.; Verkhusha, V. V.; Staroverov, D. B.; Souslova, E. A.; Lukyanov, S.; Lukyanov, K. A., Photoswitchable cyan fluorescent protein for protein tracking. *Nat. Biotechnol.* **2004,** *22* (11), 1435-1439.
34. Akerboom, J.; Carreras Calderón, N.; Tian, L.; Wabnig, S.; Prigge, M.; Tolö, J.; Gordus, A.; Orger, M. B.; Severi, K. E.; Macklin, J. J., Genetically encoded calcium indicators for multi-color neural activity imaging and combination with optogenetics. *Front. Mol. Neurosci.* **2013,** *6*, 2.
35. Wu, J.; Liu, L.; Matsuda, T.; Zhao, Y.; Rebane, A.; Drobizhev, M.; Chang, Y.-F.; Araki, S.; Arai, Y.; March, K., Improved orange and red Ca2+ indicators and photophysical considerations for optogenetic applications. *ACS Chem. Neurosci.* **2013,** *4* (6), 963-972.
36. Bindels, D. S.; Haarbosch, L.; Van Weeren, L.; Postma, M.; Wiese, K. E.; Mastop, M.; Aumonier, S.; Gotthard, G.; Royant, A.; Hink, M. A., mScarlet: a bright monomeric red fluorescent protein for cellular imaging. *Nat. Methods* **2017,** *14* (1), 53-56.
37. Head, B.; La Du, J.; Barton, C.; Zhang, J.; Wong, C.; Ho, E.; Tanguay, R. L.; Traber, M. G., RedEfish: generation of the polycistronic mScarlet: GSG-T2A: Ttpa zebrafish line. *Antioxidants* **2021,** *10* (6), 965.
38. Nouri, P.; Zimmer, A.; Brüggemann, S.; Friedrich, R.; Kühn, R.; Prakash, N., Generation of a NES-mScarlet red fluorescent reporter human iPSC line for live cell imaging and flow cytometric analysis and sorting using CRISPR-Cas9-mediated gene editing. *Cells* **2022,** *11* (2), 268.
39. Liu, A.; Huang, X.; He, W.; Xue, F.; Yang, Y.; Liu, J.; Chen, L.; Yuan, L.; Xu, P., pHmScarlet is a pH-sensitive red fluorescent protein to monitor exocytosis docking and fusion steps. *Nat. Commun.* **2021,** *12* (1), 1-12.
40. Gohil, K.; Wu, S.-Y.; Takahashi-Yamashiro, K.; Shen, Y.; Campbell, R. E., Biosensor Optimization Using a Förster Resonance Energy Transfer Pair Based on mScarlet Red Fluorescent Protein and an mScarlet-Derived Green Fluorescent Protein. *ACS Sens.* **2023**.
41. Subach, O. M.; Vlaskina, A. V.; Agapova, Y. K.; Dorovatovskii, P. V.; Nikolaeva, A. Y.; Ivashkina, O. I.; Popov, V. O.; Piatkevich, K. D.; Khrenova, M. G.; Smirnova, T. A., LSSmScarlet, dCyRFP2s, dCyOFP2s and CRISPRed2s, Genetically Encoded Red Fluorescent Proteins with a Large Stokes Shift. *Int. J. Mol. Sci.* **2021,** *22* (23), 12887.
42. Zhao, Y.; Araki, S.; Wu, J.; Teramoto, T.; Chang, Y. F.; Nakano, M.; Abdelfattah, A. S.; Fujiwara, M.; Ishihara, T.; Nagai, T.; Campbell, R. E., An Expanded Palette of Genetically Encoded Ca2+ Indicators. *Science* **2011,** *333* (6051), 1888-1891.
43. Chen, T.-W.; Wardill, T. J.; Sun, Y.; Pulver, S. R.; Renninger, S. L.; Baohan, A.; Schreiter, E. R.; Kerr, R. A.; Orger, M. B.; Jayaraman, V., Ultrasensitive fluorescent proteins for imaging neuronal activity. *Nature* **2013,** *499* (7458), 295-300.
44. Zhao, Y.; Hu, Q.; Cheng, F.; Su, N.; Wang, A.; Zou, Y.; Hu, H.; Chen, X.; Zhou, H. M.; Huang, X.; Yang, K.; Zhu, Q.; Wang, X.; Yi, J.; Zhu, L.; Qian, X.; Chen, L.; Tang, Y.; Loscalzo, J.; Yang, Y., SoNar, a Highly Responsive NAD+/NADH

Sensor, Allows High-Throughput Metabolic Screening of Anti-tumor Agents. *Cell Metab.* **2015,** *21* (5), 777-89.
45. Topell, S.; Hennecke, J.; Glockshuber, R., Circularly permuted variants of the green fluorescent protein. *FEBS Lett.* **1999,** *457* (2), 283-289.
46. Baird, G. S.; Zacharias, D. A.; Tsien, R. Y., Circular permutation and receptor insertion within green fluorescent proteins. *Proc. Natl. Acad. Sci. U.S.A.* **1999,** *96* (20), 11241-11246.
47. Gibson, D. G.; Young, L.; Chuang, R. Y.; Venter, J. C.; Hutchison, C. A., 3rd; Smith, H. O., Enzymatic assembly of DNA molecules up to several hundred kilobases. *Nat. Methods* **2009,** *6* (5), 343-5.
48. Wu, T.; Pang, Y.; Ai, H.-w., Circularly permuted far-red fluorescent proteins. *Biosensors* **2021,** *11* (11), 438.
49. Chen, Z.-j.; Ren, W.; Wright, Q. E.; Ai, H.-w., Genetically encoded fluorescent probe for the selective detection of peroxynitrite. *Journal of the American Chemical Society* **2013,** *135* (40), 14940-14943.
50. Schindelin, J.; Arganda-Carreras, I.; Frise, E.; Kaynig, V.; Longair, M.; Pietzsch, T.; Preibisch, S.; Rueden, C.; Saalfeld, S.; Schmid, B., Fiji: an open-source platform for biological-image analysis. *Nat. Methods* **2012,** *9* (7), 676-682.
51. Rego, M.; Hanley, L. M.; Ersing, I.; Guerin, K.; Tasissa, M.; Haery, L.; Mueller, I.; Sanders, E.; Fan, M., Improved yield of AAV2 and rAAV2-retro serotypes following sugar supplementation during the viral production phase. *bioRxiv* **2018**, 488585.
52. Wang, Y.; Wang, S.; Harvat, T.; Kinzer, K.; Zhang, L.; Feng, F.; Qi, M.; Oberholzer, J., Diazoxide, a KATP channel opener, prevents ischemia–reperfusion injury in rodent pancreatic islets. *Cell Transplant.* **2015,** *24* (1), 25-36.
53. Zhang, J.; Li, Z.; Pang, Y.; Fan, Y.; Ai, H., Genetically Encoded Boronolectin as a Specific Red Fluorescent UDP-GlcNAc Biosensor. *bioRxiv* **2023**, 2023.03. 01.530644.
54. Swindle, E. J.; Hunt, J. A.; Coleman, J. W., A comparison of reactive oxygen species generation by rat peritoneal macrophages and mast cells using the highly sensitive real-time chemiluminescent probe pholasin: inhibition of antigen-induced mast cell degranulation by macrophage-derived hydrogen peroxide. *The Journal of Immunology* **2002,** *169* (10), 5866-5873.
55. Forman, H. J.; Torres, M., Reactive oxygen species and cell signaling: respiratory burst in macrophage signaling. *American journal of respiratory and critical care medicine* **2002,** *166* (supplement_1), S4-S8.
56. Rada, B.; Leto, T. L., Oxidative innate immune defenses by Nox/Duox family NADPH oxidases. *Trends in Innate Immunity* **2008,** *15*, 164-187.
57. Pick, E.; Keisari, Y., Superoxide anion and hydrogen peroxide production by chemically elicited peritoneal macrophages—induction by multiple nonphagocytic stimuli. *Cell. Immunol.* **1981,** *59* (2), 301-318.
58. Segal, A. W.; Abo, A., The biochemical basis of the NADPH oxidase of phagocytes. *Trends in biochemical sciences* **1993,** *18* (2), 43-47.
59. Lenzen, S., The mechanisms of alloxan-and streptozotocin-induced diabetes. *Diabetologia* **2008,** *51* (2), 216-226.
60. Szkudelski, T., The mechanism of alloxan and streptozotocin action in B cells of the rat pancreas. *Physiol. Res.* **2001,** *50* (6), 537-546.

61. Friesen, N.; Büchau, A.; Schott-Ohly, P.; Lgssiar, A.; Gleichmann, H., Generation of hydrogen peroxide and failure of antioxidative responses in pancreatic islets of male C57BL/6 mice are associated with diabetes induced by multiple low doses of streptozotocin. *Diabetologia* **2004,** *47* (4), 676-685.
62. Komary, Z.; Tretter, L.; Adam-Vizi, V., H2O2 generation is decreased by calcium in isolated brain mitochondria. *Biochimica et Biophysica Acta (BBA)-Bioenergetics* **2008,** *1777* (7-8), 800-807.
63. Adam-Vizi, V.; Starkov, A. A., Calcium and mitochondrial reactive oxygen species generation: how to read the facts. *Journal of Alzheimer's disease* **2010,** *20* (s2), S413-S426.
64. Görlach, A.; Bertram, K.; Hudecova, S.; Krizanova, O., Calcium and ROS: A mutual interplay. *Redox Biol.* **2015,** *6*, 260-271.
65. Jaskulska, A.; Janecka, A. E.; Gach-Janczak, K., Thapsigargin—from traditional medicine to anticancer drug. *Int. J. Mol. Sci.* **2020,** *22* (1), 4.
66. Matz, M. V.; Fradkov, A. F.; Labas, Y. A.; Savitsky, A. P.; Zaraisky, A. G.; Markelov, M. L.; Lukyanov, S. A., Fluorescent proteins from nonbioluminescent Anthozoa species. *Nat. Biotechnol.* **1999,** *17* (10), 969-973.
67. Shen, Y.; Dana, H.; Abdelfattah, A. S.; Patel, R.; Shea, J.; Molina, R. S.; Rawal, B.; Rancic, V.; Chang, Y.-F.; Wu, L., A genetically encoded Ca 2+ indicator based on circularly permutated sea anemone red fluorescent protein eqFP578. *BMC Biol.* **2018,** *16*, 1-16.
68. van der Krogt, G. N.; Ogink, J.; Ponsioen, B.; Jalink, K., A comparison of donor-acceptor pairs for genetically encoded FRET sensors: application to the Epac cAMP sensor as an example. *PLoS One* **2008,** *3* (4), e1916.
69. Piljić, A.; De Diego, I.; Wilmanns, M.; Schultz, C., Rapid development of genetically encoded FRET reporters. *ACS Chem. Biol.* **2011,** *6* (7), 685-691.
70. Komatsu, N.; Aoki, K.; Yamada, M.; Yukinaga, H.; Fujita, Y.; Kamioka, Y.; Matsuda, M., Development of an optimized backbone of FRET biosensors for kinases and GTPases. *Mol. Biol. Cell* **2011,** *22* (23), 4647-4656.
71. Fritz, R. D.; Letzelter, M.; Reimann, A.; Martin, K.; Fusco, L.; Ritsma, L.; Ponsioen, B.; Fluri, E.; Schulte-Merker, S.; van Rheenen, J., A versatile toolkit to produce sensitive FRET biosensors to visualize signaling in time and space. *Science signaling* **2013,** *6* (285), rs12-rs12.
72. Nagai, T.; Yamada, S.; Tominaga, T.; Ichikawa, M.; Miyawaki, A., Expanded dynamic range of fluorescent indicators for Ca2+ by circularly permuted yellow fluorescent proteins. *Proc. Natl. Acad. Sci. U.S.A.* **2004,** *101* (29), 10554-10559.
73. Allen, M. D.; Zhang, J., Subcellular dynamics of protein kinase A activity visualized by FRET-based reporters. *Biochemical and biophysical research communications* **2006,** *348* (2), 716-721.
74. Bajar, B. T.; Wang, E. S.; Zhang, S.; Lin, M. Z.; Chu, J., A guide to fluorescent protein FRET pairs. *Sensors* **2016,** *16* (9), 1488.
75. McCullock, T. W.; MacLean, D. M.; Kammermeier, P. J., Comparing the performance of mScarlet-I, mRuby3, and mCherry as FRET acceptors for mNeonGreen. *PLoS One* **2020,** *15* (2), e0219886.

76. Zhang, D.; Redington, E.; Gong, Y., Rational engineering of ratiometric calcium sensors with bright green and red fluorescent proteins. *Communications Biology* **2021,** *4* (1), 924.

Chapter 5 Development and characterizations of a redox-active far-red biosensor for live cell imaging

5.1 Introduction

Reactive oxygen species (ROS), such as superoxide anion (O_2^-), hydrogen peroxide (H_2O_2) and hydroxyl radical (HO•), are actively involved in various physiological signaling and immune response. One well-known example is that phagocytes can produce oxidative burst through NOX2 NADPH-oxidase to eradicate pathogens. [1, 2] On the other hand, overproduction of ROS leads to oxidative stress, which can react with and damage biological components such as DNA, protein or lipids.[3] Accumulation of ROS has been associated with the initiation and progression of many pathological processes, including cancer, neurodegeneration and respiratory stress.[4-6] Understanding the mechanism of redox activities in the live cells would be crucial for unveiling the causes of diseases, leading to the development of potential therapeutics. Therefore, there is a strong demand to create effective tools for tracking and monitoring redox real-time dynamics within the natural cellular environment.

Genetically-encoded fluorescent redox indicators (GERIs) have emerged as powerful tools for detecting redox molecules in living cells due to several advantages over other detection methods. Compared to the enzymatic assays, which require cell lysis procedure, GERIs can be expressed under natural cellular milieu, minimizing the possibility of artifacts or disruption to the system being studied. Secondly, GERIs can provide real-time dynamics of redox signaling with high spatial and temporal resolution. GERIs can also be targeted to specific cell type or be readily localized to various subcellular compartments by fusing promoters/localization sequences to the

termini. Moreover, GERIs are easily modifiable and can be adapted across different study systems since they existed as plasmids or viral vectors. [7]

One simple but robust strategy to generate GERIs was incorporating cystine pairs to appropriate locations of a single fluorescent protein (FP) scaffold. The surrounding redox environment can cause the cysteine residues to form intramolecular disulfide bonds, which subsequently results in the confirmational change of the FP.[8, 9] The conformational change of FP would further modulate the photophysical properties, such as fluorescence intensity and spectrum or lifetime, of the chromophore. Thus far, a series of GERIs with different colors have been generated with this design strategy. [8-11] The cysteines residues were introduced to different locations, in proximity to chromophore, of wild-type (wt) yellow FP (YFP) and green FP (GFP) to generate rxYFP and roGFPs for general redox status measurement. [8, 9]

Compared to shorter wavelength emitting FPs, such as GFP or BFP, red and far-red emitters are favorable for imaging live specimens, specifically for whole-animal imaging. Firstly, illuminating biological samples with long-wavelength emitters can markedly lower the cytotoxic effects to maintain the samples in a healthier condition. Secondly, the red and far-red spectrum are ideal for maximal penetration of cells and tissues because they fall within the 'optical window', ranging from 600 to 1200 nm, where the endogenous absorbers display least light absorption.[12] Moreover, GERIs in longer wavelength can provide an additional channel for multi-parameter imaging with good signal-to-noise ratio due to the reduced scattering and autofluorescence.

Our group previously expanded the color palette to longer wavelength region by creating redox-active red FPs (rxRFPs). Instead of introducing cysteine pairs into the surface of a wt-FP, we attached cysteine residues to the C- and N- termini of a circularly-permutated (cp) RFP and the sensor properties were tuned by adjusting the amino acids adjacent to the active cysteines. [10, 11]

Based on our previous work, we are seeking to further expand the spectrum of redox-active single FP to the far-red region. We previously identified five circularly-permutated far-red FPs (FrFPs) based on the two bright FrFPs mMaroon1 (NCBI GenBank KX874478)[13] and mCarmine (NCBI GenBank MH062789).[14, 15] Among these mutants, cpmMaroon185-186 was utilized as readout modality to generate a genetically-encoded far-red indicator for detecting synaptically released Zn^{2+} (FRISZ). [16] In this study, we generated a redox-active FrFP, rxcpmMaroon1, via engineering the FRISZ to tune the fluorescence change in response to redox change. We performed in-vitro characterizations of rxcpmMaroon1 and applied it into different compartments to monitor the redox status of mammalian cells.

5.2 Methods and Materials

5.2.1 Reagents and General Methods

All chemicals were purchased from Thermo Fisher Scientific. Synthetic DNA oligos were purchased from Integrated DNA Technologies (IDT) or Eurofins Genomics. Restriction enzymes or other molecular biology reagents were purchased from Thermo Fisher Scientific or New England Biolabs. DNA sequences were analyzed by Eurofins Genomics. Absorbance and fluorescence spectra measurements were collected with a monochromator-based BioTek Synergy Mx Microplate Reader.

5.2.2 Engineering and Evolution of rxcpmMaroon1 and rxcpmMaroon2

Zinc hook domain were truncated with the active cysteine maintained. Next, oligonucleotides with degenerated codon were utilized to build library for optimizing the linker between active cysteines and cpmMaroon185 to achieve redox sensitivity. The amino acids

adjacent to the inserted active cysteines were then mutated by using oligonucleotides with degenerated codons. Last, error-prone based directed evolution was performed to further optimize the redox response. Take rxcpmMaroon1 as an example. First, oligonucleotides 1C-2NNK-F and pBAD-cpmMaroon-R were used to build library for optimizing linker between truncated hook domain and cpmMaroon185. The amplified insert was digested with Xho I and Hind III and ligated to a compatible pBAD/His B vector via T4 ligase. The ligation product was transformed into E. cloni® 10G competent cells and the cell culture was plated on a 2×YT agar plates supplemented with 100 μg/mL ampicillin and 0.02% (w/v) L-arabinose for incubation at 37 °C overnight. The next day, colonies with relatively good brightness under a customized imaging system[15] were selected to inoculate into a 96 deep well plate with each well containing 1 mL 2×YT supplemented with 100 μg/mL ampicillin. Cells were grown at 37 °C, 250 rpm for ~8 hr, and 0.2% (w/v) L-arabinose was added to each well to induce the protein expression. The cell culture was first incubated at room temperature, 250 rpm overnight and then transferred to 16°C, 250 rpm for another 48 h. Cells were pelleted by centrifugation the plate at 3000 ×g for 20 minutes and lysed with 300 μL Bacterial Protein Extraction Reagents (B-PER) on ice to get the cell lysate. The fluorescent intensity (excitation at 610 nm and emission at 660 nm) of each cell lysate with or without DTT addition was examined using a BioTek Synergy Mx Microplate Reader. Second, after identifying a mutant with some redox response, oligonucleotides 1XC-F/1CX-F and pBAD-cpmMaroon-R were used to adjust the amino acid next to the active cysteines. Last, the best mutant was selected for further directed evolution with oligonucleotides pBAD-F and pBAD-R. Different libraries were all cloned and screened as above-mentioned protocol. Similar engineering process was applied to generate rxcpmMaroon2 with different pairs of oligonucleotides. Oligonucleotides pair 2C-2NNK-F and 2C-2NNK-R were used for linker optimization of rxcpmMaroon2.

Oligonucleotides 2XC-F/2CX-R and 2CX-F/2XC-R were used to mutate and screen the amino acids adjacent to the active cysteines. Last, pBAD-F and pBAD-R were used for directed evolution of rxcpmMaroon2. All oligonucleotides were listed in **Table 5.1**.

Table 5.1 Oligonucleotides used in this study.

Primers	Sequence 5'- 3'
1C-2NNK-F	ctcgagaccactgtgctatgctgaattaacagatnnknnkaagaaacccgcaaag
pBAD-cpmMaroon-R	aagcttatttcttggatctgtatgtggtt
1XC-F	ctcgagaccannktgctatgctgaattaacagatagtagtaagaaacccgcaaag
1CX-F	ctcgagaccactgtgcnnkgctgaattaacagatagtagtaagaaacccgcaaag
2C-2NNK-F	ccgagctcgagaccagtatgcggtgctgaattaacagatnnknnkaagaaacccgcaaa
2C-2NNK-R	gccaaaacagccaaagcttacacagggcacttacctttagcactmnnmnnnttcttgga
2XC-F	ccgagctcgagaccannktgcggtgctgaattaacagat
2CX-R	cgccaaaacagccaagcttacacagggcgmnnacatttag
2CX-F	ccgagctcgagaccagtatgcnnkgctgaattaacagat
2XC-R	cgccaaaacagccaagcttacacagggcgtttacamnnagc
pBAD-F	atgacgataaggatccgagctcgag
pBAD-R	ctcatccgccaaaacagccaaagctta
pcDNA3-rxcpmMaroon1-F1	cgataaggatccgagctcgagaccactgtgctatgctgaattaac
pcDNA3-rxcpmMaroon1-R1	ctatagaatagggccctctagattatttcttggatctgtatgtggtt
pcDNA3-rxcpmMaroon2-F2	atccgagctcgagcccagtatgcggtgctgaattaac
pcDNA3-rxcpmMaroon2-R2	tagaatagggccctctagattacacagggcacttacctttagc
pMito-rxcpmMaroon1-F1	atccattcgttgggggataccggtcatcatcatcatcatcatggtatggc
pMito-rxcpmMaroon1-R1	tacgactcactatagttctagaggctcgagttatttcttggatctgtatgtggttt
pMito-rxcpmMaroon2-R2	taatacgactcactatagttctagaggctcgagttacacagggcacttaccttt

5.2.3 Protein expression and purification

pBAD-rxcpmMaroon1 or pBAD-rxcpmMaroon2 plasmid was transformed into E. cloni® 10G competent cells (Lucigen) and the cell culture was subsequently plated on 2×YT agar plates supplemented with 100 μg/mL ampicillin and 0.02% (w/v) L-arabinose. The plates were incubated at 37 °C overnight and a single colony was next selected to inoculate a 5 mL 2×YT starter culture supplemented with 100 μg/mL ampicillin. The starter culture was incubated at 37 °C with shaking at 250 rpm overnight, followed by a 100-fold dilution into 500 mL 2×YT supplemented with 100 μg/mL ampicillin. When the optical density at 600 nm (OD_{600}) reached around 0.6, a final concentration of 0.2% (w/v) L-arabinose was added to induce the protein expression. The culture was shaken 250 rpm at room temperature for 24 hr and next moved to 16 °C and 250 rpm for another 48 h. Bacterial cells were then collected by centrifugation at 4150 ×g for 20 min. The cell pellet was resuspended in 1× phosphate-buffered saline (PBS, pH 7.4) and sonication was performed to lyse the cells. After removing the cell debris by centrifuge at 15000 ×g for 30 min at 4 °C, the His6-tagged protein purified via Ni-NTA agarose beads (Genesee Scientific) according to the manufacturer's instructions. The eluted proteins were further applied to a size-exclusion HiLoad 16/600 Superdex 200 pg column (Cytiva) and eluted with 1× PBS (pH 7.4).

5.2.4 In vitro characterization

Protein concentration was determined via the alkali denaturation method. Excitation and emission spectra of 1 μM purified protein in 1 × PBS (pH 7.4) were recorded respectively. To record excitation spectra, the emission wavelength was set at 660 nm, and the excitation spectrum was scanned from 500 to 640 nm. Similarly, the excitation wavelength was set at 590 nm, and the emission spectrum was scanned from 610 to 780 nm. mMaroon1 (QY = 0.11) was used as the

reference and quantum yields were determined according to a published protocol.[17] To fully reduce the protein, concentrated proteins (10 μM) was incubated with 10 mM DTT in sealed microcentrifuge tubes and stored in a oxygen-free dome at room temperature overnight. The fluorescence intensity after DTT overnight treatment was compared with fully oxidized purified protein to achieve the maximal redox dynamic change. To determine the pH-profile of purified protein, a series of liquid buffer (200mM citric acid and 200 mM boric acid) with pH within 3-10 were incubated with 1 μM purified protein. The fluorescence intensities were recorded using the BioTek Synergy Mx Microplate Reader. Fluorescence intensities at each pH value were recorded with excitation set at 610 nm and emission at 660 nm. The fluorescence intensities were plotted against different pH values. To determine the redox titration of purified protein to the GSSG/GSH mixtures, 1 μM of protein was incubated with oxidized glutathione (1 – 2000 μM) mixed with reduced glutathione (1 – 100 mM) in sealed microcentrifuge tubes at RT. Next, fluorescence intensity endpoints were measured on the microplate reader with excitation and emission wavelength set at 610 nm and 660 nm respectively.

5.2.5 Construction of mammalian cell expression plasmid

Oligonucleotides pcDNA3-rxcpmMaroon1-F1 and pcDNA3-rxcpmMaroon1-R1 were used to amplify rxcpmMaroon1 from the plasmid pBAD-rxcpmMaroon1. The amplified product was Gibson assembly into a compatible pcDNA3 vector predigested with Xho I and Xba I. To attach mitochondria localization sequence (MLS) to the N-terminal of rxcpmMaroon1, oligonucleotides pMito-rxcpmMaroon1-F1 and pMito-rxcpmMaroon1-R1 were utilized to amplify rxcpmMaroon1 insert from corresponding pcDNA3 plasmid. The amplified product was ligated with a pCS2+ vector predigested with Age I and Xba I via T4 ligase. The pcDNA3- or

pMito-rxcpmMaroon2 was prepared as the same procedure with oligonucleotides pcDNA3-rxcpmMaroon2-F2 and pcDNA3-rxcpmMaroon2-R2 or pMito-rxcpmMaroon1-F1 and pMito-rxcpmMaroon2-R2 (**Table 5.1**).

5.2.6 Imaging redox response in cultured mammalian cells

Human Embryonic Kidney (HEK) 293T cells were cultured in Dulbecco's Modified Eagle's Medium (DMEM) with 10% fetal bovine serum (FBS) at 37 °C with 5% CO_2 humidified air. Cells were seeded into 35 mm culture dishes and mammalian cell expression plasmids were transfected at 70% confluency. For set up the transfection reaction, 3 μg of plasmid DNA was mixed with 9 μg of PEI (polyethylenimine, linear, M.W. 25kD) following manufacture's instruction. Cells were imaged in 1× Dulbecco's Phosphate Buffered Saline (DPBS) with 1 mM Ca^{2+}, 1 mM Mg^{2+} 48 hr post-transfection. For time-lapse series, aldrithiol-2 was added to the cells and the fluorescence signals were recorded with Leica DMi8 microscope equipped with a Photometrics Prime 95B Scientific CMOS (complementary metal-oxide semiconductor) camera. through a Cy5 filter set (Iridian, catalog no. FFS000008), which contains a 628/40 nm band-pass excitation filter and a 692/40 nm band-pass emission filter.

5.3 Results and Discussion

5.3.1 Engineering redox-sensitive far-red fluorescent biosensor

Inspired by our previous development of a far-red Zinc sensor by fusing the circularly-permutated far-red protein (cpmMaroon185),[16] we speculated that cpmMaroon185 can be tuned to be a redox-active far-red biosensor via protein engineering. We first truncated the zinc hook domain in FRISZ to minimize the zinc response but still maintain the active cysteine residues. Two

versions were initially generated. One version was created by fusing cpmMaroon185 with a single truncated hook domain at its N-terminus. The other version was built by fusing two truncated hook domains at the N- and C- terminus of cpmMaroon185 respectively (**Figure 5.1A**). After obtaining two parental mutants, we utilized degenerate codon to build libraries for screening the linker between truncated hook domain and cpmMaroon185. The fluorescence intensity of protein crude lysate with or without DTT were measured. We identified two promising variants, showing ~114% and 150% fluorescence increase respectively upon oxidation (**Figure 5.1A**). With the initial success, we further engineered the amino acids adjacent to the active cysteine residues to adjust the environment around the cysteine. One residue at each end of active cysteine was fully randomized to build library for screening. The mutant with good brightness and improved fluorescence change was selected for next stage engineering. Last, we performed error-prone polymerase chain reaction (EP-PCR)-based directed evolution to screen for variant with better brightness and greater response to DTT addition. After several rounds of directed evolution, we identified two variants with enhanced fluorescence change. We termed one variant rxcpmMaroon1 which presented ~150% fluorescence turn-on when fully oxidized. The other variant was named rxcpmMaroon2 with ~200% fluorescence increases in the fully oxidized state (**Figure 5.1A**).

We then aligned the sequence of rxcpmMaroon1 and rxcpmMaroon2 to their corresponding parental variants. As to rxcpmMaroon1, the linker between truncated hook domain and cpmMaroon185 changed from Gly-Ser to Ser-Ser and 2 mutations were gained through the engineering process. As to rxcpmMaroon2, the linkers were maintained the same as FRISZ while 6 mutations were gained via the sensor development (**Figure 5.1B**).

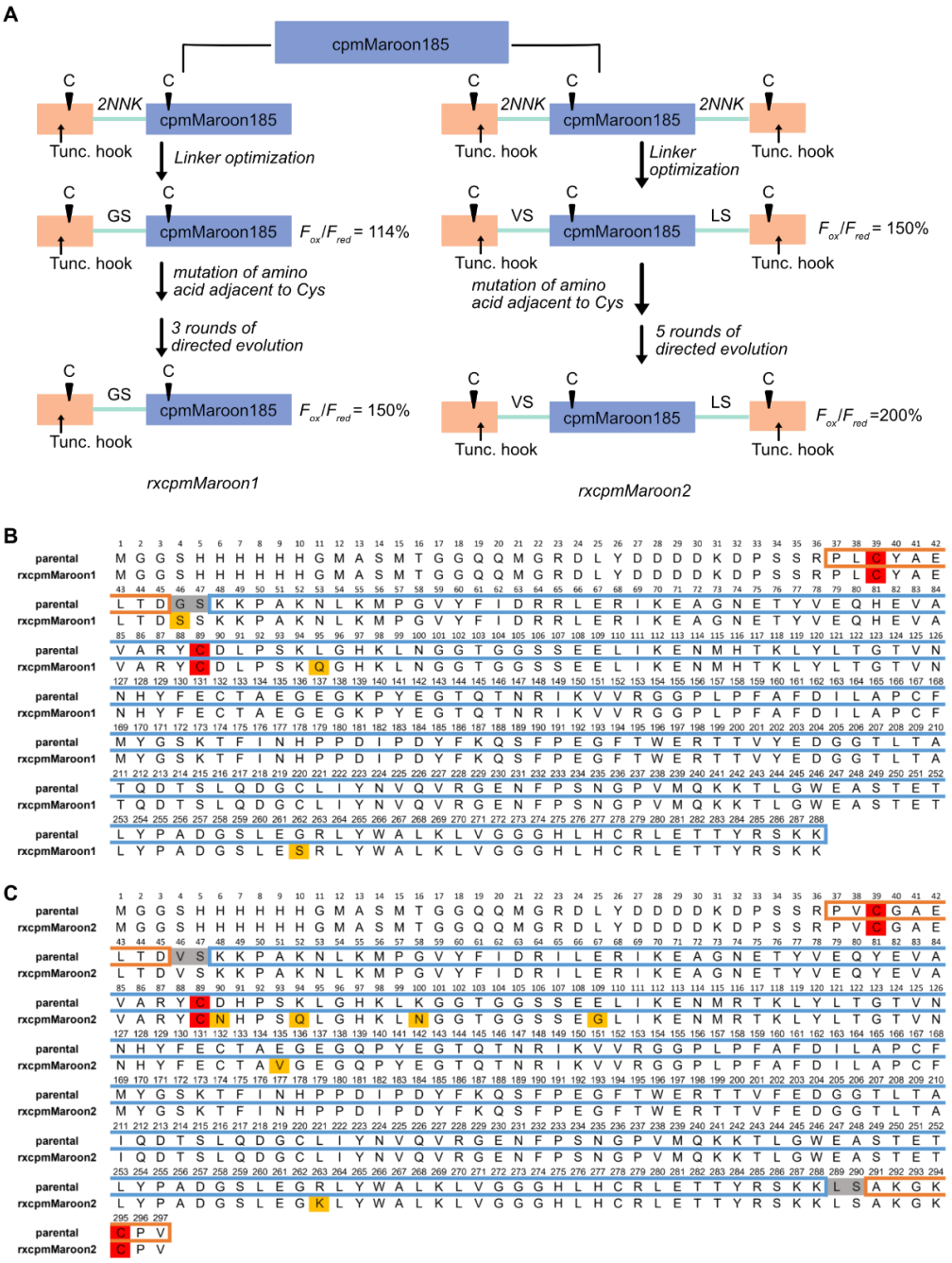

Figure 5.1 Engineering and sequence alignments of redox-active far-red biosensors.

(A) Engineering process of rxcpmMaroon1 (left panel) and rxcpmMaroon2 (right panel). **(B)** Sequence alignments of rxcpmMaroon1 and corresponding parental mutant. **(C)** Sequence alignments of rxcpmMaroon2 and corresponding parental mutant. The active cysteines are highlighted in red, mutations obtained through engineering are highlighted in orange. Linker between truncated hook domain and cpmMaroon185 are highlighted in grey. Orange boxes represent the truncated hook domain. Blue box represents the cpmMaroon185.

5.3.2 In vitro characterizations of rxcpmMaroon1 and rxcpmMaroon2

Both rxcpmMaroon1 and rxcpmMaroon2 were purified for in-vitro characterizations of their redox properties. At pH 7.4, rxcpmMaroon1 displayed an excitation peak at 610 nm and emission peak at 650 nm. The fluorescence intensity at the oxidized status were ~2-fold higher than that of the reduced status (**Figure 5.2A**). Similarly, rxcpmMaroon2 showed maximal excitation peak at 610 nm and emission peak at 660 nm in both oxidized and reduced state. The fluorescence intensity of rxcpmMaroon2 increased a maximal ~3-fold when it was fully oxidized (**Figure 5.2D**). Both redox-active far-red biosensors maintained the similar fluorescence spectra properties as mMaroon1, the parental mutant for creating cpmMaroon185.

We next measured the pH profile of both oxidized and reduced rxcpmMaroon1 under buffer ranging from 3-10. We derived the apparent pKa value as 8.0 for both states (**Figure 5.2B**). The apparent pKa of rxcpmMaroon2 for both redox states were also derived as 8.2 from its pH profile (**Figure 5.2E**). The apparent pKa of rxcpmMaroon1/2 were higher than mMaroon1 (pKa 6.2)[13] and their fluorescence intensity were sensitive to the pH change around the physiological range (~pH 7.4), which is similar to the pKa of cpmMaroon185 (pKa 7.7).[15]

We then further perform redox titration to measure the fluorescence response of rxcpmMaroon1/2 to a series of reduced/oxidized glutathione (GSH/GSSG) buffers with different redox potentials (**Figure 5.2C & F**). Purified rxcpmMaroon1/2 was incubated with a collection of GSH/GSSH mixture for 20 min at room temperature to achieve equilibration at pH 7.4. Fluorescence intensities were plotted against different $[GSH]^2/[GSSG]$ ratios.

The apparent equilibrium constant for the oxidation reaction (K_{ox}) was derived from the redox titration curve. The K_{ox} for rxcpmMaroon1 and rxcpmMaroon2 were determined as 0.16 M

and 0.45 M respectively. According to the GSH/GSSG redox pair standard redox potential of -264 mV at pH 7.4,[18] the midpoint redox potential of rxcpmMaroon1 and rxcpmMaroon2 were determined to be -264 mV and -299 mV at pH 7.4. These values were comparable to the previous reported redox-active fluorescent protein biosensors.[10, 19] Compared to rxYFP, roGFPs and rxRFPs,[10, 19] rxcpmMaroon1/2 have further red-shifted spectrum and allow for reduced biological sample autofluorescence, enhanced tissue penetration and lower cytotoxicity. They also provide an additional channel for integration into multicolor imaging.

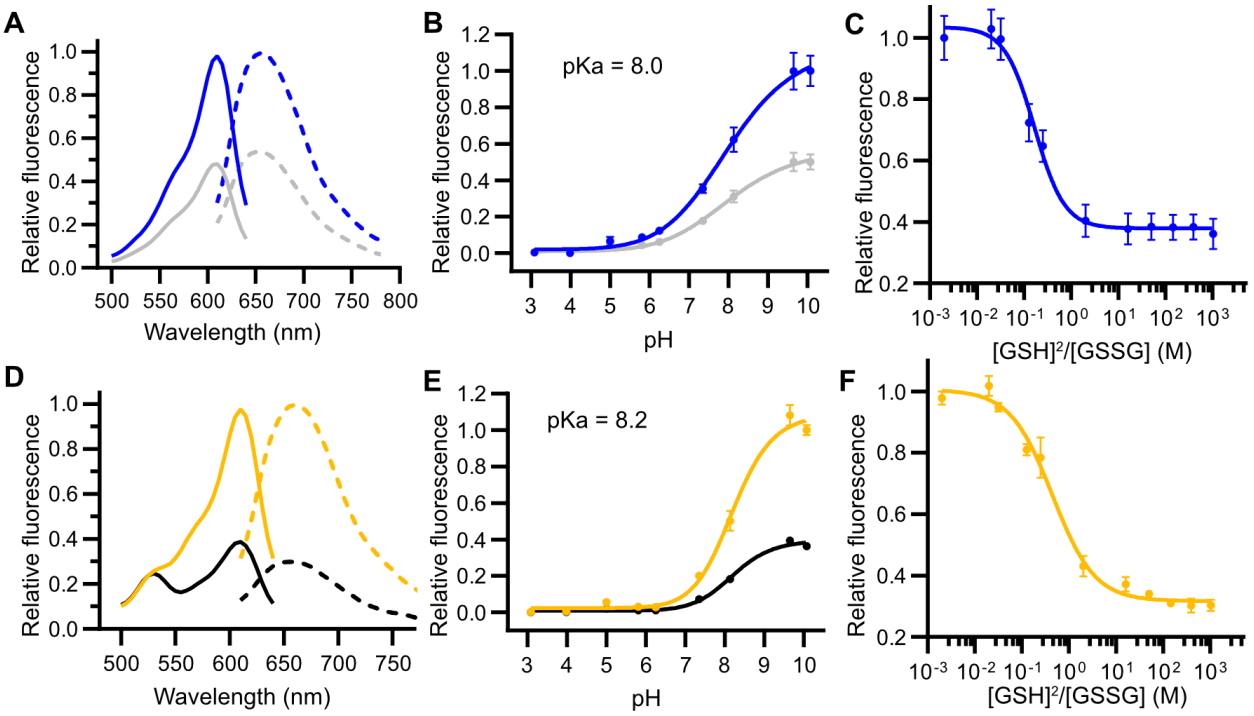

Figure 5.2 In vitro characterizations of rxcpmMaroon1 and rxcpmMaroon2.

(A & D) Fluorescence spectra of rxcpmMaroon1 in fully oxidized (blue) and fully reduced (grey) state or rxcpmMaroon2 in fully oxidized (orange) and fully reduced (black) state. Solid line represents excitation spectrum and dotted line represents emission spectrum. **(B & E)** pH profile of oxidized (blue) and reduced (grey) rxcpmMaroon1 or oxidized (orange) and reduced (black) rxcpmMaroon2. **(C & F)** Redox titration curve of rxcpmMaroon1(blue) or rxcpmMaroon2 (orange) with mixture of reduced and oxidized glutathione.

We also measured the fluorescence properties of these two redox-active far-red biosensors (**Table 5.2**). The oxidized rxcpmMaroon1 displayed similar brightness as cpmMaroon185. The quantum yield and extinction coefficient of rxcpmMaroon1 both changed when turning from oxidized state to reduced state. As to rxcpmMaroon2, it is much dimmer compared to rxcpmMaroon1. The greatest brightness of oxidized rxcpmMaroon2 was only 16% of oxidized rxcpmMaroon1, and only 9% of mMaroon1. The reduced rxcpmMaroon2 was even 3-fold dimmer than the oxidized state. And the preliminary test of both sensors in mammalian cells showed that rxcpmMaroon2 was difficult to detect even after 48-72hr transfection (data not shown). Therefore, we decided to perform following mammalian cell imaging only with rxcpmMaroon1.

Table 5.2 Fluorescent properties of rxcpmMaroon1 and rxcpmMaroon2.

Protein	Redox State	Quantum Yield (Φ)[a]	Extinction Coefficient (ε, mM^{-1} cm^{-1}) [a,b]	Brightness[c]	Midpoint potential (mV)[d]
rxcpmMaroon1	Oxidized	0.12	42.8	5.14	-264 mV
	Reduced	0.08	30.7	2.46	
rxcpmMaroon2	Oxidized	0.032	25.7	0.82	-299 mV
	Reduced	0.011	22.5	0.25	

a Values are measured at pH 7.4. b the concentration was measured by using alkaline denaturation method. c product of Φ and ε. d Derived from fluorescence measurements of proteins equilibrated with a series of GSH and GSSG mixture.

5.3.3 Mammalian cell imaging of rxcpmMaroon1 in cytosol and mitochondria of HEK 293T

To assess the performance of rxcpmMaroon1 in mammalian cells, we first transiently transfected pcDNA3-rxcpmMaroon1 in HEK 293T cells. Bright far-red fluorescence was observed in cytosol after 48 hr transfection, indicating the successful formation of chromophore in cultured mammalian cells. Next, a cell-permeable oxidant, aldrithiol-2 (500 μM) was added to stimulate the rxcpmMaroon1-expressing cells. The fluorescence intensity increase ~25% within 2 min and maintained at that level during the whole imaging period (**Figure 5.3A and 5.3B**). We also localized rxcpmMaroon1 into the mitochondria of HEK 293T cells by attaching repetitive mitochondrial localization sequence (MLS) to its N-terminus. Bright far-red fluorescence in mitochondria was also detectable under fluorescence microscopy with Cy5 filter. However, the fluorescence change pattern in response to aldrithiol-2 in mitochondria was different to that of cytosol. The fluorescence increased ~30% within 5 min and then decreased gradually (**Figure 5.3C and 5.3D**). We speculated that this different performance may due to the different basal redox potential of cytosol and mitochondria.[19] Since mitocondria is a more reducing compartment compared to cytosol, rxcpmMaroon1 may not be able to stay at the fully oxidized status in the mitochondria. As a result, the fluorescence decrease gradually after initial escalation.

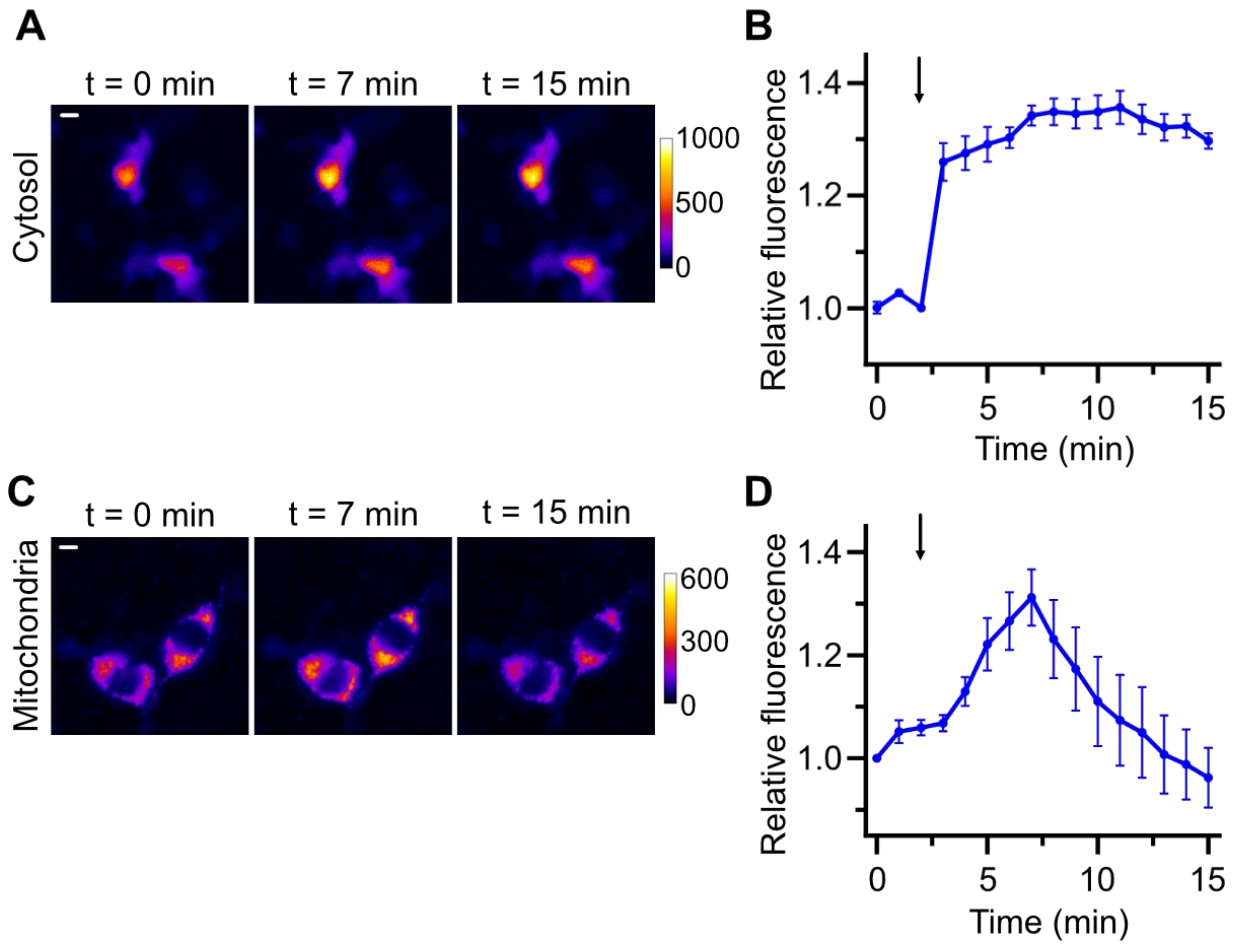

Figure 5.3 Mammalian cell imaging of rxcpmMaroon1 in different subcellular compartments.

(A & C) Time-lapse pseudocolored fluorescence response of HEK 293T cells expressing cytosol or mitochondrial localized rxcpmMaroon1 in response to 500 μM aldrithiol-2. Scale bar, 10 μm. **(B & D)** Time course of fluorescence response (F/F_0) of HEK 293T cells transfected with pcDNA3-rxcpmMaroon1 or pMito-rxcpmMaroon1 in response to aldrithiol-2 treatment. Fluorescence intensities were normalized to the values of cells at t = 0 min. Data displays the mean ± s.e.m. of 9 cells from triplicates. Arrow indicates the time point of aldrithiol-2 treatment.

5.4 Conclusions

Our previous work has expanded the redox-active single fluorescent protein to the red fluorescence spectrum. In this work, we further expanded the current collection to an even longer wavelength region. We developed a novel far-red redox-active fluorescent sensor, rxcpmMaroon1 by fusing truncated hook domain containing active cysteine to the N-termini of a circularly permuted far-red fluorescent protein (cpmMaroon185). Degenerate codon was used to optimize the linkers between active cysteine and cpmMaroon185, and adjust the amino acid close to the active cysteine. We also performed directed evolution to optimize the protein expression, brightness and responsiveness. The best mutant displayed ~2-fold fluorescence enhancement upon oxidation and was applied to living mammalian cells to detect the redox changes. The fluorescence changes in different subcellular compartments presented different patterns. Therefore, redox dynamics of various subcellular domains may be monitored simultaneously by combination of rxcpmMaroon1 and redox-active fluorescent proteins of other colors. Besides, rxcpmMaroon1 provides an additional channel for multiparameter imaging in living cells. Moreover, rxcpmMaroon1 can be fused with redox-enzyme or other redox sensory domain to build up diverse redox biosensor for specific redox molecules, such as glutathione, thioredoxin and hydrogen peroxide. Taken together, this work is critical for expanding the color palette of genetically encoded single fluorescent protein-based redox probes, and we expected that it can further facilitate new studies in redox biology.

5.5 Reference

1. To, E. E.; Vlahos, R.; Luong, R.; Halls, M. L.; Reading, P. C.; King, P. T.; Chan, C.; Drummond, G. R.; Sobey, C. G.; Broughton, B. R., Endosomal NOX2 oxidase exacerbates virus pathogenicity and is a target for antiviral therapy. *Nat. Commun.* **2017,** *8* (1), 1-17.
2. Thomas, D. C., The phagocyte respiratory burst: Historical perspectives and recent advances. *Immunol. Lett.* **2017,** *192*, 88-96.
3. Valko, M.; Rhodes, C. J.; Moncol, J.; Izakovic, M.; Mazur, M., Free radicals, metals and antioxidants in oxidative stress-induced cancer. *Chem. Biol. Interact.* **2006,** *160* (1), 1-40.
4. Srinivas, U. S.; Tan, B. W.; Vellayappan, B. A.; Jeyasekharan, A. D., ROS and the DNA damage response in cancer. *Redox Biol.* **2019,** *25*, 101084.
5. Andersen, J. K., Oxidative stress in neurodegeneration: cause or consequence? *Nat. Med.* **2004,** *10* (Suppl 7), S18-S25.
6. Bowler, R. P.; Barnes, P. J.; Crapo, J. D., The role of oxidative stress in chronic obstructive pulmonary disease. *COPD: Journal of Chronic Obstructive Pulmonary Disease* **2004,** *1* (2), 255-277.
7. Pang, Y.; Zhang, H.; Ai, H.-w., Genetically Encoded Fluorescent Redox Indicators for Unveiling Redox Signaling and Oxidative Toxicity. *Chem. Res. Toxicol.* **2021,** *34* (8), 1826-1845.
8. Hanson, G. T.; Aggeler, R.; Oglesbee, D.; Cannon, M.; Capaldi, R. A.; Tsien, R. Y.; Remington, S. J., Investigating mitochondrial redox potential with redox-sensitive green fluorescent protein indicators. *J. Biol. Chem.* **2004,** *279* (13), 13044-53.
9. Østergaard, H.; Tachibana, C.; Winther, J. R., Monitoring disulfide bond formation in the eukaryotic cytosol. *J. Cell Biol.* **2004,** *166* (3), 337-345.
10. Fan, Y.; Chen, Z.; Ai, H. W., Monitoring redox dynamics in living cells with a redox-sensitive red fluorescent protein. *Anal. Chem.* **2015,** *87* (5), 2802-10.
11. Fan, Y.; Ai, H. W., Development of redox-sensitive red fluorescent proteins for imaging redox dynamics in cellular compartments. *Anal. Bioanal. Chem.* **2016,** *408* (11), 2901-11.
12. Lin, M. Z.; McKeown, M. R.; Ng, H. L.; Aguilera, T. A.; Shaner, N. C.; Campbell, R. E.; Adams, S. R.; Gross, L. A.; Ma, W.; Alber, T.; Tsien, R. Y., Autofluorescent proteins with excitation in the optical window for intravital imaging in mammals. *Chem Biol* **2009,** *16* (11), 1169-79.
13. Bajar, B. T.; Lam, A. J.; Badiee, R. K.; Oh, Y. H.; Chu, J.; Zhou, X. X.; Kim, N.; Kim, B. B.; Chung, M.; Yablonovitch, A. L.; Cruz, B. F.; Kulalert, K.; Tao, J. J.; Meyer, T.; Su, X. D.; Lin, M. Z., Fluorescent indicators for simultaneous reporting of all four cell cycle phases. *Nat. Methods* **2016,** *13* (12), 993-996.
14. Fabritius, A.; Ng, D.; Kist, A. M.; Erdogan, M.; Portugues, R.; Griesbeck, O., Imaging-based screening platform assists protein engineering. *Cell chemical biology* **2018,** *25* (12), 1554-1561. e8.
15. Wu, T.; Pang, Y.; Ai, H.-w., Circularly permuted far-red fluorescent proteins. *Biosensors* **2021,** *11* (11), 438.
16. Wu, T.; Kumar, M.; Zhang, J.; Zhao, S.; Drobizhev, M.; McCollum, M.; Anderson, C. T.; Wang, Y.; Pokorny, A.; Tian, X., A genetically encoded far-red

fluorescent indicator for imaging synaptically released Zn2+. *Science Advances* **2023,** *9* (9), eadd2058.
17. Ai, H.-w.; Baird, M. A.; Shen, Y.; Davidson, M. W.; Campbell, R. E., Engineering and characterizing monomeric fluorescent proteins for live-cell imaging applications. *Nat. Protoc.* **2014,** *9* (4), 910-928.
18. Jones, D. P., [11] Redox potential of GSH/GSSG couple: assay and biological significance. In *Methods Enzymol.*, Elsevier: 2002; Vol. 348, pp 93-112.
19. Meyer, A. J.; Dick, T. P., Fluorescent protein-based redox probes. *Antioxid. Redox Signal.* **2010,** *13* (5), 621-650.

Chapter 6 Summary and Perspectives

Genetically encoded redox indicators (GERIs) have gained popularity for illuminating spatiotemporal regulation of redox signaling processes. Different design strategies and engineering methods have been employed to develop diverse GERIs. The most simple and robust strategy is to introduce a pair of active cysteine residues to the surface of a single fluorescent protein (FP) scaffold. The redox reaction of the thiol groups can lead to the confirmational change of the FP, leading to the subsequent modulation of the FP biophysical properties.[1, 2] However, GERIs developed via this strategy often present limited specificity to different analytes. An alternative design strategy was utilized to overcome this drawback. Instead of incorporation cysteine pairs, a redox-active enzyme was fused with a redox-active FP through a linker. The redox relay connects the redox status of the redox-active enzyme with the fused FP. GERIs display specificity to glutathione, thioredoxin and hydrogen peroxide have been developed with this strategy. [3-5] Another efficient strategy to develop GERIs is to utilize the genetic code expansion technology to introduce noncanonical amino acids (ncAAs) into specific site of FPs. The functional groups of the ncAAs provide the specificity of the indicator to the analytes of interest.[6-9] In addition to the abovementioned strategies, GERIs have also been generated via fusing a redox sensory domain of a specific analyte with a circularly permutated FP (cpFP). Several GERIs for monitoring hydrogen peroxide[10-14] or nicotinamide adenine dinucleotide (NAD^+/NADH) redox couple[15] were created by using this strategy. All these strategies expanded the collection of current GERIs and provides more powerful tools to further study the redox biology of living organisms.

In chapter 2, I successfully developed a second generation thioredoxin1 (Trx1) redox indicator—TrxRFP2. Our lab previously developed a Trx1 indicator — TrxRFP1 by fusing human Trx1 (hTrx1) enzyme with redox-active cp red FP (rxRFP1) via a Gly-Ser rich floppy linker. Based

on this version TrxRFP1, I performed directed evolution to create random mutagenesis libraries and screened the libraries with enzymatic assay for greater dynamic change. TrxRFP2 exhibited faster kinetics and greater fluorescence change compared to TrxRFP1 in vitro and in mammalian cells in response to chemical-induced Trx redox change. Using the similar engineering strategy, I fused mitochondria-specific Trx enzyme (hTrx2) with a redox-active red FP (rxRFP1.1) to generate a novel Trx indicator—MtrxRFP2. MtrxRFP2 responded more quickly with greater dynamic change than TrxRFP1 when localized in mitochondria. All these three GERIs became a powerful toolset for Trx redox signaling. They can be utilized with other GERIs of different colors for multicolor imaging of different redox parameters.

In chapter 3, I described a red fluorescent redox indicator for peroxynitrite ($ONOO^-$) detection. This indicator was generated by incorporating the ncAA, *p*-boronophenylalanine (*p*BoF), into the site localized in proximity to the chromophore of a cp red FP (cpRFP). The resultant indicator pnRFP showed ~ 5-fold of fluorescence decrease in response to $ONOO^-$ in vitro. When applied to mammalian cell culture, pnRFP also presented good response to $ONOO^-$ generation caused by chemical and physiological-relevant stimulation. Further, the mechanism of $ONOO^-$ response has been investigated with X-ray crystallography and NMR. Development of pnRFP expands the color of genetically encoded peroxynitrite biosensors red fluorescence spectrum. It also provides insight into the design strategy of ncAA-based FP redox biosensors. Instead of directly introducing ncAAs to modify the chromophores of FPs, [6-9] modifying chromophore-surrounding residues with ncAAs has now proven to be another usable strategy for turning FPs to redox biosensors. This work may provide inspiration to tuning the chemoreactivity of biosensors via different ncAA incorporation.

I described a novel genetically encoded red hydrogen peroxide (H_2O_2) biosensor in chapter 4. Starting from wild-type (wt) mScarlet-I, I first created a circularly permutated variant – cpmScarlet, showing good brightness and similar fluorescence spectrum as the parental mScarlet-I. Next, two H_2O_2 sensory domains OxyR were fused to the N- and C-terminus of cpmScarlet respectively. I then constructed saturated mutagenesis library to optimize the linkers between OxyR domains and cpmScarlet. Moreover, directed evolution was deployed to screening greater brightness and fluorescence change. The protein engineering process resulted a circularly permutated mScarlet-based genetically encoded hydrogen peroxide red fluorescent indicator with high brightness and minimal photoactivation (SHRIMP). SHRIMP displayed a dose-dependent response to H_2O_2 with a maximal 5-fold fluorescence increase. The photophysical properties test indicated that SHRIMP had minimal photoactivation compared to cpmApple-based biosensor. SHRIMP was transfected into different mammalian cell lines as well as isolated tissue to monitor the H_2O_2 generation in biological samples. I also verified the application of SHRIMP in combination with green fluorescent biosensor for multiple parameters imaging in living cells. With minimal blue-light photoactivation, SHRIMP could be a robust tool for in vivo study in combination with channelrhodopsin-based optogenetics or other green/blue illumination biosensors. In addition, this work proved cpmScarlet to be a usable readout modality for the development of GERIs. We expect it to be a valuable asset for developing not only single FP-based genetically encoded indicators but also FRET biosensors.

In chapter 5, I developed a redox-sensitive far-red fluorescent biosensor — rxcpmMaroon1 for live cell imaging. rxcpmMaroon1 was adapted from a far-red zinc biosensor via effective protein engineering processes, including saturated mutagenesis, site-specific mutagenesis and random mutagenesis. The attached active cysteine residues at its N- and C-terminus tuned

cpmMaroon185 to be sensitive to the environmental redox changes. I applied rxcpmMaroon1 to different subcellular compartments of mammalian cells to detect real-time redox dynamics in response to chemical stimulation. This work further expanded the color palette of redox-active single FP to more red-shifted spectrum range. Further work could be performed to enhance the fluorescence dynamic range of this biosensor as well as fusing it with redox-active enzyme to create redox-relay based GERIs.

To summarize, my work has greatly expanded the library of current GERIs. With extended emission wavelength to red and far-red spectrum range, live cell or in vivo imaging of redox dynamics can be achieved with lower cytotoxicity, reduced sample scattering as well as better tissue penetration. The expanded color palettes allow multicolor imaging to monitor different parameters simultaneously, allowing a more far-reaching understanding of cellular signaling pathways and their cross-talking.

6.1 Reference

1. Hanson, G. T.; Aggeler, R.; Oglesbee, D.; Cannon, M.; Capaldi, R. A.; Tsien, R. Y.; Remington, S. J., Investigating mitochondrial redox potential with redox-sensitive green fluorescent protein indicators. *J. Biol. Chem.* **2004,** *279* (13), 13044-53.
2. Ostergaard, H.; Henriksen, A.; Hansen, F. G.; Winther, J. R., Shedding light on disulfide bond formation: engineering a redox switch in green fluorescent protein. *EMBO J.* **2001,** *20* (21), 5853-62.
3. Gutscher, M.; Pauleau, A. L.; Marty, L.; Brach, T.; Wabnitz, G. H.; Samstag, Y.; Meyer, A. J.; Dick, T. P., Real-time imaging of the intracellular glutathione redox potential. *Nat. Methods* **2008,** *5* (6), 553-9.
4. Fan, Y.; Makar, M.; Wang, M. X.; Ai, H. W., Monitoring thioredoxin redox with a genetically encoded red fluorescent biosensor. *Nat. Chem. Biol.* **2017,** *13* (9), 1045-1052.
5. Gutscher, M.; Sobotta, M. C.; Wabnitz, G. H.; Ballikaya, S.; Meyer, A. J.; Samstag, Y.; Dick, T. P., Proximity-based protein thiol oxidation by H2O2-scavenging peroxidases. *J. Biol. Chem.* **2009,** *284* (46), 31532-40.
6. Chen, S.; Chen, Z. J.; Ren, W.; Ai, H. W., Reaction-based genetically encoded fluorescent hydrogen sulfide sensors. *J. Am. Chem. Soc.* **2012,** *134* (23), 9589-92.
7. Chen, Z. J.; Ren, W.; Wright, Q. E.; Ai, H. W., Genetically encoded fluorescent probe for the selective detection of peroxynitrite. *J. Am. Chem. Soc.* **2013,** *135* (40), 14940-3.
8. Chen, Z. J.; Ai, H. W., A highly responsive and selective fluorescent probe for imaging physiological hydrogen sulfide. *Biochemistry* **2014,** *53* (37), 5966-74.
9. Chen, Z.; Zhang, S.; Li, X.; Ai, H. W., A high-performance genetically encoded fluorescent biosensor for imaging physiological peroxynitrite. *Cell Chem Biol* **2021**.
10. Belousov, V. V.; Fradkov, A. F.; Lukyanov, K. A.; Staroverov, D. B.; Shakhbazov, K. S.; Terskikh, A. V.; Lukyanov, S., Genetically encoded fluorescent indicator for intracellular hydrogen peroxide. *Nat. Methods* **2006,** *3* (4), 281-6.
11. Markvicheva, K. N.; Bilan, D. S.; Mishina, N. M.; Gorokhovatsky, A. Y.; Vinokurov, L. M.; Lukyanov, S.; Belousov, V. V., A genetically encoded sensor for H2O2 with expanded dynamic range. *Biorg. Med. Chem.* **2011,** *19* (3), 1079-1084.
12. Bilan, D. S.; Pase, L.; Joosen, L.; Gorokhovatsky, A. Y.; Ermakova, Y. G.; Gadella, T. W.; Grabher, C.; Schultz, C.; Lukyanov, S.; Belousov, V. V., HyPer-3: a genetically encoded H(2)O(2) probe with improved performance for ratiometric and fluorescence lifetime imaging. *ACS Chem. Biol.* **2013,** *8* (3), 535-42.
13. Ermakova, Y. G.; Bilan, D. S.; Matlashov, M. E.; Mishina, N. M.; Markvicheva, K. N.; Subach, O. M.; Subach, F. V.; Bogeski, I.; Hoth, M.; Enikolopov, G.; Belousov, V. V., Red fluorescent genetically encoded indicator for intracellular hydrogen peroxide. *Nat Commun* **2014,** *5*, 5222.
14. Pak, V. V.; Ezerina, D.; Lyublinskaya, O. G.; Pedre, B.; Tyurin-Kuzmin, P. A.; Mishina, N. M.; Thauvin, M.; Young, D.; Wahni, K.; Martinez Gache, S. A.; Demidovich, A. D.; Ermakova, Y. G.; Maslova, Y. D.; Shokhina, A. G.; Eroglu, E.; Bilan, D. S.; Bogeski, I.; Michel, T.; Vriz, S.; Messens, J.; Belousov, V. V., Ultrasensitive Genetically Encoded Indicator for Hydrogen Peroxide Identifies Roles for

the Oxidant in Cell Migration and Mitochondrial Function. *Cell Metab.* **2020,** *31* (3), 642-653 e6.
15. Zhao, Y.; Hu, Q.; Cheng, F.; Su, N.; Wang, A.; Zou, Y.; Hu, H.; Chen, X.; Zhou, H. M.; Huang, X.; Yang, K.; Zhu, Q.; Wang, X.; Yi, J.; Zhu, L.; Qian, X.; Chen, L.; Tang, Y.; Loscalzo, J.; Yang, Y., SoNar, a Highly Responsive NAD+/NADH Sensor, Allows High-Throughput Metabolic Screening of Anti-tumor Agents. *Cell Metab.* **2015,** *21* (5), 777-89.